GPS-based investigations of Greenland Ice Sheet dynamics

Samuel Huckerby Doyle

A thesis submitted in fulfilment of the requirements for the degree of Doctor of Philosophy

10 December 2014

Aberystwyth University

Supervisors: Prof. Alun Hubbard and Prof. Bryn Hubbard

Declaration and statements

Declaration

This work has not previously been accepted in substance for any degree and is not being concurrently submitted in candidature for any degree.

Signed ..... Date .....

Statement 1

This thesis is the result of my own investigations except where otherwise stated. Other sources are acknowledged giving explicit references. A bibliography is appended.

Signed ..... Date .....

Statement 2

I hereby give consent for my thesis, if accepted, to be available for photocopying and for inter-library loan, and for the title and summary to be made available to outside organisations.

Signed ..... Date .....

Acknowledgements

I'd like to to thank Alun Hubbard for the opportunity to undertake this investigation and for his guidance over the years. I also thank my secondary supervisor, Bryn Hubbard, for his invaluable advice. I am also indebted to Glenn Jones and Jason Box for the informal supervision they have provided and to Christine Dow for discussion of glacier hydrology. I'm grateful for advice on Track software from Matt King, Ian Bartholomew, Tom Herring and Bob King during the early stages of this study. I also thank Shin Sugiyama, Peter Jansson and two anonymous reviewers for their helpful and constructive reviews of two articles published from the work presented here, as well as Andrew Sole and Hilmar Gudmundsson for their comments during the examination of this thesis. I would also like to thank Lillemor Claesson-Liljedahl, Anne Lehtinen and the many members of the Greenland Analogue Project for facilitating collaboration.

For assistance in the field I thank Heidi Sevestre, Christian Helanow, Rickard Pettersen, Katrin Lindback, Lindsay Mackay, Tom Cowton and the inevitable people I have inadvertently overlooked. I also thank Dave Kelly at Aberystwyth University and Neil McNiven at ReUK for technical advice.

The work undertaken in this thesis was funded by SKB-Posiva through the Greenland Analogue Project and by the UK's Natural Environment Research Council (NERC) grants NE/G007195/1 and NE/G005796/1. The NERC Geophysical Equipment Facility, Seis-UK at the University of Leicester, UNAVCO and the Massachusetts Institute of Technology are thanked for equipment, data and software provision. I acknowledge the support of an Aberystwyth University doctoral scholarship.

Finally, I thank my friends, family and colleagues for their support over the last four years.

Abstract

Accurate forecasting of the Greenland Ice Sheet's contribution to global sea level change requires detailed knowledge of how ice flow responds to surface water inputs. Both ice velocities and surface melt have increased significantly over the last decade but recent research suggests that ice flow acceleration over the summer is regulated by the seasonal evolution of the subglacial drainage system. To investigate these and associated processes, a network of continuously-operating, dual-frequency global positioning system (GPS) receivers was deployed on a 140-km-long land-terminating transect in West Greenland, providing centimetre-precise, high-frequency records of ice motion. These data reveal that the enhanced summer flow regime is comprised of discrete, transient accelerations driven by the diurnal melt cycle, rapid in situ supraglacial lake drainage and rainfall/melt events. In 2010, a comprehensive array of instruments captured the rapid (~ 2 hour) drainage of a large supraglacial lake via a 3-km-long fracture, hydraulically-driven through km-thick ice. A further pronounced, widespread and sustained acceleration driven by rainfall and melt, observed in late August 2011, suggests that the predicted increase in cyclonic activity over Greenland may drive widespread off-season melt, rainfall and flow acceleration across the ice sheet. Together these events provide new insights into the basal hydrodynamic controls on ice sheet motion. Furthermore, observations of a persistent year-on-year acceleration in ice flow between 2009 and 2012 at a high elevation site located ~ 50 km inland of the equilibrium line support the hypothesis that the observed inland expansion of supraglacial lakes is driving faster ice flow at high elevations. These observations contrast with the prevailing self-regulation model and reveal that despite surface melt increasing water inputs to the bed are still insufficient to develop effective subglacial drainage in the ice sheet's interior.

Contents

List of Figures

List of Tables

List of acronyms

APPS Automatic Precise Positioning Service

ASTER Advanced Spaceborne Thermal Emission and Reflection Radiometer

AWS Automatic Weather Station

DEM Digital Elevation Model

DMI Danish Meteorological Institute

DOY Day of year

ELA Equilibrium Line Altitude

GEUS Geological Survey of Denmark & Greenland

GPS Global Positioning System

GrIS Greenland Ice Sheet

GNSS Global Navigation Satellite System

IGS International GNSS Service

IMAU Institute for Marine and Atmospheric research Utrecht

MODIS Moderate Resolution Imaging Spectrometer

PDD Positive Degree Day

PPP Precise Point Positioning

PPS Precise Positioning Service

RADAR Radio Detection and Ranging

RINEX Receiver Independent Exchange File

SGL Supraglacial lake

SPP Single Point Positioning

SPS Standard Positioning Service

SLR Sea Level Rise

UTC Coordinated Universal Time

N.b. All times are given in UTC unless otherwise stated.

Chapter 1

Introduction

The overall aim of this thesis is to gain insights into basal hydro-dynamical forcing on Greenland Ice Sheet (GrIS) motion. It is motivated by the need to understand how the ice sheet will dynamically respond to projected increases in atmospherically forced melt: it specifically addresses the concern that surface melt-induced acceleration could increase mass loss under a projected warmer climate.

The pace of publishing in Greenland ice dynamics is rapid and the following introduction only considers studies published before the end of 2012. Attempting to accommodate every new study as they were published would require continuous and impractical updates. Instead, studies published after this date are discussed in relation to the contemporaneous findings of this thesis in Chapter 8.

1.1 The Greenland Ice Sheet: mass loss and climate change

The GrIS is one of three contemporary ice sheets on Earth, together with the East and West Antarctic Ice Sheets. Covering an area of 1.71 million km^2, the GrIS extends to an elevation of ∼3,300 m above sea level, and is in excess of > 3 km thick in places. It is the largest ice mass in the northern hemisphere representing one tenth of the global ice surface area (Bamber and others, 2001). It is currently deglaciating: it is losing mass and is out of balance with the climate. The loss of ice from Greenland has important implications for society as 2.85 million gigatonnes (Gt) of frozen fresh water are locked within it. This is equivalent to a global sea level rise (SLR) of 7.36 m (Bamber and others, 2013), if it were to melt completely.

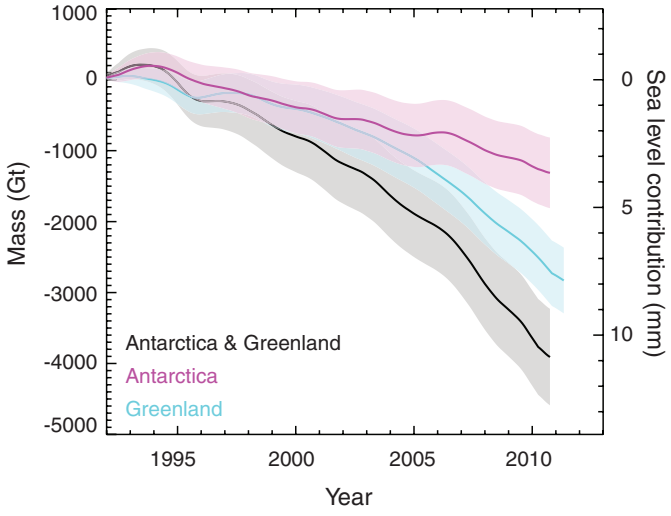

Figure 1.1: Cumulative changes in the mass of the Greenland and Antarctic ice sheets between 1992 and 2011 determined from a reconciliation of measurements acquired using multiple techniques. After Shepherd and others (2012).

Even small changes in ice sheet mass balance are of considerable societal importance as they affect global sea levels and ocean circulation. It is estimated that between 1992

and 2011, the GrIS's contribution to global SLR averaged 0.39 ± 0.14 mm yr^{-1}, which is approximately double the combined contribution of the larger East and West Antarctic Ice Sheets (Shepherd and others, 2012, Figure 1.1). These reconciled estimates suggest that Greenland's contribution to SLR accelerated over the last decade, from 0.14 ± 0.18 mm yr^{-1} between 1992 and 2000 to 0.58 ± 0.10 mm yr^{-1} between 2000 and 2011 (Shepherd and others, 2012). During the five years between 2005 and 2010, Greenland's mass loss was greater still, equivalent to a SLR of 0.72 ± 0.08 mm yr^{-1} (Shepherd and others, 2012).

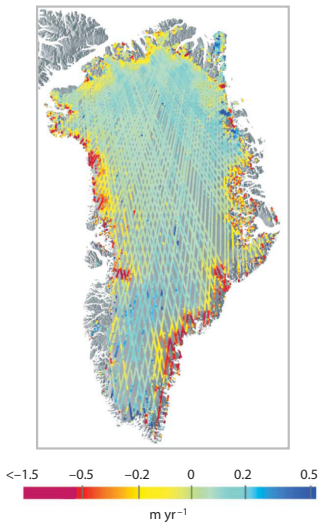

Figure 1.2: Rate of surface elevation change for Greenland for the period 2003-2007. After Pritchard and others (2009).

It has been estimated that GrIS's mass loss is equally split between mass-balance processes (runoff and precipitation) and ice dynamics (van den Broeke and others, 2009). Under a warmer climate, increases in snowfall at higher elevations are expected (Schuenemann and Cassano, 2010) and thickening of the ice sheet's interior on the order of a couple of decimetres per year has been observed over the last two decades (e.g. Krabill and others, 1999, 2000; Johannessen and others, 2005; Pritchard and others, 2009, Figure 1.2). The increase in ablation at the margin is, however, anticipated to far outweigh the increase

in accumulation in the interior and thinning of almost the entire GrIS margin has been observed (Pritchard and others, 2009, Figure 1.2).

Overall, relatively small magnitude thinning is indicated for slow-flowing land-terminating margins (mean = 0.12 m yr^{-1}), attributed to a negative surface mass balance, with relatively large magnitude (mean = 0.84 m yr^{-1}) thinning on fast-flowing marine-terminating glaciers attributed to acceleration and 'dynamic thinning' (Pritchard and others, 2009). The term dynamic thinning represents ice loss due to glacier acceleration instigated by either (i) loss of buttressing at marine termini, through enhanced calving of icebergs, submarine melt or the disintegration of ice shelves, and (ii) surface melt induced acceleration. If the flow of an ice mass accelerates, more ice is transported to lower elevations, where melt rates are higher and where ice is lost through calving and submarine melt. It has been argued that no significant dynamic thinning signal (i.e. significantly above the thinning expected from surface mass balance) has been observed for land-terminating regions of the ice sheet (Sole and others, 2008), although it remains unclear how such regions of the ice sheet will respond to climate warming.

Until recently, and including the Third Assessment Report of the Intergovernmental Panel on Climate Change (IPCC; Church and others, 2001), it was assumed that the Greenland and Antarctic ice sheets would not respond rapidly to climate warming, having response time scales on the order of 100 to 10,000 years. Contemporary modelling studies suggested a warming of 3°C would lead to the virtually-complete elimination of the Greenland Ice Sheet over millennia. The sensitivity of the ice sheet to climate change was thought to be primarily attributed to direct changes in snowfall and surface melt, although the potential for dynamic ice loss was realised:

> 'A key question is whether ice-dynamical mechanisms could operate which would enhance ice discharge sufficiently to have an appreciable additional effect

on sea level rise.' (Church and others, 2001, p. 650).

For a warm based ice mass the majority of ice flow typically occurs at the bed through basal sliding and the deformation of a sediment layer if present, while atmospheric forcing operates at the surface. Surface temperature changes, even of a high magnitude, cannot be effectively transmitted to the bed of ice masses over short (e.g. 100-year timescales, Cuffey and Peterson, 2010). If surface meltwater could penetrate to the ice-bed interface, such hydrological coupling, would facilitate sliding. As an example of the understanding at the time: although Clarke and others (1999) asserted that hydrological coupling does occur on mountain glaciers and that it can potentially be both fast and strong, they state that it "is extremely unlikely that [hydrological coupling] is a significant process in modern continental ice sheets" as "...summer meltwater would have to percolate through great thicknesses of extremely cold ice before a surface to bed coupling could be activated" (Clarke and others, 1999, p. 249).

Based on the consensus that surface-to-bed hydrological coupling does not occur on ice sheets, initial computer simulations of the response of the GrIS to climate warming neglected hydrological coupling entirely. Focussing on thermodynamics, they predicted millennial response time scales to atmospheric warming and the consensus was that moderate warming over Greenland would lead to gradual ice sheet retreat over the next millennium, with increased mass loss in the ablation zone and increased mass gain in the accumulation zone (e.g. Oerlemans, 1991; van de Wal and Oerlemans, 1997; Huybrechts and de Wolde, 1999; Church and others, 2001).

1.2 Hydrological coupling

In 2002, it was demonstrated that ice sheet surface velocities at the equilibrium line altitude (ELA) were coupled to surface melt intensity. Using positive degree days (PDDs; e.g. Braithwaite, 1993) as a proxy for surface melt, Zwally and others (2002) reported a direct correlation between surface melt intensity and summer-time acceleration of $\sim$ 3 to 25% above the winter mean over four years at a site near the equilibrium line, $\sim$35 km from the ice margin (Figure 1.3). The publication of these findings in the high-profile journal Science, led to widespread reporting in the world's media with headlines of "Ice sheet slip-sliding away" and "Greenland's warming ice flowing faster" (Kirby, 2002; Hotz, 2006). The observation of faster summer ice flow in warmer years led the argument for positive feedback between ice flow and melt. In this mechanism, more melt would increase the flow of ice to lower elevations, where temperatures and melt rates are higher.

Subsequent satellite observations (Joughin and others, 2008, 2010) confirmed that both land and marine terminating margins exhibit seasonal flow variability, indicating that surface melt induced acceleration was a widespread process. Initial numerical simulations predicted that the Greenland Ice Sheet would respond much faster than previously thought and estimated that the additional dynamic contribution to sea level rise from Greenland would be 15 to 40 cm by 2500 AD (Parizek and Alley, 2004), and that the surface melt induced acceleration would speed up the decay of the Greenland Ice Sheet (Greve and Sugiyama, 2009). These assertions led the IPCC to state in its Fourth Assessment Report:

> 'Much uncertainty remains, especially related to whether fast-moving glaciers and ice streams are similarly affected, and whether access of melt water to the bed through more than 1 km of cold ice would migrate inland if warming caused surface melting to migrate inland (Alley and others, 2005b). This could thaw

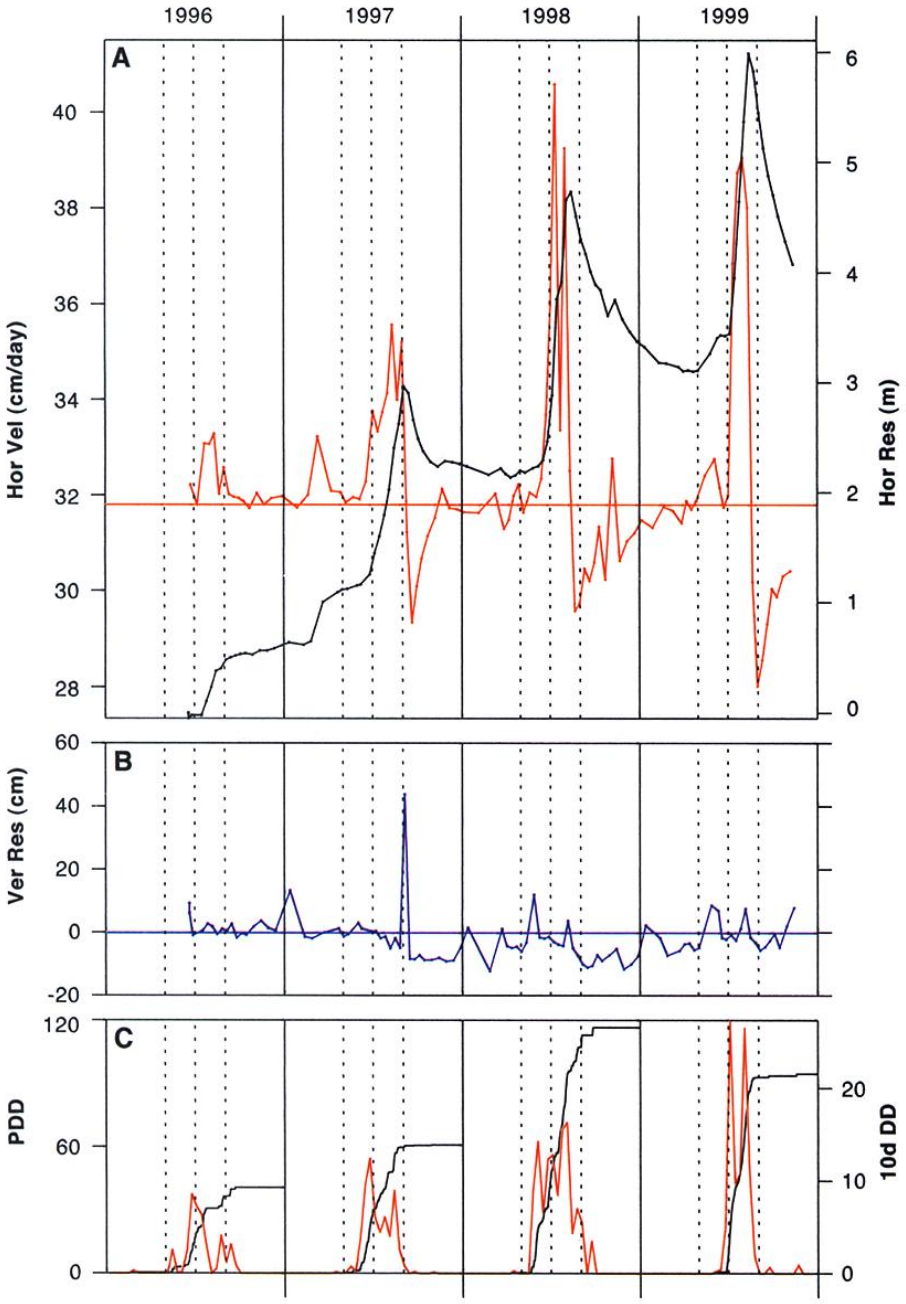

Figure 1.3: Horizontal ice surface velocity (a) compared to (b) relative vertical motion and (c) PDDs and cumulative PDDs over 10 day intervals at Swiss Camp, 35 km from the ice margin. The black line on (a) indicates the cumulative additional motion above that if ice flowed at the winter mean all year round. After Zwally and others (2002).

ice that is frozen to the bed, allowing faster flow through enhanced basal sliding or sub-glacial sediment deformation. Data are not available to assess whether effects of increased surface melting in Greenland have been transmitted to the bed and contributed to ice flow acceleration.' (Lemke and others, 2007, p. 368)

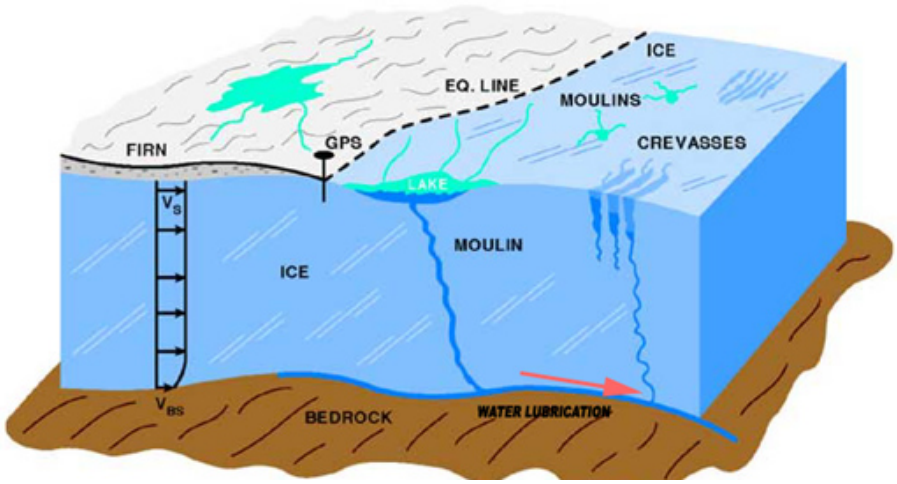

Figure 1.4: Conceptual diagram of the link between ice sheet hydrology and motion at and above the equilibrium line. After Zwally and others (2002).

The correlation between surface melt and ice flow (Figure 1.3) suggests the rapid transport of water to the ice bed interface, which requires hydraulic pathways through kilometre-thick polythermal ice (Figure 1.4). Although it had previously been thought that such 'hydrological coupling' was impossible for the thick, cold ice of the GrIS (e.g. Clarke and others, 1999) others (e.g. Alley and others, 2005a) invoked the process of hydraulically driven fracture, hereafter termed hydrofracture for brevity. Hydrofracture of ice had received much theoretical consideration (e.g. Weertman, 1971a,b, 1973; van der Veen, 1998) but had only been directly observed on a relatively thin (150 m thick) Arctic Glacier (Boon and Sharp, 2003). Renewed interest in the hydrofracture mechanism followed the findings of Zwally and others (2002). Previously, Alley and others (2005a) had postulated that

storage of water in supraglacial lakes may be important for providing the large volumes of water required to drive a fracture through Greenland's kilometre-thick ice.

Although the rapid drainage of supraglacial lakes had already been observed in Svalbard (Liestol and others, 1980), Ellesmere Island (Boon and Sharp, 2003), and on Russell (Russell, 1993) and Ryder (Joughin and others, 1996) glaciers in Greenland, the importance of such drainage events for ice dynamics was not fully realised until 2008. In 2006, Das and others (2008) captured the rapid in situ drainage of a large supraglacial lake using global positioning system (GPS) receivers, broadband seismometers and water level loggers. These records revealed metre-scale ice surface uplift, horizontal acceleration and seismicity during the rapid (< 2 h) drainage of a large supraglacial lake through 980 m-thick ice on the western margin of the Greenland Ice Sheet (Fig. 1.5). The observation of surface uplift and horizontal acceleration during lake drainage suggests the rapid delivery of surface water to the ice-bed interface overwhelmed the capacity of the subglacial drainage system, driving transient high subglacial water pressures, hydraulic jacking and ice sheet acceleration (e.g. Box and Ski, 2007; Das and others, 2008; Pimental and Flowers, 2010).

Estimates from subsequent modelling experiments suggested that lakes larger than 0.25 to 0.8 km in diameter contain sufficient water to propagate a hydrofracture through 1 to 1.5 km thick ice (Krawczynski and others, 2009). Many lakes on the margin of the Greenland Ice Sheet attain this size or larger (e.g. Box and Ski, 2007) suggesting rapid in situ lake drainage via hydrofracture has the potential to be a widespread process. A plethora of remote sensing and modelling studies have now investigated supraglacial lakes (e.g. Echelmeyer and others, 1991; Lüthje and others, 2006; Box and Ski, 2007; McMillan and others, 2007; Sneed and Hamilton, 2007; Georgiou and others, 2009; Sundal and others, 2009; Lampkin, 2011; Lampkin and VanderBerg, 2011; Selmes and others, 2011; Leeson and others, 2012; Liang and others, 2012; Sneed and Hamilton, 2011; Johansson, 2012; Johansson and Brown,

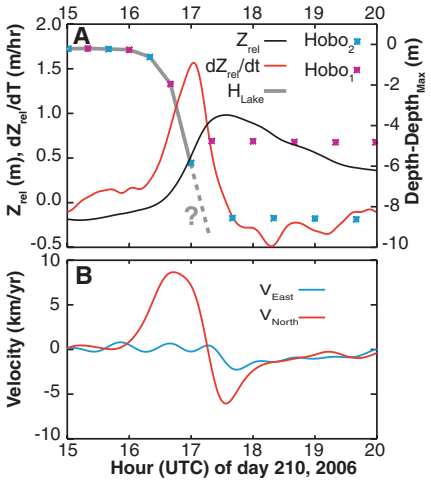

Figure 1.5: GPS and lake level data from the lake drainage event captured by Das and others (2008). (a) relative elevation (Z_{rel}, black line), rate of elevation change (red line) and lake level (grey line) recorded by the two HOBO loggers, (b) north (red) and east (blue) components of velocity for the same GPS. After Das and others (2008)

.

2012; Howat and others, 2013; Joughin and others, 2013; Lettang and others, 2013; Morriss and others, 2013; Fitzpatrick and others, 2014). To summarise witha focus on ice dynamics: these studies have revealed that (i) fast (< 1 day) draining lakes are most prevalent in the southwest sector of the Greenland Ice Sheet, which accounted for 61% of all fast draining lakes in Greenland (Selmes and others, 2011), (ii) supraglacial lake drainage is responsible for spatial variations in ice sheet flow (Joughin and others, 2013), and (iii) supraglacial lakes form at higher elevations during warmer years (Liang and others, 2012; Howat and others, 2013; Fitzpatrick and others, 2014).

As early as 2007, it was speculated that "should warming allow the inland migration of ... meltwater lakes ... then thawing and enhanced lubrication of the bed in those regions will be likely" (Bamber and others, 2007, p. 4). The expected expansion of meltwater lakes to higher elevations has now been observed (Liang and others, 2012; Howat and others,

2013; Fitzpatrick and others, 2014) but as Howat and others (2013, p. 203) asserted "data are not yet available to investigate a corresponding change in ice dynamics". As originally asserted by Zwally and others (2002), "short-term [i.e. seasonal] velocity variations have [still] not been observed in the flow of ice sheets away from ice streams and outlet glaciers". Similarly Parizek and Alley (2004, p.1025) asserted that their findings highlight "the importance of additional field studies in determining the upglacier extent of ... [the melt-induced acceleration] mechanism for enhanced sliding, the surface-meltwater catchment area that ultimately contributes to basal lubrication, and the minimum quantity of meltwater required to initiate and sustain increased flow rates."

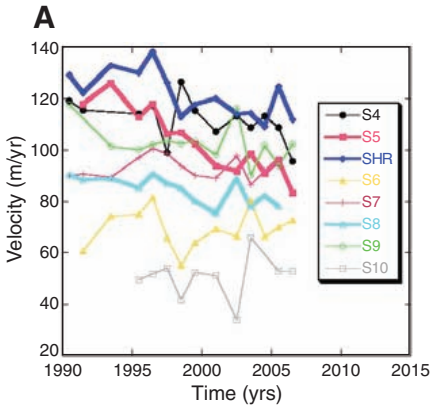

Figure 1.6: Velocities across the Kangerlussuaq (K-) transect between 1990 and 2007. Site names are given in the legend. After van de Wal and others (2008)

Subsequent studies have, however, questioned the validity of the so called 'Zwally effect' over long (i.e. interannual) timescales. Price and others (2008) argued that the acceleration observed by Zwally and others at the ELA could be the result of longitudinal coupling to marginal ice. This assertion is at least partly incorrect as Zwally and others also observed coincident ice sheet surface uplift (Figure 1.3b) that is indicative of localised hydraulic ice-bed separation (e.g. Iken, 1981; Sugiyama and Gudmundsson, 2004). Nevertheless, the question of whether ice in the interior is longitudinally coupled to marginal ice remains

both important and unanswered. It was partially addressed by Bartholomew and others (2011a) who revealed that the seasonal velocity variation does extend further upglacier in warmer years. The observation by van de Wal and others (2008) of a slight, but significant, decline in annual velocities on Russell Glacier between 1990 and 2007 (Figure 1.6) despite increasing surface melt (measured using surface mass balance stakes) suggested that the positive feedback mechanism between melt and ice flow was a seasonal process and that over longer periods the ice sheet self-regulated its dynamic response to increased surface melt. Earlier, Truffer and others (2005) had criticised the extrapolation of the simple correlation between melt and velocity, while presenting evidence of low annual velocities on Black Rapids Glacier despite record setting melt rates during the exceptionally warm summer (in North America) of 2004. It has long been known that the subglacial drainage efficiency of alpine glaciers adapts to the melt water flux (e.g. Iken, 1981; Fountain, 1994; Hubbard and Nienow, 1997). Drawing on existing glaciohydrological theory both Truffer and others (2005) and van de Wal and others (2008) argued that the regulating effect of subglacial drainage development on ice flow should be taken into account in Greenland.

1.3 The regulation of ice flow by subglacial hydrology

The dynamics of a land-terminating ice mass are relatively simple. Ice moves downhill under the gravitational driving stress. The velocity is governed by the frictional resistance (or traction) at its base, and the amount of internal deformation within the ice column (e.g. Cuffey and Peterson, 2010). If we assume variations in internal deformation are negligible then variations in surface ice motion are a result of spatial and temporal variations in basal traction. Shearing of soft subglacial sediment allows the fastest motion, in for example ice streams, with frozen bed conditions representing the other, slower, end of the continuum.

The input of water to the ice-bed interface affects traction at the bed for both hard and soft beds, by either sediment weakening or hydraulic ice bed separation (jacking). High magnitude inputs of water cause extensive reductions in traction, but they also have the propensity to form efficient subglacial drainage systems, which thereafter drain the bed leading to a consequent lowering of effective pressure, and therefore lower rates of basal sliding. The feedbacks between water inputs, subglacial hydrological development and velocities are key to the dynamic response of a land-terminating ice mass to changes in external forcing.

Land terminating outlet glaciers in Greenland show a similar dynamic behaviour to Alpine and high Arctic valley glaciers: as melt progresses upglacier the hydrological system increases in capacity in response to the increased water flux to the bed (e.g. Bartholomew and others, 2010). The highest velocities typically occur at the onset of the melt season (known as the spring event on Alpine Glaciers) when the first influx of surface water to the bed overwhelms the inefficient drainage system present at the end of winter (Harper and others, 2002; Mair and others, 2003; Bartholomew and others, 2010; Hoffman and others, 2011). During the 'spring event', water is forced under high pressure into the distributed drainage system leading to a rapid reduction in basal traction and coupling (e.g. Iken and others, 1983; Kamb, 1987; Harper and others, 2002). Ice velocities then gradually decrease into mid-summer, despite generally high melt rates (Figure 1.7), as it is argued, a more efficient system of channelised drainage develops (e.g. Hubbard and Nienow, 1997; Fountain and Walder, 1998; Bartholomew and others, 2010). Such Röthlisberger channels, which are incised upwards into the ice by heat released by the turbulent flow of water, evacuate large volumes of water at low-pressure, draining the distributed system and increasing basal coupling (Röthlisberger, 1972).

Transient accelerations still occur whenever the capacity of the drainage system is chal-

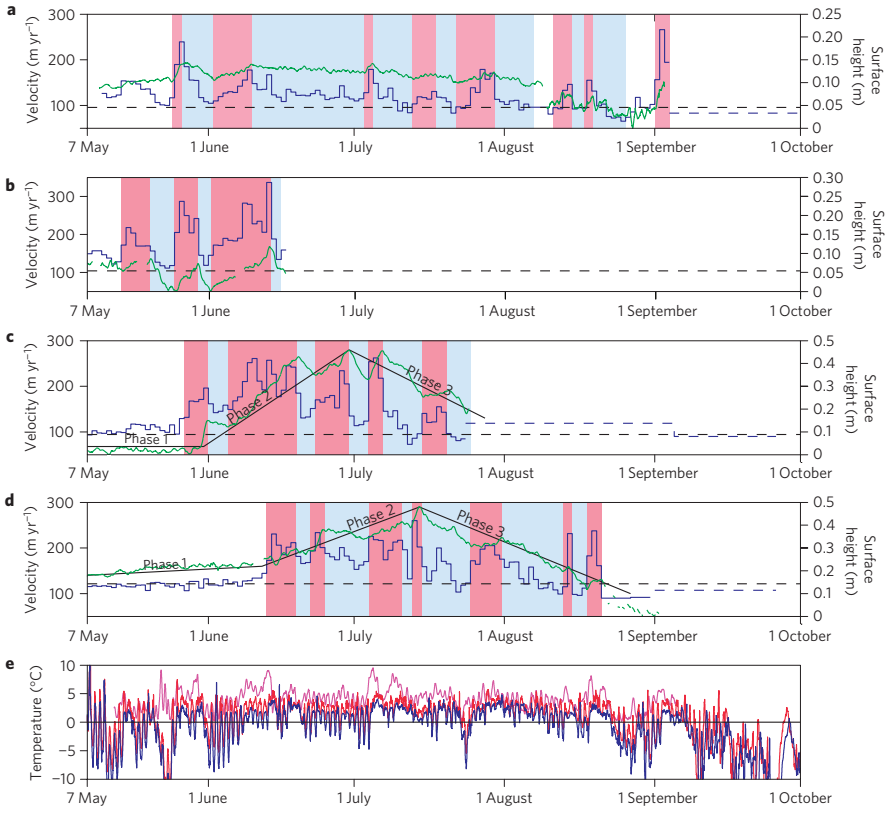

Figure 1.7: The seasonal development of melt-induced ice velocity variations. Adapted from Bartholomew and others (2010)

lenged by increases in surface water delivery (Schoof, 2010; Bartholomew and others, 2012). Such transient accelerations, which are superimposed on the seasonal velocity cycle, occur in response to exceptional melt events or supraglacial lake drainage events (e.g. Figure 1.5, Hoffman and others, 2011). The velocity minimum occurs at the end of the melt season when declining melt rates are delivered to a drainage system with tranisent over capacity (e.g. Colgan and others, 2009; Bartholomew and others, 2010, 2011a; Colgan and others, 2011, 2012). During winter it is theorised that the subglacial drainage system closes through creep closure of the ice. Ice velocities in Greenland are known to increase over

winter (by as much as $\sim 20\%$) from the end-of-melt-season minimum (Joughin and others, 2010; Fitzpatrick and others, 2013), presumably as the remaining basal water pressurises in response to creep closure and the subglacial drainage system reverts to a distributed, inefficient mode. Over short time scales, GPS observations confirm the direct coupling between melt and ice flow: diurnal variations in ice sheet motion peak around 2 hours after peak daily melting (Shepherd and others, 2009, Figure 1.8). Such GPS observations are spatially limited to the discrete points they sample and remote sensing measurements are more practical for examining the wider spatial variation.

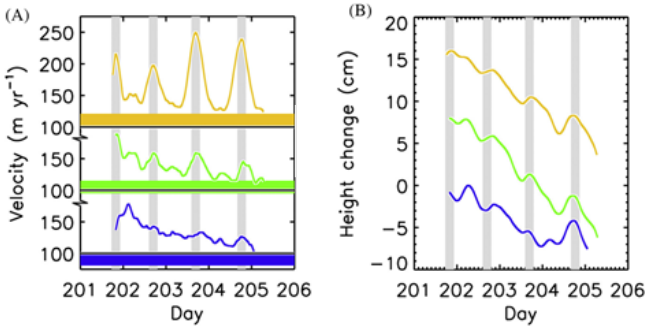

Figure 1.8: Diurnal variations in (a) surface ice velocity and (b) surface uplift measured at three sites 37 km (yellow), 53 km (green) and 72 km (blue) from the terminus of Russell Glacier. After Shepherd and others (2009).

In 2011, Palmer and others (2011) captured a unique and unrepeated snapshot into the spatial velocity variation across Russell Glacier catchment, West Greenland, when the two European Remote Sensing (ERS) satellites orbited in tandem in 1995/96 allowing 1 day repeat synthetic aperture radar interferometry (InSar) that has not been possible since. These velocity maps (e.g. Fig 1.9) revealed that high-magnitude velocity variations occur up to 100 km from the ice margin with a strong spatial variation in flow. Acceleration is focused into fractal flow units, which arguably reflect the control of subglacial topography on ice flow. It remains unclear, however, whether the velocity map of Figure 1.9, and

particularly the strength and inland extent of the acceleration observed, is either (i) representative of typical late summer velocities as postulated by the authors, (ii) indicating the short-lived dynamic response of the ice sheet to supraglacial lake drainage events, or (iii) is capturing a more unusual event.

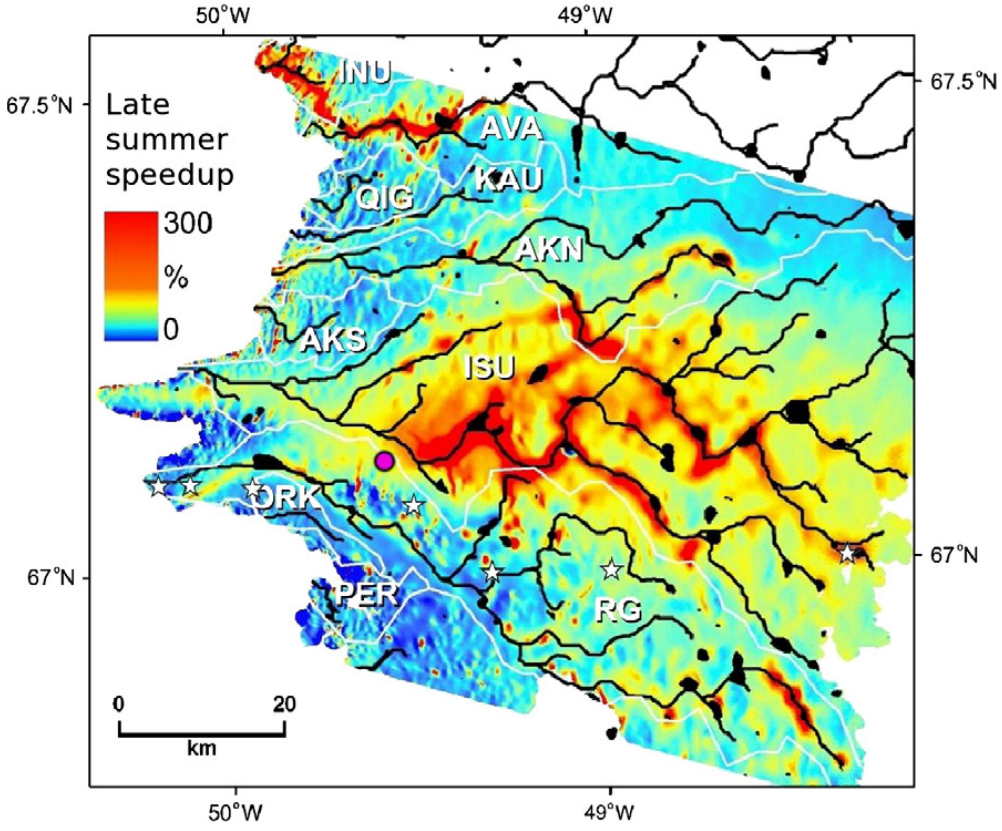

Figure 1.9: Late summer velocity map minus the mean winter velocity map superimposed on supraglacial drainage catchments (white), surface hydrology (black) and the K-transect locations (white stars). After Palmer and others (2011).

Drawing on the conclusions of Schoof (2010), Sundal and others (2011) presented evidence that increased melt during warmer summers leads to an earlier transition to efficient subglacial drainage and an overall lower annual velocity during warmer years (Fig. 1.10). Due

to the limitations of the remote sensing technique used, the analysis of Sundal and others (2011) is, however, restricted to the first $\sim$ 40 km of five outlet glaciers on the western margin. There are several reasons why this marginal area may not be representative of the behaviour of the ice sheet at higher elevations. Hence, the application of processes from alpine glaciers to the Greenland Ice Sheet as a whole may not be straightforward.

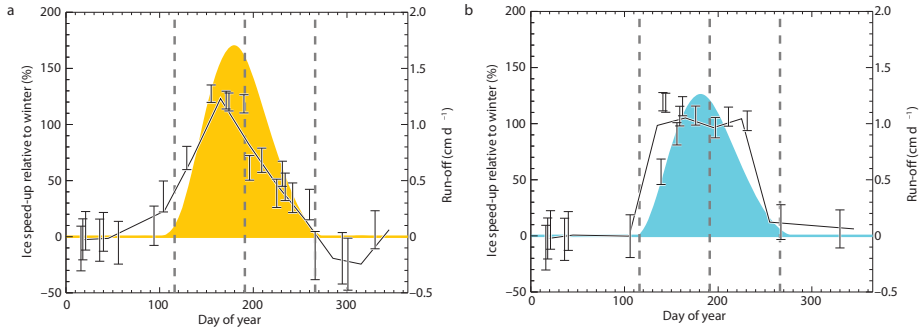

Figure 1.10: Ice velocity relative to the winter mean for (a) years of high melting (1995 and 1998) and (b) years of low melting (1993, 1996 and 1997). Velocity data were calculated between 35-day intervals using European Remote Sensing satellite radar data and represent averages from two glaciers in the elevation bands 500 to 600 m and 400 to 500 m. The orange and blue shading are estimates of daily surface runoff. After Sundal and others (2011).

1.3.1 Problems with the Alpine analogue

The Alpine analogue hinges on the development of efficient subglacial drainage which is hypothesised to evacuate large volumes of water through low-pressure Röthlsberger (R-) channels, increasing basal coupling and regulating basal sliding (e.g. Röthlisberger, 1972; Bartholomew and others, 2011a; Nienow and others, 2005). Although several studies have shown that the dynamic behaviour (specifically the seasonal surface velocity cycle) of Greenland's land-terminating outlet glaciers is analogous to that of valley glaciers (e.g. Bartholomew and others, 2010; Sundal and others, 2011, Figure 1.7) there are important

thermal and geometric differences between the Greenland Ice Sheet and smaller alpine and arctic valley glaciers that demand consideration before the Alpine analogue can be applied as a general rule, especially to higher elevations.

First, ice thicknesses in Greenland (Bamber and others, 2001) are an order of magnitude greater than those found on valley glaciers. As a result the overburden pressure is higher and creep closure rates of unpressurised subglacial channels are expected to be rapid for kilometre thick ice, on the scale of days to hours (e.g. Bartholomaus and others, 2008). Second, at high elevations (above 1400 m a.s.l.), lower rates of surface melt and runoff over a shorter melt season (van As and others, 2012) result in lower volumes of water being delivered to the basal drainage system thereby reducing the capacity of the system to develop an efficient network (Schoof, 2010). The expansion of subglacial channels is further hindered by low surface and bed gradients in the ice sheet's interior resulting in less energy available for turbulent flow, and therefore less channel expansion by wall melting (Röthlisberger, 1972). Third, although the thermal regime for much of the Greenland Ice Sheet is unknown outside of a small number of boreholes (e.g. Lüthi and others, 2002) it is expected to be significantly colder than the temperate ice of alpine valley glaciers, hindering channel development further still.

The ice sheet may overcome these hindrances by focussing water in space and time and moulins on the GrIS (e.g. Fig. 3.2d) typically have larger drainage basins (Fitzpatrick, 2013) and deliver greater volumes of water to the subglacial environment (McGrath and others, 2011) than moulins on valley glaciers. Indeed, the preponderance of supraglacial lakes across much of the ice sheet margin, which provide the water volumes required for hydrofracture through thick ice (e.g. Das and others, 2008; Krawczynski and others, 2009), may play an important role in developing Greenland Ice Sheet englacial and subglacial hydrology by focussing water inputs to the bed in space and time. Furthermore, the

inherent sporadic distribution of water inputs from moulins and rapidly draining lakes may explain the fractal flow units identified by Palmer and others (2011) on Fig. 1.9. Supraglacial and proglacial lakes do drain under and through valley glaciers in the European Alps, (e.g. Sugiyama and others, 2008), Arctic canada (e.g. Boon and Sharp, 2003) and Svalbard (e.g. Liestol and others, 1980) but such events are not as widespread, or perhaps as important for hydrology and ice flow, as they are in Greenland, especially on the ice sheet's western margin (e.g. Selmes and others, 2011).

Hence, it is conceivable that near the ice sheet margin where ice thicknesses are low, surface gradients high and water inputs large that efficient subglacial drainage does develop in a manner akin to that of alpine glaciers. If, on the other hand, we consider a transect across the ice sheet, from the margin to the interior, it is plausible that at a certain distance along the transect the conditions, as described above, are unfavourable for the development of effective subglacial drainage and its regulating influence on ice flow. Beyond this theoretical point warmer and longer melt seasons could drive a net acceleration of ice flow. This hypothesis, which has been posited several times (e.g. Zwally and others, 2002; Parizek and Alley, 2004; Bamber and others, 2007; Lemke and others, 2007), requires further testing.

1.4 Summary

The GrIS is deglaciating and its contribution to global SLR has accelerated (e.g. Shepherd and others, 2012). Ice mass loss from Greenland is equally split between ice dynamics and runoff processes (van den Broeke and others, 2009). The dynamics of the Greenland Ice Sheet were previously thought to be relatively insensitive to external forcing such as climate change (e.g. Church and others, 2001), but recent studies (e.g. Zwally and others,

2002; Parizek and Alley, 2004) have hypothesised that the positive feedback mechanism of 'hydrological coupling' could accelerate the ice sheet's response to a climate warming. Subsequent studies (e.g. Truffer and others, 2005; Bartholomew and others, 2010; Sundal and others, 2011) have, however, argued that Greenland's outlet glaciers respond to surface melt inputs in a manner that is analogous to that of valley glaciers. High magnitude inputs of water overwhelm the subglacial drainage system causing extensive reductions in traction, but they also have the propensity to form efficient subglacial drainage systems, which thereafter drain the bed with a consequent lowering of effective pressure and therefore reduced basal motion.

There exist, however, important geometric and thermal differences between temperate valley glaciers and the Greenland Ice Sheet. Namely, lower melt rates, shorter melt seasons, thicker ice and shallower surface and bed slopes, which would theoretically impede the development and longevity of efficient subglacial drainage and its regulating influence on ice flow, at least at high elevations in the ice sheet's interior. These differences require careful consideration before the 'Alpine analogue' can be applied to the GrIS as a whole.

Supraglacial lakes play an important role in establishing surface-to-bed hydraulic pathways through kilometre thick polythermal ice that can remain open for the remainder of the melt season. The observation of surface uplift during rapid in situ supraglacial lake drainage (e.g. Das and others, 2008) and forced by the diurnal melt cycle (Shepherd and others, 2009) provides direct evidence for the penetration of surface water to the ice-bed interface through kilometre-thick ice. Further investigation is required to constrain the mechanism of rapid in situ lake drainage and data is required to test whether the observed expansion of supraglacial lakes to higher elevations in Greenland (Liang and others, 2012; Howat and others, 2013; Fitzpatrick and others, 2014) is driving an expansion of melt-induce velocity variations and an acceleration of ice flow in the interior.

1.5 Aims and objectives

The overarching aim of this project is to further our knowledge of basal hydrological forcing on ice sheet motion. For reasons outlined in the following chapter, Chapter 2, this is achieved using global positioning system measurements of surface ice motion supported by meteorological and hydrological records. Transect-based GPS studies have already been undertaken by the Institute of Marine and Atmospheric research in Utrecht (IMAU, e.g. van de Wal and others, 2008) and Edinburgh University (e.g. Bartholomew and others, 2010, 2011a, 2012). Instead, this thesis focuses on specific events, using them as natural experiments to gain insight into the processes at work. This thesis also focusses on behaviour in the lower accumulation zone — at a higher elevation and in more detail than previous studies — as the importance of dynamic changes in the interior is widely recognised yet data from this logistically-difficult-to-access zone remain unavailable. It is hoped that the insights gained will contribute to our collective understanding of the dynamic behaviour of land-terminating sectors of the Greenland Ice Sheet, providing evidence for how the ice sheet has responded to recent warm summers and insight into what the future portends. Within these broad aims the following specific objectives have been identified:

1. To develop an efficient and robust method for acquiring and processing GPS datasets for determining surface ice velocities on the GrIS over sub-diurnal to annual time scales.

2. To investigate basal hydrological forcing on a land-terminating margin of the GrIS, which is therefore isolated from the complicating influence of marine processes.

3. To investigate the mechanisms driving variations in ice sheet flow on sub-diurnal to inter-annual time scales.

4. To further our knowledge of rapid in situ supraglacial lake drainage events via the hydraulic fracture mechanism.

5. To test whether velocities in the ice sheet's interior are increasing in response to recent warm summers and the observed inland expansion of supraglacial lakes.

6. To test whether alpine glaciers are an appropriate analogue for the dynamics of the Greenland Ice Sheet.

1.6 Structure of thesis

This thesis is structured into eight chapters. Chapter 1 has introduced the Greenland Ice Sheet, synthesised the current knowledge concerning mass balance and the response of ice sheet flow to atmospheric forcing, and placed this thesis into context. Chapter 2 reviews the techniques used to measure surface ice motion with a focus on global positioning system (GPS) techniques. Chapter 3 introduces the field site before detailing the methods used to make dual-frequency GPS measurements of surface ice motion. Chapter 3 describes GPS theory, data collection and processing, and the interpretation of such measurements. Supplementary datasets used to complement the ice motion records are described briefly in Section 3.4 and more fully as appropriate in the relevant results chapters. Chapter 4 presents an overview of the results, and by focussing on the general patterns in ice velocities, it provides the spatio-temporal context for the following three more specific results chapters (Chapters 5, 6, and 7), which take the form of standalone experiments. Due to the wide array of GPS processing techniques and supporting datasets available each of these results chapters contains specific and in-depth details of its associated methods. Chapter 5 reports the geophysical capture of a rapid in situ supraglacial lake drainage event. Chapter 6 identifies a new forcing mechanism for ice sheet acceleration — rainfall

and melt driven by cyclonic weather. Chapter 7 reports on the seasonal and inter-annual acceleration from the highest GPS site located within the accumulation zone, and offers explanations for its causes. Chapter 8 synthesises the results presented in Chapters 4 to 7 and discusses them in the wider context of other studies. Chapter 8 also identifies directions for future research. Finally, the main conclusions of this thesis are summarised in Chapter 9.

Chapter 2

Measurements of surface ice motion: a review

An ice mass only becomes a glacier when it begins to move. Hence, by the definition of the word 'glacier' as a moving body of ice the study of ice motion has, is, and will continue to be an inherent and important aspect of glaciology. This chapter briefly reviews the methods used by glaciologists to measure ice motion. It intentionally focusses on GPS measurements as, for reasons that will become clear, this is the technique used in this study.

2.1 Traditional surveying techniques

The earliest studies of glacier motion relied on the repeat survey of poles drilled into the ice surface using theodolites (e.g. Agassiz, 1847; Iken and others, 1983) and similar techniques are still applied today (e.g. Copland and others, 2003). Traditional surveying

techniques still have their merits: they allow multiple poles to be surveyed at a daily or sub-daily sampling interval without a large financial investment in equipment. Automated theodolites combined with an electronic distance meter (EDM; e.g. Gudmundsson and others, 2000) can save much of the manual labour involved with such surveys. Despite this, these techniques now appear less frequently in the published literature and their decline since the 1980's reflects the move to the Global Positioning System (GPS) and remote sensing.

2.2 GPS measurements of ice motion

The Global Positioning System (GPS) — the first of several Global Navigation Satellite Systems (GNSS) — allows accurate positioning without reference to landmarks or visibility of the sun or stars. Glaciologists were amongst the first geoscientists to adopt GPS surveying (e.g. Hinze and Seeber, 1988, see Fig. 2.1) due to the difficulty in carrying out traditional surveying techniques in polar regions where line of sight to bedrock can be impossible, and survey conditions are often hostile.

Since the first studies, the array of GPS surveying methods used in determining ice velocities has steadily increased. Due to the high cost of GPS receivers, initial studies (e.g Eiken and others, 1996; Hagen and others, 2005; MacGregor and others, 2005) often relied on the surveying of multiple stake locations at discrete points in time followed by post-processing using commercially available software. This method allows the survey of a number of stakes using a single receiver, but it is inherently limited by both the repeat time and the requirement for the operator to be in the field. GPS receivers are less expensive than they used to be and it is now common practice to install continuously-operating GPS receivers at individual sites for long periods of time, allowing continuous high-frequency

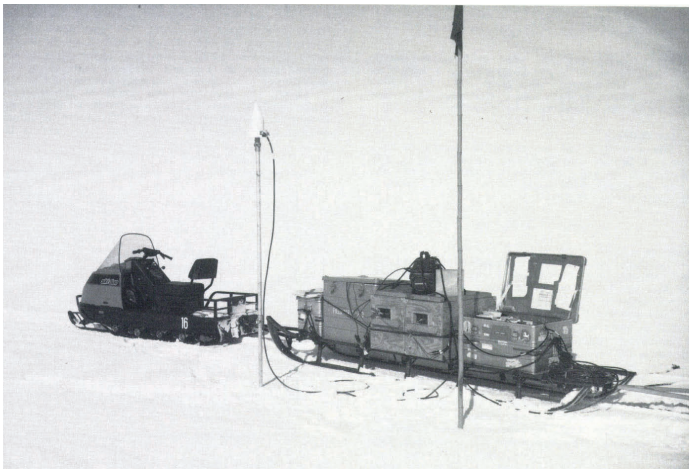

Figure 2.1: The Texas Instruments TI 4100 receiver transport and measurement sledge on Ekstrom ice shelf in 1987, from Hinze and Seeber (1988). GPS receivers suitable for precise measurements of ice motion are now smaller, more portable, easier to operate and less expensive than early systems.

records of ice motion to be acquired, so long as the GPS remains on (e.g. Howat and others, 2008; Bartholomew and others, 2010). Limitations on battery capacity encouraged some glaciologists (e.g. Larson and others, 2002; Zwally and others, 2002) to operate GPS on a scheduled basis, with receivers programmed to 'wake-up' and begin recording for discrete periods of time. Another option for low-power GPS observations are single-frequency measurements.

Single-frequency GPS measurements

Single-frequency positioning, known as the standard positioning service (SPS), is used in handheld GPS devices and car navigation systems, and is precise at the 1 to 10 m level. At this level of precision glacier velocities can still be effectively estimated by averaging over longer time periods (e.g. Den Ouden and others, 2010). The main advantages of single-frequency GPS systems is their ability to operate continuously with small battery

supplies (often small lithium cells) providing long, uninterrupted records (> 1 year) of ice motion at low cost. Such systems (e.g. Fig. 2.2) were used first by van de Wal and others (2008) and later by Bosmans (2009), Den Ouden and others (2010) and Dunse and others (2012). The level of precision achieved by single-frequency GPS receivers is not, however, sufficient to detect subtle sub-daily variations in ice velocity, which are typically of a small magnitude over short timescales. Russell Glacier, for example, moves at an average speed of 100 m yr^{-1} which is equivalent to 27 cm day^{-1} or 11 mm hr^{-1}. To measure variations in ice velocity of this magnitude on sub-daily time-scales we need to achieve cm-level precision or better.

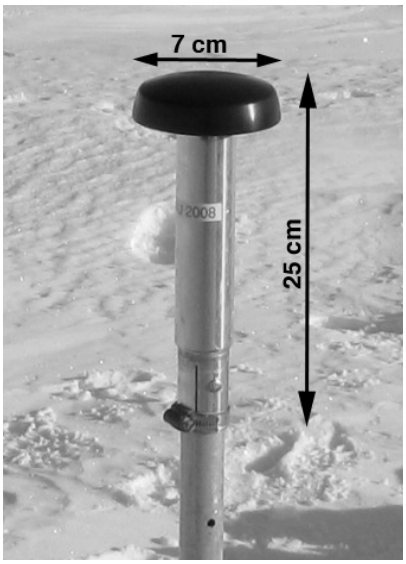

Figure 2.2: An L1 GPS receiver installed on a mass balance stake as used by van de Wal and others (2008). Compare with Figures 2.1 and 3.3. Adapted from Den Ouden and others (2010).

2.2.1 GPS theory

To understand the measurement capability of GPS we must first briefly introduce GPS theory. For a comprehensive description the reader is referred to Leick (2004), on which the following summary is predominantly sourced.

GPS receivers measure the travel time of radio signals broadcast by a constellation of satellites. The satellites transmit at two main frequencies (although a third has now been introduced) known as the L1 (1575.42 MHz) and L2 (1227.6 MHz) frequencies. These frequencies are modulated by two types of code: (1) the coarse acquisition (C/A) code for the standard positioning service (SPS) and the precise (P-) code for the precise positioning service (PPS). Two types of measurements made by receivers are inherent to GPS positioning. The first is the pseudorange: a measure of the travel time of the radio signal between the satellite and the receiver with the addition of a small corrective term due to clock errors, ionospheric and tropospheric delay, and signal multipath. Given a favourable satellite geometry, four pseudoranges are sufficient to compute the position of the receiver and its clock error. The second measurement is the carrier phase: the difference between the received phase and the phase generated by the receiver at the epoch of measurement. Receivers are programmed to make measurements at the same equally spaced epochs and they keep track of the number of complete cycles received since the beginning of a measurement. Thus the actual output is the accumulated phase observable at the present epoch. The position of the receiving antenna is calculated from these range measurements using trilateration.

If the Earth had no atmosphere this calculation would be easy and very precise. Unfortunately the radio signal emitted by the satellites, which travels unhindered at the speed of light through the vacuum of space, is refracted and dispersed: first, by charged electrons in

the ionosphere and second by water vapour in the troposphere. These refractions create a time-variable delay, which must be accounted for if we are to achieve the precision required to measure ice sheet motion over sub-daily time scales. Fortunately, the tropospheric delay is relatively simple to model and it is now possible to largely remove its effects. Ionospheric errors — often the single largest source of error in GPS positioning and navigation — are caused by refraction and dispersion of the GPS radio signals through a layer of charged electrons known as the ionosphere (Klobuchar, 1991). At frequencies below $\sim$ 30 MHz the ionosphere reflects radio waves allowing long-distance radio communications such as high-frequency radio. Radio waves at frequencies higher than $\sim$ 30 MHz travel through the ionosphere and the high-frequency L1 and L2 GPS signals penetrate the ionosphere relatively well. The ionospheric delay varies in time: for a signal arriving at zenith, the ionospheric delay can range from 10 ns (3 m) at night to as much as 50 ns (15 m) during the day. The ionospheric delay also varies spatially and signals received from different directions will have propagated through different portions of the ionosphere, and will have suffered different amounts of ionospheric delay. For satellites observed at low elevation angles the ionospheric delay may be almost three times greater than at zenith (Kaplan, 1996). At low satellite elevation angles (0–10 °) the delay can range from 30 ns (9 m) at night to 150 ns (45 m) during the day (Kaplan, 1996). As the ionospheric delay is inversely proportional to the frequency, measurements at two frequencies (e.g. L1 and L2) can be used to reduce most of the ionospheric delay, by forming, for example, the 'ionosphere free' linear combination. In contrast, the SPS used in single-frequency measurements either accepts the reduced precision, or uses a simple ionospheric model broadcast by the satellites.

The measurement capability of GPS lies in its ability to measure the carrier phase to one hundredth of a cycle, equivalent to a distance of 2–3 mm. As discussed above, the

high-frequency L1 and L2 signals propagate through the ionosphere relatively well, and by combining these measurements the ionospheric delay can be estimated and removed. Furthermore, GPS satellite orbits are stable due to their high-altitude where only the gravitational pull of the sun and the moon has a significant effect, and this can be modelled. The remaining sources of error: solar pressure, signal multi-path and clock errors can be largely eliminated by post-processing.

Single- (SPS) and dual-frequency (PPS) observations provide the two main types of GPS measurements, and further variations are predominantly related to the processing strategy applied to dual-frequency measurements. Two principal types of post-processing exist: relative processing and precise point positioning (PPP).

2.2.2 Relative GPS positioning

Relative positioning involves the determination of the vector between two co-observing receivers. Usually, one station is 'fixed', that is, it is static and its coordinates are known, whilst the coordinates of the other station are estimated. Relative GPS processing (sometimes termed differential GPS, or DGPS) can be used to cancel out clock errors amongst others. In simple terms, GPS receivers usually use the travel time measurements to satellites to calculate their position but if a static receiver knows its position, it can instead estimate the timing (or range) error. This correction can then be applied to the roving receiver. Leick (2004) explained how the differential correction is applied. If receivers k and m have observations of the same satellite p at the same time the difference between these two carrier phases φ is called a single difference and is given by Equation 2.1.

$$\varphi^p_{km}(t) = \varphi^p_k(t) - \varphi^p_m(t) \tag{2.1}$$

Satellite clock errors and satellite hardware delay errors cancel in the single-difference equation but receiver clock errors and signal multipath remain. Given observations of a second satellite q the difference between two single-difference observations is called the double-difference (Equation 2.2). Importantly, receiver clock errors cancel with double-difference observations in addition to the cancelling of satellite clock errors and satellite hardware delay errors.

$$\varphi_{km}^{pq}(t) = \varphi_{km}^{p}(t) - \varphi_{km}^{q}(t) \tag{2.2}$$

The triple-difference is the difference of two double-differences over time:

$$\Delta\varphi_{km}^{pq}(t_2, t_1) = \varphi_{km}^{pq}(t_2) - \varphi_{km}^{pq}(t_1) \tag{2.3}$$

The triple differences allow cycle slips to be mapped as outliers and removed. The remaining cycle-slip-free observations can then be used in the double-difference solution. In this way, relative processing typically makes use of the double- and triple- difference observations (although single-differences may also be used) to yield the vector between the co-observing receivers. This vector is added to the geocentric position of the reference receiver to get the geocentric position of the roving receiver. In relative processing the uncertainty in the reference receiver's position is entirely transferred to the roving receiver. For measuring surface ice motion and velocity only relative positioning is required as velocity is the differential of displacement, and the errors associated with absolute positioning can therefore be neglected.

Relative GPS processing is used extensively in the construction industry for surveying, however, they usually survey over short baselines and take static measurements. The use

of GPS to measure ice sheet velocities is more problematic due to (i) the long (e.g. 10+ km) baselines necessary when on-ice GPS are installed far from exposed bedrock, and (ii) the fact that a GPS antenna installed on the surface of an ice sheet is constantly in motion. Over even longer baselines (50 to 100+ km) kinematic processing is more difficult as the number of satellites observed simultaneously at both the reference receiver and the roving receiver is lower (meaning less double-difference observations) and the relative ionospheric delay is higher (King, 2004). Some studies, especially those measuring very slow moving ice (e.g. Sunil and others, 2007), have used static relative processing such as that provided by GAMIT software. In this processing technique the roving antenna is assumed to be static for short periods of time. King (2004) demonstrates, however, that this assumption is invalid for ice that is moving, and instead recommends that coordinates are determined kinematically at every measurement epoch.

Track, a script from the GAMIT/GLOBK software package, enables relative kinematic positioning (Chen, 1998; Herring and others, 2010). The Track script was designed for positioning survey aircraft for airborne laser altimetry, and it has been widely applied to earthquake ground motion studies (e.g. Wang and others, 2007). Track processing was first used on the Greenland Ice Sheet by Das and others (2008) to measure ice sheet motion during rapid in situ supraglacial lake drainage, followed by Shepherd and others (2009) to measure the diurnal melt-forced velocity cycle. It is well suited to measuring variations in ice sheet velocity over short timescales provided data from a nearby (within 100+ km) bedrock-mounted reference GPS receiver are available.

2.2.3 Precise point positioning

The requirement for a static reference receiver is a disadvantage of relative processing: it involves extra expense, requires installation on nearby bedrock that is not always available

(e.g. in Antarctica) and the reference receiver may fail. Precise Point Positioning (PPP) does not require a second receiver. While single point positioning (SPP) does not use precise satellite clocks and only uses pseudorange observations. In PPP both the pseudorange and the more precise carrier phase observations are used. SPP produces coordinates accurate at the 1 to 10 m level; PPP can achieve centimetre-level accuracy given 24 hours of static observations (King and others, 2002). The positioning of roving receivers using PPP with the ionosphere-free pseudo range and carrier phase functions is, however, less accurate, achieving sub-decimetre accuracy. Therefore PPP allows coordinate determination of roving receivers with a precision comparable to, but not as high as, relative processing. The first PPP processing software, GIPSY/OASIS II, was released by NASA's Jet Propulsion Laboratory in the 1990s and this processing technique was used to calculate ice velocities near the ELA at Swiss Camp in West Greenland (see Larson and others, 2002; Zwally and others, 2002). Online PPP services are now available providing the fast, automated processing of GPS data. These services include the Automated Precise Positioning Service (APPS, `http://apps.gdgps.net/`) and the Canadian Spatial Reference Systems Precise Point Positioning Service (`http://geod.nrcan.gc.ca`). The PPP software package 'Bernese' offers an alternative to GIPSY/OASIS software and its online equivalents, and has been used in a number of glaciological studies, especially where receivers located on bedrock are not available or difficult to install (e.g. Gudmundsson, 2006, 2007). However, the high cost of Bernese software rules out its widespread use amongst glaciologists.

2.3 Remote sensing measurements of ice motion

Remote sensing and GPS are complementary techniques with regard to measuring the motion of ice masses: remote sensing provides large spatial coverage at the expense of an

Table 2.1: Techniques for measuring ice motion; their advantages and disadvantages and example studies.

Technique	Advantages	Disadvantages	Example studies
Theodolite / Electronic Distance Meter (EDM)	Can be automated. Can sample multiple stakes.	Requires user to be in the field and line of sight.	Iken and others (1983); Iken and Truffer (1997); Gudmundsson and others (2000)
GPS techniques:			
Repeat GPS surveying	Requires only 1 (or 2) GPS receivers. High-accuracy. Line of sight not required.	Requires operator to visit each site.	Eiken and others (1996), Hagen and others (2005)
Dual-frequency continuously-operating GPS.	Stand-alone operation. High sampling frequency and high precision	Expensive. May fail if power outage. Large data set.	Shepherd and others (2009), Bartholomew and others (2010)
Remote sensing techniques:			
Optical feature tracking.	Large spatial coverage.	Poor temporal resolution.	Fitzpatrick and others (2013)
InSAR & Speckle tracking	Not affected by clouds or periods of darkness.	Often poor temporal and/or spatial resolution.	Joughin (2002); Joughin and others (2008, 2010); Palmer and others (2011); Moon and others (2012)
Stereo time lapse photogrammetry	Potentially high sampling frequency (governed by ice velocity). Large spatial coverage. Well suited to crevassed termini of tidewater glaciers.	Difficult processing techniques. Not yet fully developed.	Ahn and Box (2010)

often poor sampling interval, while GPS provides high-frequency measurements at discrete points. A comprehensive review of the satellite data suitable for determining glacier velocities is given by Fitzpatrick (2013) and Gao and Liu (2001) and will not be repeated here. Instead, remote sensing will be briefly compared to GPS and other techniques to demonstrate its strengths and weaknesses.

Two types of remote sensing imagery are used to determine ice velocities: (i) optical imagery, and (ii) radar imagery. Feature tracking on optical imagery such as ASTER (e.g. Howat and others, 2007), LANDSAT (e.g. Joughin and others, 2004) or SPOT imagery (e.g. Berthier and others, 2005) is the most common method and involves the tracking of features on the ice surface in two sequential images. Feature tracking is either manual or automatic and can also be applied to aerial photographs (e.g. Brecher, 1986). A major disadvantage of optical feature tracking is the requirement that the surface is visible — cloud cover and darkness prevent the technique from working. To overcome this problem, a large number of studies (e.g. Luckman and others, 2006; Rignot and Kanagaratnam, 2006; Erten and others, 2009; Joughin and others, 2010; Palmer and others, 2011; Moon and others, 2012) use radar imagery. With all satellite imagery there is a trade-off between spatial resolution and the temporal sampling interval, with high-resolution imagery generally having a longer repeat interval than low resolution imagery. Although MODIS imagery is available daily its spatial resolution (250 m) is not fine enough to derive glacier velocities from. For imagery of sufficient spatial resolution, these factors typically vary between the 11-day repeat time of 3-m-resolution TerraSAR-X data or the 16 day repeat time of 15-m-resolution LANDSAT imagery to the 35 day repeat time of 30 m resolution ENVISAT radar data (Fitzpatrick, 2013). Clearly, even using the optimal satellite sensor the repeat time of imagery with a sufficient spatial resolution is usually too long to investigate ice dynamics over short time scales. A further, and important, drawback of remote sensing measurements of ice velocity

is that current techniques are unable to measure velocities in the featureless accumulation area during the summer (e.g. Joughin and others, 2010). Remote sensing techniques also fail in fast-moving heavily-crevassed regions: the features to be tracked must have moved sufficiently for the displacement to be detected, but not destroyed in the process (e.g. Quincey and Luckman, 2009).

2.4 Determining surface ice motion using other techniques

Feature tracking, either applied to stereo photographs obtained by time lapse cameras (e.g. Ahn and Box, 2010) or unmanned aerial vehicles (UAVs, e.g. Whitehead and others, 2013; Ryan and others, 2014) have been recent developments in the techniques used to study surface ice motion. These new techniques may be particularly suited to determining ice velocities on the heavily crevassed termini of tidewater glaciers. Installing GPS receivers is difficult in these regions and although not impossible; the longevity of the GPS installation is often short due to serac collapse, calving and crevasse formation. To address these issues in these difficult regions glaciologists have utilised GPS receivers which transmit their data, either using a satellite modem (e.g. Den Ouden and others, 2010) or radio communications to a nearby off-ice reference receiver (e.g Fahnestock and others, 2007), thereby avoiding the requirement to revisit the GPS receiver in order to download the data. Despite the success of these methods, GPS measurements still only offer point measurements of ice motion and techniques with greater spatial coverage are required to ensure these point measurements are representative of ice dynamics on a wider spatial scale. Whilst remote sensing techniques, which offer a greater spatial coverage, have been widely and successfully used on tidewater glaciers and their termini (e.g. Joughin and others, 2008, 2010), remote sensing is fundamentally limited by the availability of satellite

imagery as previously mentioned. Thus, the new techniques described by Ahn and Box (2010); Whitehead and others (2013) and Ryan and others (2014) provide the opportunity to measure ice velocities at a sampling frequency that is high relative to remote sensing techniques and with a spatial coverage that is large relative to GPS surveying. Although time lapse cameras may be set up to operate automatically, UAV-based photogrammetry is limited by the requirement to conduct a survey, not to mention the difficulty in operating a UAV. Both techniques require substantial post-processing to derive glacier velocities, although the same can be said of dual-frequency GPS techniques and remote sensing.

For practical reasons, this thesis and review chapter has focussed on measurements of surface ice motion, yet substantially more insight into ice dynamics can be gained from additional measurements. Combining records of surface ice motion with internal deformation measured by repeat borehole inclinometry allows basal ice motion to be determined and the two dimensional velocity field to be reconstructed (e.g. Harper and others, 1998; Lüthi and others, 2002). Alternatively, direct measurements of basal motion made in cavities accessed from the margin, via tunnels, or at the base of boreholes (e.g. Blake and others, 1994; Copland and others, 1996; Hubbard, 2002; Willis and others, 2003) can be subtracted from the surface velocity to estimate the depth-integrated internal deformation. Although such approaches yield substantially more insight into ice motion, they are difficult and expensive to acquire and have yet to be undertaken in Greenland. By contrast measurements of surface ice motion are relatively inexpensive and allow more sites to be studied.

2.5 Summary and implications for this study

The measurement of ice velocity is a fundamental aspect of glaciology and glaciologists were amongst the first geoscientists to use GNSS techniques. Traditional surveying methods,

which are virtually impossible on much of the Greenland Ice Sheet where bedrock reference sites are out of sight, are becoming less popular as the use of GPS surveying becomes routine. Remote sensing techniques offer good spatial coverage but are limited by their often poor temporal sampling interval and by the inability to measure velocities in the ice sheet's interior during summer.

The processes that drive basal hydrological forcing of ice sheet motion (e.g. the diurnal melt cycle) operate over sub-daily time-scales (see Chapter 1). To measure variations in ice sheet motion over these short time scales precise positioning at a high temporal frequency is required. Although single frequency GPS measurements are clearly well-suited and worthwhile for monitoring long-term changes in ice flow due to their low cost and power consumption, only dual-frequency measurements provide the precision required.

As continuous dual-frequency GPS measurements of ice velocity have a power consumption which exceeds the practical battery and solar/wind charging capacities available to this investigation it is to be expected that the GPS will turn off at some point during winter. Often the highest velocities occur shortly after melt onset, when water accesses the bed for the first time since the previous winter (see Chapter 1). Measurements of ice velocity during these 'spring-events', which typically occur in May to June on the GrIS depending on elevation and latitude, either require the operator to be in the field before the start of the melt season or the GPS receiver to restart automatically when the sun returns in spring. The latter option is far more desirable considering the difficulty and expense involved in accessing sites on the Greenland Ice Sheet at the start of the season.

GPS measurements of ice sheet motion must also be post-processed taking into account the characteristically-long baselines involved and the fact that the antenna is never stationary (see Subsection 2.2.2 and King, 2004). For these reasons, this study will predominantly analyse data from continuously-operating GPS receivers post-processed kinematically rel-

ative to bedrock-mounted reference stations using Track software (Chen, 1998).

Due to the inherent characteristics and limitations of each of the various techniques available for determining surface ice motion (including the disadvantages of GPS measurements) future studies would be wise to use multiple techniques to measure velocity, thereby allowing a more comprehensive picture of ice dynamics to be compiled. Nevertheless, to answer the research questions identified in Section 1.5, dual-frequency GPS measurements and relative processing represent the best techniques available.

Hence, the objectives of this study (Section 1.5) will be predominantly met by comparing dual-frequency GPS measurements of surface ice motion with meteorological and hydrological data. Where possible and appropriate remote-sensing techniques will be used to support the GPS observations presented in this study. The following chapter describes the development of a methodology for collecting, processing and interpreting GPS measurements of surface ice motion in Greenland.

Chapter 3

Study area, data and methods

The main aim of this thesis is to investigate basal hydrological forcing on GrIS motion. For reasons outlined in Chapter 2, it is primarily based upon measurements of ice surface motion made by continuously-operating dual-frequency GPS receivers installed across a land-terminating section of the Greenland Ice Sheet. This chapter (i) introduces the field site, Russell Glacier catchment, (ii) describes the methods used to collect, process and interpret GPS data, and (iii) briefly details supporting datasets collected by collaborators. The following sections are intended to provide a general overview of the study area and methods; as outlined in Section 1.6, specific details are given in each of the results chapters.

3.1 Study area: Russell Glacier catchment

Russell Glacier is a land-terminating outlet glacier in West Greenland located at 67° N, 50° W. Russell Glacier catchment provides an ideal case study for investigating basal hy-

drological forcing as it is isolated from marine processes, easy to access from Greenland's only international airport, and is the subject of intense glaciological research.

Russell Glacier catchment is arguably the best instrumented, and most-studied section of the Greenland Ice Sheet. Established in 1990, the Kangerlussuaq (K-) transect is the longest running transect of surface mass balance stakes and automated weather stations (AWS) in Greenland (e.g. van de Wal and Russell, 1994; van de Wal and others, 2005, 2012, Fig. 3.1). The mean annual surface mass-balance at the lowest site of the K-transect (S4, 383 m a.s.l.) between 1990 and 2010 was -4.22 m water equivalent (w.e.). The mean surface mass balance gradient is 3.8×10^{-3} m w.e. m^{-1} and the mean equilibrium line altitude (ELA) is 1553 m a.s.l (van de Wal and others, 2012). The mean (1990 to 2010) surface mass balance was only positive at the highest site, S10 (1840 a.s.l.), located 140 km from the ice margin, $\sim$50 km from the ELA, and with an average accumulation between 1990 and 2010 of 0.27 m w.e. yr^{-1}. Measurements from single-frequency (L1) GPS receivers provide a long term record of ice motion at each site on the K-Transect. At sites in the ablation zone these measurements indicate a slight, but significant decline in ice flow despite an increasingly negative surface mass balance (see Chapter 1, van de Wal and others, 2008).

Additionally the Geological Survey of Denmark & Greenland (GEUS) maintain a transect of four AWSs with one located on tundra (KAN_B) and three on ice (KAN_L, KAN_M and KAN_U). The KAN_L AWS is co-located with the SHR GPS receiver and is the site of a borehole drilled to the bed and instrumented with an array of pressure transducers, thermistor strings and tilt sensors (see Smeets and others, 2012). KAN_U is co-located with the S10 K-transect site and KAN_M is located in between KAN_L and KAN_U (Fig. 3.1). Edinburgh University also operate a transect of seven dual-frequency GPS receivers on Russell/Leverett Glacier catchments (e.g. Bartholomew and others, 2010). Hence, three

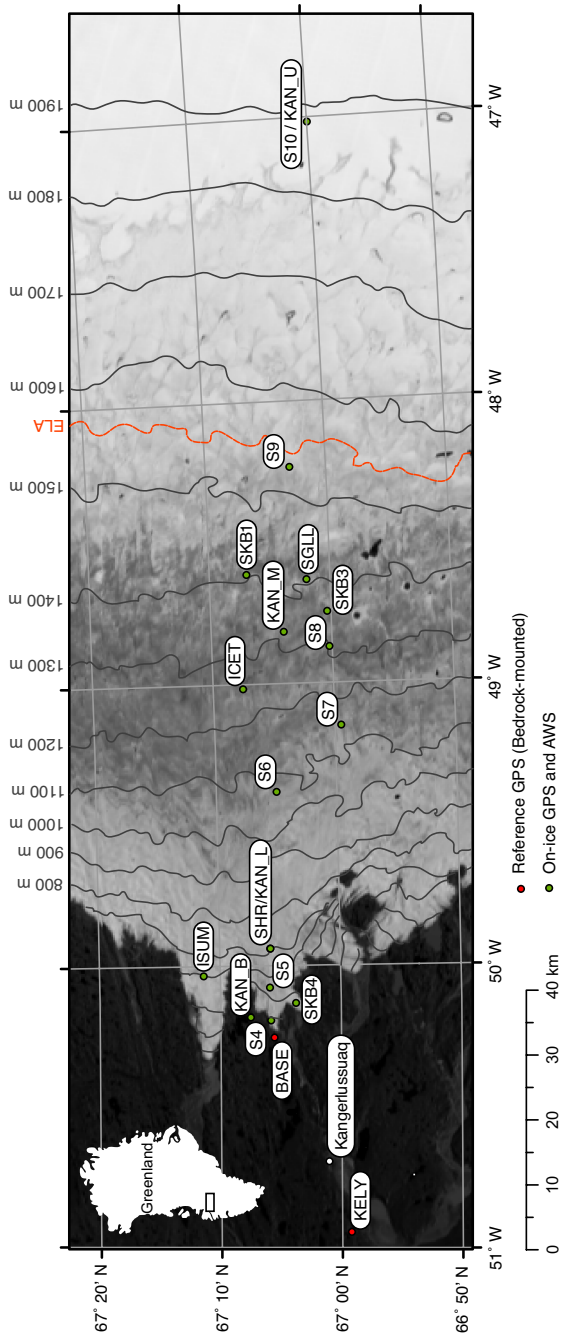

Figure 3.1: Map of Russell Glacier catchment showing the locations of the (i) GPS receivers (ii) K-transect sites (S4, S5, SHR, S6, S7, S8, S9 and S10) (iii) AWS maintained by GEUS (KAN_B, KAN_L, KAN_M and KAN_U) (iv) Kangerlussuaq town and airport and (v) the bedrock-mounted Kellyville reference GPS maintained by UNAVCO. The twenty-one (1990-2011) year mean mass-balance equilibrium line altitude (ELA) estimated by van de Wal and others (2012) at 1553 m a.s.l. is indicated with a red line. The contours are based on the DEM of Howat and others (2013). The background MODIS image was acquired on 17 August 2011

different GPS transects are maintained across the same study area resulting in competition and collaboration that has stimulated research. Russell Glacier catchment has also been the focus of several key remote sensing studies investigating ice sheet dynamics (e.g. Palmer and others, 2011; Sundal and others, 2011; Fitzpatrick and others, 2013) and the seasonal formation and drainage of supraglacial lakes (e.g. Box and Ski, 2007; McMillan and others, 2007; Sundal and others, 2009; Howat and others, 2013; Fitzpatrick and others, 2014).

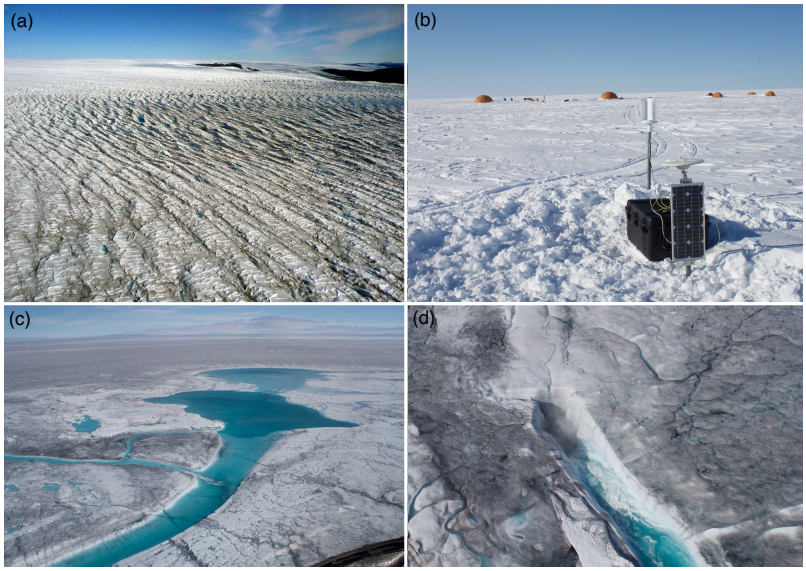

Figure 3.2: Characteristics of Russell Glacier catchment: (a) a crevassed area of Russell Glacier close to the ice margin (22 June 2009), (b) snow at site S10 in the accumulation area (4 May 2012), (c) a partially drained lake at GPS site Ice-T located $\sim$ 50 km from the margin draining via a supraglacial river into (d) a $\sim$ 20 m diameter moulin $\sim$ 5 km downstream of (c). Both (c) and (d): 31 July 2010.

Like much of the western margin of the Greenland Ice Sheet, which is generally more gently sloping and less crevassed than the eastern margin, Russell Glacier catchment (especially between 800 and 1600 m a.s.l.) is characterised by an abundance of supraglacial lakes during the melt season (e.g. Fitzpatrick and others, 2014). These lakes drain via supraglacial streams and rivers into moulins (Fig. 3.2c, d) or by the in situ propagation of hydraulic

fractures (e.g. Das and others, 2008). At and below S5 (490 m a.s.l.) a bare ice surface is maintained year round by low rates of snowfall during the winter and the redistribution of snow into crevasses by the wind (van den Broeke and others, 2008a, Fig. 3.2a). Much of the margin (approximately below S6) is heavily crevassed making access by snowmobile or on foot from the margin difficult (Fig. 3.2a). Above the long-term ELA (e.g. at S10) snow typically lies year-round (Fig. 3.2b) and provided there is enough snow during the previous winter, sites as far west as S6 are accessible by snowmobile in the spring, although the crevasse hazard is not inconsiderable.

3.2 GPS methods

The following section describes the methods used to collect and process the GPS data. Section 3.3 discusses the interpretation of GPS measurements of surface ice motion. Section 3.4 introduces the supporting datasets and their methods, both of which are detailed specifically in each results chapter.

3.2.1 GPS data collection

In 2008, ten GPS receivers were deployed along a transect extending to Site 10 (S10) on the K-transect, 140 km from the margin of Russell Glacier (Fig. 3.1). This GPS transect has been maintained each year since then and continues to operate at the time of writing. Dual-frequency GPS receivers were installed on Russell Glacier (S4), Isunngata Sermia (ISUM) and Leverett Glacier (SKB4). Further inland, GPS receivers were installed by large supraglacial lakes referred to as Ice-T, SKB1 and SKB3. Dual-frequency GPS receivers were also installed at the K-transect sites (S4, SHR, S10, and in 2012, S9) to complement the single-frequency GPS measurements made by IMAU. In 2010, the GPS

network reached a peak when 24 receivers were in operation. Additional, and more specific, maps of the study site and instrument locations are provided in Figures 5.1, 5.2, 6.1 and 7.2.

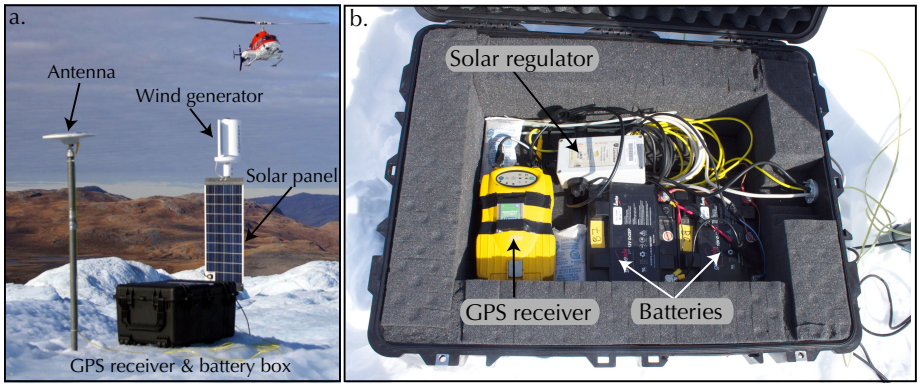

Figure 3.3: An example GPS setup, (a) antennae were mounted on 48 mm outer diameter steel pipes drilled several metres into the ice surface. Power was supplied by a 48 W solar panel and a wind generator, (b) the receiver, battery and solar regulator were housed in an insulated and waterproof case with marine glands allowing the cables to enter the box.

At each site antennae were mounted on 48 mm outer diameter threaded steel pipes drilled into the ice surface using a Kovacs drill, leaving $\sim$ 1m above the ice surface (Fig. 3.3a). The depth of drilling was adjusted for the expected surface ablation, which was based on surface mass balance data (e.g. van de Wal and others, 2012). Sites near the ice margin were drilled to 7 m depth and sites in the accumulation zone were drilled to 2 m depth. The poles subsequently froze in and the GPS thereafter recorded surface ice motion. The GPS were serviced in spring and autumn allowing data to be downloaded, batteries to be replaced, and the pole to be reset before it melted out. The GPS receiver, batteries and solar regulator were enclosed in an insulated, waterproof case with marine glands allowing water-tight cable access (Fig. 3.3b). Power was supplied by a 100 Ah battery bank charged by a 48 W solar panel and wind generator. Periods of power outage occurred, especially

during winter, often causing substantial gaps in the dataset. Several models of receiver were used including Trimble 5700, Trimble R7, Trimble NetRS and Leica System 500 (SR520 and SR530). Each receiver was configured to log continuously at a 10 second interval. Before further processing could be applied, raw binary files produced by the receivers were converted to daily time-binned Receiver INdependent EXchange (RINEX) file format using a combination of proprietary software and TEQC (Estey and Meertens, 1999).

Problems with GPS data collection

Operating GPS receivers continuously and unattended on the Greenland Ice Sheet is challenging. The field site, Russell Glacier catchment, is located at 67°N, which is approximately 80 km north of the Arctic Circle. During mid-winter, days of 24 hour darkness occur and at the highest site, S10, temperatures drop to below −50° C. Despite the GPS receiver being powered by a 100 Ah battery bank charged by a 48 W solar panel and a wind generator (Fig. 3.3) it is likely that the receiver will shutdown due to insufficient power in the winter. It is therefore critical that the GPS 'starts up' automatically when the sun returns in the spring or during periods of strong wind. Unfortunately, the majority of the GPS receivers in use — standard Trimble 5700 and Trimble R7 — were found to require 15 V to start up automatically. The 12 V DC power systems typically reach a peak voltage of 14.7 V, which is the regulated output of the solar charge controller, although periods of strong wind and sunshine can produce battery voltages in excess of 15 V. An additional problem is that the Trimble 5700 and R7 receivers draw a small but nevertheless significant amount of current even when they are off, and it is suspected that in some cases this may have resulted in flattening the battery beyond the point of potential recovery (typically below 10.5 V). To solve both these problems a combined low voltage disconnect (LVD) and step-up voltage regulator was developed at Aberystwyth University. Unfortunately, sub-

sequent problems with these LVD circuit led to the need to find a replacement, which was provided by RE-UK. The LVD was connected to an off-the-shelf variable output step-up circuit (LM2577) which was set to regulate the output voltage to 16.5 V. The RE-UK LVD has a small (2 mA) quiescent current when the load is disconnected, ensuring it does not deplete the batteries beyond recovery. To ensure the circuits would operate in low temperatures all the circuits were tested by leaving them running overnight in the Aberystwyth University Cold Laboratory, with the temperature set at -17° C.

3.2.2 GPS data processing

Data from the on-ice GPS receivers were processed kinematically (King, 2004) relative to bedrock-mounted reference stations using the differential carrier-phase positioning software, Track (Chen, 1998; Herring and others, 2010) and precise ephemeris from the International GNSS Service's (IGS) final products (Dow and others, 2009) available from: `ftp://igscb.jpl.nasa.gov/igscb/product/`. In some rare cases problems were found processing with the IGS data, and ephemeris from the Massachusetts Institute of Technology (MIT) were used instead (`ftp://cddis.gsfc.nasa.gov/pub/gps/products`). For convenience, daily precise ephemeris, downloaded using automated shell scripts, were concatenated into weekly files allowing for 1 day of overlap at the start and end so that the interpolation routine could work across the day boundary. Reference stations were located on bedrock, 1 km from the terminus of Russell Glacier (BASE) and at Kellyville (KELY), giving maximum baseline lengths of 141 and 171 km respectively (Fig. 3.1). Wherever possible, the baseline length was minimised by using data from the BASE reference station (Fig. 3.5), which also recorded at a shorter sampling interval (10 seconds). Data from the KELY reference station are provided by UNAVCO at a 30 second interval and are available via anonymous FTP from: `ftp://garner.ucsd.edu/pub/rinex`. The processing workflow

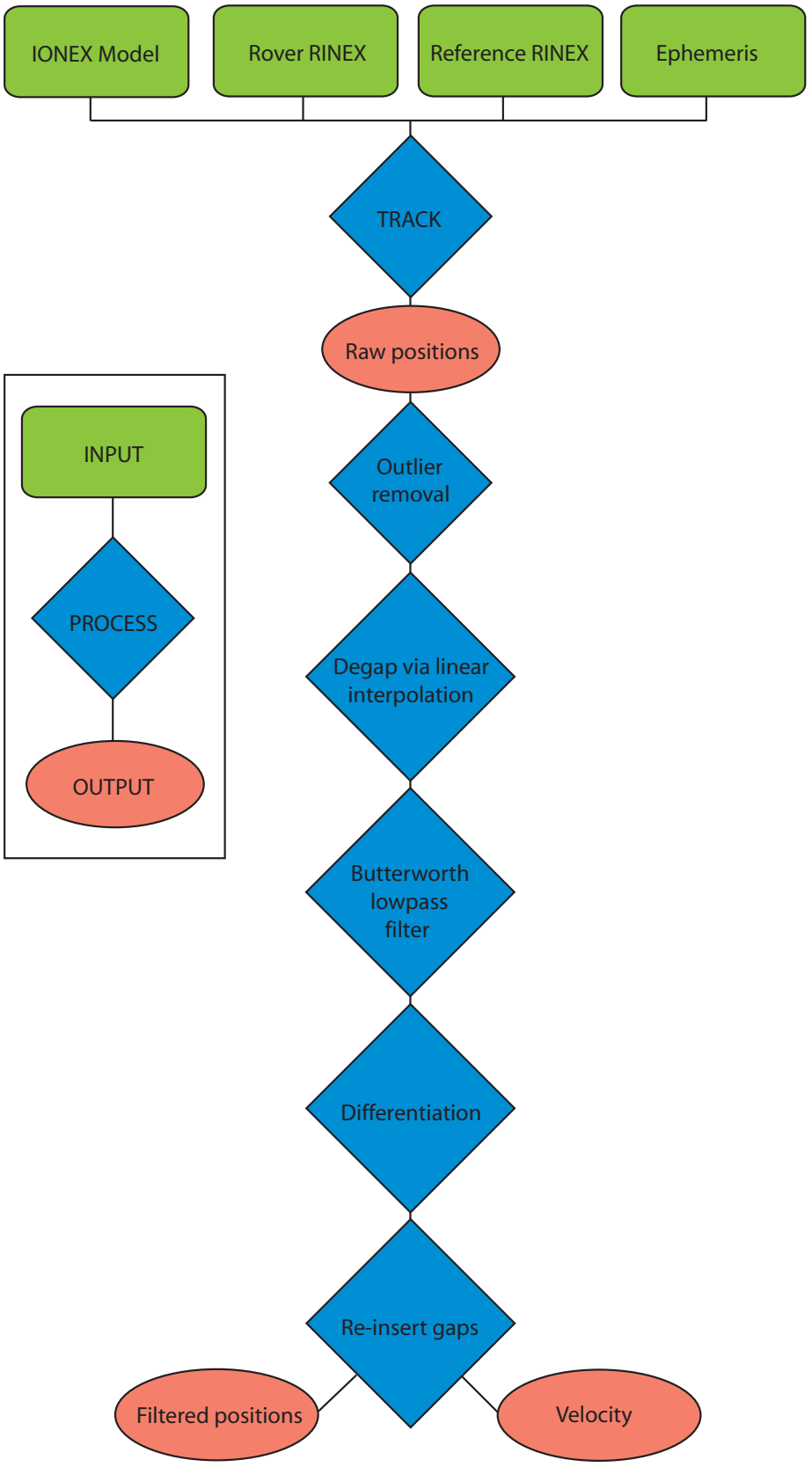

Figure 3.4: Flowchart showing the sequence of processing applied to RINEX data in order to calculate ice surface velocity and surface uplift.

is summarised in Figure 3.4.

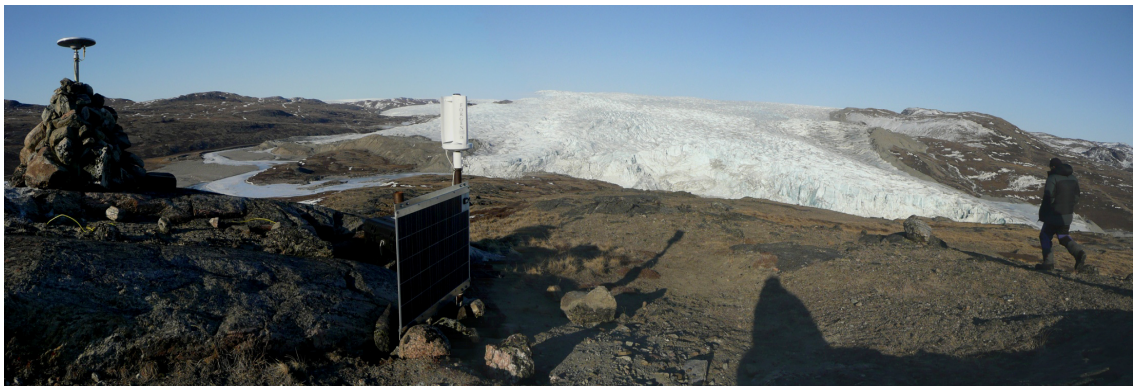

Figure 3.5: The GPS reference station, BASE, located on a knoll $\sim$ 1 km from the terminus of Russell Glacier, which can be seen in the background. The GPS antenna is located on bedrock on the far left of the photo.

To ensure comparable results from relative processing against different base stations, the origin of the relative coordinate system, which usually defaults to the first static reference station in the Track command file, was fixed as the position of reference station, BASE, at an arbitrarily selected epoch. To ensure good position solutions and to fix the maximum number of ambiguities, tight *a priori* coordinates determined using the APPS or from the previous day's Track solution were input into the Track command file. As the majority of cycle slips occur when the satellites are observed at low elevations it is conventional to neglect all observations below an elevation cutoff angle of 15°. It is also more difficult to correct for the tropospheric delay at low elevations and the data is typically noisier. Bar-Sever and others (1998), however, suggested that using an elevation cutoff angle lower than the traditional 15° improves the resolution of vertical positions and Larson and others (2002) later demonstrated that using 10° improved vertical positioning with little influence on the horizontal. Accordingly, an elevation cutoff angle of 10° was applied throughout. To improve the positioning, daily maps of the ionosphere were input into Track software, using the IONEX format (Schaer and others, 1998), although earlier versions of Track used in this

study were not compatible with the IONEX maps. To minimise the errors caused by the day boundary, 36-hour-long RINEX files were processed and the first and last six hours of the output position time series were trimmed to create 24-hour-long files. These daily files were then concatenated together before importing into MATLAB software. Initial quality control involved removing coordinate solutions with: (i) horizontal position uncertainties greater than 3.5 cm; (ii) an insufficient number of double-differences (typically < 3); or (iii) too many unfixed ambiguities (varied between 0 and 2). The positions were then corrected for servicing of the antenna (e.g. lowering and/or horizontal re-positioning to adjust for ablation).

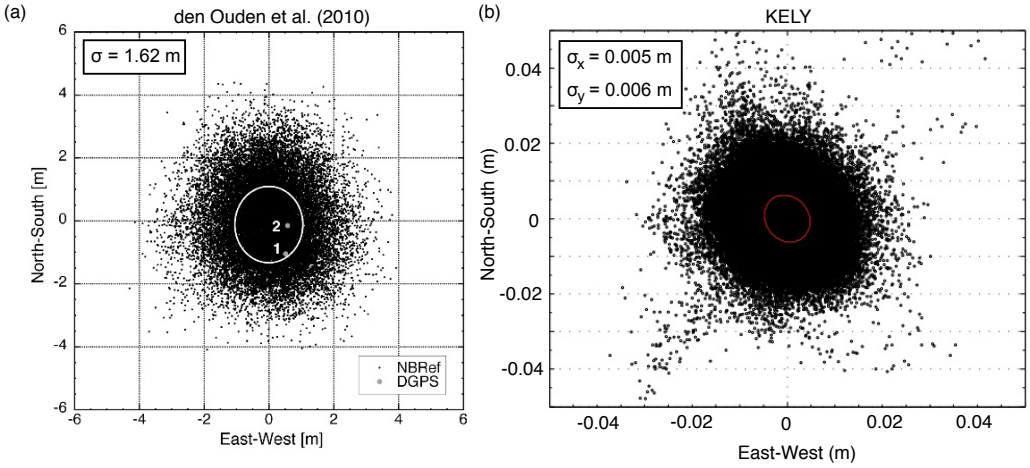

Figure 3.6: Comparison of the precision between (a) single (L1) and (b) dual (L1 + L2) frequency GPS positioning for data collected by static receivers mounted on bedrock. Note the substantial difference in axis scaling and the 1 sigma ellipse, which is shown in white on (a) and red on (b). The dual-frequency data shown in (b) is 1 month of Kellyville (KELY) reference station data processed against the Russell Glacier base station (BASE) using Track. Subplot (a) is adapted from Den Ouden and others (2010).

3.2.3 Uncertainty estimate

Uncertainty in this GPS positioning technique was estimated by processing data from the static Kellyville (KELY) reference receiver kinematically against the BASE receiver located on bedrock near the terminus of Russell Glacier. A month of 30-second interval KELY data were processed using the same parameters applied to the on-ice receivers. Over this period, it is reasonable to assume that the Kellyville antenna, which is mounted on bedrock, is static. Furthermore, as the processing is relative and the baseline short (∼40 km) the effects of glacio-isostacy, ocean tidal loading and earth-tides cancel. The XY scatter of the KELY position solutions is compared to a similar test applied to single-frequency GPS solutions by Den Ouden and others (2010) on Figure 3.6. The standard deviations of the KELY solutions ($\sigma_{\mathrm{E}} = 5$ mm and $\sigma_{\mathrm{N}} = 6$ mm) contrast with the much larger standard deviation of 1.62 m for the L1 solutions of Den Ouden and others (2010). The dramatic (300 x) improvement in precision with dual-frequency receivers is a manifestation of the ability to effectively cancel out the majority of the errors affecting single-frequency measurements (see Subsection 2.2). This simple test is, however, limited by at least two factors. First, the 40 km baseline means the uncertainty of positioning over longer baselines may be underestimated. Unfortunately, data from static reference receivers over comparable baseline lengths used in this study (up to 140 km) are not available to extend this test. The next nearest reference GPS is located more than 250 km from our study area and a comparison over such a long baseline would be as — or less — representative as a comparison over a 40 km baseline. Second, uncertainties may be greater when positioning a receiver that is not static as motion inherently results in changes in the travel time of the GPS signal, which can be mistaken for a change in ionospheric delay or a cycle slip. This second issue is already addressed by the ambiguity fixing algorithm of Track. Nevertheless, the precision of 6 mm can be considered a best case scenario and consistent with previous studies (e.g. Bartholomew and others, 2011a; Sole

and others, 2013) a horizontal positioning uncertainty of ±1 cm is assumed hereafter. This is in good agreement with the standard deviation of individual epoch positions estimated by Track software, and the resultant noise after short-periods (e.g. 1 hour) of winter-time high-frequency (0.1 Hz) on-ice GPS positions are linearly de-trended. (If steady ice motion is assumed then the resultant noise after linear de-trending represents the noise introduced by processing and measurement errors).

3.2.4 Calculating velocity

Three methods to calculate velocity from the position time series output by Track were used in this study. The simplest method was to divide the Euclidian displacement by the time interval. The mean horizontal velocity (V) between two positioning times (t_1 and t_2) can be calculated by summing the north (N) and east (E) displacements in quadrature, and then dividing by the time interval:

$$V = \frac{\sqrt{(N_2 - N_1)^2 + (E_2 - E_1)^2}}{t_2 - t_1} \tag{3.1}$$

Equation 3.1 was applied to the raw position time series to estimate the velocity over daily or greater time intervals and the uncertainties can be propagated through the calculation. The uncertainty in the displacement north ($\delta\,\mathrm{dN}$) can be estimated by adding the uncertainty in each position of ±0.01 m in quadrature:

$$\delta\,\mathrm{dN} = \sqrt{\delta\,\mathrm{N}^2 + \delta\,\mathrm{N}^2} \tag{3.2}$$

$$\delta\,\mathrm{dN} = \sqrt{0.01^2 + 0.01^2} = 0.014\ \mathrm{m} \tag{3.3}$$

As the uncertainty estimate in north and east positioning is the same, $\delta\,\mathrm{dE}$ also equals 0.014 m. Assuming the uncertainty in dT is 0, the fractional uncertainty in $\mathrm{V_N}$ (or $\mathrm{V_E}$) is equal to the fractional uncertainty in dN (or dE):

$$\frac{\delta V_N}{|V_N|} = \frac{\delta\,\mathrm{dN}}{dN} \tag{3.4}$$

The uncertainty in the resultant velocity (V) is calculated in a similar manner. From these estimates, the uncertainty in velocities of the order of 100 $\mathrm{m\,yr^{-1}}$ is very low for annual time periods (± 0.01 $\mathrm{m\,yr^{-1}}$) but increases when the time interval is shortened because the displacement approaches the detection limit. An interval of a month gives an uncertainty of ± 0.17 $\mathrm{m\,yr^{-1}}$, a week gives ± 0.73 $\mathrm{m\,yr^{-1}}$, and a day ± 5.16 $\mathrm{m\,yr^{-1}}$. With a time interval of an hour, the uncertainty exceeds the velocity. For comparison, the L1 positioning uncertainty of ± 1.62 $\mathrm{m\,yr^{-1}}$, propagates to ± 2.3 $\mathrm{m\,yr^{-1}}$ over annual periods, ± 27.9 $\mathrm{m\,yr^{-1}}$ over monthly periods and exceeds the velocity for weekly or shorter periods. The necessary time interval between the positioning times is therefore dependent on the precision of the positioning technique, the speed at which the ice is moving and the perturbations in speed that are to be detected. A longer time interval is required when the velocity is lower, or the positioning uncertainty greater.

Table 3.1: A comparison of the estimated uncertainty in single and dual frequency GPS measurements of velocity for ice moving at 100 $\mathrm{m\,yr^{-1}}$ over different time periods. These estimates are based on horizontal positioning uncertainties of ± 0.01 $\mathrm{m\,yr^{-1}}$ for dual-frequency measurements and ± 1.6 $\mathrm{m\,yr^{-1}}$ for single-frequency measurements.

Period	Dual-frequency ($\mathrm{m\,yr^{-1}}$)	Single frequency ($\mathrm{m\,yr^{-1}}$)
Annual	± 0.01	± 2.30
Month	± 0.17	± 27.9
Week	± 0.73	$>$ detection limit
Day	± 5.16	$>$ detection limit
Hour	$>$ detection limit	$>$ detection limit

Importantly, however, these uncertainty estimates of velocity relate to differencing single-epoch measurements. In reality, the velocity uncertainty can be effectively reduced by averaging multiple positions before differencing — or by filtering out the high-frequency noise that is characteristic of GPS data. To avoid single anomalous results having a large effect on the velocities estimated by Eq. 3.1, the positions sampled at a 10 or 30 second interval were averaged over a 6 hour window before differencing. Although averaging over 6 hours is appropriate for calculating the velocity over long time intervals it is not useful for investigating velocity variations over short (e.g. sub-daily) time scales. Hence, to investigate transient variations in ice motion low pass filters were applied to the position time series before differentiation.

3.2.5 Filtering the time series

The second and third methods of velocity calculation involve low pass filters being applied to continuous position time series before differentiation. GPS data is characterised by high-frequency noise, which can be reduced and even removed using certain filtering techniques. The second method to calculate velocity involves applying the simplest low-pass filter — a symmetrical moving average — before differentiation. The symmetrical moving average for X_k can be calculated using Eq. 3.5 below:

$$X_k = \frac{1}{2w+1} \sum_{k-w}^{k+w} x_i, \tag{3.5}$$

where w is the moving average half-length. The cut-off period for the moving average is $(2w + 1) \times$ sample interval or, when the sampling frequency is high, approximately $2w \times$ sample interval.

As the raw position time series often contain variable-length gaps, due to (i) periods of power outage (ii) processing issues or (iii) the rejection of values during quality control, short gaps in the data were estimated using linear interpolation before filters were applied. The gaps were later re-inserted to ensure no interpolation artefacts or artificial data remained in the final time series. Inherent to the centred moving average is the inability to calculate results for a certain number of values (a number governed by the cutoff period) at the start and end of a time series. These missing values were identified and not allowed to propagate through subsequent processing steps. With this in mind, it was necessary to apply the shortest averaging period that suitably filtered the time series. This was determined by comparing the precision of the processing technique to the expected range in ice velocities. As discussed in the previous subsection, the uncertainty in the horizontal positions was estimated at ± 0.01 m. Annual velocities in the study area are typically $100\,\mathrm{m\ yr^{-1}}$, with higher velocities on the ice falls south of Russell Glacier (up to $500\,\mathrm{m\ yr^{-1}}$) and velocities generally reducing up-glacier to $\sim 50\,\mathrm{m\ yr^{-1}}$ at site S10. The typical velocity of $100\,\mathrm{m\ yr^{-1}}$ is equivalent to $27\,\mathrm{cm\ day^{-1}}$ or $11.4\,\mathrm{mm\ h^{-1}}$. With a position uncertainty of ± 0.01 m (± 10 mm) this processing technique should be able to resolve typical glacier velocities down to an hourly time period. Assuming the worst horizontal position uncertainty of 0.035 m (values higher than this were removed from the dataset), and a mean glacier speed of $100\,\mathrm{m\ yr^{-1}}$, the period over which velocities can be resolved extends to ~ 4 hours. As the majority of position uncertainties are ≤ 0.01 m, the practical moving average window length was selected at 3 hours. For coordinate time series sampled at a 30 second interval a centred 361-point moving average was therefore applied. This is the same moving average period applied by Shepherd and others (2009) who measured similar velocities in the same region of the Greenland Ice Sheet using the same processing techniques and over similar baseline lengths. A shorter averaging window of 1 hour was used if finer detail was required and velocities were expected to be above average (e.g.

during rapid lake drainage events).

$$\frac{\mathrm{dx}}{\mathrm{dt}} = \frac{\mathrm{x}_{k+1} - \mathrm{x}_{k-1}}{2h} \tag{3.6}$$

Following symmetrical differentiation (Eq. 3.6) of the filtered positions, the resulting velocity time series was resampled to a 10 minute interval before a 13-point symmetrical moving-average (equivalent to a $\sim$ 2 hour cutoff period) was applied to further smooth the velocity time series. Velocity was calculated individually for the east (E) and north (N) components and then the magnitude of the resultant velocity was calculated using Pythagorus's Theorem (Eq. 3.7):

$$V = \sqrt{{V_N}^2 + {V_E}^2} \tag{3.7}$$

Applying 3-hour-period moving averages and differentiation to year-long datasets sampled at a 10 or 30 second interval involves a large number of calculations. For a dataset a few months in length, the initial scripts that were used to filter the data could take several hours to run and the development of more efficient method was desired. Furthermore, the moving average is a poor filter in the frequency domain due to its slow roll-off and poor stop-band attenuation. In response, a second order low-pass Butterworth filter with a cutoff period of 12 hours was designed. To cancel phase-shifts forward and reverse filtering was applied using the MATLAB function *filtfilt*. The Butterworth filter was applied to the position time series before differentiation and no further filtering of the velocity time series was required. The MATLAB scripts used to implement the Butterworth filter were optimised and the improvement in computational efficiency was dramatic. Time series that took $>$ 12 hours to process with the moving average script could now be processed in

less than a minute. This allowed the filtering process to be iterated while different filter parameters and quality control methods were tested.

3.3 Interpreting GPS measurements of ice motion

If we assume that GPS antennae firmly mounted on poles drilled into the ice surface perfectly record the motion of the ice surface, then the surface velocity $\boldsymbol{u_s}$ consists of basal slip $\boldsymbol{u_b}$ and motion due to internal ice deformation $\boldsymbol{u_d}$ (Eq. 3.8, Cuffey and Peterson, 2010).

$$\boldsymbol{u_s} = \boldsymbol{u_b} + \boldsymbol{u_d} \tag{3.8}$$

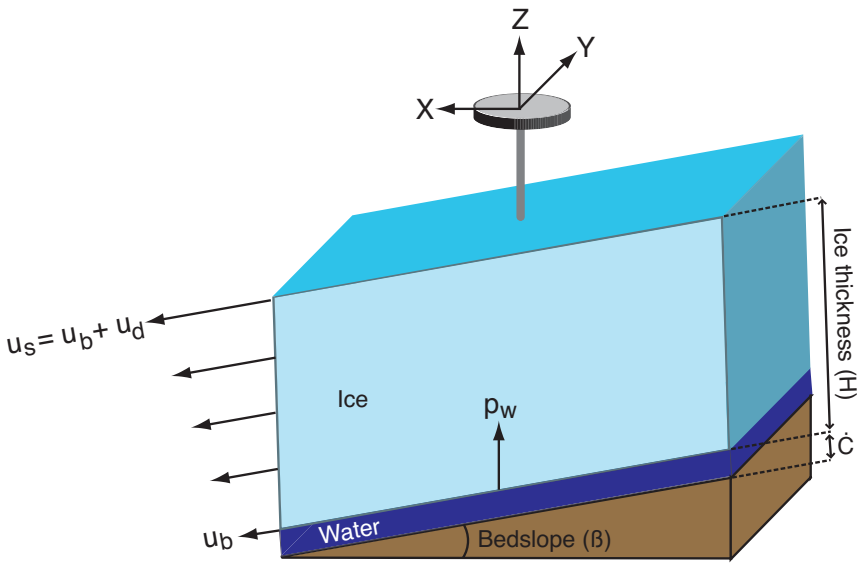

Figure 3.7: A GPS mounted on the ice surface measures the horizontal motion caused by basal sliding (u_b) and internal deformation (u_d) and vertical motion consisting predominantly of bed-parallel motion, ice-bed separation $\dot{c}$ and the vertical strain rate.

Variations in vertical motion

Variations in the vertical surface motion of a glacier were first detected by Agassiz (1847) on Unteraargletscher in the Swiss Alps and later confirmed by Iken and others (1983). Iken and others (1983) measured 0.6 m of uplift coincident with the 'spring event' annual-maximum in horizontal velocity, suggesting that the uplift was caused by water storage at the bed.

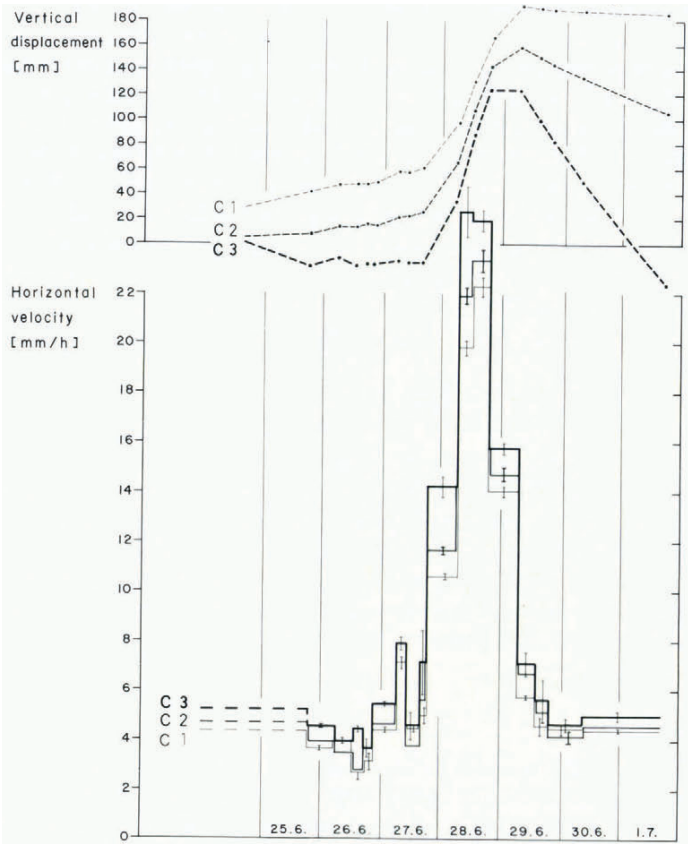

Figure 3.8: Theodolite measurements of horizontal and vertical motion made by Iken and others (1983) showing an uplift event that followed a brief period of strong melt.

The detailed theodolite measurements made by Iken and others on Unteraargletscher also showed that peak horizontal acceleration coincided with peak upward vertical velocity and

not peak vertical displacement (Fig. 3.8). This finding led to the hypothesis that the sliding velocity is governed by the subglacial water pressure, which is highest during the transient stage of cavity opening. This hypothesis was supported by numerical modelling results (Iken, 1981) and remains in use today (e.g Bartholomaus and others, 2008; Schoof, 2010).

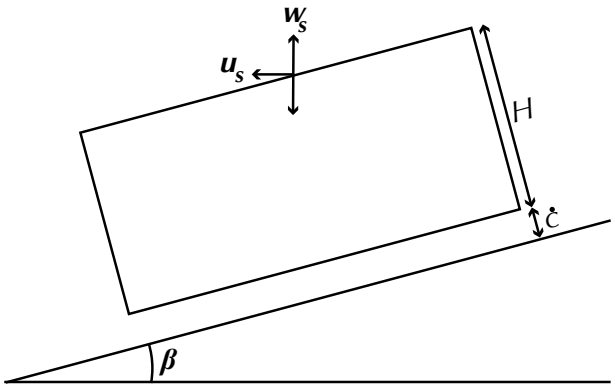

Figure 3.9: Removing bedslope from surface velocity to get cavity opening

Theoretically, the vertical component of surface velocity w_s can be expressed as:

$$w_s = \boldsymbol{u_s} \tan\beta + (\dot{\epsilon}_{zz})\, H + \dot{c} \tag{3.9}$$

Eq. 3.9 corrects vertical surface velocity for the bedslope β and vertical strain rate $\dot{\epsilon}_{zz}$ averaged over the ice thickness H leaving the residual $\dot{c}$ which has classically been interpreted as cavity opening (e.g. Röthlisberger and Iken, 1981; Hooke, 1989; Mair and others, 2002, Fig. 3.9). The residual $\dot{c}$ actually represents any change in the geometry of the vertical column of ice and there is therefore an array of potential contributors to vertical surface motion. For example, changes in bedslope, removal/compaction or addition/dilation of sediment, erosion of the bedrock, and melting (or freeze-on) of basal ice will all influence the vertical motion of the surface. Furthermore, the calculation of vertical strain also disregards lateral

spreading and assumes ice is incompressible (Anderson and others, 2004). Nevertheless, it is frequently assumed that transient and seasonal ice surface uplift can be interpreted as indicative of water storage at the bed (e.g. Iken and others, 1983; Bartholomaus and others, 2008; Bartholomew and others, 2010). Several studies (e.g. Anderson and others, 2004; Howat and others, 2008; Hoffman and others, 2011) have attempted to isolate the cavity opening term in Eq. 3.9 from surface height records by measuring, or assuming values for, the other terms. Where the bedslope and vertical strain rate are unknown another approach is to linearly detrend the surface height record (e.g. Bartholomew and others, 2011a). This approach assumes the bed is linear over the distance travelled by the GPS and the vertical strain rate is zero. As no suitable data exist on the bedslope and vertical strain rates at each of the GPS sites, this study either presents uncorrected height time series or applies linear detrending.

3.4 Supporting datasets

GPS measurements of surface ice motion can only provide half of the story and simultaneous measurements of hydrology and meteorology are required to complement the records of ice motion.

Hence, this study draws on meteorological measurements from three on-ice automated weather stations (AWSs) located 13 km (KAN_L), 61 km (KAN_M) and 140 km (KAN_U) from the terminus of Russell Glacier, and one on tundra AWS (KAN_B) located 1 km west of the ice margin (Fig. 3.1). The lowest AWS, KAN_L, is co-located with the dual-frequency GPS receiver at K-transect site, SHR, together with an L1 GPS and mass-balance stake maintained by the Institute of Marine and Atmospheric research at Utrecht University (IMAU) and an instrumented borehole drilled to the bed (Smeets and others, 2012). The

highest AWS is co-located with the S10 dual-frequency GPS, and IMAU L1 GPS and mass-balance stake. The AWS recorded surface height change due to accumulation and ablation, air pressure, temperature, humidity, wind speed and direction, and downward and upward shortwave and longwave radiation at 2 to 3 m above the surface. The AWS sampled at a 10-minute interval, from which hourly averages were calculated. The energy available for melt was determined using a surface energy balance model (van As, 2011), validated using the AWS measurements of surface temperature and surface height change (van As and others, 2012). Additional meteorological records from Kangerlussuaq Airport are provided by the Danish Meteorological Institute (DMI; Cappelen and others, 2001, 2011, 2012, 2013).

The supraglacial lake statistics of Fitzpatrick (2013) and Fitzpatrick and others (2014), which expanded the method for obtaining lake volumes developed by Box and Ski (2007) for the entire catchment between 2002 and 2012, were particularly useful for relating supraglacial lake drainage events to changes in ice motion.

Fed by the proglacial discharge from Russell and Leverett glaciers, the Akuliarusiarsuup Kuua river joins the Qinnquata Kuussua several kilometres before it enters Kangerlussuaq Fjord where it is referred to locally as the Watson River. Discharge measurements (e.g. Hasholt and others, 2013) have been made at Watson River bridge in Kangerlussuaq by Bent Hasholt and Andreas Mikkesen since 2007.

Finally, radio echo sounding measurements of ice thickness (Lindback and others, 2014) have been used to complement the GPS observations of this investigation.

Chapter 4

Results I: An overview of variations in ice motion

4.1 Introduction

This chapter presents an overview of the results of this thesis and places the following three results chapters, which describe specific experiments, into context. It begins by describing spatial variations in velocity across the study area before presenting a transect of daily-averaged velocities to illustrate the characteristic pattern of seasonal velocity variations. Transient high-magnitude perturbations in ice motion caused by the rapid drainage of supraglacial lakes are introduced by examining a drainage event in 2009 which frames a more detailed experiment at the same site in 2010 (see Chapter 5). An additional transient peak in the velocity record, this time in late summer 2011, is also highlighted: driven by unusual meteorological conditions this pronounced acceleration event is used as a natural experiment to investigate basal hydrological forcing in Chapter 6. Using site SHR as a

case study, this chapter also presents the velocity records in greater detail revealing diurnal variations in ice surface velocity and examining the relationships between surface velocity, uplift, subglacial water pressure and melt. SHR is selected here for three reasons (i) it is the fastest site on the K-transect (van de Wal and others, 2008), (ii) it represents one of the longest and most complete records collected during the course of this study, and (iii) it is co-located with an instrumented borehole (Smeets and others, 2012) and an AWS (van As and others, 2012) allowing comparisons of ice motion, meteorological and hydrological variables.

4.2 Spatial variations in velocity

Across Russell Glacier catchment, annual velocities vary from ~ 50 m yr^{-1} to ~ 150 m yr^{-1}, with the slowest velocities occurring at the highest elevations (e.g. S10, 1840 m a.s.l.). Counterintuitively, the highest velocities do not occur near the ice margin, which exhibits typical velocities of 80 to 100 m yr^{-1} (Figs. 4.1 and 4.2). Instead, the fastest flow is found at mid-elevations (600 to 1400 m a.s.l.) at sites SHR (675 m a.s.l.) and Ice-T (1287 m a.s.l.) for example. With an annual velocity of 120 m yr^{-1}, SHR is the fastest site on the K-Transect (van de Wal and others, 2008) but faster flow of ~ 150 m yr^{-1} was recorded at Ice-T GPS and Isum GPS. Both of these sites are located on fast flow units (see Palmer and others, 2011; Fitzpatrick and others, 2013) presumably associated with subglacial valleys and therefore, thicker ice, warmer basal conditions and preferential routing of subglacial water. Ice-T is also located by a large supraglacial lake which, in 2010 at least, drained into a ~ 20 m diameter moulin situated 5 km downstream (Fig. 3.2c and d).

The slowest GPS site that was occupied was S10, located 140 km from the ice margin and 50 km above the long-term ELA (Figs. 3.1 and 3.2b; van de Wal and others, 2012).

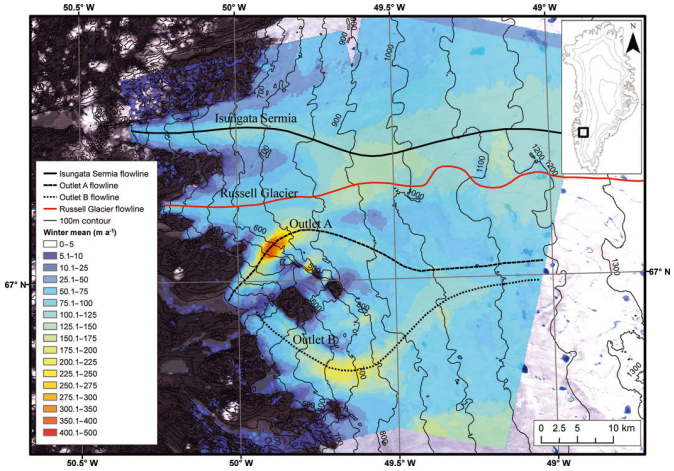

Figure 4.1: Winter mean (2009 and 2010) velocity maps across the lower glacier catchments derived from TSX feature tracking overlaid on a June 2008 Landsat image. The winter mean was derived from TSX imagery with mid-dates of 11 November 2009, 7 February 2010, 9 November 2010 and 20 November 2010. After Fitzpatrick and others (2013).

Daily averaged velocities at S10 of $\sim$ 50 m yr^{-1} show no significant variation above the background noise (Fig. 4.2). Similarly, van de Wal and others (2008) find no significant inter-annual trend in either the S10 or S9 velocities from their single-frequency GPS results (see Figure 1.6). Although Bartholomew and others (2011a) reported a small seasonal variation of 0.2% at their highest site (their Site 7; 1715 m a.s.l.) located 115 km from the margin, they concluded that this site represents the inland extent of melt-induced velocity variations. In accordance with this conclusion Colgan and others (2009); Colgan and others (2011) and Phillips and others (2013) argued that seasonal velocity variations do not propagate above their highest GPS site at 98 km inland on the Dead Glacier transect (71° N) in West Greenland. Despite the current consensus on the up-glacier limit of seasonal velocity variations, the hypothesised dynamic response of interior ice to the inland expansion of melt and supraglacial lakes (e.g. Bamber and others, 2007; Howat and others, 2013), as discussed in Chapter 1, will be tested by rigorous processing (e.g. King, 2004) of

the S10 GPS dataset (see Chapter 7).

Velocities on Isunnguata Sermia (Isum GPS) appear to be higher and slightly less variable than typical of GPS on Russell and Leverett Glaciers (Fig. 4.2), suggesting that the over-deepened trough of Isunnguata Sermia (Lindback and others, 2014) facilitates fast and less variable flow, perhaps due to a deforming sediment bed. The characteristically different behaviour of Russell Glacier and Isunnguata Sermia highlights an important question: how variable are velocity variations from one glacier to another? Following on from this: how representative are velocity variations on one glacier to the wider ice sheet margin? Unfortunately, such questions are beyond the scope of this study which is limited to one glacier catchment. Similarly, due to the paucity of GPS receivers installed on Isunnguata Sermia the variations in ice motion on this glacier are not studied in detail here.

In summary, the GPS network (Fig. 3.1) captures a wide array of dynamic behaviour, ranging from slow and steady flow in the accumulation zone to the fastest and most variable flow units in the catchment (Fig. 4.2). Although the GPS network misses the fastest ice velocities in the study area, which occur on two unnamed ice falls south of Russell Glacier (Fig. 4.1, Fitzpatrick and others, 2013), these icefalls are outside of Russell Glacier catchment (Fitzpatrick and others, 2014). Maintaining GPS receivers on these icefalls would be problematic and they are routinely neglected in remote sensing studies as they are considered unrepresentative of the ice sheet margin. Finally, it should be noted that GPS receivers provide only point measurements of ice velocity; remote sensing methods offer considerably better spatial coverage and accordingly the reader is directed to Fitzpatrick and others (2013),Joughin and others (2008),Joughin and others (2010), and Palmer and others (2011) for a more comprehensive analysis of the spatial variation in velocity across the study area.

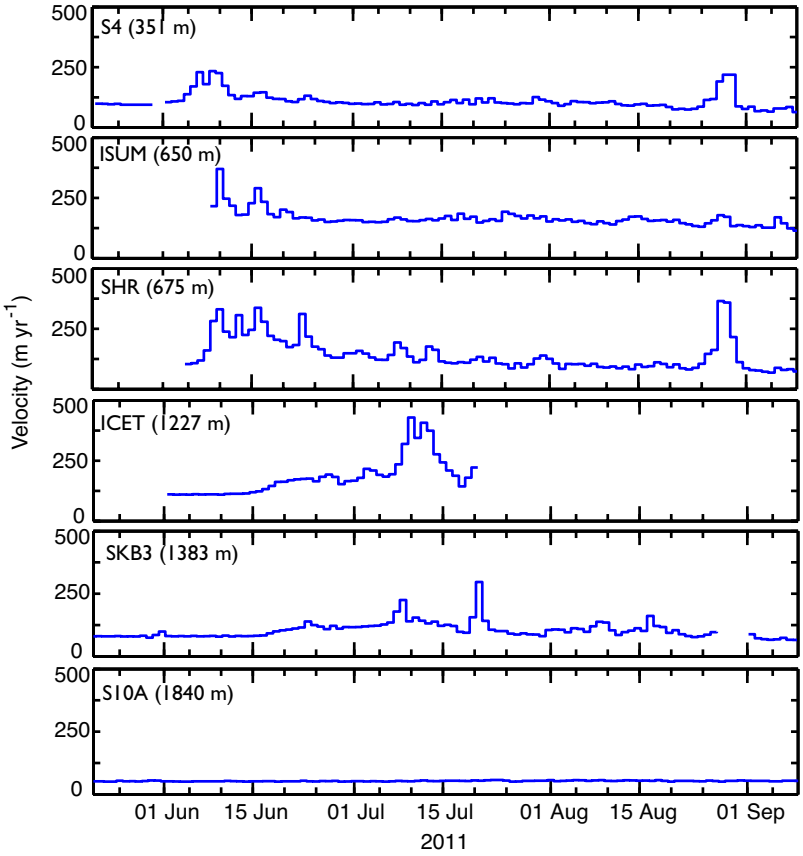

Figure 4.2: Daily averaged horizontal velocities at six sites on Russell Glacier and Isunnguata Sermia in 2011. See Figure 3.1 for the locations of these sites.

4.3 Seasonal velocity variations

The seasonal variations in ice motion recorded across Russell Glacier catchment are consistent with previous observations (van de Wal and others, 2008; Bartholomew and others, 2010, 2011a; Hoffman and others, 2011; Bartholomew and others, 2012; Colgan and others, 2011, 2012; Fitzpatrick and others, 2013). Maximum velocities typically occur at melt onset followed by gradual deceleration into mid summer with an all-year minimum at the

end of the melt season (Fig. 4.2). The melt onset peak — synonymous with the spring event on alpine glaciers (e.g. Mair and others, 2003) — typically occurs in late May to June across Russell Glacier catchment, dependent on the site's elevation and the timing of each melt season. The melt onset peak begins at the ice margin and migrates to higher elevations following the up-glacier progress of surface melt.

Although the GPS records are often discontinuous, there is evidence for a steady increase in velocity over winter. Winter time acceleration can be deduced from the observation that velocities are typically higher in spring just before melt begins than they are in autumn just after melt has ceased (see for example S4 on Figure 4.2). This observation agrees with remote sensing measurements that indicate up to a ∼20% acceleration over winter, presumably as the basal hydrological system closes and the remaining basal water is pressurised driving faster basal motion (e.g. Joughin and others, 2010; Fitzpatrick and others, 2013).

Transient accelerations driven by high-magnitude water inputs to the basal hydrological system are superimposed on the seasonal velocity cycle at many sites especially at mid to high elevations (800 to 1400 m a.s.l.; Fig. 4.2). Such transient accelerations are driven by brief periods of anomalously high melt (see for example the velocity peak in late August 2011 (day of year (DOY) 236) evident on Figure 4.2) or the establishment of drainage into moulins. A number of these discrete, transient acceleration which infrequently punctuate the velocity records in summer are driven by rapid supraglacial lake drainage events (Das and others, 2008; Hoffman and others, 2011). A good example was recorded by the SKB3 GPS record during 2009.

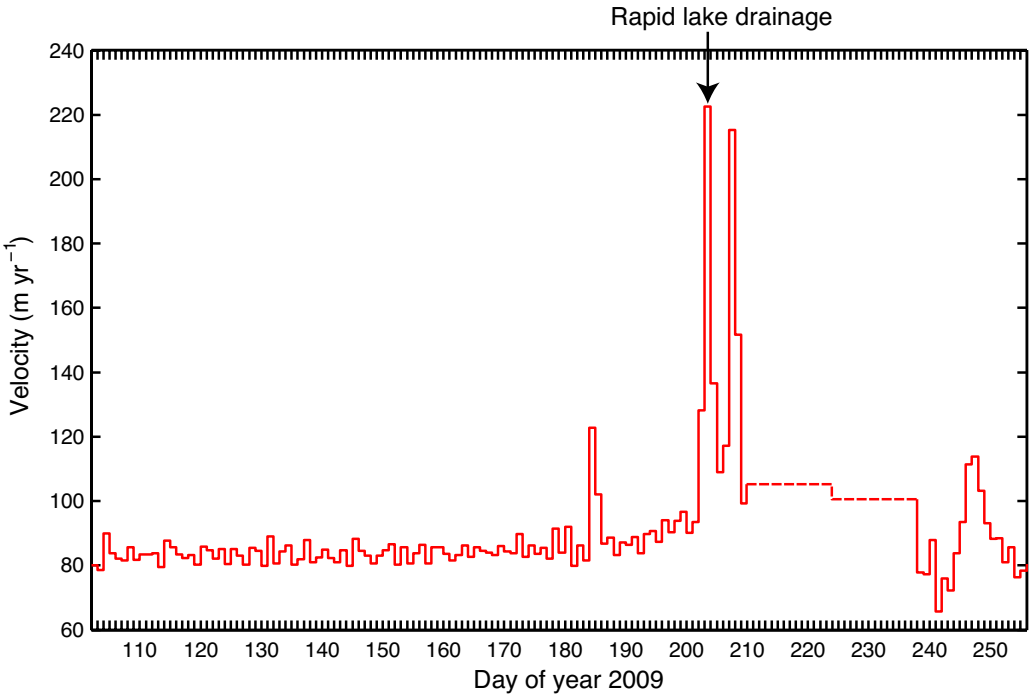

Figure 4.3: Daily average velocity for SKB3 GPS in 2009 revealing a transient acceleration event driven by lake drainage in late July (DOY 202). The arrow highlights the timing of the lake drainage and red dashed lines indicate periods with no data. Data were processed using APPS precise point positioning (see Subsection 2.2.3) due to a lack of contemporaneous reference station data.

4.4 Rapid lake drainage

Rapid lake drainage was suspected from a pronounced peak detected in the daily averaged velocities at SKB3 in late July 2009 (DOY 202; Fig. 4.3). Velocities peaked at 223 m yr^{-1} on 21 July 2009, 160% above the mean velocity during late May 2009 of $\sim$ 85 m yr^{-1}. Although the peak appears to be short-lived, further analysis of post-event velocities is prevented by a gap in the dataset.

The rapid disappearance of the adjacent lake between 14:15[1] on the 17 and 14:15 on the 21

[1] All times are given in UTC.

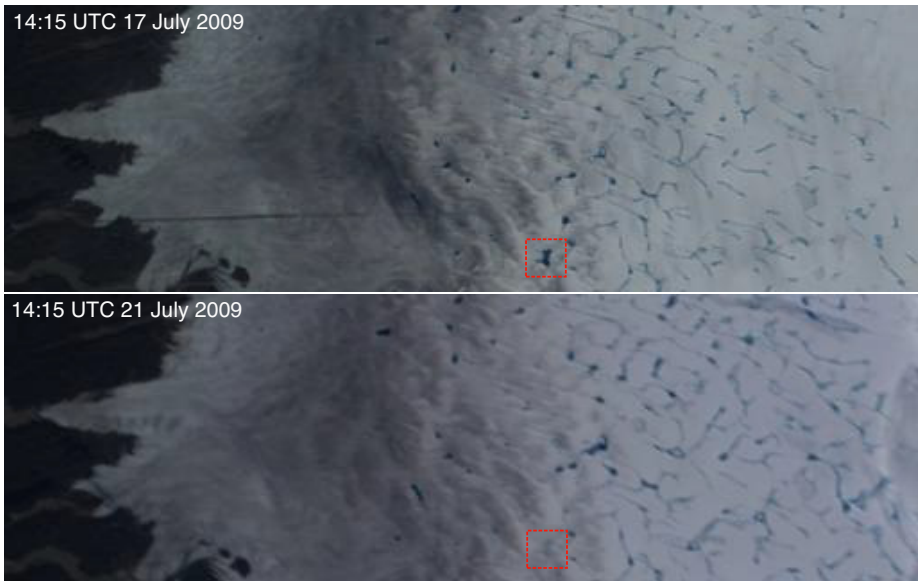

Figure 4.4: MODIS images revealing the drainage of the lake adjacent to SKB3 GPS in late July 2009. The red dashed boxes highlight the position of the lake. Images between these dates were obscured by cloud.

July 2009 was confirmed by sequential MODIS imagery (Fig. 4.4) acquired by Fitzpatrick (2013).

Detailed analysis of the SKB3 GPS data revealed that during the drainage event the GPS receiver, which is located ~ 300 m to the west of a large (> 2 km wide) supraglacial lake, was temporarily displaced 0.57 m to the north and 0.5 m to the west. Displacement to the west began at 07:09 on 21 July 2009 reaching a maximum at 08:32, 0.50 m west of the position before the event (Fig. 4.5b). Motion then reversed to the east, and the GPS returned to its pre-event position in the east-west plane by 10:04. Uplift began ~ 20 min after the commencement of westerly displacement at 07:31 peaking at 08:42, 1.54 m above pre-event levels, before gradually subsiding at a decaying rate over subsequent days (Fig. 4.5c). Meanwhile the receiver was displaced 0.57 m to the north between 07:52 and 09:33, following which the GPS receiver gradually returned to its pre-event position in the north-

south plane over several days (Fig. 4.5a).

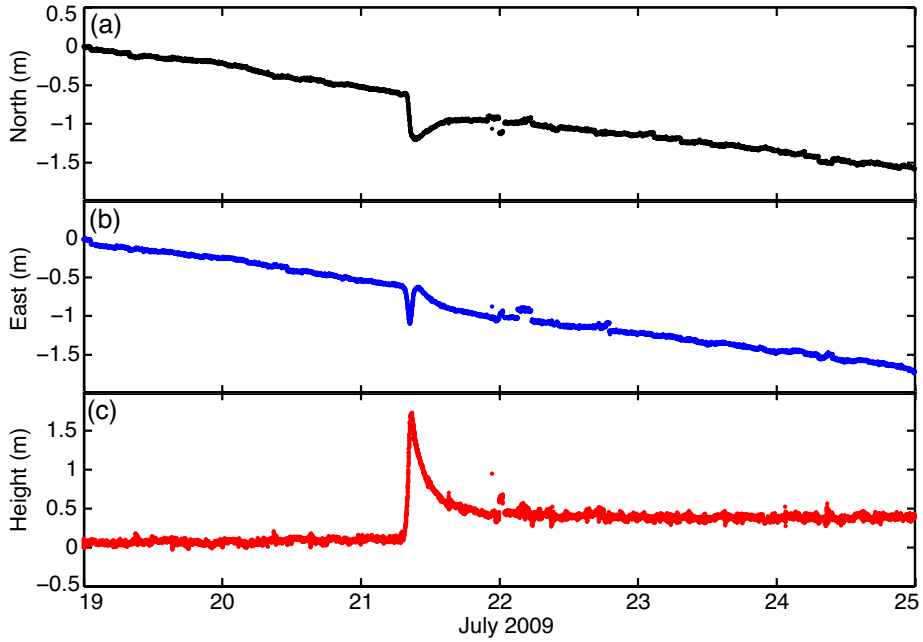

Figure 4.5: Position (north, east and height) time series for SKB3 GPS capturing a rapid lake drainage event on 21 July 2009. Data were processed using APPS precise point positioning.

The motion of the GPS is highly comparable in both magnitude and form to that documented by Das and others (2008) (cf. Figure 1.5) and at the time this was only the second GPS observation of such an event. The short timescale of the motion of the GPS indicates that the drainage event was rapid, perhaps completed within a couple of hours. The rapid metre-scale surface uplift suggests that the lake water quickly accessed the bed causing hydraulic ice-bed separation (e.g. Iken and others, 1983; Sugiyama and Gudmundsson, 2004; Das and others, 2008). Without more data, from for example other adjacent GPS, it is difficult to explain the reversal in horizontal motion recorded by the SKB3 GPS — similarly Das and others (2008) offered no explanation for this behaviour. Analysis of MODIS and other satellite imagery (Fitzpatrick, 2013; Fitzpatrick and others, 2014) revealed that

the lake formed gradually, and rapidly drained, each summer in all the years with available data (2002 to 2009). In 2010 this site was targeted with an array of geophysical techniques and instrumentation. Radio echo sounding (Lindback and others, 2014) was conducted over the site during May 2010 and a comprehensive instrument array, including a GPS strain diamond[2], water pressure loggers and a network of seismometers, was installed in late June 2010 (see Chapter 5). The SKB3 GPS site was also the location of three seismic reflection experiments conducted post-drainage, which indicate the presence of lodged till underlying a $< 2\,\mathrm{m}$ thick water-saturated dilatant till layer (Booth and others, 2012; Kulessa and others, 2012).

4.5 Diurnal velocity variations

The diurnal cycle in horizontal velocity, which lags the diurnal melt cycle, provides strong evidence for basal hydrological coupling (Shepherd and others, 2009). Cross-correlation analysis reveals that the lag time between runoff[3] and horizontal velocity at SHR in 2011 decreased from $\sim 7\,\mathrm{hours}$ at the melt onset peak to $\sim 3\,\mathrm{hours}$ in mid-August[4] (Figs. 4.6 and 4.7). Even during mid-summer, cold periods of cloud cover and snowfall reset the system and when the diurnal cycles return with the return of melt the lag time is greater and the velocity response is higher than during the preceding period (Fig. 4.6). This resetting indicates that the basal hydrological system is sensitive to variations in melt inputs: short periods of low water inputs presumably allow the system to close, re-priming the ice sheet for a larger response when high melt rates return. Hence, 'mini spring events' occur throughout the melt season whenever the capacity of the hydrological system is challenged by surface water inputs. This behaviour is consistent with Schoof (2010) who amalgamated

[2]Note that the SKB3 GPS is renamed GPS_W in Chapter 5.
[3]Runoff is defined as melt that does not refreeze, see van As and others (2012).
[4]Note that the correlation coefficient is often high when both variables are steady giving a zero time lag.

the two existing models of glacier hydrology (distributed and channelised) and concluded that melt supply variability, not mean melt, would drive net ice sheet acceleration.

To investigate further, three characteristic periods (I to III) with strong diurnal variations were identified and these are shaded on Figure 4.6. Period I includes the 'spring event' or melt-onset peak, Period II represents mid-summer, and Period III portrays typical late-summer behaviour. A fourth period (IV) during an anomalous high-magnitude runoff and acceleration event and a 'winter' period (V) are also examined.

4.5.1 Period I: The spring event

In 2011 the spring event (or melt-onset peak) commenced on 8 June approximately 1 week after melt onset at SHR. Velocity peaked at 22:50 on 8 June at $580\,\mathrm{m\,yr^{-1}}$ substantially above pre-event levels (Fig. 4.8a). Velocities preceding the spring event were slightly lower ($105\,\mathrm{m\,yr^{-1}}$) than the long term mean at SHR of $\sim 120\,\mathrm{m\,yr^{-1}}$ (van de Wal and others, 2008). The rate of surface height change (dZ/dt) shows strong correlation with the horizontal velocity with no lag (Fig. 4.8b,c). Surface height during Period I exhibits both a diurnal cycle, peaking after peak daily velocity, and a long term linear trend (Fig. 4.8) remarkably similar to the 0.6 m of uplift measured by Iken and others (1983) during the spring event on Unteraargletscher in 1975. During Period I ~ 0.5 m of surface uplift is recorded. Surface velocity and uplift appear to be strongly coupled to the diurnal melt cycle, which peaked at $\sim 4\,\mathrm{mm\,w.e.\,h^{-1}}$ several hours (mean of 7.1 hours, Figure 4.7) before peak velocity. Daily total melt was approximately 3 to 4 cm w.e. and lower daily melt rates are reflected by lower velocities and uplift (Fig. 4.8).

During Period I, variations in borehole water pressure at SHR begin later than variations in ice motion, perhaps due to the delayed connection of the borehole to the subglacial

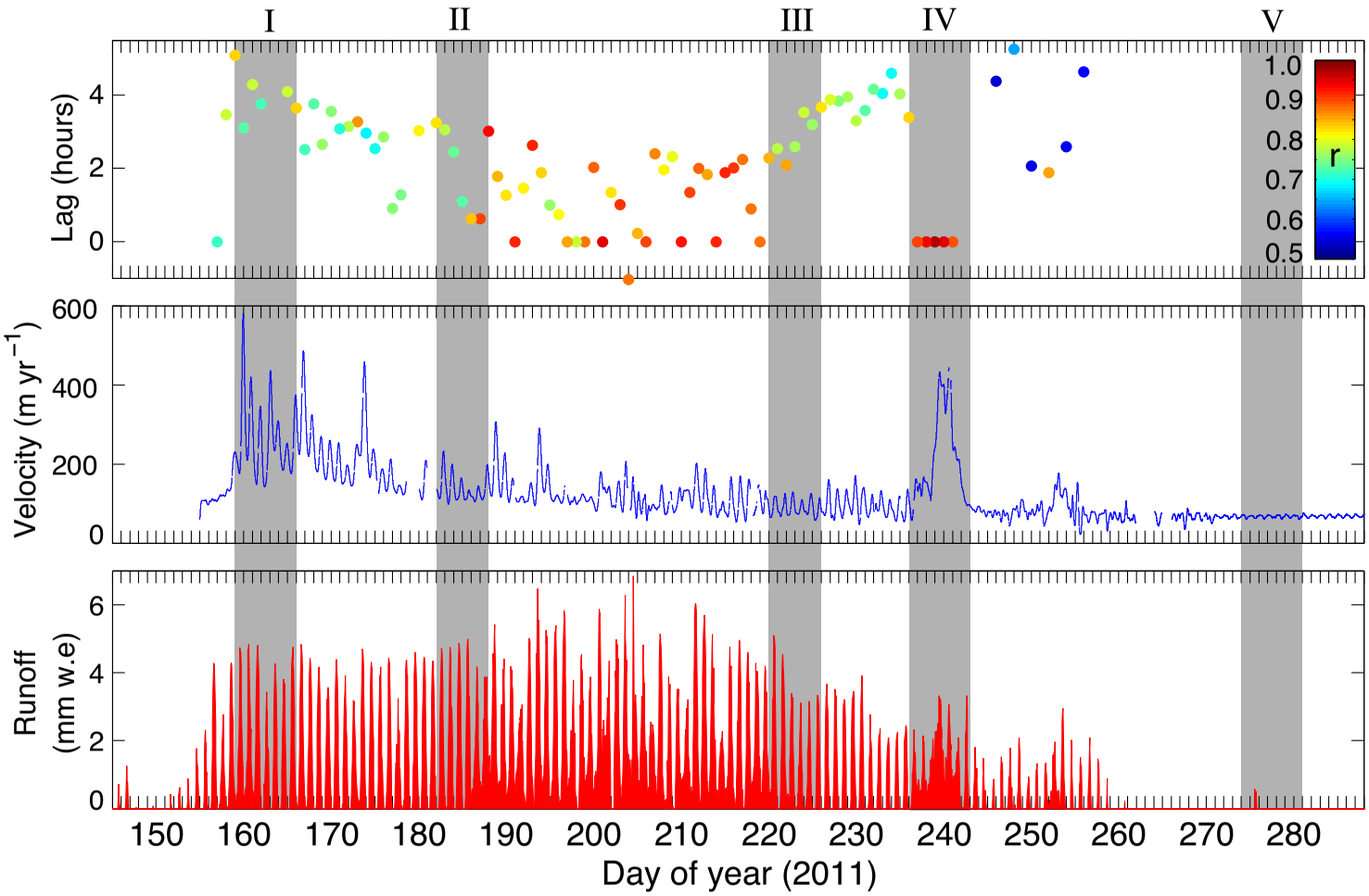

Figure 4.6: (a) Evolution of the lagged correlation between velocity (b) and melt runoff (c) at SHR during 2011. Lag is defined as positive when runoff leads and only plotted when $r > 0.5$. The colour scale on (a) portrays the correlation coefficient (r). The grey shading highlight the three (I to III) periods in Figure 4.7, a late-season acceleration event (IV) and a winter period (V).

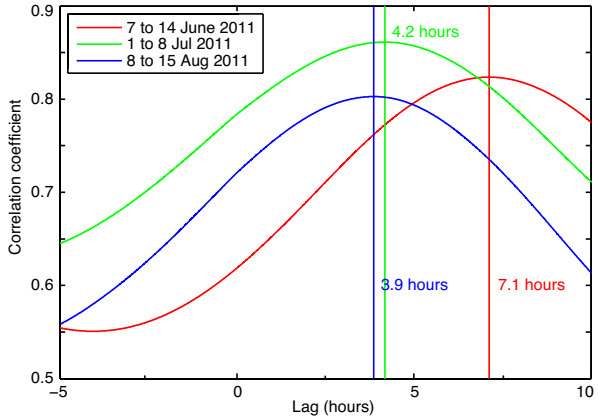

Figure 4.7: The seasonal evolution of the time lag between velocity and runoff at SHR averaged over three week-long periods selected to be representative of Periods I to III shaded in Figure 4.6. Lag is positive when runoff leads.

hydrological system. Subglacial water pressure (interpreted from the borehole water level) is steady and high prior to the spring event velocity increase and no variation in water level is detected until 2 days after peak velocity (Fig. 4.8c). Water level in the borehole then lowered before beginning a diurnal cycle that correlates with horizontal velocity and surface height change with no lag. Once the diurnals are established, peak rates of water pressure change ($\mathrm{dP_w/dt}$) precede peak horizontal velocities and surface height change. The delay and imperfect relationship between ice motion and water pressure variations can be explained by the different scales which relate them: horizontal and vertical ice motion are theorised to be driven by regional basal water pressure (e.g. Harper and others, 2002, 2007) while the borehole represents a spatially discrete, and therefore localised, measurement of subglacial water pressure. Furthermore, it is impossible to do more than speculate how well the borehole is connected to the subglacial drainage system, if indeed it is connected at all, at any point in time especially at the start of the spring event. An imperfect connection of the borehole to the subglacial system could explain why the cycles in borehole

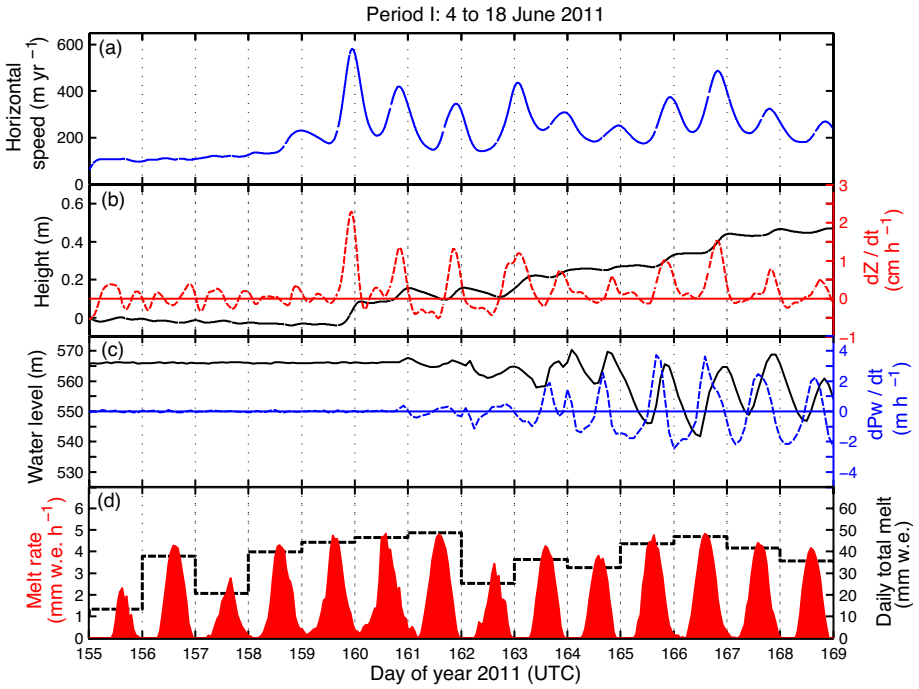

Figure 4.8: Selected time series for Period I (4 to 18 June 2011) at SHR: (a) horizontal velocity, (b) surface height (black) and the rate of surface height change (red dashed line), (c) borehole water level (black) and the rate of water level change (blue dashed line), and (d) melt rate (red) and daily total melt (dashed line). Note that the GPS time series in Figs. 4.8 to 4.13 have been filtered using a 12-hour period Butterworth filter (see Section 3.2.5) and that water pressure is sampled every 2 hours.

water pressure are out of phase with the diurnal melt cycle (Gordon and others, 1998). Despite these limitations, the data presented in Figure 4.8 provide strong evidence for, and detailed insight into, basal hydrological coupling during a 'spring event' on the Greenland Ice Sheet.

4.5.2 Period II: Mid-summer

By mid-summer (1 to 7 July 2011) velocities have decreased from the peak values at melt onset to $\sim 175\ \mathrm{m\,yr^{-1}}$ on average (Fig. 4.9a). Diurnal variations in ice velocity are still

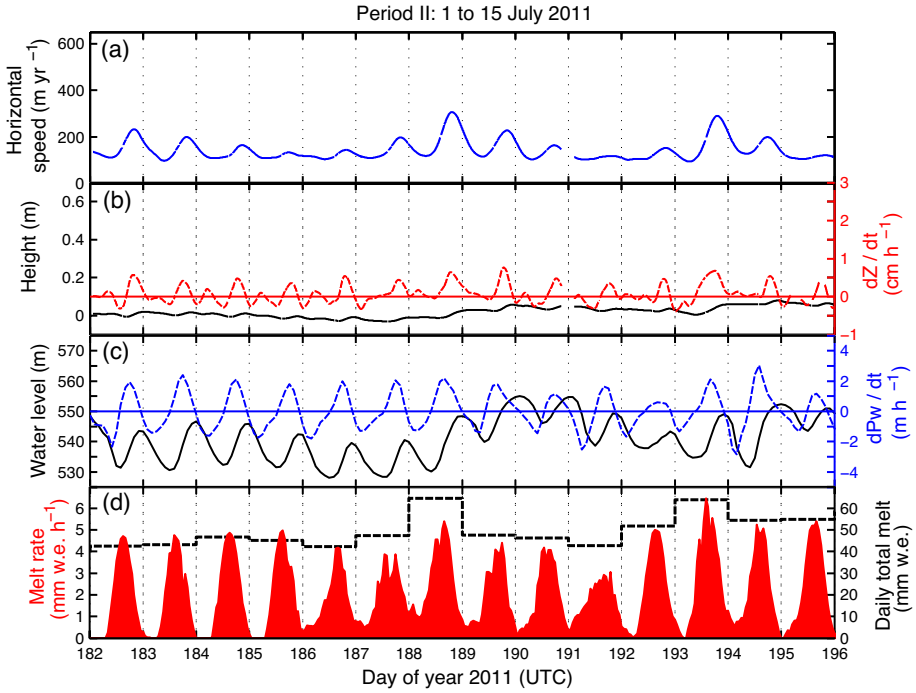

Figure 4.9: Selected time series for Period II (1 to 15 July 2011) at SHR: (a) horizontal velocity, (b) surface height (black) and the rate of surface height change (red dashed line), (c) borehole water level (black) and the rate of water level change (blue dashed line), and (d) melt rate (red) and daily total melt (dashed line). Note that to aid comparison the axes scales are constant for Figs. 4.8, 4.9, 4.11, 4.12, and 4.13.

present but their amplitude is generally lower despite strong melt of 40 to 60 mm w.e. d^{-1} prevalent throughout Period II (Fig. 4.9). Horizontal velocities, surface uplift and water pressure all respond to days with higher than normal total melt (Fig. 4.9). High daily total melt is often a manifestation of melt occurring round the clock at modest rates rather than by the highest peak melt rates. At least two modes of melt are apparent: (1) clean diurnal cycles with melt ceasing at night presumably under clear sky conditions when radiative heat loss lowers night time temperatures to below freezing, and (2) the diurnal variation is evident but melt also continues through the night at a lower rate — indicative of cloudy conditions (e.g. Ambach, 1974; Alt, 1978). During 'Mode 2' melt, above-freezing

air temperatures during the night prevent a frozen crust forming on the ice surface, thereby freeing up the energy that would usually be required to melt this crust for further ice melt. Following a period of 'Mode 2' melt there is a substantial rise in the borehole water level which is reflected in the surface height and a brief (2-day-long) increase in velocities (Fig. 4.9).

Consistent with previous observations and modelling (e.g. Iken, 1981; Iken and others, 1983) throughout Period II peak velocities occur at peak rates of vertical uplift, not their maxima. This relationship is seen clearly when the two variables are overlaid (Fig. 4.10). During mid-summer (Period II) the mean lag between horizontal and vertical velocity was zero, with a correlation coefficient (r) of 0.46. During this period, horizontal velocity and rates of surface uplift peak at ~20:00 UTC, ~ 4.2 hours after peak runoff (Figs. 4.7, 4.8 and 4.10).

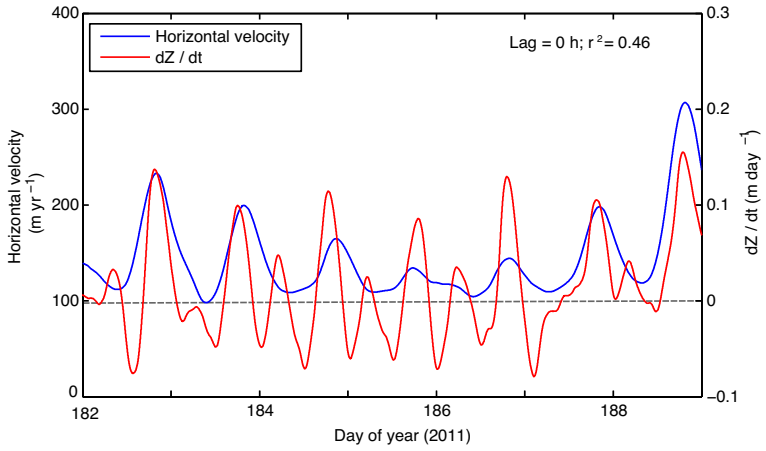

Figure 4.10: Horizontal and vertical (dZ / dt) velocity at SHR during the first week of Period II. The mean lag from cross-correlation and the correlation coefficient (r) are given. Note that the vertical strain rate was not removed from the surface height record before differentiation (see Section 3.3).

4.5.3 Period III: Late-summer

By late-summer 2011 (Period III) the magnitude and amplitude of diurnal velocity variations at SHR had decreased in comparison to Period II (Fig. 4.11a). Declining melt rates into mid-August were accompanied by a gradual reduction in the amplitude of diurnal variations in both velocity and water level (Fig. 4.11). Peaks in horizontal velocity still approximately coincided with maximum rates of surface uplift and water pressure.

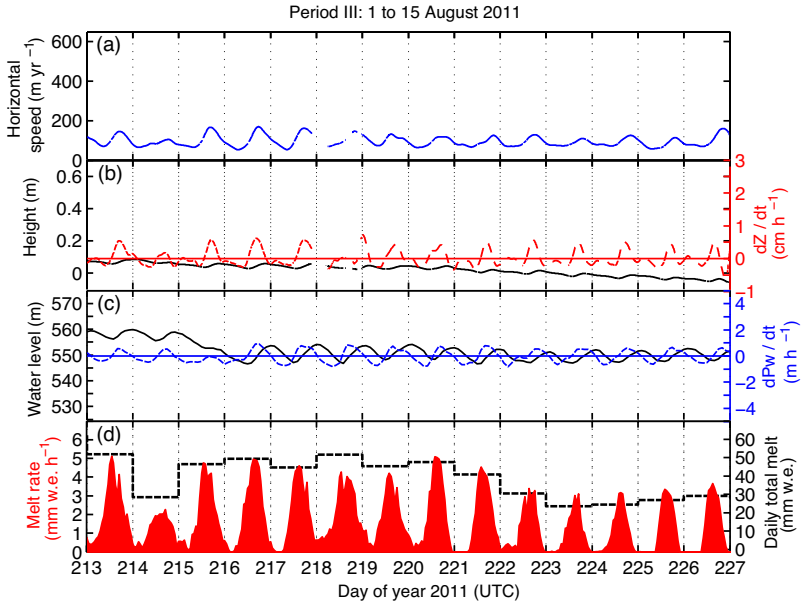

Figure 4.11: Selected time series for Period III (1 to 18 August 2011) at SHR: (a) horizontal velocity, (b) surface height (black) and the rate of surface height change (red dashed line), (c) borehole water level (black) and the rate of water level change (blue dashed line), and (d) melt rate (red) and daily total melt (dashed line).

The relationships and lags between velocity and runoff, and between horizontal velocity and vertical velocity, are clear and consistent with previous work (e.g. Iken, 1981; Iken and others, 1983; Bartholomaus and others, 2008). The lag time between melt and velocity decreased with the progression of the melt season from Period I to Period III (Fig. 4.7).

The rate of decrease in the lag between melt and velocity was initially rapid, decreasing from 7.1 hours in Period I to 4.2 hours in Period II. Between Periods II and III the rate of decrease had declined and the lag between melt and horizontal velocity is 3.9 hours in Period III (Fig. 4.7). The strength of the diurnal variations is apparent in the correlation coefficient during the periods: the mean r value is highest in mid-summer (Period II) and lowest during late-summer (Period III) when the amplitude in diurnal velocity variations reaches a minimum.

The relationship between water pressure and horizontal velocity is, however, less easy to discern. Examining Figures 4.8, 4.9 and 4.11 reveals that water pressure either slightly leads or slightly lags horizontal velocity at different times in the season. This time-variant relationship can, however remain consistent with previous work that investigates the hysteresis between water pressure and surface velocity (e.g. Sugiyama and Gudmundsson, 2004) and suggests that the horizontal velocity is governed by the regional not localised subglacial water pressure (e.g. Hubbard and others, 1995; Harper and others, 2007).

The correlation between borehole water pressure and velocity is however high (with no lag) during pronounced acceleration events, presumably as the local subglacial water pressure (i.e. in the borehole) is similar to the regional water pressure field when large inputs of surface water hydraulically decouple the ice from its bed over a large area (Harper and others, 2007; Bartholomaus and others, 2008). One such event occurred in late August 2011 (Period IV) when high magnitude runoff was sustained during the day and night for a week-long period (Fig. 4.6).

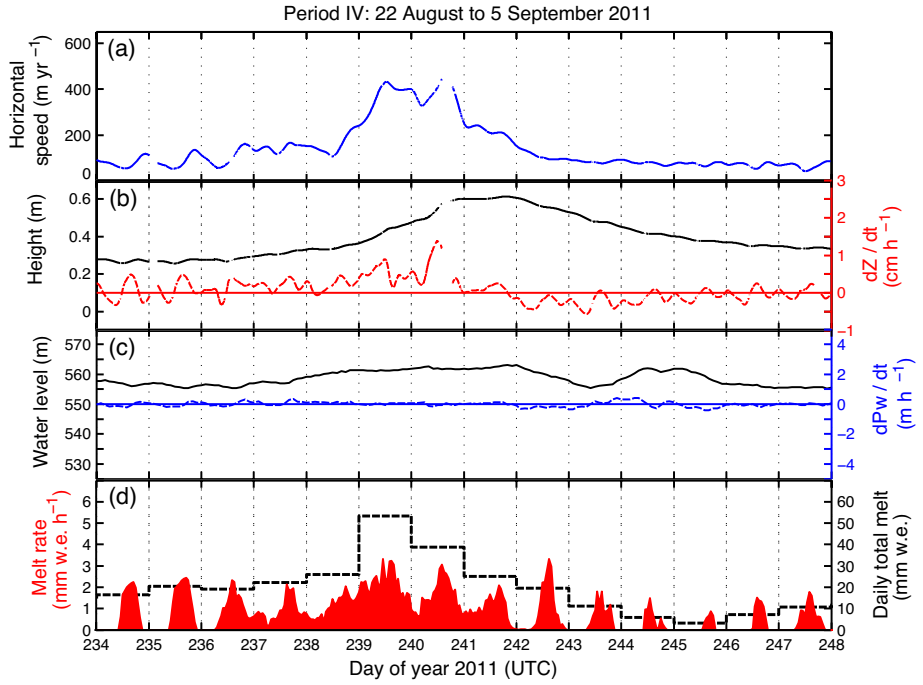

Figure 4.12: Selected time series for Period IV (22 August to 5 September 2011) at SHR: (a) horizontal velocity, (b) surface height (black) and the rate of surface height change (red dashed line), (c) borehole water level (black) and the rate of water level change (blue dashed line), and (d) melt rate (red) and daily total melt (dashed line).

4.5.4 Period IV: Late-summer acceleration event

Subglacial water pressures approximately 10 m of water head higher than during Period III were maintained throughout the late-August event (Fig. 4.12), which was also associated with 0.35 m of surface uplift recorded by the SHR GPS receiver. This event, which can be seen at all GPS sites on Russell Glacier catchment (Fig. 4.2) provides a natural experiment through which insight can be gained into basal hydrological forcing. Further examination is reserved for Chapter 6.

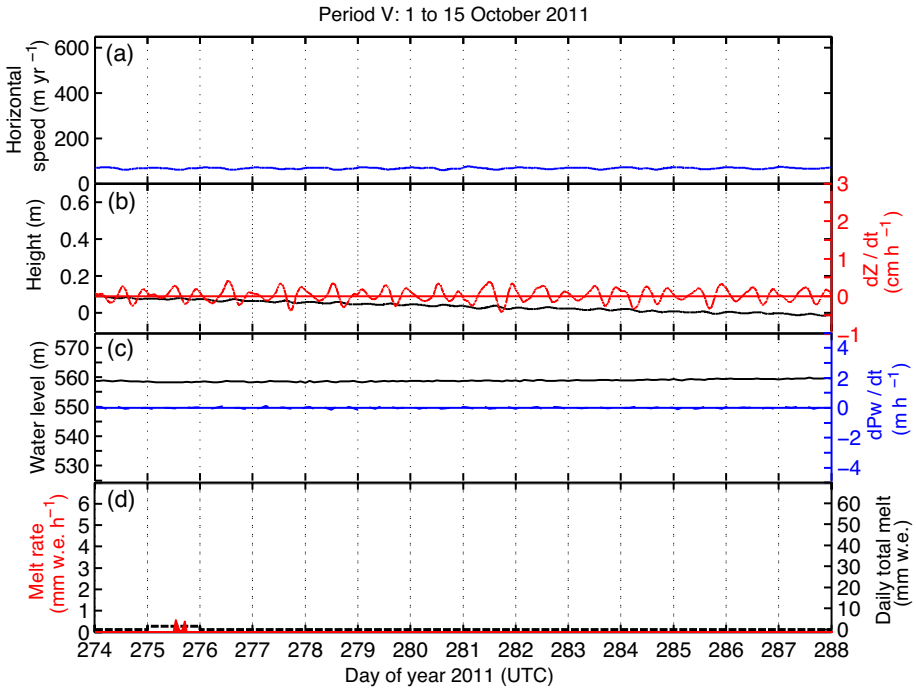

Figure 4.13: Selected time series for Period V (22 August to 5 September 2011) at SHR: (a) horizontal velocity, (b) surface height (black) and the rate of surface height change (red dashed line), (c) borehole water level (black) and the rate of water level change (blue dashed line), and (d) melt rate (red) and daily total melt (dashed line).

4.5.5 Period V: Winter

During Period V (1 to 15 October 2011) melt was negligible, occurring only on one day and totalling just 2 mm w.e (Fig. 4.13d). Horizontal velocity shows a steady positive linear trend increasing from 66 m yr^{-1} to 69 m yr^{-1} during Period V (Fig. 4.13a) that is consistent with remote sensing observations (Fitzpatrick and others, 2013; Joughin and others, 2010) of a slight catchment wide acceleration over winter. Water pressure also steadily increased during Period V (Fig. 4.13c) supporting the hypothesis that basal water pressurises as subglacial cavities and channels close (Joughin and others, 2010; Fitzpatrick

and others, 2013). Surface height declined steadily subsiding 0.1 m during the two-week-long period (Fig. 4.13b), consistent with the combination of bed parallel motion and surface lowering due to the release of stored water at the bed. Small cyclical variations in the uplift rate during Period V may not be real motion and could be attributed to the amplification of errors in the height time series caused, for example, by sub-diurnal variations in the ionospheric delay or signal multi-path that have not been cancelled out during post-processing (King, 2004).

4.6 Summary

This chapter has introduced a selection of the velocity time series collected during the course of this study. It has demonstrated that dual-frequency GPS receivers are capable of collecting high-frequency measurements of ice velocity at point locations at a precision sufficient to study variations on relativey slow-moving ice ($\sim 100\ \mathrm{m\,yr^{-1}}$) on sub-diurnal — and even sub-hourly — time scales. Such measurements can be made unattended over long periods of time.

The seasonal variation in velocity recorded by the GPS receivers across Russell Glacier catchment is consistent with previous studies (e.g. Bartholomew and others, 2010, 2011a; Hoffman and others, 2011): velocities peak at melt onset, gradually decelerate into mid-summer attaining an all year minimum in late summer when declining melt inputs are presumably easily accommodated by an efficient hydrologic network. Transient acceleration events are superimposed on the seasonal cycle, driven by lake drainage events, initiation of drainage into moulins or simply high melt rates driven by atmospheric conditions.

Detailed analysis of the short-term variations in velocity at SHR confirm that the diurnal velocity cycle is strongly coupled to the diurnal melt cycle. The lag time between peak

melt and peak velocity decreased markedly as the melt season progressed indicating that supra-, en- and sub-glacial hydraulic pathways evolve to greater efficiency with cumulative inputs of surface water to the bed. Throughout the melt season surface velocities remain sensitive to variations in melt (although this sensitivity does decrease into late summer) and periods of low melt result in low velocities followed by a 'mini spring event' when melt returns. This finding indicates that the basal hydrological system continually adapts to the flux of water from the surface. Consistent with the theory of cavity opening (Iken, 1981), velocity is correlated with rates of surface uplift not absolute displacement. During two weeks that include the spring event at SHR (Period 1) the surface height increased by 0.5 m — a strong indicator of water storage at the bed that is remarkably similar to the 0.6 m of uplift recorded by Iken and others (1983) during the spring event on Unteraargletscher in 1975.

For reasons outlined in Chapter 1 a transect based study incorporating all the velocity records will not be repeated here as such studies have already been undertaken in the same study area (e.g. van de Wal and others, 2008; Bartholomew and others, 2010, 2011a). Instead, the following three chapters focus on specific events and sites. These case studies include a rapid in situ lake drainage event (Chapter 5), detailed analysis of the late-summer acceleration event depicted on Figure 4.12 (Chapter 6), and a rigorous investigation of ice surface velocities in the ice sheet's interior at site S10 on the K-transect (Chapter 7).

Chapter 5

Results II: Ice tectonic deformation during the rapid in situ drainage of a supraglacial lake on the Greenland Ice Sheet

Author Contributions

Several authors contributed to this chapter which was published in The Cryosphere as Doyle and others (2013) and is included in Appendix A. Andrew Fitzpatrick made the remote sensing observations that formed Figures. 5.1 and 5.2. Glenn Jones prepared the passive seismic data (Fig. 5.8). Katrin Lindback and Rickard Pettersson provided the subglacial and supraglacial DEMs which Christine Dow used to calculate the hydraulic potential gradients (Fig. 5.11). Christine Dow also calculated the discharge from the lake

bathymetry and lake level time series. Sam Doyle led the field campaign, processed the GPS records, collated the datasets and wrote the text. Alun Hubbard, Bernd Kulessa, Alessio Gusmeroli and Jason Box advised and commented on drafts.

5.1 Summary

This chapter presents detailed records of lake discharge, ice motion and passive seismicity capturing the behaviour and processes preceding, during and following the rapid drainage of a $\sim 4\,\mathrm{km}^2$ supraglacial lake through 1.1-km-thick ice on the western margin of the Greenland Ice Sheet. Peak discharge of $3300\,\mathrm{m}^3\,\mathrm{s}^{-1}$ coincident with maximal rates of vertical uplift indicate that surface water accessed the ice-bed interface causing widespread hydraulic separation and enhanced basal motion. The differential motion of four Global Positioning System receivers located around the lake record the opening and closure of the fractures through which the lake drained. On the basis of the results presented it is hypothesised that the majority of discharge occurred through a ~ 3-km-long fracture with a peak width averaged across its wetted length of $\sim 0.4\,\mathrm{m}$. Hence, it can be argued that the fracture's kilometre-scale-length allowed rapid discharge to be achieved by combining reasonable water velocities with sub-metre fracture widths. These observations add to the currently limited knowledge of in situ supraglacial lake drainage events, which rapidly deliver large volumes of water to the ice-bed interface.

5.2 Introduction

Variations in the delivery of surface water to the base of the Greenland Ice Sheet induce fluctuations in ice sheet velocity on inter-annual, seasonal, diurnal and sub-diurnal time

scales (Zwally and others, 2002; van de Wal and others, 2008; Das and others, 2008; Shepherd and others, 2009; Bartholomew and others, 2010, 2011a; Hoffman and others, 2011). For water to access the bed of the Greenland Ice Sheet, a hydraulic pathway must first be established through often kilometre-thick ice. Given sufficient water supply, a water-filled fracture will propagate to the base of an ice mass when the overburden stress at the fracture tip is offset by the density contrast between ice and water (Weertman, 1973; Alley and others, 2005b; van der Veen, 2007).

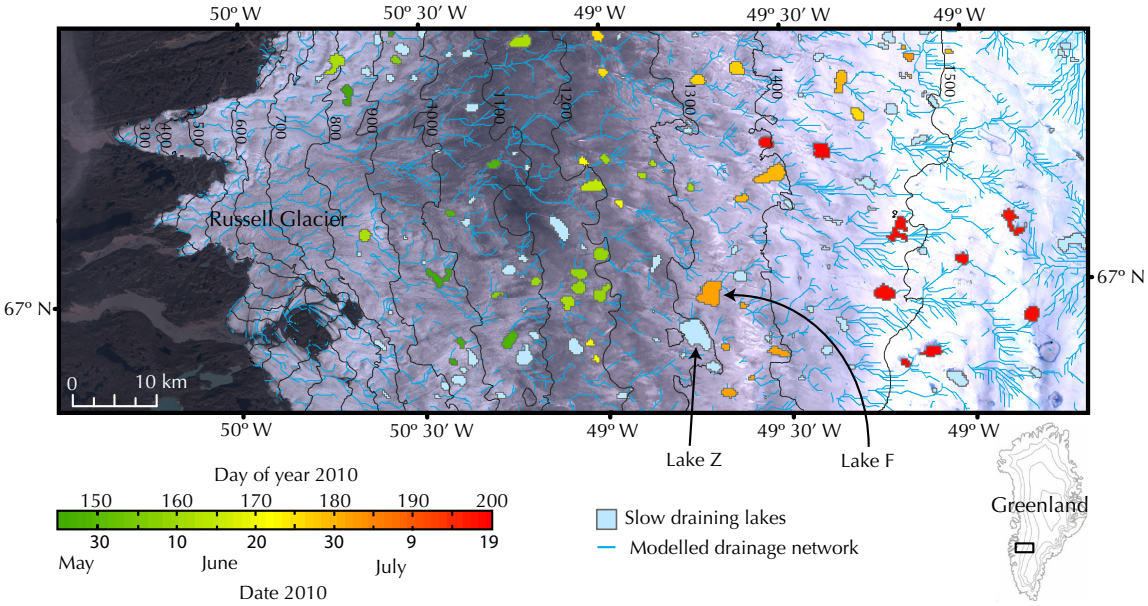

Figure 5.1: The maximum extent of supraglacial lakes within the Russell Glacier catchment during the 2010 melt-season and the location of the field site, Lake F. The green-red colour scheme indicates the timing of rapidly draining ($<$ 4 days) lakes, with slow-draining ($>$ 4 days) lakes in blue. The modelled supraglacial drainage network is shown. The background is a 30 m resolution Landsat image acquired on the 18 August 2010.

Krawczynski and others (2009) calculated that supraglacial lakes 250 to 800 m across and 2 to 5 m deep contain sufficient water to drive a fracture to the base of kilometre-thick ice. Many lakes on the Greenland Ice Sheet attain this size or larger (Echelmeyer and others, 1991; Box and Ski, 2007; Georgiou and others, 2009) of which a small proportion

(13 % between 2005–2009) drain in less than 2 days (Selmes and others, 2011). Surface lakes can drain rapidly into moulins via supraglacial rivers, however many drain by the in situ propagation of hydraulically driven fractures (e.g. Das and others, 2008), a process hereafter termed lake tapping.

Lake tapping events provide water fluxes that exceed the capacity of the subglacial drainage system, leading to transient high subglacial water pressures, hydraulic jacking and ice sheet acceleration (Bartholomaus and others, 2008; Das and others, 2008; Pimental and Flowers, 2010). The integrated effect of multiple lake tapping events, and continued water flow into the hydraulic pathways they create, has the capacity to impact the annual ice flux in future years, especially as, in a warming climate, lakes are expected to form and drain earlier in the season (Liang and others, 2012) and at higher elevations (Howat and others, 2013). It is, however, uncertain whether this increase in water delivery will enhance the annual ice flux through a net increase in basal lubrication (e.g. Zwally and others, 2002), or reduce it due to an earlier seasonal transition to an efficient subglacial drainage system (e.g. Sundal and others, 2011).

Whilst supraglacial lake-tapping events represent major perturbations of the subglacial hydrological system and provide natural experiments for process-based investigations of glacier-hydromechanics, few studies have succeeded in capturing them. Boon and Sharp (2003) measured premonitory drainage events preceding the complete and rapid (< 1 h) drainage of a 6.9 m deep supraglacial pond through a 150 m thick Arctic glacier on Ellesmere Island. Das and others (2008) observed horizontal and vertical ice motion and seismicity during the rapid (~ 1.4 h) tapping of a large supraglacial lake through 980 m of ice to the bed of the Greenland Ice Sheet. This study presents detailed measurements of ice motion, lake volume change and seismicity capturing the rapid tapping of a large supraglacial lake through 1.1-km-thick ice on the western margin of the Greenland Ice Sheet.

5.3 Field site and methods

The field site, Lake F (67.01° N 48.74° W), is located 70 km from the terminus of Russell Glacier, West Greenland (Fig. 5.1). Russell Glacier catchment represents a typical land-terminating sector of the Greenland Ice Sheet which, during the melt-season accumulates supraglacial lakes (McMillan and others, 2007) and shows diurnal (e.g. Shepherd and others, 2009) and seasonal (e.g. Bartholomew and others, 2010) covariations in ice velocity and surface uplift.

Remote sensing observations indicate annually repeating growth and rapid drainage of Lake F in the same location, with a mean date of drainage between 2002 and 2009 of 14 July. During the abnormally warm melt seasons of 2003, 2007 and 2010 (see Cappelen and others, 2001, 2011) Lake F tapped 3 to 4 weeks earlier compared to other years in the 2002 to 2010 period.

On 26 June 2010, Lake F was instrumented with four Global Positioning System (GPS) receivers, six seismometers and two water level sensors. Five days later at 01:40 on the 30 June, the lake drained completely in ~ 2 h. Following drainage, the bathymetry of the lake bed and the locations of fractures and moulins were surveyed. Lake volume (V) and discharge (Q) are estimated by combining water level measurements with the lake bathymetry. All times are expressed in Coordinated Universal Time (UTC) which is three hours ahead of West Greenland Time.

5.3.1 Measurements of ice motion

Four dual-frequency GPS receivers (Trimble R7 and Leica SR520) were installed surrounding Lake F (Fig. 5.2). GPS antennae were installed on 6 m poles drilled 5 m into the ice,

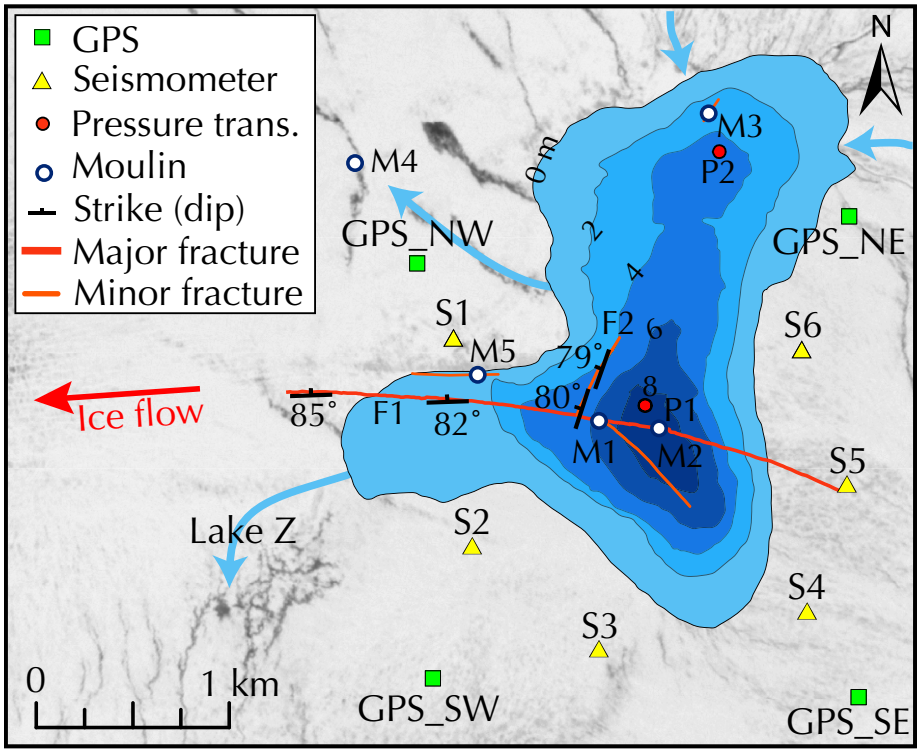

Figure 5.2: Map of Lake F showing the instrument array, the fractures and moulins surveyed post-drainage and the lake perimeter and depth immediately before rapid tapping. The direction of mean ice flow is indicated by the red arrow. The background image is a 5 m resolution SPOT image acquired 7 July 2008. The main supraglacial rivers entering and leaving Lake F are shown by blue arrows.

which subsequently froze in and thereafter provided a record of 3-dimensional ice surface motion. Data, sampled continuously at a 10 s interval, were processed against a bedrock-mounted reference station using the differential phase kinematic positioning software, Track v. 1.24 (Chen, 1998; Herring and others, 2010), and final precise ephemeris from the International GNSS Service (Dow and others, 2009). The reference station was located 1 km from the terminus of Russell Glacier giving baseline lengths ≤ 70 km. To improve solutions at the day boundary, 36 h files were processed and the first and last six hours of the output position time series were discarded. Assuming steady ice motion, uncertainties in the positions were estimated at < 0.02 m in the horizontal and < 0.05 m in the vertical by examining the detrended position time series for GPS_NW over a 2 day period in May 2011. The output position data are characterised by high frequency noise caused by receiver and data processing errors. To suppress this high-frequency noise without causing a shift in phase, positions were filtered with a 1 h centred moving average. To quantify differential motion between GPS receivers, relative inter-GPS separation and the rate of separation were calculated from the filtered positions at a 10-min interval.

5.3.2 Measuring seismic activity

The passive seismic array consisted of six GS-11D geophones with a natural frequency of 4.5 Hz and a bandwidth of 5 to 1000 Hz, continuously recording micro-seismic velocity at a 1 kHz sampling rate on to a RefTek-130 digitiser. To improve coupling with the ice the geophones were mounted on 15 kg concrete slabs (dimensions $= 0.5 \times 0.25 \times 0.05$ m), buried to a depth of ~ 0.5 m and routinely reset every 3 to 5 days before they melted out.

The limited number of seismic stations together with the large array aperture (1 to 2 km) and the high rate of seismicity make it difficult to correlate particular onset times with individual events. The inability to identify individual events prevents the location of seis-

micity using standard methods (e.g. Walter and others, 2008; Roux and others, 2010). Whilst Jones and others (2013) demonstrate that a technique based on amplitudes may be used to locate such seismicity, the application of this method is beyond the scope of this study.

In this study, the normalised root mean square (RMS) amplitude was calculated for each seismometer using an envelope function with 1-min time windows after applying a 2-pass, 4-pole Butterworth filter. The 5 to 50 Hz passband of the Butterworth filter was selected to reduce both high frequency noise (> 50 Hz) associated with surface crevassing (e.g. Neave and Savage, 1970) and any low frequencies (< 5 Hz) associated with the instrument response. To identify step changes in seismicity the normalised cumulative (seismic) energy was calculateed from the RMS amplitudes.

5.3.3 Measurements of lake dynamics

Two pressure transducers (P1 and P2, Solinst M15 Levelogger) were installed in Lake F, logging pressure in metres of water head at two minute intervals with a specified accuracy of ± 1 cm (Fig. 5.2). The records of P1 and P2 were compensated for changes in atmospheric pressure using a third Solinst Levelogger located at GPS_NW.

Post-tapping, six transects were surveyed across the lake bed with a Leica SR520 GPS receiver recording at 1 Hz. The transects were differentially corrected and interpolated to form a digital elevation model (DEM) of the lake bathymetry with a grid spacing of 10 m. Time series of lake volume (V) and discharge (Q) were calculated by combining the DEM with the water level data. The uncertainty in the lake volume and discharge is estimated at ± 8400 m^3 and ± 130 m^3 s^{-1} respectively.

To extend the lake volume record, a time series of Lake F volume was estimated from

daily-acquired atmospherically-corrected Moderate-resolution Imaging Spectroradiometer (MODIS) images by applying the method of Box and Ski (2007). Uncertainty in this method was estimated at ±15 % by comparing MODIS-derived lake volumes with an independently collected lake bathymetry dataset.

To investigate the extent and timing of rapid draining lakes within the Russell Glacier catchment, an automatic lake classification was applied to daily-acquired, cloud-free MODIS images. Lakes were classified using the Normalised Difference Water Index (NDWI) following the method described in Huggell and others (2002). An empirically determined NDWI threshold was used to distinguish between water and other objects with a low NDWI (e.g. ice with a low albedo). The lake classification was trained using lake perimeter measurements derived from Landsat 7 images and differential GPS surveys. In combination with the NDWI threshold, thresholds for both the red and blue bands were used to further reduce misclassification of pixels with a similar spectral signal to water. Images with partial cloud cover were manually inspected. Rapid draining is defined as lakes that disappear within a 4 day interval and the date of drainage as the mid-point between the date it was last seen and the date it disappeared. Typically, slow-draining lakes took much longer to drain than the 4 day threshold and there is a clear distinction between lakes that drain rapidly and those that drain slowly. Figure 5.1 shows the date of drainage of rapidly draining lakes and the maximum extent of all lakes across the Russell Glacier catchment in 2010. The drainage network shown in Figure 5.1 was created using hydrological modelling software (ArcGIS hydrological toolkit) from a 30 m resolution DEM derived from Système Pour l'Observation de la Terre (SPOT) data acquired on 2 July 2008.

5.3.4 Mapping hydraulic potential gradients

Basal and surface elevation DEMs collected by skidoo-based radio echo sounding following the method of Pettersson and others (2011) were used to calculate the gradients of hydraulic potential, assuming basal water pressures were everywhere equal to the ice overburden pressure (Shreve, 1972). The resulting hydraulic potential gradients can only be used to approximate the direction of subglacial water flow due to the variability in subglacial water pressure and basal hydraulic conductivity.

5.4 Results

5.4.1 Regional scale lake dynamics

Within Russell Glacier catchment in 2010, 45 % of the lakes were classified as rapid (< 4 days) draining. The earliest rapid drainage occurred in late-May and the latest in mid-July and in general lower elevation lakes drained earlier than those located at higher elevations. Rapid lake drainage events occur in clusters; multiple lakes within the same elevation band drain simultaneously (Fig. 5.1). The rapid tapping of Lake F coincided with the rapid drainage of several adjacent lakes and an isolated peak (30 June to 2 July) in the discharge of catchment-wide proglacial Watson River (see Fig. 8 of van As and others, 2012).

5.4.2 Formation and drainage of Lake F

In 2010, Lake F began to form on 5 June attaining its maximum extent on 24 June with an area of 4.5 km^2 and a volume of 1.8×10^7 m^3 (Fig. 5.3). Following the installation of

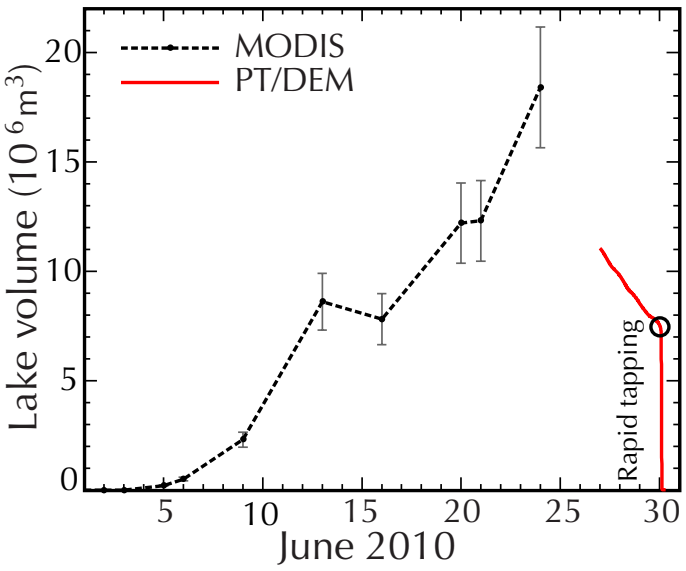

Figure 5.3: Time series of Lake F volume in 2010 estimated from MODIS using the method of Box and Ski (2007) and the pressure transducer (PT)/digital elevation model (DEM) calculations. The transition from slow drainage to rapid tapping is indicated by the black circle. Error bars indicate the $\pm 15\,\%$ uncertainty in the lake volumes calculated from MODIS.

the pressure transducers on 26 June the lake volume steadily decreased at a mean rate of 13.8 $\mathrm{m^3\,s^{-1}}$ from 1.1×10^7 $\mathrm{m^3}$ to 7.4×10^6 $\mathrm{m^3}$ immediately prior to rapid tapping. This period of low discharge amounts to a volume of 3.6×10^6 $\mathrm{m^3}$ and could be entirely accounted for by supraglacial discharge into Lake Z and moulin M4 (see Figs. 5.1 and 5.2). On 28 June 2010, water from Lake F traveled through a slow-flowing series of elongate ponds before a < 1 m wide supraglacial stream fed the water into moulin M4. During the slow-period of drainage the majority of water left Lake F via a 5- m-wide supraglacial river feeding into Lake Z.

Rapid discharge (here defined as $Q > 50$ $\mathrm{m^3\,s^{-1}}$), associated with the tapping of the lake via in situ fracture propagation, occurred between 01:40 and 03:15 on the 30 June 2010 with the discharge peaking at $Q_{\max} = 3300$ $\mathrm{m^3\,s^{-1}}$ at 02:47. Lake F had completely drained

by 03:50. Immediately prior to rapid tapping, Lake F had a maximum depth of 9.9 m, an area of 3.8 km^2 and a volume of 7.4×10^6 m^3.

5.4.3 Observations

On 29 June 2010, a healed crevasse, similar to Fig. S5 of Krawczynski and others (2009), was observed from the western margin of the lake running through the lake in a W-E direction. Closed moulins were observed in the approximate positions of M1 and M5. It is likely that these relic features were formed by lake tapping events in previous years.

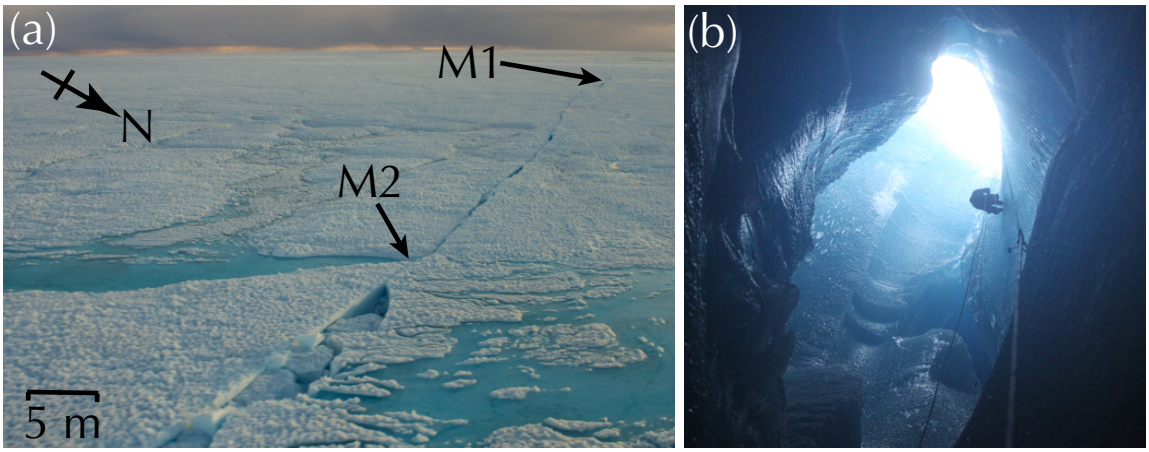

Figure 5.4: Photos of Lake F post-drainage: **(a)** the main fracture 8 days after lake tapping showing the location of moulins M1 and M2 with the deepest region of the lake located 10 m east of M2; and **(b)** the largest moulin M1, ∼10 m in diameter. Fallen ice blocks blocked the moulin at 45 m below the surface.

At 04:50 on 30 June 2010, less than 2 hours after the end of rapid discharge, ∼0.3 m deep standing water was observed in the centre of the lake overflowing across the clean-cut edge of the main fracture F1. Fracture F2 was clean cut and open by ∼0.2 m.

On 1 July, the location, dip and strike of fractures were surveyed. The main fracture, F1, was mapped for 3 km but extended beyond this as a thin (< 1 cm wide) crack. F1 and F2

were sub-vertical, dipping towards the north and west, respectively (Fig. 5.2). Differential vertical displacement was observed along F1 with the northern hanging wall displaced typically 0.1 to 0.3 m (but up to 1 m near the centre of the lake) above the southern foot wall. This structure can be interpreted as a reverse dip-slip fault and evidence for transverse (cross-flow) compression (Fig 5.5a). The largest vertical displacement was measured in the deepest region of the lake, ∼10 m east of M2.

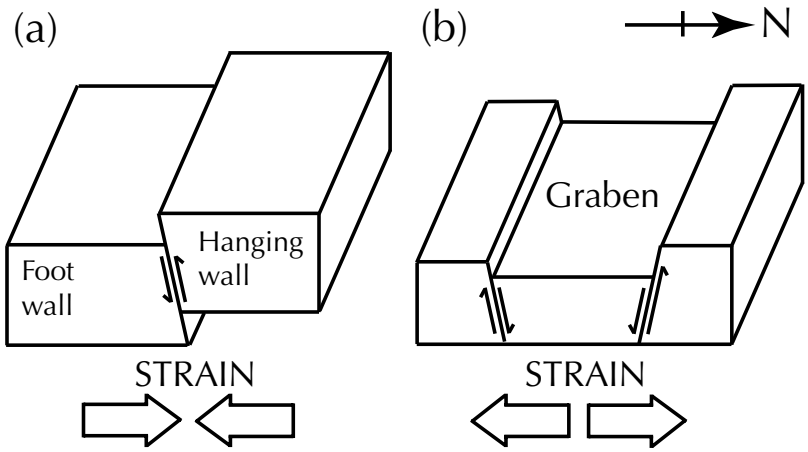

Figure 5.5: Supraglacial fracture structures observed along F1: **(a)** a reverse dip-slip fault, dipping 82 to 85° to the north, with the northern hanging wall vertically displaced above the southern foot wall, is evidence for a compressional strain regime; and **(b)** a high-angle normal fault with a dropped graben is evidence for extension across F1. Note the greater vertical offset of the northern wall compared to the southern. The diagrams are based on field measurements interpreted with the aid of Price and Cosgrove (1994).

Along F1 a number of ice blocks, detached from the ice surface, had subsided into the fracture or been uplifted by floatation (see Fig. 5.4a). The structure of the subsided blocks is that of a high-angle normal fault with a dropped 2 to 5 m wide graben (Fig 5.5b). Normal faults are evidence for transverse (cross-flow) extension across F1 (Cloos, 1955; Price and Cosgrove, 1994). Similar supraglacial fracture structures associated with hydraulic fracturing were observed following the Skeiðárjökull and Sólheimajökull jökulhaups in 1996 and 1999 respectively (see Fig. 12 of Roberts and others, 2000).

Five moulins (M1 to 5) were also mapped on 1 July (Fig. 5.2). The largest moulin (M1), ~ 10 m in diameter, was explored to a depth of 45 m below the surface (Fig. 5.4b). At 45 m depth, M1 continued vertically downwards but access was restricted by fallen blocks of ice. Water entering M2 could be heard to flow englacially along F1 at a shallow depth before descending vertically down M1.

The main ~ 5-m-wide supraglacial river flowing into Lake F from the north was intercepted by a fracture forming three moulins, collectively named M3 (Fig. 5.2). The evolution of the M3 moulins was observed over a number of days and is consistent with Stenborg (1968). Initially, water flowed into the clean-cut fracture at three discrete points and began to cut channels due to the frictional heat of melting. Over time the channels became wider and deeper. The channel of the largest moulin incised the fastest and ultimately captured all the flow. A similar evolution was observed for M2 which also continued to receive water throughout the melt season. Moulins M1 and M5 were not connected to supraglacial streams after rapid tapping.

5.4.4 Ice displacement

The horizontal and vertical ice motion recorded by the GPS receivers preceding, during and following the lake tapping event are depicted on Figure 5.6. The first abnormal GPS motion occurred on 29 June when GPS_SE accelerated to the west concomitant with ~ 0.2 m of uplift. GPS_NE and GPS_SW also accelerated, albeit with a lower magnitude. The northern two GPS receivers (GPS_NW and GPS_NE) show anomalous motion in the north-south plane including transient reverse ice flow at GPS_NW. The mean daily vector for the 29 June is of a lower magnitude for the western GPS stations compared to the eastern GPS stations, implying a compressive strain regime that is also evident in the decreasing separations between GPS NW–SE, NW–NE and SW–SE (Fig. 5.9a, b and f).

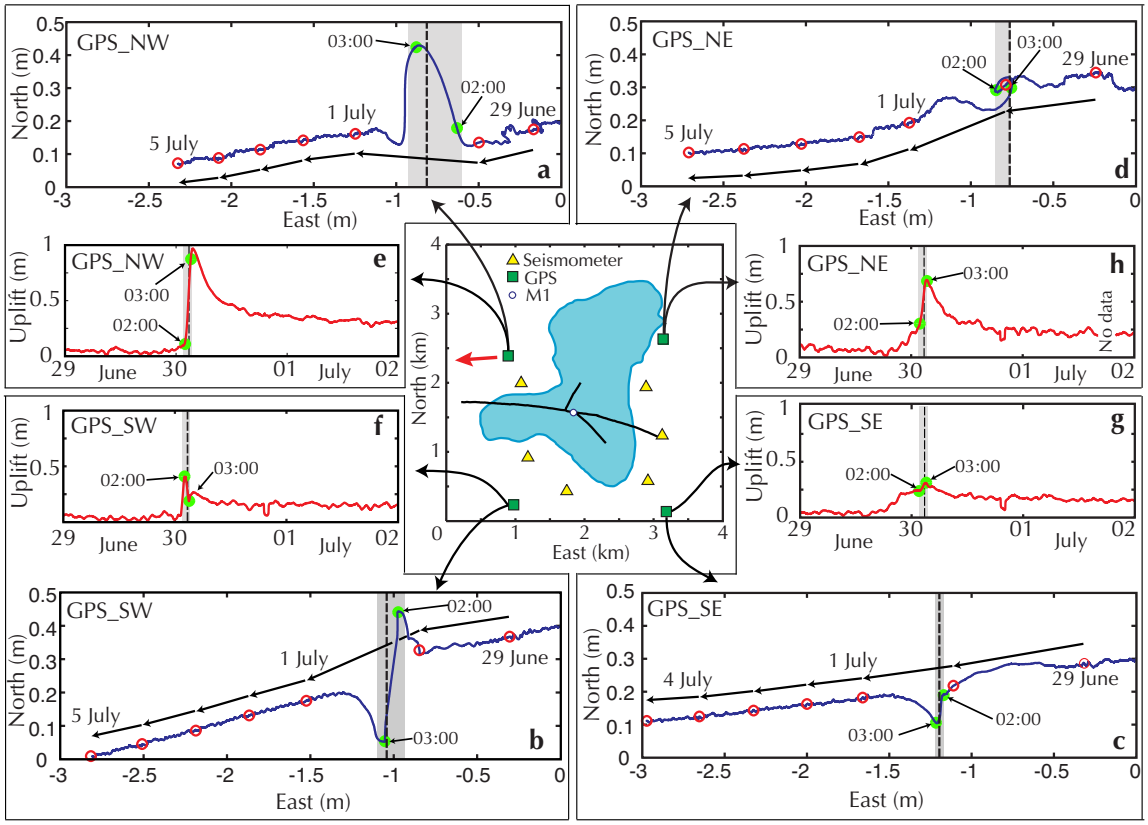

Figure 5.6: Horizontal and vertical ice motion recorded by the four GPS receivers. Plots **(a–d)** are plan views of the horizontal motion and **(e–h)** are time series of vertical uplift. To emphasise the transverse (cross-flow) motion the y-axes of **(a–d)** are exaggerated by a factor of 2. The red arrow on the map shows the direction of mean ice flow. On **(a–d)** hollow red circles indicate day boundaries and arrows represent daily vectors. On **(a–h)** solid green circles indicate the times of 02:00 and 03:00; the grey shade indicates the period of rapid ($Q > 50$ m^3 s^{-1}) discharge; and the vertical dashed line indicates the time of maximum discharge $Q_{\max}$.

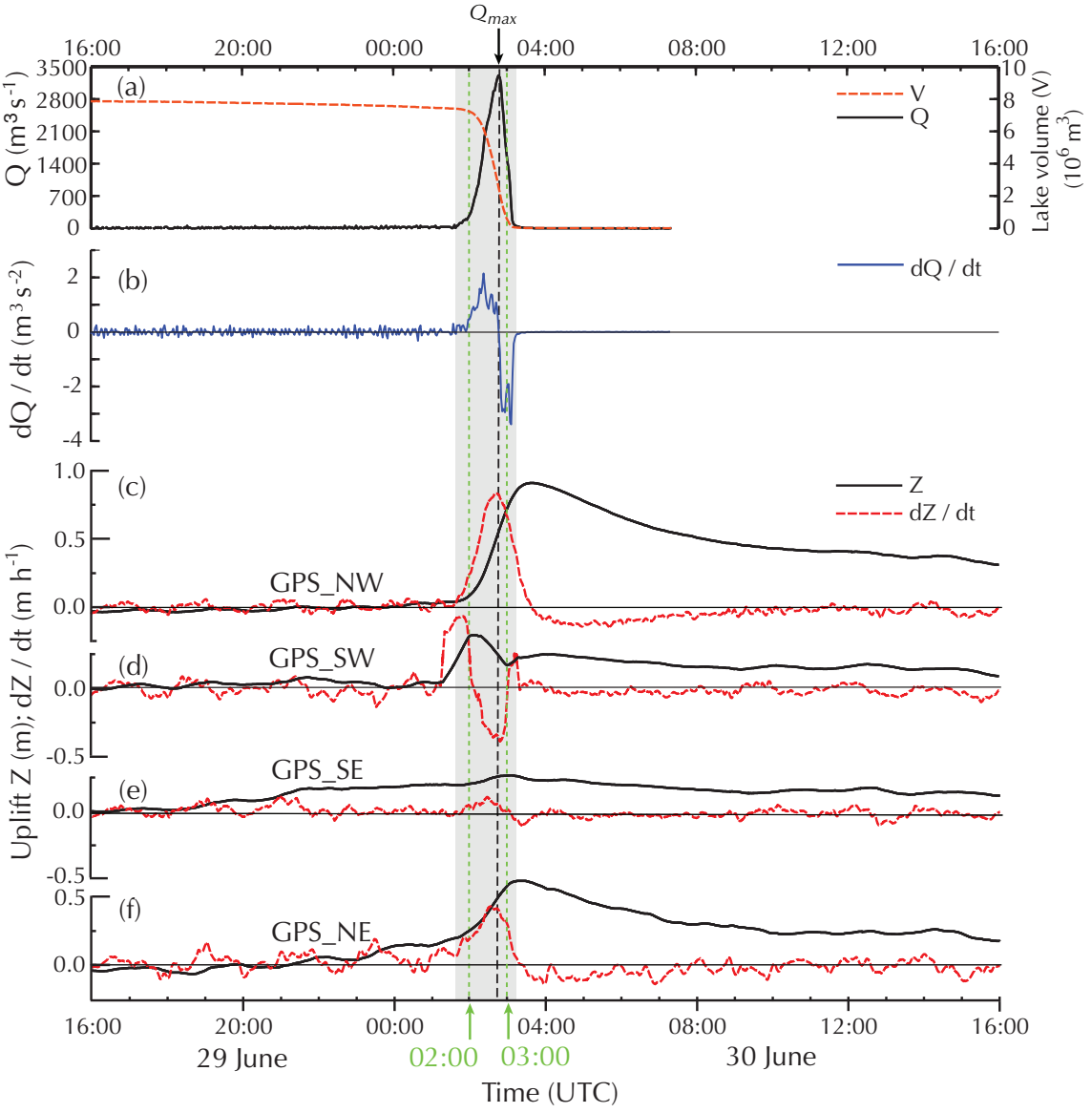

Figure 5.7: Time series of **(a)** volume V and discharge Q **(b)** rate of discharge $\mathrm{d}Q/\mathrm{d}t$ and **(c–f)** uplift Z and the rate of uplift $\mathrm{d}Z/\mathrm{d}t$ for each GPS receiver. The grey shade indicates the time of rapid ($Q > 50$ m^3 s^{-1}) discharge. The black dashed line indicates the time of peak discharge Q_{max} and the green dashed lines indicate the times of 02:00 and 03:00.

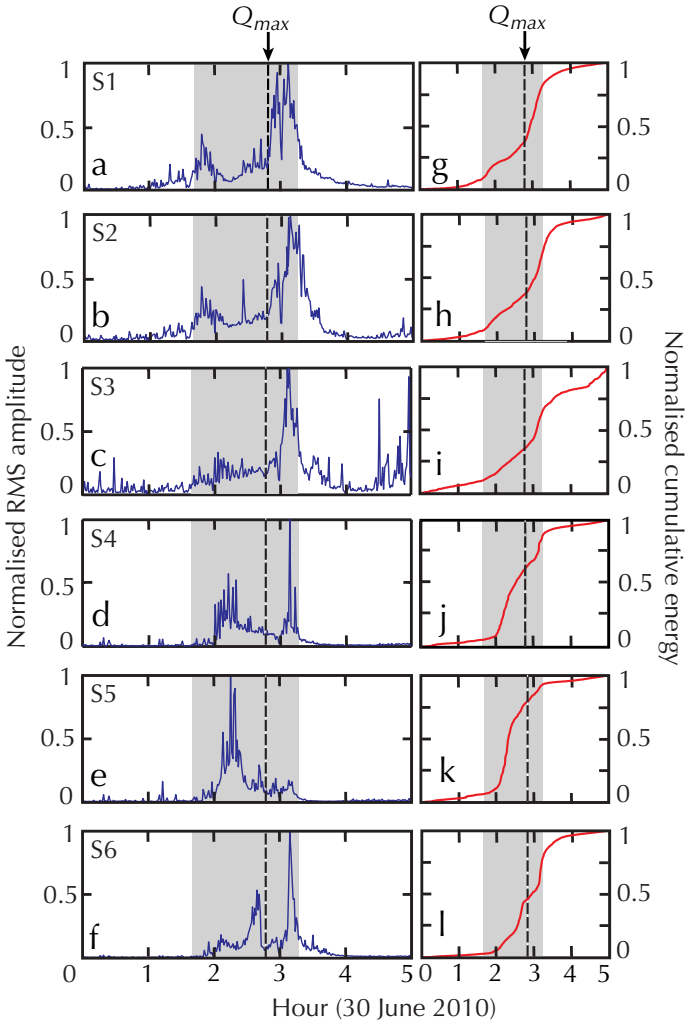

Figure 5.8: Normalised seismic RMS amplitude (**a**–**f**) and normalised seismic cumulative energy (**g**–**l**) for the passive seismic array ordered anti-clockwise from west (S1) to east (S6). The time of rapid ($Q > 50$ m^3 s^{-1}) discharge (grey shade) and the time of maximum discharge (dashed vertical line) are indicated.

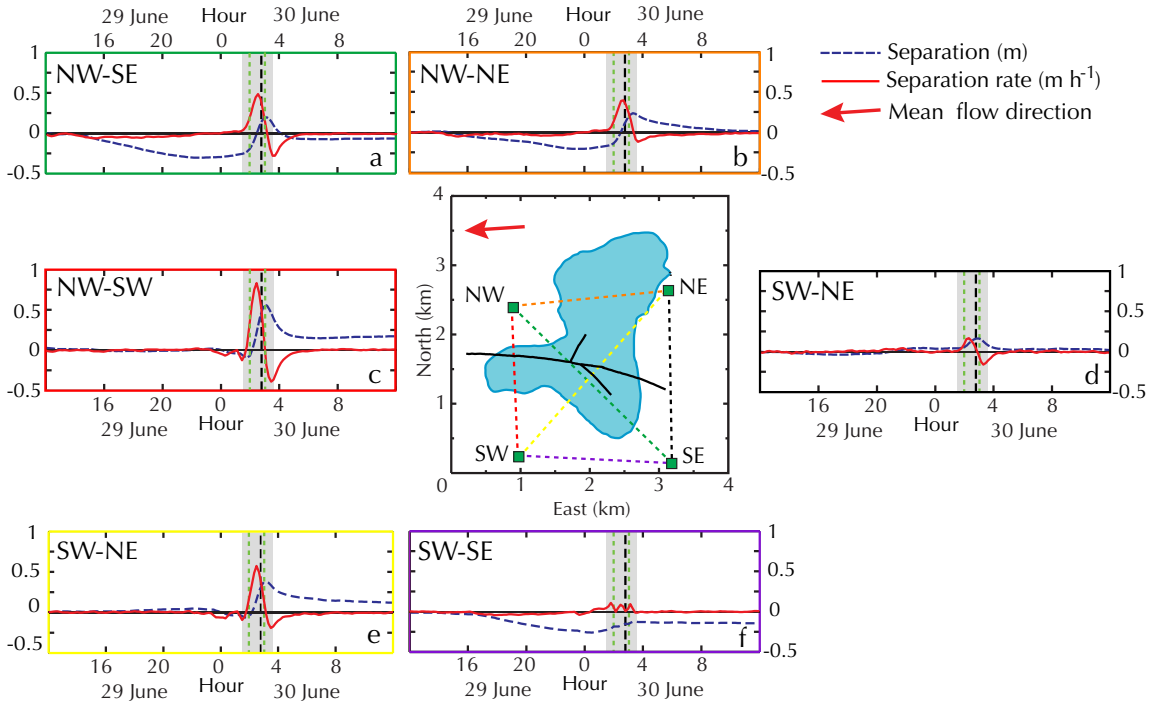

Figure 5.9: Inter-GPS separation (blue dashed line) and rate of separation (solid red line). The colour of the axes correspond to the dashed lines on the central map. The red arrow shows the direction of mean ice flow. The grey shade indicates the time of rapid ($Q >$ 50 $\mathrm{m^3\,s^{-1}}$) discharge, the black dashed line indicates the time of peak discharge $Q_{\max}$ and the green dashed lines indicate the times of 02:00 and 03:00.

A detailed time series of discharge (Q), rate of discharge ($\mathrm{d}Q/\mathrm{d}t$), uplift (Z) and rate of uplift ($\mathrm{d}Z/\mathrm{d}t$) is presented in Figure 5.7. At 01:15 on 30 June 2010 the uplift rate at GPS_SW suddenly increased leading to a maximum 0.34 m of uplift at 02:09. In this period, GPS_NW and GPS_NE were uplifted by 0.07 m and 0.1 m respectively, and there was no discernible uplift at GPS_SE. Coincident with the start of rapid discharge at 01:40 the uplift rate at GPS_NW increased. In the interval 01:40–02:00, the lake volume decreased by 1.75×10^5 m^3 (2.4 % of the lakes pre-tapping volume) and GPS_NW and GPS_SW moved north-west (Fig. 5.6a and b) with slight compression (Fig. 5.9c). At 02:00, GPS_NW continued to move in the north-west direction, accelerating and reaching a maximum displacement to the north of 0.3 m. At the same time (02:00), GPS_SW reversed in direction moving to the south-west (Fig. 5.6b) coincident with a step increase in the discharge (Fig. 5.7a and b), seismicity (Fig. 5.8), uplift rate at GPS_NW (Fig. 5.7c), and separation rate between all the GPS receivers with the exception of GPS SW–SE (Fig. 5.9). Rapid separation continued until 03:00 when GPS_SW reversed to the north (Fig. 5.6b) and GPS_NW reversed to the south (Fig. 5.6a), causing the separation rates to become negative (Fig. 5.9). The maximum discharge $Q_{\max}$ of 3300 m^3 s^{-1} occured at 02:47 simultaneous with the peak uplift rate at GPS_NW of 0.8 m h^{-1} (Fig. 5.7). The maximum relative separation between GPS NW–SW, NW–SE, NW–NE and SW–NE was attained at 03:00 (Fig. 5.9), simultaneous with a lull in seismicity across all six seismometers (Fig. 5.8) and a transient 1 m^3 s^{-2} increase in the discharge rate ($\mathrm{d}Q/\mathrm{d}t$) which remained negative (Fig. 5.7b). At 03:00 there was a short-lived (15-min) period of uplift at GPS_SW. Post 03:00, inter-GPS separations decreased as the discharge reduced. Rapid discharge ended at 03:15 with $V = 4.8 \times 10^4$ m^3 (0.65 % remaining). Peak uplift at GPS_NW of 0.9 m was not reached until 03:40. Following peak uplift, GPS_NW subsided at a gradually reducing rate (mean uplift rate of -0.07 m h^{-1}) remaining 0.3 m above its pre-tapping elevation by the end of 30 June 2010. Accordingly, GPS_SW, GPS_SE and GPS_NE remained uplifted

by 0.1 m, 0.18 m and 0.24 m respectively.

5.5 Interpretation and Discussion

On the basis of the observations described above, the rapid in situ tapping of Lake F on the 30 June 2010 can be decomposed into three episodes: (1) initial drainage (01:40–02:00); (2) fracture opening (02:00–03:00); and (3) fracture closure (03:00–03:15). The horizontal and vertical ice surface velocities during each episode are illustrated on Figure 5.10. These episodes are arbitrarily bounded by the duration of rapid discharge and it should be noted that closure of fractures extended beyond 03:15 (see Fig. 5.9). The timings of each episode, together with the time of $Q_{\max}$, are indicated on Figs. 5.6, 5.9 and 5.7.

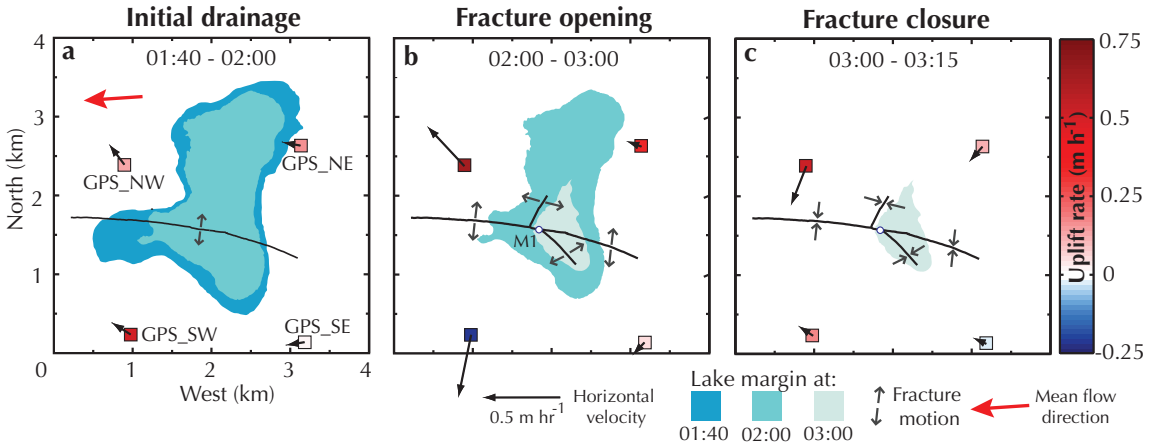

Figure 5.10: Horizontal and vertical velocities during the three episodes of Lake F's rapid drainage: **(a)** initial drainage; **(b)** fracture opening; and **(c)** fracture closure. Black arrows represent horizontal velocity vectors. The red arrow represents the mean ice flow direction and is not scaled by magnitude. The colour of each GPS symbol represents the mean uplift rate. The lake margin at each time step is shown.

Episode 1 begins at the onset of rapid discharge and ends when GPS_SW changes direction to the south causing north-south extension across the lake (Fig. 5.10a). In episode 1, a small

(1.7×10^5 m^3, 2.4 % of the lakes pre-tapping volume) amount of water drained coincident with uplift concentrated at GPS_SW and an increase in seismicity for the western half of the seismic array (S1–3, Fig. 5.8). Little or no increase in seismicity was recorded by the eastern seismometers (S4–6, Fig. 5.8).

As the fractures open in episode 2, Q rapidly increased peaking at 02:47 ($Q_{max} = 3300$ m^3 s^{-1}) simultaneous to the maximum rate of uplift at GPS_NW ($\mathrm{d}Z/\mathrm{dt} = 0.8$ m h^{-1}), indicating that water rapidly attained the ice bed interface causing hydraulic ice-bed separation. The divergence of GPS NW–SE, NW–SW, SE–NE and SW–NE (Fig. 5.9a, c, d and e) are interpreted as the opening of the main fracture F1 (Fig. 5.10b). Likewise, short-term longitudinal (with-flow) extension between GPS_NW and GPS_NE of ~ 0.2 m (Fig. 5.9b), involving the reverse motion of GPS_NE commencing at 02:00 (see Fig. 5.6d), is interpreted as the opening of subsidiary fracture F2. The opening of F2 involves the displacement of GPS_NE to the east up the bed-slope (Fig. 5.11). As soon as discharge begins to decrease after 02:47 the force holding F2 open reduces and, aided by the bed-slope, GPS_NE reversed in direction to the west (Fig. 5.6d), closing F2. The circular path of GPS_NE during lake tapping (Fig. 5.6d) can be interpreted as the combined effect of fractures F1 and F2 opening and closing. In episode 2, 90 % (6.7×10^6 m^3) of the lakes pre-tapping volume drained compared to just 6.8 % (5.1×10^5 m^3) in episode 3.

At 03:00, the boundary between episodes 2 and 3, the fractures attained their maximum width and the short respite in fracturing was coincident with a lull in seismicity evident in the records for all six seismometers (Fig. 5.8). This quiescence suggests that seismicity is predominantly generated by the opening and closure of fractures and not by water flow which was continuing at a high rate ($Q = 1450$ m^3 s^{-1}).

Immediately after 03:00, there was a step-increase in seismicity particularly evident at seismometer S4 (Fig. 5.8j), as the inter-GPS separation rates between GPS 1–3, 1–4, 1–

2, 3–4 and 2–4 became negative (Fig. 5.9) as the fractures closed (Fig. 5.10c). Episode 3 is characterised by decreasing discharge and uplift (Fig. 5.7). Following, the end of rapid discharge the rate of closure reduces but it takes several hours before the inter-GPS separation rates stabilised (Fig. 5.9). The elevated seismicity post-03:15 (Fig. 5.8) can be attributed to continuing fracture closure (Fig. 5.10c) and the subsidence of GPS_NW and GPS_NE (Fig. 5.7c and f).

Following lake tapping the inter-GPS separations show a stable increase between GPS NW-SW and GPS SW-NE and a stable shortening between GPS SW-SE and NW-SE (Fig. 5.9). This supports the observation of juxtaposed extensional and compressional supraglacial fracture structures (Fig. 5.5). The separation between GPS NW-NE and GPS SE-NE reduced to $\sim$0 m by 12:00 on 30 June suggesting the total closure of F2 and the most eastern section of F1 respectively. This observation is consistent with the small (cm-scale) fracture width measured in the field.

The characteristics of the rapid tapping of Lake F are consistent with Das et al. (2008) who observed the rapid (1.4 h) drainage of a 4.4×10^7 m^3 supraglacial lake through 980 m-thick ice on the western margin of the Greenland Ice Sheet at 68.7° N. The reverse and circular motion of the singular GPS station of Das and others are comparable to those of GPS_NE which was similarly located on westerly flowing ice, north of a longitudinal (with-flow) fracture and west of a transverse (cross-flow) fracture. The step-increases in seismicity observed during the tapping of Lake F (Fig. 5.8) are also comparable (see Fig. S3 of Das and others, 2008).

Prior to lake tapping a healed crevasse, consistent with Fig. S5 of Krawczynski and others (2009), was observed running from the western margin of the lake easterly towards its centre. Closed moulins were observed in the approximate positions of M1 and M5. It is likely that the healed crevasse and the closed moulins are relic features formed during

tapping events in previous years. It is possible that the rapid tapping in 2010 was the re-opening of fractures and moulins formed in previous years, however our observations do not reveal whether tapping involved the formation of a new fracture or the re-activation of a healed crevasse.

5.5.1 Trigger mechanism

Various mechanisms have been proposed as triggers for the initiation of hydraulic fractures through ice. Several studies (e.g. van der Veen, 2007; Krawczynski and others, 2009; Clason and others, 2012) invoke a critical-depth trigger whereby a hydrofracture is propagated to the bed when the lake level reaches a certain threshold. The observation of rapid tapping after — instead of coincident to — the peak lake size was attained (Figs. 5.3 and 5.7a) suggests that a critical-depth threshold is not the sole pre-requisite for triggering hydrofracture, a view supported by similar remote sensing observations (Liang and others, 2012).

Drainage of water into moulin M4, located to the west of Lake F, during the slow-discharge period prior to rapid tapping could theoretically cause localised uplift and acceleration leading to longitudinal (with-flow) extension. Alley and others (2005b) assert that the tensile stress caused by the acceleration of downstream ice may be important for initiating hydrofractures. However, discharge into 1- m-wide M4 was relatively low and prior to the tapping of Lake F there is no evidence for longitudinal (with-flow) extension (Fig. 5.9). On the contrary, the two western GPS receivers (GPS_NW and GPS_SW) were uplifted and accelerated several hours later than the two eastern GPS receivers (GPS_SE and GPS_NE), causing longitudinal (with-flow) compression across the lake in the hours preceding lake tapping (Fig. 5.9b and f).

In the 4 day interval that Lake F tapped a number of adjacent lakes also drained and some of these are located upstream and south-east of Lake F (Fig. 5.1). These lakes drained within a cloudy period and it is impossible to determine from the available MODIS imagery which lake drained first. The drainage of one or more of these lakes could hypothetically route water down the subglacial valley south-east of GPS_SE (Fig. 5.11) which would explain the earliest observed uplift at GPS_SE at 12:00 on 29 Jun. Rapid draining lakes appear to drain in spatial and temporal clusters (see Fig. 5.1 and Lampkin, 2011) suggesting that lake tapping events may trigger each other. This hypothesis may be the answer to the Lake F trigger but it also raises the question as to what caused the first lake to tap.

The observation of a compressive strain regime prior to lake tapping is in agreement with Krawczynski and others (2009) who found that water-filled crevasses can propagate without longitudinal (with-flow) tension and that a given volume of water has the propensity to propagate a water-filled crack further in regions with less tension (or even slight compression), as thinner cracks require less water to remain water filled.

Although it is possible that small drainage events were masked by variations in supraglacial discharge, the lack of notable changes in the lake volume prior to 01:40 on 30 June 2010 (Fig. 5.7a) suggests that premonitory drainage events as observed by Boon and Sharp (2003) did not occur.

5.5.2 Hydraulic pathways

It is likely that during lake tapping, discharge occurred along most of the fractures' lengths that were located within the lake bed. Assuming first that the inter-GPS separation is entirely a result of fracturing and second following Krawczynski and others (2009), that the fractures are parallel-sided with constant width, the fractures' cross-sectional area

at the time of peak separation (03:00) can be estimated. Interpolating the maximum separation between GPS NW–SW, NW–SE, SW–NE and SE–NE gives a peak fracture width averaged over F1's 2.6 km-wetted-length of 0.4 m and an estimated maximum cross-sectional area of 842 m^2. This fracture width agrees well with the modelling results of Krawczynski and others (2009) that suggest an idealised conical lake of a similar size to Lake F (diameter = 2.2 km, area = 3.8 km^2) would drain via a 0.4- m-wide fracture across the width of the lake in ~ 2 h. The maximum cross-sectional area of F2 is estimated at 140 m^2. Combined, F1 and F2 have a total cross-sectional area at 03:00 of 982 m^2. Dividing the discharge at 03:00 (Q = 1450 $m^3 s^{-1}$) by the combined cross-sectional area gives a mean flow velocity of 1.5 $m s^{-1}$. Hence, due to the length of the fractures, rapid discharge can be achieved by combining reasonable water velocities with sub-metre fracture widths. Assuming an ice thickness of 1100 m the total volume of the fractures at 03:00 is 1.1×10^6 m^3 or 15 % of the lake volume prior to tapping. The actual volume of water that drained between 01:40 and 03:00 was much larger at 6.8×10^6 m^3.

During rapid discharge the frictional heat of turbulent flow would preferentially melt the sections of the fracture transporting the greatest flux, leading to the concentration of flow (Walder, 1982) and the development of moulins. There is a clear distinction between moulins that formed during rapid discharge and moulins that formed afterwards. Immediately, post-tapping, moulins M1 and M5 were fully formed but dry whilst moulins M2 and M3 were clean-cut fractures accepting water. It can be hypothesised that discharge was initially concentrated down the largest (∼10 m diameter) moulin M1 (Fig. 5.4b). When the water level fell below the elevation of M1 surface water-flow would have been concentrated through F1 in the deepest region of the lake, ∼10 m east of M2 (Fig. 5.2).

At 04:50 on 30 June 2010, $<$ 2 h after rapid tapping, there were no supraglacial channels in the lake bed. A shallow (~ 0.3 m deep) pond of water in the deepest region of the lake

was overflowing the clean cut edge of F1. Over a number of days channels formed by the frictional heat of preferential water flow, concentrating water flow into discrete moulins. Continued water flow into moulins would work to keep moulins open for the remainder of the melt season. On 1 July, sections of the fracture were water-filled and water draining into moulin M2 could be heard to flow laterally along F1 at a shallow depth before draining into moulin M1, suggesting that post-tapping large sections of the fracture were closed.

5.5.3 Vertical ice surface motion

Ice surface uplift is typically attributed to bed-parallel motion, vertical strain and ice-bed separation due to high subglacial water pressures (Hooke, 1989). Fault displacement (Fig. 5.5) may also cause vertical ice motion (e.g. Walder and others, 2005). All four factors must be considered when interpreting the vertical motion of a GPS receiver installed on the ice surface.

The bed-slope within the study area is highly variable (Fig. 5.11) and may be responsible for some of the differential ice motion (Fig. 5.6). In contrast to the smooth vertical motion of GPS_NW, GPS_SE and GPS_NE the vertical motion of GPS_SW is characterised by sudden steps coincident with the start and end of the fracture opening episode. GPS_SW is located on the strongest subglacial gradient of all the GPS receivers, south of a conical subglacial peak (see Fig. 5.11). Horizontal motion along the inclined bed-slope can satisfactorily explain the vertical motion of GPS_SW. At 00:00 on 30 June 2010 the trajectory of GPS_SW was perturbed to the north-west coincident with $\sim$5 cm of uplift. This vertical motion can be explained by north-westerly motion up the bed-slope (Fig. 5.11). The subsequent southerly-motion of GPS_SW down the bed-slope between 02:00 and 03:00 is coincident with subsidence. This lowering is simultaneous with uplift at GPS_NW, GPS_SE and GPS_NE suggesting that the water delivered to the bed during

rapid discharge did not access the bed beneath GPS_SW. Finally, at 03:00 when GPS_SW moves north up the bed-slope there is a second low magnitude (10 cm) period of uplift exclusive to GPS_SW.

Sugiyama and others (2008) observed the greatest uplift near to the drainage centre during the subglacial drainage of ice-marginal lake Gornersee in Switzerland and we therefore assert, like Das and others (2008), that surface uplift was likely greater near the centre of the lake. The highest-magnitude uplift observed in this study of 0.9 m by GPS_NW is the most consistent with the 1.2 m of uplift measured by Das and others. The bed-slope underneath GPS_NW slopes down towards the north-west (Fig. 5.11) so north-west acceleration during the fracture opening episode is not responsible for the observed uplift at GPS_NW. Vertical strain cannot account for the uplift as extension (which would cause thinning and lowering) was observed for all the inter-GPS separations involving GPS_NW during this episode (Fig. 5.9a, b, c). Fault displacement in the form of vertical offset of the fracture walls in a reverse dip-slip fault is attributed to compressional strain (Fig. 5.5b) which is unlikely to have occurred during the fracture opening episode when all inter-GPS separations were extensional (Fig. 5.9). As neither motion along an inclined bed-slope, vertical strain or fault displacement can explain the observed vertical motion of GPS_NW during the fracture opening episode, the uplift at GPS_NW can be attributed to ice-bed separation resulting from high subglacial water pressures caused by the delivery of a large quantity (6.7×10^6 m^3 or 90 % of the lakes pre-tapping volume) of water to the ice-bed interface.

5.5.4 Subglacial water routing

Subglacial water delivered to the ice-bed interface along F1 would be preferentially routed through a subglacial valley to the north-west (Fig. 5.11) . Field measurements of the

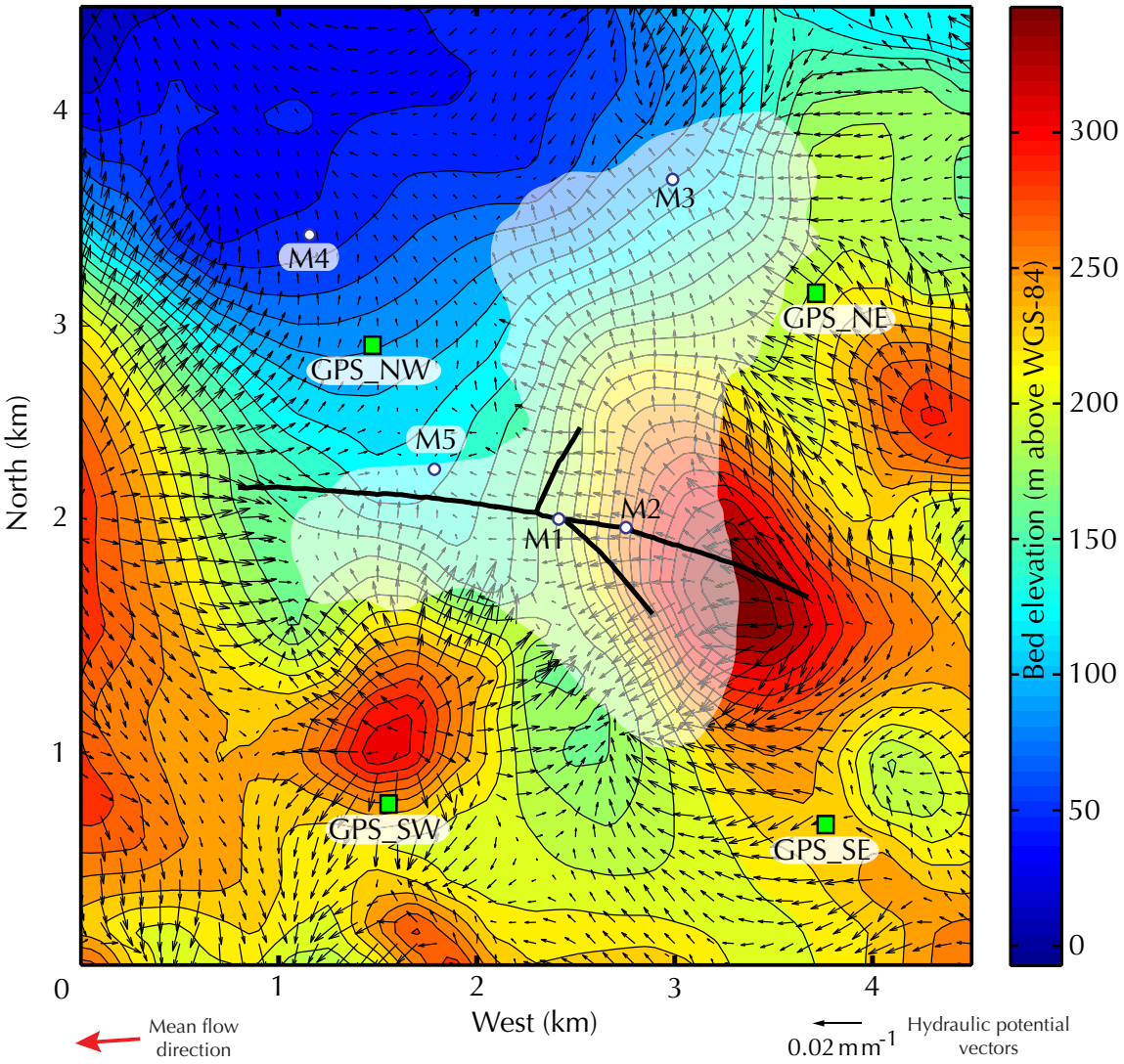

Figure 5.11: Map of the hydraulic potential gradients and subglacial topography for Lake F. The black arrows are vectors of hydraulic potential gradient scaled by the metres of hydraulic potential change per metre. The gradients of hydraulic potential were calculated assuming basal water pressures were everywhere equal to the ice overburden pressure. The lake margin immediately prior to lake tapping is shown together with the locations of moulins, fractures and GPS receivers. The contour interval for the basal topography is 10 m.

fracture structure and the differential motion of the GPS receivers support this assertion. Based on the locations of F1 and F2, we can conceptualise the ice-mass structurally into three semi independent blocks: the southern, north-eastern and north-western. The direction of dip of sub-vertical fractures F1 and F2, to the north and west respectively (see Fig. 5.2 and 5.5), together with the permanent offset of the northern hanging wall above the southern foot wall of F1, suggest that during the fracture opening episode, the north-western block was preferentially uplifted and ejected to the north-west. This is consistent with the observation of the greatest horizontal and vertical motion of the north-western block on which GPS_NW was located (Fig. 5.6a and e) and the highest rate of seismicity recorded by the most western seismometers (S1–3, Fig. 5.8). Extensive ice surface uplift due to hydraulic ice-bed separation at GPS_NW, GPS_SE and GPS_NE imply that subglacial water flowed as a laterally-expansive but non-uniform sheet consistent with the subglacial drainage of ice marginal lake Gornersee (Sugiyama and others, 2008). Das and others assert that this water could be accommodated in a transient subglacial lake and the slow subsidence of GPS_NW, GPS_SE and GPS_NE could indicate the drainage of this subglacial lake. In contrast. the vertical motion of GPS_SW rapidly returned to a steady height following the end of rapid discharge (Fig. 5.7) suggesting that water was not routed or stored at the bed in this area.

5.6 Conclusions

Detailed measurements of ice surface motion, discharge and seismicity during the rapid in situ drainage of a large annually-tapping supraglacial lake through kilometre-thick ice on the western margin of the Greenland Ice Sheet contribute to the currently limited knowledge of rapid supraglacial lake tapping events.

Horizontal ice motion during lake tapping is dominated by ice tectonic deformation involving the transient opening and closure of multiple fractures. It is hypothesised that during rapid discharge, water flowed down most of the fractures' lengths. By reconstructing the peak cross-sectional area of the fractures from the inter-GPS separations it is estimated that the fractures' kilometre-scale lengths allow rapid discharge to be achieved by combining reasonable water velocities with sub-metre fracture widths.

The maximum uplift rate of 0.8 $\mathrm{m\,h^{-1}}$ occurred simultaneous with the maximum discharge of 3300 $\mathrm{m^3\,s^{-1}}$ providing evidence that water rapidly attained the ice-bed interface raising subglacial water pressures above overburden over a large area of the bed. Basal topography and the gradient of hydraulic potential exerted control on water routing, horizontal ice motion and uplift. The greatest horizontal displacement and vertical uplift was observed above the preferential subglacial drainage route.

Lake tapping events rapidly deliver large pulses of surface water to the bed of the Greenland Ice Sheet causing transient ice-bed separation and acceleration however it remains unclear what impact this water delivery will have on the annual ice flux.

Acknowledgements

This research was funded by the Greenland Analogue Project, Sub-Project A and by UK Natural Environment Research Council (NERC) grants NE/G007195/1 and NE/G005796/1. The seismic instruments were provided by Seis-UK at the University of Leicester. Ian Bartholomew and Matt King are thanked for advice on GPS processing. Christian Helanow, Adam Booth and Henry Patton are thanked for assistance in the field. Nolwenn Chauché is thanked for helpful discussion. TEQC software was used to convert the raw GPS data to Receiver INdependent EXchange (RINEX) format (Estey and Meertens, 1999). MODIS

data are distributed by the Land Processes Distributed Active Archive Center (LP DAAC), located at the USGS EROS Center (`http://lpdaac.usgs.gov`). Landsat data are distributed by the US Geological Survey (`http://glovis.usgs.gov`).

Chapter 6

Results III: Widespread late season rainfall, melt and acceleration on the Greenland Ice Sheet driven by cyclonic weather

Author Contributions

Several authors contributed to the research presented in this chapter, which has been submitted for publication. Dirk van As collected the AWS data and modelled the surface energy balance. Roderik van de Wal and Paul Smeets provided the single-frequency GPS data and the borehole water pressure record. Kilian Scharrer processed the TanDEM-X

datasets. Toby Meierbachtol and Joel Harper collected two of the GPS records from Issunngata Sermia. Emma Bosson corrected the precipitation records for wind and adhesion losses. Jason Box provided the reanalysis data and advised on meteorology and climatology. Andreas Mikkelsen provided the proglacial discharge record. Sam Doyle processed the GPS records, collated the datasets, and wrote the text. In addition to those authors previously named, Alun Hubbard, Bryn Hubbard and Poul Christoffersen advised on the writing.

6.1 Summary

Accurate forecasting of the Greenland Ice Sheet's contribution to global sea level rise requires detailed knowledge of how surface melt and ice flow respond to atmospheric forcing (Lemke and others, 2007; Hanna and others, 2014). Both processes have increased significantly over the last decade (van den Broeke and others, 2009; Shepherd and others, 2012; Moon and others, 2012). Recent research demonstrates that surface meltwater delivery to the bed accelerates ice flow over the course of summer (Zwally and others, 2002) yet is regulated annually through the melt-induced seasonal transition between inefficient and efficient subglacial drainage systems (Bartholomew and others, 2010; Hoffman and others, 2011; Sundal and others, 2011; Sole and others, 2013). This chapter demonstrates that substantial episodes of melt and acceleration also occur after this drainage system switch. Records of ice velocity, subglacial water pressure and meteorological data reveal that a period of warm, wet cyclonic weather in late August 2011 produced sufficient melt and rainfall to overwhelm the ice sheet's subglacial drainage system, leading to a pronounced and widespread acceleration in ice sheet flow of up to 220%. The acceleration, which occurred after the subglacial drainage system had shutdown, occurred on at least two outlet

glaciers and extended at least 88 km (1520 m a.s.l.) into the ice sheet's interior. The cyclonic conditions driving this event prevailed over half of Greenland are predicted to become more pronounced in future, concurrent with a warmer and cloudier regional climate (Fettweis and others, 2011; Franco and others, 2013) and a northward shift in North Atlantic storm tracks (Schuenemann and Cassano, 2010). In light of the increasing frequency and intensity of extreme Arctic cyclones in climate reanalysis data and historical climate simulations (e.g. Schuenemann and Cassano, 2010; Vavrus, 2013), the finding that the ice sheet is sensitive to such events portends a future where Greenland's outlet glaciers experience more melt- and rainfall-induced acceleration events, similar to those currently affecting coastal Alaskan glaciers.

6.2 Introduction

Recent studies have argued that the basal drainage system, at least within the ablation area, adapts its efficiency to accommodate surface meltwater delivery, thereby regulating basal water pressures and ice motion over the summer season (Sundal and others, 2011; Chandler and others, 2013; Sole and others, 2013; Tedstone and others, 2013). The enhanced summer flow regime appears to comprise a series of discrete transient accelerations driven by the rate and duration of water accessing the bed, and the ability of the hydrological system to adapt to them (Bartholomaus and others, 2008; Schoof, 2010; Bartholomew and others, 2011a; Hoffman and others, 2011). The seasonal velocity cycle is typically characterised by an initial maximum at melt onset, gradual deceleration in mid-summer, and an all year minimum in August, when the drainage system can easily accommodate declining melt inputs (van de Wal and others, 2008; Bartholomew and others, 2010, 2011a; Colgan and others, 2011; Hoffman and others, 2011; Bartholomew and others, 2012; Colgan

and others, 2012; Fitzpatrick and others, 2013). Surface velocities recorded at eight GPS sites on Russell Glacier and Isunngata Sermia in West Greenland during 2011 (Fig. 6.1) are consistent with these systematic variations with one exception: a prominent acceleration between the 24 August and 1 September (Fig. 6.4b-i). The mechanisms driving this pronounced, widespread and sustained late-season acceleration demand further investigation.

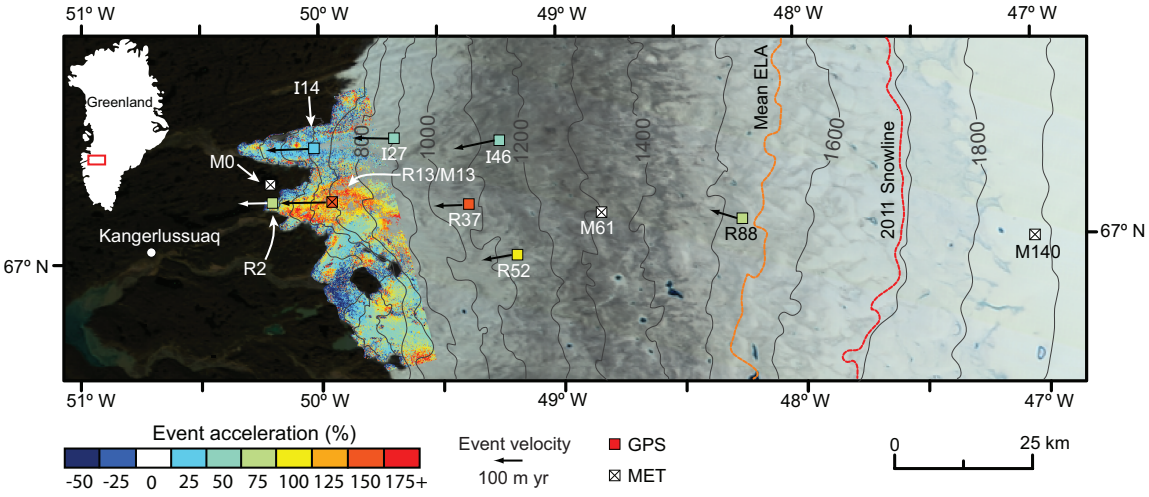

Figure 6.1: Map of the Kangerlussuaq sector of the Greenland Ice Sheet showing the locations of GPS receivers and meteorological stations. The number in the GPS site labels refers to the distance in kilometres upglacier from the terminus of Russell Glacier (R) and Issungata (I) Sermia. Meteorological stations (M) are labelled with the distance from the terminus of Russell Glacier. Acceleration during the late-August event (23 August48 W3 September 2011) relative to the preceding period (1–23 Aug 2011) was derived from TanDEM-X velocity maps. The colour of the GPS symbols represent the percentage acceleration during the event (Table 6.2) and they do not correspond to the longer TanDEM-X periods. The velocity vector shows the mean velocity during the late-August acceleration. The background image is a MODIS scene from a week before the event (17 August 2011). The mean (1990–2011) equilibrium line altitude (ELA) estimated by van de Wal and others (2008) and the maximum 2011 snowline (Box and others, 2009; Box and Chen, 2012) are marked. The black box on the inset map shows the location of the study site in Greenland.

6.3 Data and methods

Surface ice motion was measured using a transect of 8 global positioning system (GPS) receivers and offset tracking on repeat pass TanDEM-X imagery. A comprehensive array of meteorological measurements were made by three on-ice automated weather stations (AWS) and one off-ice AWS. Precipitation was measured at the off-ice AWS and by the Danish Meteorological Institute (DMI) in Kangerlussuaq. Reanalysis data from the National Centers for Environmental Prediction/National Centre for Atmospheric Research (NCEP/NCAR) reanalysis project (Kalnay and others, 1996) was used to estimate precipitation (Fig. 6.3) and to track weather systems (Fig. 6.6) over Greenland. Finally, proglacial discharge was gauged at Watson River Bridge in Kangerlussuaq (Hasholt and others, 2013). The methods are described in detail below.

6.3.1 GPS measurements

This study employed five dual-frequency global positioning system (GPS) receivers (R2, R13, I14, I27 and I46) capable of resolving three dimensional ice surface velocities at a high temporal resolution (< 1 hour), and three single-frequency GPS receivers (R37, R52, and R88). Data from the dual-frequency receivers were processed kinematically (King, 2004) at a 30-second interval relative to bedrock-mounted reference stations using the carrier phase differential positioning software, Track v. 1.24 (Chen, 1998), and final precise ephemeris from the International GNSS Service (Dow and others, 2009). Reference GPS stations were located 1 km from the terminus of Russell Glacier (BASE) and at Kellyville (KELY) giving baseline lengths of 5 to 46 km. Assuming steady ice motion, uncertainties in the positions were estimated at ± 0.01 m in the horizontal and ± 0.05 m in the vertical by examining the de-trended position time series for GPS receiver R13 in early June 2011. High frequency

noise was filtered with a two-pole, low-pass Butterworth filter with a 12-hour cut-off period. To reduce the effect of bed parallel motion the surface height record was detrended by subtracting a line of linear regression which was fitted to the full record.

The single-frequency receivers recorded horizontal position every hour and the resulting time-series were filtered with a 48-hour period average (Den Ouden and others, 2010). No attempt was made to resolve vertical motion from the single-frequency GPS records as the detection limit exceeds the magnitude of ice surface uplift (Den Ouden and others, 2010).

Daily averaged horizontal velocity was calculated by differencing the filtered positions at a daily time step. The annual velocity was calculated from positions of the antenna on 6 June 2010 and 6 June 2011 for Russell Glacier GPS and from 2 September 2011 and 2 September 2012 for Isunngata Sermia GPS. These dates were selected on the basis of available data and to avoid times when antenna poles were relocated (e.g. 7 June 2011 for GPS R13 and R2).

6.3.2 TanDEM-X methods and verification against GPS records

Offset tracking was applied to repeat pass TanDEM-X data to derive surface velocities for the ice sheet margin in August 2011. TanDEM-X (TerraSAR-X add-on for Digital Elevation Measurement) is a bi-static Synthetic Aperture Radar (SAR) mission launched in June 2010 with the two satellites orbiting in a closely controlled formation with typical distances of between 250 and 500 m. The satellites circle on an 11-day repeat orbit, acquiring synthetic aperture radar (SAR) images, with a 30×50 km footprint, at a 3 m spatial resolution (Krieger and others, 2007).

Three ascending images acquired on 1 August, 23 August, and 3 September 2011 were

used: the first two acquisitions (1 August, 23 August; 22 days separation) were combined in order to derive the average August ice velocities, and the images recorded on 23 August and 3 September (11-day separation) were used to detect the late August acceleration (Fig. S1). SAR amplitude images were computed for each of the scenes and applied an image-to-image cross-correlation technique to track the motion of features on the glacier surface (Strozzi and others, 2002). The accuracy of the derived flow speeds was investigated by a comparison with velocities for the same time intervals at two GPS locations: R2 and R13 (see insert on Fig. 6.2). Strong agreement was found for both periods, with differences ranging between 0.011 m d^{-1} (R2, 1 to 23 August) and 0.058 m d^{-1} (R13, 23 August to 3 September).

6.3.3 Borehole water pressure

Subglacial water pressure was recorded by a wired pressure sensor installed 0.5 m from the ice-bed interface at site R13/M13 (see Smeets and others, 2012). Borehole water pressure was expressed as a percentage of the ice overburden pressure, assuming an ice thickness of 610 m and a density of ice of 917 kg m^{-3}.

6.3.4 Meteorological measurements

Meteorological measurements were made by three on-ice automated weather stations (AWS) located 13 km (M13), 61 km (M61) and 140 km (M140) from the terminus of Russell Glacier, and one on-tundra AWS (M0) located 1 km west of ice margin (Fig. 6.1, Table 6.1).

To keep consistency with the GPS site names, the numbers in the AWS labels refer to the distance from the terminus of Russell Glacier. The on-ice AWS were previously referred to

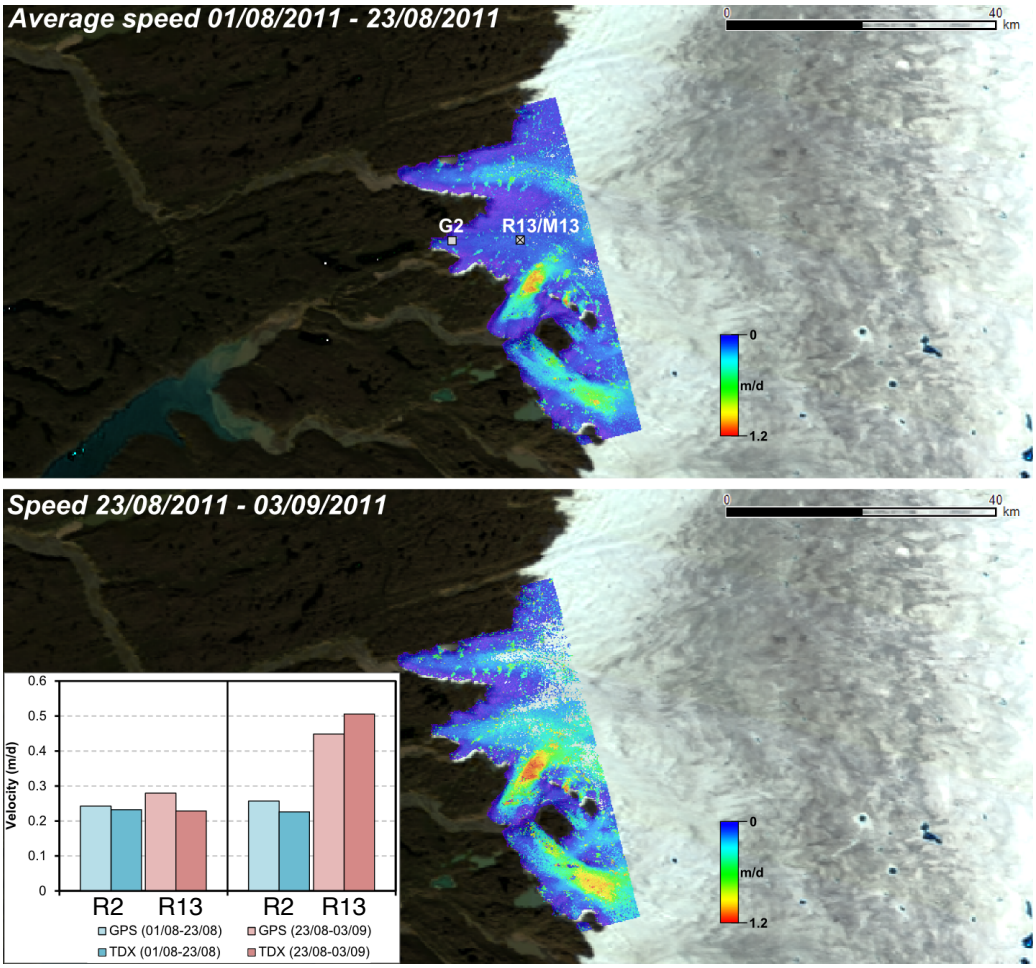

Figure 6.2: TanDEM-X velocities during (top) the preceding period (1 to 23 August 2011) and (bottom) the late-August acceleration (23 August to 3 September 2011). The lower-left insert shows the good agreement between TanDEM-X (TDX) and GPS velocities for sites R2 and R13 for both periods.

Table 6.1: Position and elevation of the meteorological stations

Site	Position	Elevation (m a.s.l.)
M0	N67°08', W050°11'	345
M13	N67°06', W049°56'	732
M61	N67°04', W048°49'	1280
M140	N67°00', W047°01'	1840

as KAN_L (M13), KAN_M (M61) and KAN_U (M140), and the reader is directed to van As and others (2012) for further information on the AWS methods. The AWS recorded surface height change due to accumulation and ablation, air pressure, temperature and humidity, wind speed and direction, and downward and upward shortwave and longwave radiation at 2 to 3 m above the surface. The AWS sampled at a 10-minute interval, from which hourly averages were calculated. The energy available for melt was determined using a surface energy balance model (van As, 2011), validated using the AWS measurements of surface temperature and surface height change (van As and others, 2012).

Cloud cover was approximated making use of the strong dependence of downwards longwave radiation on atmospheric moisture (van As, 2011). A full cloud cover was assumed for high downward longwave radiation values at a certain air temperature, clear skies for low values, with a linear transition for values in between. The elevation of the freezing level was estimated using lapse rates calculated from M61 and M140 air temperature measurements.

Precipitation records from site M0 and Kangerlussuaq (DMI station 04231, Cappelen and others, 2012) were corrected for wind and adhesion loss effects, using site-specific correction factors (Alexandersson, 2003; Bosson and others, 2013). Correction factors of 33 % for snow and 16 % for rain were applied to the data recorded by the automatic GEONOR gauge deployed < 1 km from the ice margin at M0, a site that is exposed to the wind. For the

manual gauge at Kangerlussuaq, a site that is more sheltered from the wind, correction factors of 12 % for snow and 4.5 % for rain were applied. At both sites the adhesion loss was set to 0.1 mm per precipitation event, and mass loss due to evaporation was assumed to be zero.

6.3.5 Calculating the elevation of the snowline

The elevation of the snowline — the maximum elevation that snow remains at the end of the melt season — was retrieved from end-of-melt-season visible-band Moderate Resolution Imaging Spectrometer (MODIS) images (Box and others, 2009; Box and Chen, 2012). The ice-sheet-wide, MODIS-retrieved snowlines, which are calibrated against the K-transect surface mass balance observations (van de Wal and others, 2012), are available at `http://bprc.osu.edu/wiki/Greenland_Ice_Sheet_Snowline`.

6.3.6 Reanalysis

Data from the National Centers for Environmental Prediction/National Centre for Atmospheric Research (NCEP/NCAR) reanalysis project (Kalnay and others, 1996) was used to estimate precipitation (Fig. 6.3) and to track weather systems (Fig. 6.6) over Greenland between 23 August and 3 September 2011.

6.3.7 Proglacial discharge records

Proglacial discharge was gauged at Watson River Bridge in Kangerlussuaq (Fig. 6.4k). Water stage measured by an automatic pressure transducer mounted in a river channel cut through solid rock was used to calculate the discharge. Further details are described by Hasholt and others (2013).

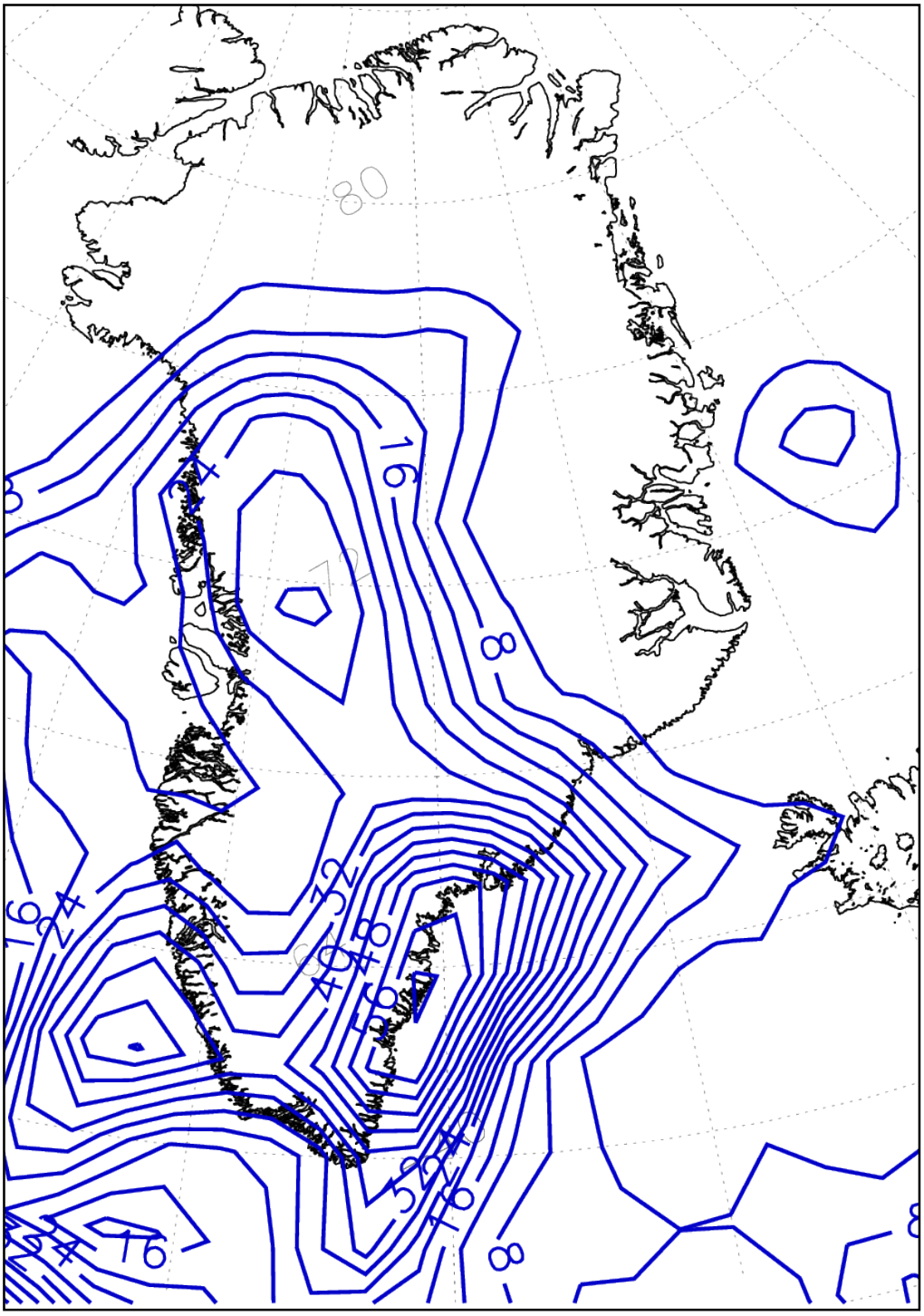

Figure 6.3: Total precipitation (mm) between 24 to 30 August from NCEP/NCAR reanalysis data.

6.4 Results

6.4.1 GPS and TanDEM-X Results

Surface velocities derived from offset tracking with TanDEM-X data show the widespread acceleration (of up to 220%) of large areas of the ice sheet margin for the period 23 August to 3 September compared to August background velocities (1 to 23 August; Figs. 6.1 and 6.2). During the event, the average velocity at the GPS sites on Russell Glacier: R2, R13, R37, R52 and R88 (where the number in the site label refers to the distance from the glaciers terminus) increased by 91%, 166%, 161%, 98% and 87% above the preceding velocity (Table 6.2). The acceleration was particularly large at site R13 (Fig. 6.4e) where the daily average velocity (365 m yr^{-1}) exceeded the sites melt onset peak (337 m yr^{-1} on 8 June), which typically represents the highest velocity within a given year (Bartholomew et al., 2012, Bartholomew et al., 2010, Bartholomew et al., 2011a). The velocity response was muted on Isunngata Sermia where background flow is faster than at Russell Glacier: velocities at sites I14, I27 and I46 increased by 22%, 58% and 55% (Table 6.2).

The acceleration event in late August 2011 provides a unique opportunity to investigate the dynamic response of an ice sheet to a spatially uniform, tightly constrained yet previously unreported forcing mechanism. Simultaneous ice acceleration at all the GPS sites (Fig. 6.4) and across the ice margin (Fig. 6.1) indicates that the melt and rainfall during the late-August event overwhelmed the basal hydrological system, to at least 88 km inland, and on at least two outlet glaciers (Fig. 6.1). In contrast to the short-lived and localised accelerations induced by the rapid in situ drainage of supraglacial lakes (Das and others, 2008; Hoffman and others, 2011; Doyle and others, 2013, Chapter 5), the week-long acceleration in late August was widespread, observable on at least two outlet glaciers, and extended at least 88 km into the ice sheet's interior (Fig. 6.4).

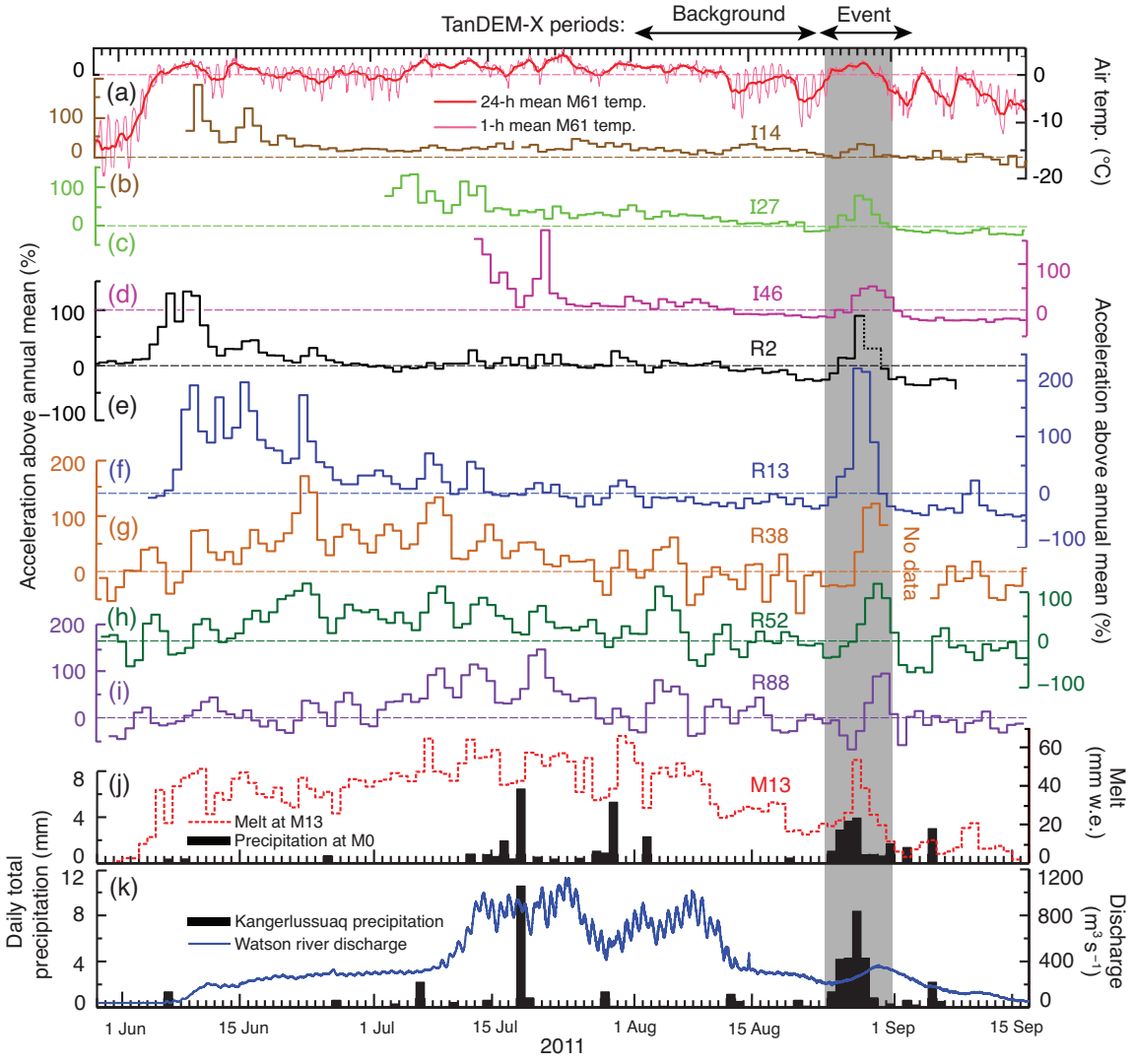

Figure 6.4: Records of ice motion, meteorology and Watson river discharge for the 2011 melt season. The timing of the late-August acceleration is shaded in grey. (a) Air temperature at M61 with a 1- and 24-hour average applied, (b-i) daily-averaged velocity at the eight GPS sites expressed as acceleration above the annual mean (j) daily total melt at M13 and corrected daily total precipitation at M0, and (k) corrected daily total precipitation in Kangerlussuaq and proglacial Watson River discharge. The locations of GPS and meteorological sites are shown on Figure 6.1.

Table 6.2: Position, elevation, ice thickness and velocity statistics for the GPS sites on Russell Glacier and Isunngata Sermia.

	Ice thickness (m)	Mean annual velocity (m yr^{-1})	Preceding velocity (m yr^{-1})	Event velocity (m yr^{-1})	Acceleration (%)
Russell Glacier GPS sites:					
R2 (383 m a.s.l.) N67° 06', W050° 12'	158	100	81	176	91
R13 (732 m a.s.l.) N67° 06', W049° 56'	610	113	95	228	166
R37 (1010 m a.s.l.) N67° 05', W049° 24'	883	73	68	116	161
R52 (1110 m a.s.l.) N67° 00', W049° 09'	923	96	88	144	98
R88 (1520 m a.s.l.) N67° 03', W048° 15'	1223	101	83	121	87
Isunnguata Sermia GPS sites:					
I14 (635 m a.s.l.) N67° 11', W050° 02'	491	130	137	162	22
I27 (894 m a.s.l.) N67° 12', W049° 43'	521	100	99	133	58
I46 (1156 m a.s.l.) N67° 12', W049° 17'	830	115	99	147	55

6.4.2 Meteorological analysis

The acceleration can be ascribed to high-magnitude runoff, an unusual combination of rainfall and melt that resulted from meteorological conditions associated with Baffin Bay cyclones. The magnitude of precipitation during the event — which represented a fifth (23.6 mm) of the annual total (115.1 mm) in nearby Kangerlussuaq — is rare for this region (Cappelen and others, 2001) yet the main contributor to runoff was surface melt.

Although peak midday values of melt during the event (e.g. 3.2 mm w.e. h^{-1} at M13 on 27 August) were less than peak summer values (e.g. 6 mm w.e. h^{-1} at M13 on 30 July 2011),

they were sustained over a large area continuously through the day and night (Fig. 6.8b). Day-round high melt under cyclonic weather conditions can be explained by the longwave cloud effect (Ambach, 1974; van den Broeke and others, 2011; Gascon and others, 2013) and enhanced turbulent heat fluxes (van den Broeke and others, 2011) resulting from high wind speeds and the advection of warm, moist air (see Section 6.4.2). Extensive cloud cover (Fig. 6.5a) played a key role in this melt event. Although clouds reduce net shortwave radiation, under certain conditions this decrease can be more than offset by an increase in net longwave radiation, as a larger fraction of the outgoing longwave radiation is absorbed by clouds and re-radiated back to the surface (Ambach, 1974; van den Broeke and others, 2011; Gascon and others, 2013). This unusually sustained period of continuous melt totalled 331 mm water equivalent (w.e.) at M13 between 24 August and 1 September; this represents 10% of the annual melt and a two-fold increase relative to the preceding week (Fig. 6.4j). Given the lower (15 mm) and upper (24 mm) estimates of precipitation from observations and reanalysis, melt accounted for 90 to 93 % of the surface runoff at M13 during the event. The total melt produced during the event was only slightly lower at M61 (315 mm w.e.) compared to M13 and at this site the event resulted in a higher proportion (15%) of the annual melt. Melt extended through the entire ablation area beyond the mean (1990 to 2011) equilibrium line altitude (ELA) of 1553 m a.s.l. At site M140 (1840 m a.s.l.), 50 mm w.e. of melt (8 % of the annual total) was recorded during a period (24 to 29 August) of above-freezing air temperatures at this site (Fig. 6.7). A consequent increase in the M140 surface height record (not presented), coincident with below-freezing air temperatures (Fig. 6.7) suggests that precipitation was subsequently deposited as snow at M140. Most precipitation, however, occurred while air temperatures at M140 were above freezing (24 to 29 August) and the highest daily total precipitation on 27 August (8.4 mm in Kangerlussuaq and 3.9 mm at M0) are coincident with the highest daily total melt (e.g. 53 mm w.e. at M13), and a transient excursion of the freezing level

from $\sim$ 1000 m to 2450 m a.s.l. (Fig. 6.7).

As the ice sheet's surface gradient decreases with increasing elevation, the surface area of the catchment that receives precipitation as rain and is exposed to melt increases disproportionately in relation to a rising freezing level. The high freezing level, which when extrapolated indicates melt and rainfall occurred up to 280 km inland, can be explained by the advection of warm, moist air over the ice sheet. When a saturated air mass condenses, it releases latent heat that reduces the rate at which an air mass cools with increasing altitude. Accordingly, the lapse rate during the late-August acceleration was lower (0.48° C per 100 m) than the annual mean (0.7° C per 100 m), resulting in the 0° C isotherm attaining an elevation of $\sim$ 2450 m a.s.l. on 27 August 2011 (Fig. 6.7).

Further insight into the abnormal runoff caused by this weather event was gained by decomposing the surface energy budget (SEB) for the AWS at site M13 (Fig. 6.5). The shortwave (SR_{net}) and net longwave (LR_{net}) radiation, the sensible (SHF) and latent (LHF) heat fluxes and the ground flux (GF) are defined as positive when they add heat to the surface.

Although clouds reduce the net shortwave radiation, they increase net longwave radiation as a larger fraction of the outgoing longwave radiation is absorbed by clouds and re-radiated back to the surface (Ambach, 1974; van den Broeke and others, 2011). Net longwave radiation typically represents a heat sink in the SEB but under certain atmospheric conditions (e.g. Bennartz and others, 2013; Gascon and others, 2013) LR_{net} can be positive resulting in higher net radiation ($SR_{net} + LR_{net}$) than under clear skies. Accordingly, although net daily total shortwave radiation on 27 August was less than half (4.9 MJ m^{-2} day^{-1}) that recorded under clear sky conditions seven days previously on 21 August (10.3 MJ m^{-2} day^{-1}), net radiation was greater on the 27 August
(5.2 MJ m^{-2} day^{-1}) compared to 21 August (4.5 MJ m^{-2} day^{-1}) as a result of a positive

LR_{net} (Fig. 6.5c).

The largest energy source during the event was, however, the sensible heat flux which accounted for more than 50 % of the surface energy budget between 26 to 28 August — a marked increase on the pre-event values (e.g. 19% on 21 August 2011) under clear skies (Fig. 6.5c) and with low wind speeds (Fig. 6.5b). The increase in SHF can be attributed to the high near-surface temperature resulting from the advection of warm air over the ice sheet. Moisture condensation onto the ice surface due to high specific humidity and wind speed resulted in a positive latent heat flux (LHF, e.g. 3.0 MJ m^{-2} day^{-1}, or 18 % of the SEB on 27 August), as opposed to surface evaporative cooling (e.g. -0.73 MJ m^{-2} day^{-1} on 21 August), which is more frequent under the prevalent clear sky conditions.

Both turbulent heat fluxes (SHF and LHF) are enhanced by high wind speeds (e.g. 8 m s^{-1} on 27 August, Fig. 6.5b), which increase the vertical mixing of air (van den Broeke and others, 2008b, 2011). Air temperatures at M61 were continuously above-freezing during the late August event (Fig. 6.4a). At M140, $\sim$ 50 km inland from the mean 1990–2011 equilibrium line, positive air temperatures suggest precipitation was liquid at least 140 km inland (Fig. 6.7).

The rain heat flux

The surface energy balance model does not account for the heat delivered by rain, which the calculation below suggests was minimal. The heat flux of rain Q_R is given by:

$$Q_R = \rho_w C_w R(T_r - T_s) \tag{6.1}$$

where ρ_w is the density of water, C_w is the specific heat capacity of water (4.2 kJ kg^{-1} K^{-1}),

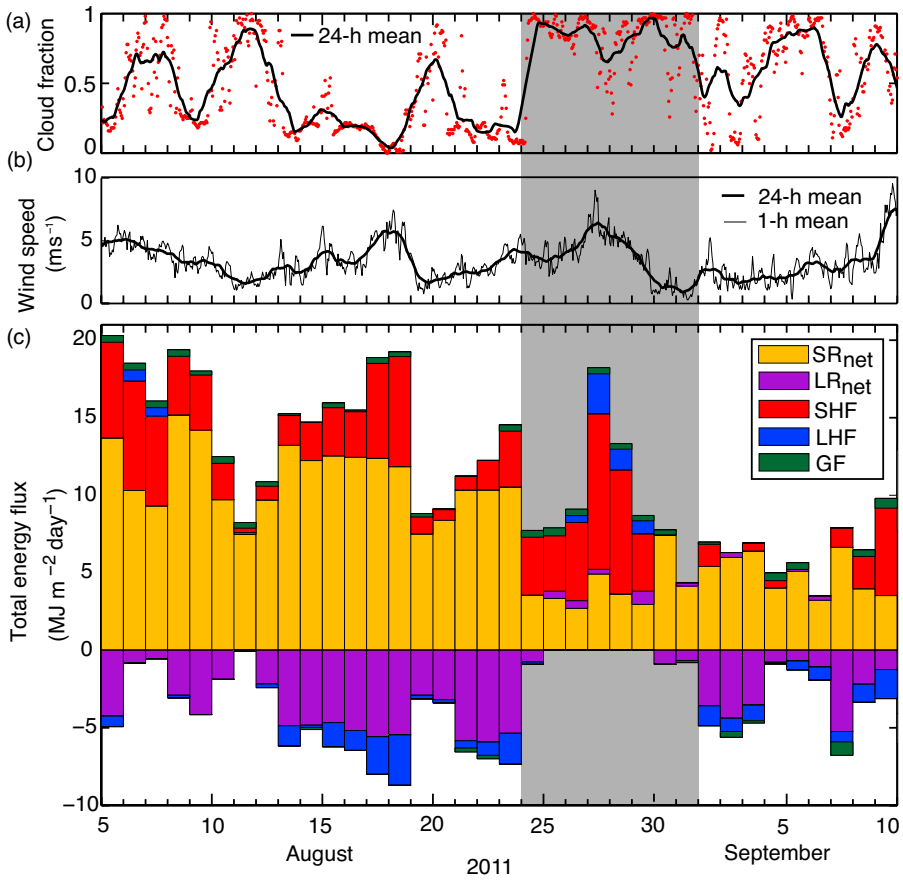

Figure 6.5: Selected meteorological variables and the surface energy budget that explain high melt conditions during the late August event: (a) hourly estimates of the cloud fraction at M13 (red dots) and the 24-hour running mean cloud fraction, (b) 2-m wind speed at M13 with a 1 and 24-hour running mean, (b) components of the daily surface energy balance at M13. The components: net shortwave (SR_{net}) and net longwave (LR_{net}) radiation, the sensible (SHF) and latent (LHF) heat fluxes and the ground flux (GF) are defined as positive when they add heat to the surface.

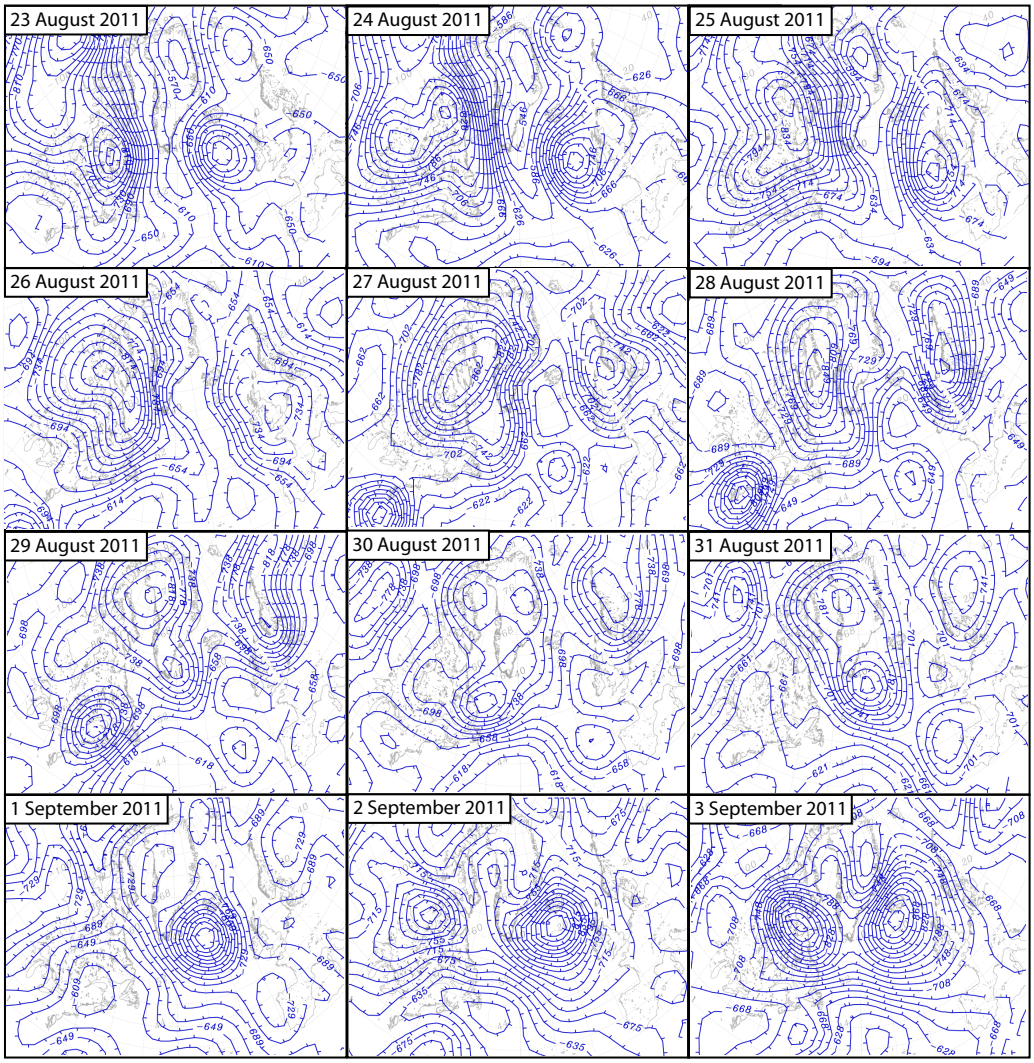

Figure 6.6: 1000 hPa geopotential height maps for Greenland from NCEP/NCAR reanalysis data between 23 August and 3 September 2011.

R is the rainfall rate, and T_r and T_s are the temperatures of rain and the surface respectively (Hock, 2005). Given a surface temperature of 0°C, a rain temperature of 6°C, and the lower (15 mm) and upper (24 mm) estimates of rainfall during the event, the rain heat flux contributed an estimated 0.06 to 0.1 MJ m^{-2} day^{-1}.This is equivalent to an additional 1.1 to 1.8 mm w.e. of melt during the entire event.

At higher elevations the sensible and latent heat released by rainfall cooling and freezing in a surface snowpack may have played an important role in bringing the sub-freezing snowpack to the melting point. The energy flux Q_R supplied by rain freezing in a snowpack is given by:

$$Q_R = \rho_w C_s R(T_r - T_{sn}) + \rho_w \lambda_w R \tag{6.2}$$

Where C_s is the specific heat capacity of snow (2090 J Kg^{-1} K^{-1}), and λ_w is the latent heat of fusion (334 kJ Kg^{-1}). The rain temperature of 2° C is taken to be the air temperature at M140 during the rainfall event and the temperature of the snowpack (T_{sn}) of −15° C is based on the air temperature during the preceding week. Given these estimates, 14 mm of rain at 2° C would bring a 15 cm w.e. snowpack at −15° C to the melting point. Hence, the energy released by rain cooling and freezing is a very effective heating mechanism for sub-freezing snowpacks and this may have substantially enhanced melt rates at high elevations during the late August event.

All these energy sources — an abnormally positive net longwave radiation, the sensible heat flux, the latent heat flux from condensation and the rain heat flux — contributed to high melt conditions peaking on 27 August (6.4j), coincident with the highest precipitation (6.4j,k), wind speeds (Fig. 6.5b) and freezing level (Fig. 6.7), and resulting in abnormally high magnitude runoff for this time of year (Fig. 6.4k).

For eight days during the August 2011 event, reanalysis data (Kalnay and others, 1996) indicate that a cyclone (minimum surface pressure of 991 hPa) centred on Baffin Bay off the west coast of Greenland advected warm, south-westerly airflow over the southern Greenland Ice Sheet (Fig. 6.6) bringing extensive precipitation, which was especially heavy on the south-east coast (Fig. 6.3). In summary, cyclonic weather conditions were responsible for sustained day-round melt and rainfall, at abnormally high elevations, which combined to produce enhanced surface runoff over large areas of the ice sheet in south Greenland.

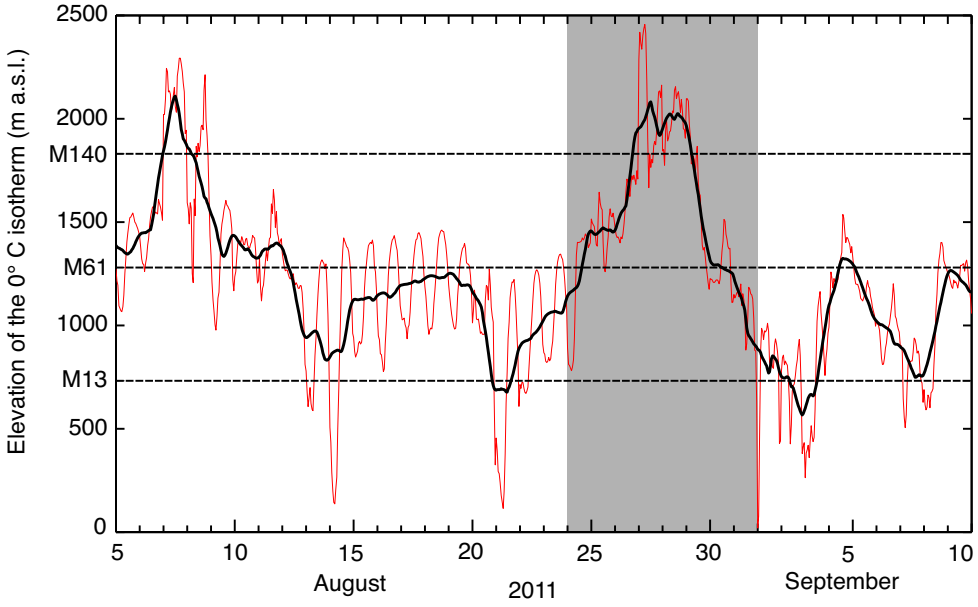

Figure 6.7: Elevation of the 0° C degree isotherm. The elevations of AWS stations M13, M61 and M140 are plotted as horizontal dashed lines for reference. The red line is the hourly freezing level and the black line is the 24-h running mean.

6.5 Discussion

The decadal-high, end-of-season snowline (1693 m a.s.l.) exposed a large expanse of bare ice (Fig. 6.1): hence runoff during the late August event would have been efficiently

concentrated into surface channels and moulins, developed by meltwater in the preceding summer months. Proglacial discharge, nearly double that of the preceding week, and high total runoff during the late-August event were, however, lower than mid-summer values when ice velocities were below the annual mean — inferring that runoff volume is not the sole factor governing acceleration (Fig. 6.4). Efficient subglacial drainage explains low mid-summer ice velocities at times of high melt input (e.g. Schoof, 2010; Bartholomew and others, 2011a; Sundal and others, 2011; Colgan and others, 2011, 2012; Bartholomew and others, 2012) and previous studies (e.g. O'Neel and others, 2001; Fudge and others, 2009) found that the antecedent conditions of the subglacial hydrological system modulate basal sliding. It is therefore significant that this event occurred in late August, immediately following a period of low air temperatures (Fig. 6.4a) and declining meltwater production (Fig. 6.4j).

6.5.1 Priming of the subglacial drainage system

On 21 August temperatures at the lowest-elevation AWS, M13, dropped below freezing for the first time since the onset of melt on 1 June, resulting in the lowest daily melt rates, proglacial discharge and ice velocities since that date (Figs. 6.4, 6.7 and 6.8). The gradually reducing diurnal variability and simultaneously increasing trend in the borehole water pressure during the preceding period (Fig. 6.8) provides evidence of a pre-event transition of the basal hydrological system to a less efficient winter-type mode (Schoof, 2010).

Near the ice margin, where thin ice results in low closure rates it is conceivable that efficient subglacial drainage endures transient summer-time cold periods and effectively offsets the melt-induced acceleration (Sundal and others, 2011; Sole and others, 2013), as occurs on alpine glaciers (e.g. Anderson and others, 2004). Theoretically (Nye, 1953; Röthlisberger,

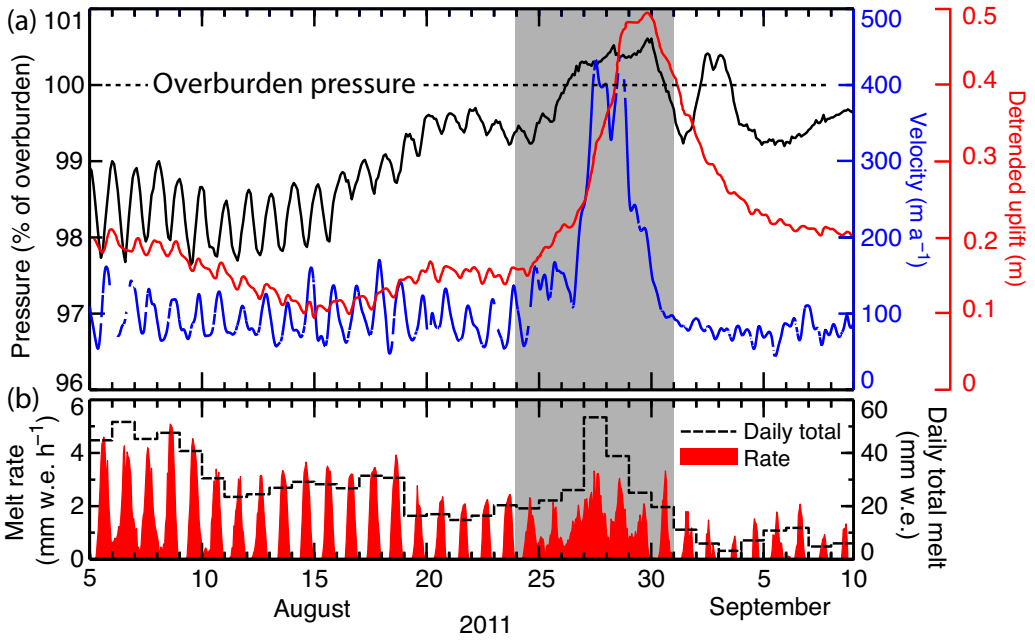

Figure 6.8: (a) Borehole water pressure, velocity, uplift and (b) melt at the R13 site. The timing of the late-August acceleration is shaded in grey.

1972; Schoof, 2010; Chandler and others, 2013), the time (t) to close an unpressurised subglacial channel to one tenth of its original radius is given by Equation 6.3:

$$t = \frac{\ln(R/R_0)}{-2An^{-n}\rho_i g H)^n} \tag{6.3}$$

where R and R_0 are the channels initial and final radius, ρ_i is the density of ice (910 kg m^{-3}), A and n are the rate factor and exponent in Glen's flow law respectively, g is acceleration due to gravity, and H is the ice thickness. Values of $A = 5.3 \times 10^{24}$ Pa^{-3} s^{-1} and $n = 3$ were used. Ice thickness was interpolated from NASA IceBridge ice penetrating radar data (Shi and others, 2010) and skidoo-based ice-penetrating radar measurements (Pettersson and others, 2011; Lindback and others, 2014). Using Equation 6.3, the time to reduce a subglacial channel to one tenth of its original radius is estimated to increase from 1 hour

under 1660-m-thick ice to 3 days under 400-m-thick ice (Fig. 6.9). Hence, at higher elevations, which are beyond the reach of remote-sensing measurements of ice velocity (e.g. Sundal and others, 2011), kilometre-thick ice (Table 6.2) results in high creep-closure rates (Fig. 6.9) forcing the ice sheet's basal hydrological system to rapidly shut down when water inputs are low (Bartholomaus and others, 2008; Schoof, 2010; Chandler and others, 2013).

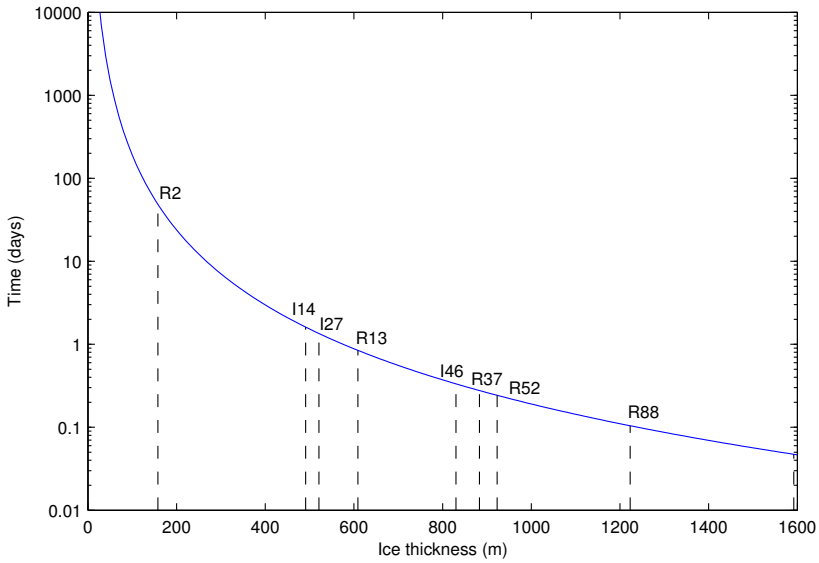

Figure 6.9: The time to reduce an unpressurised subglacial conduit to one tenth of its original size for ice thicknesses between 0 and 1600 m. The ice thickness at each of the GPS sites, which was determined from ice penetrating radar measurements, is plotted for reference.

The broad, dampened peak in proglacial discharge (Fig. 6.4k) supports the hypothesised closure of subglacial conduits prior to the event, as water transit times are high when subglacial drainage is under-developed (Chandler and others, 2013). It is hypothesised that low air temperatures (Fig. 6.4a) and melt rates (Figs. 6.4g and 6.8b) in the preceding period primed the ice sheet for a high-magnitude velocity response to the ensuing increase

in runoff in late August.

The sudden increase in subglacial water pressure to levels exceeding the ice overburden pressure suggests the ice sheet was hydraulically decoupled from its bed during the acceleration (Fig. 6.8a). This is confirmed by decimetre-scale surface uplift (Iken, 1981; Sugiyama and Gudmundsson, 2004; Bartholomaus and others, 2008, Fig. 6.8a). Uplift at site R13, for example, began at 18:00 UTC on 24 August and by 21:40 UTC on 28 August had reached 0.33 m above the surface height recorded on 21 August (Fig. 6.8a). Consistent with the theory of cavity opening (Iken, 1981; Kamb and others, 1985; Sugiyama and Gudmundsson, 2004), peak acceleration was coincident with the highest rates of water pressure and uplift—not their maxima. Uplift was sustained at R13 for ∼22 hours before the site subsided, returning to its pre-event height by 12:30 UTC on 3 September (Fig. 6.8a). The sudden drop in water pressure and ice velocity on 31 August, together with the observation of ice velocities that were lower than those observed prior to the acceleration event are consistent with the theory that the rapid decline in surface melt following the event delivered a dramatically-reduced water flux (Fig. 6.4j) to a drainage system with transient over-capacity (O'Neel and others, 2001; Schoof, 2010).

6.5.2 Previous similar events and their frequency

The late summer 2011 event was driven by a low-pressure system with its centre located in Baffin Bay to the west of Greenland (Fig. 6.6). Such Baffin Bay cyclones are the second most frequent synoptic pattern that bring precipitation to Greenland (Schuenemann and Cassano, 2009). Baffin Bay cyclones often bifurcate over the southern Greenland Ice Sheet forming an Icelandic Low by lee-cyclogenesis on the southeast coast, while the parent cyclone tracks north delivering precipitation to the west coast of Greenland (Chen and others, 1997; Schuenemann and Cassano, 2009). They advect warm moist air onshore from

the open North Atlantic, which is lifted orographically over the ice sheet to an elevation of 2800 m a.s.l. in less than 200 km. As the air rises, it cools adiabatically becoming saturated and releasing precipitation. Baffin Bay cyclones occur more frequently during the summer (6.35 % of days) than during winter (2.90 % of days; Schuenemann and Cassano, 2009) and atmospheric models (Schuenemann and Cassano, 2010) predict that they will increase in annual frequency from 3 % of days in 1961-99 to 4 % of days in 2081–2100 — equivalent to an extra ∼4 days per year.

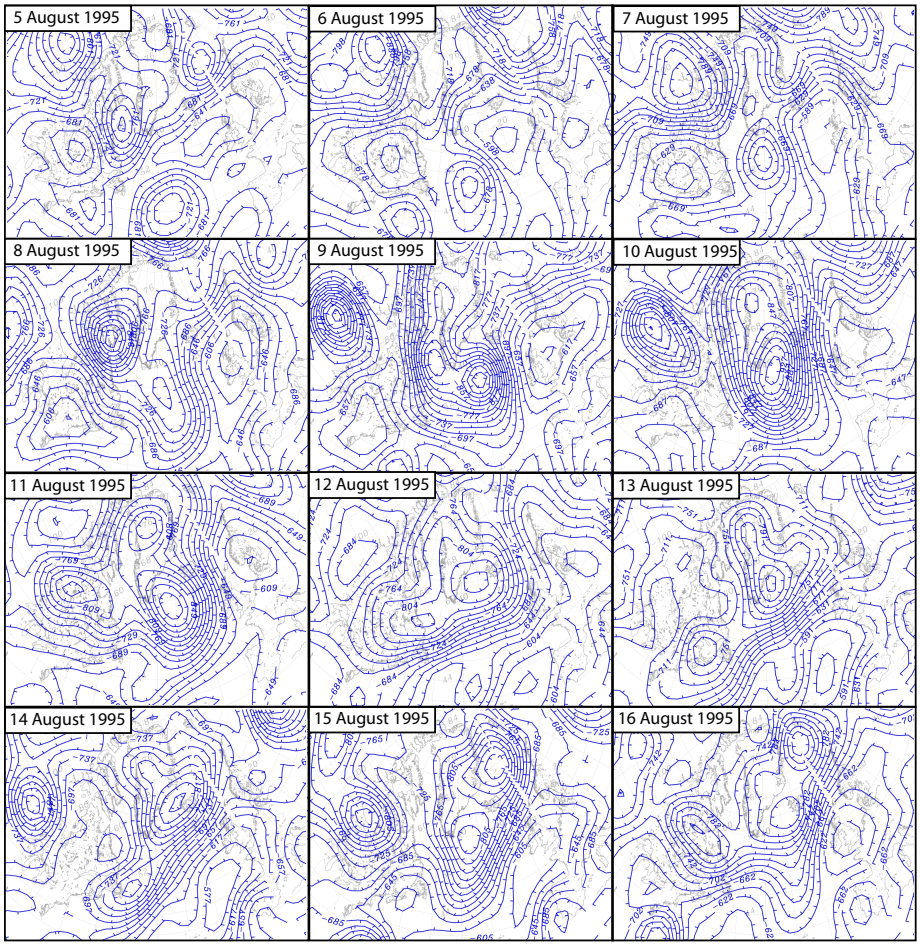

Figure 6.10: 1000 hPa geopotential height maps for Greenland from NCEP/NCAR reanalysis data between 5 and 16 August 1995.

Other synoptic patterns that bring precipitation to widespread areas of south Greenland include the Labrador Sea cyclone and the Southern Tip cyclone (Schuenemann and Cassano, 2009). In early August 1995 a cyclone tracked over the southern tip of Greenland (Fig. 6.10) bringing heavy precipitation (Fig. 6.11) and driving a widespread acceleration, which was captured using interferometric synthetic aperture radar (InSAR) on European Remote Sensing (ERS) satellite images (Palmer and others, 2011, Figs. 1.9 and 6.12).

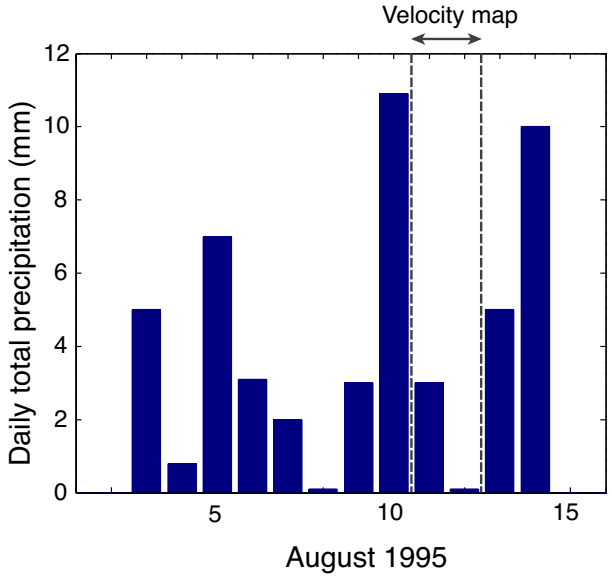

Figure 6.11: Kangerlussuaq daily total precipitation in early August 1995. The timing of the Palmer and others (2011) velocity map (11-12 August) is indicated by dashed lines.

The acceleration (of up to 360%) extended at least 100 km inland (Figs. 1.9 and 6.12). This event in August 1995 was originally interpreted as characteristic of late summer shortwave-radiation-driven melting (Palmer and others, 2011) but further analyses (Figs. 6.10 and 6.11) reveal it was driven by similar cyclonic weather conditions to the August 2011 event. Between 3 August and 14 August 1995, 49.8 mm of rain was recorded in Kangerlussuaq, with 10.9 mm on the 10 August (Fig. 6.11).

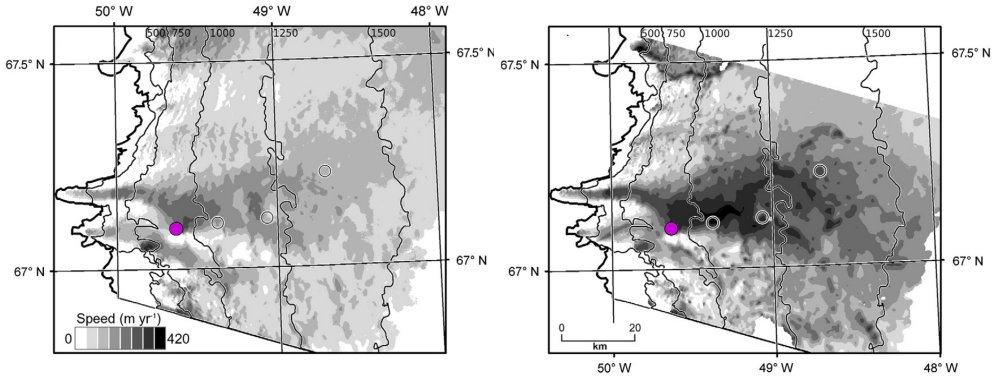

Figure 6.12: Velocity map of Russell Glacier catchment showing (a) the velocity during winter (20 October 1995 to 3 February 1996) and (b) during late summer 1995 (11-12 August 1995), adapted from Ref. 30. The late summer velocity map captures a substantial rainfall/melt event driven by cyclonic weather conditions.

The widespread nature of the acceleration suggests that the driving mechanism — ice sheet melt and rainfall — affected a broad region of the ice sheet. The incursion of warm, moist air was responsible for the high melt conditions and rainfall at abnormally high elevations of the ice sheet that ultimately drove the widespread and prominent acceleration events in both August 1995 and August 2011. The acceleration event observed in late August 2011 is therefore not an isolated event.

6.5.3 Long term trends in rainfall seasonality

Long-term trends in the Kangerlussuaq precipitation record (Cappelen and others, 2013) were examined to investigate changes in the seasonal distribution of rainfall between 1977 and 2012. The phase of precipitation was determined as liquid if the mean temperature over the corresponding 12-hour period was greater than or equal to 2° C, allowing daily total rainfall to be calculated.

Following standard statistical measures applied by previous studies (Walsh and Lawler,

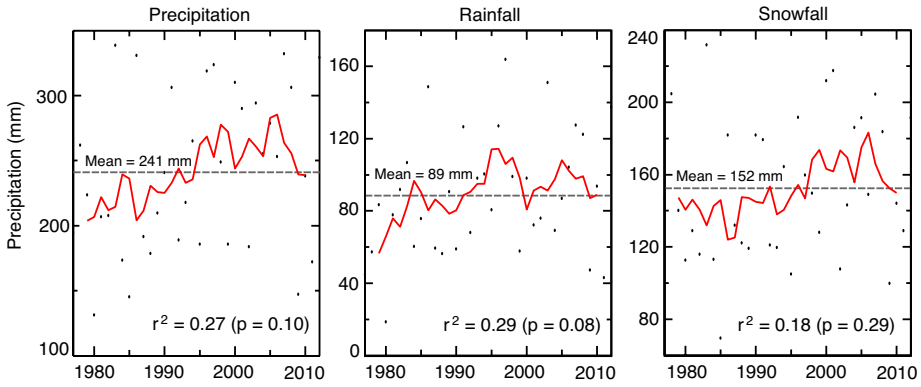

Figure 6.13: Total annual precipitation, rainfall and snowfall in Kangerlussuaq between 1977 and 2012. The red line shows the five-year moving average.

1981; Pryor and Schoof, 2008) the seasonality index (SI) and the day of year on which the 10^{th} (P10), 25^{th} (P25), 50^{th} (P50), 75^{th} (P75) and 90^{th} (P90) percentiles of the annual total rainfall were achieved were calculated. The dispersion in the seasonal distribution of rainfall was assessed by calculating the interquartile ($IQR = P75 - P25$) and interdecile ($IDR = P90 - P10$) range.

The seasonality index (SI):

$$SI = \frac{1}{R} \sum_{n=1}^{12} \left| \bar{X} - \frac{R}{12} \right| \tag{6.4}$$

where R is the total annual rainfall and $\bar{X}$ is the total monthly rainfall in month n, is a standard measure of rainfall seasonality (Walsh and Lawler, 1981). SI theoretically ranges from 0, if all the months have equal rainfall to 1.83, if all the rainfall falls in one month. SI values of 1 to 1.19 indicate that the majority of rainfall occurs in 3 months or less with $SI > 1.2$ indicating the majority of rainfall falls in 2 months or less. The results indicate an increasing trend in the annual total precipitation, rainfall and snowfall in Kangerlussuaq superimposed on large inter-annual variability (Fig. 6.13). The linear

trend in annual precipitation ($r^2 = 0.27$) and rainfall ($r^2 = 0.29$) is significant at the 90 % level. Coincident with this increase is a decline in the rainfall seasonality index from 1.32 in 1980-89 to 1.30 in 1990-99 to 1.21 in 2000-09, indicating that the seasonal distribution of rainfall has become more dispersed (Fig. 6.14d).

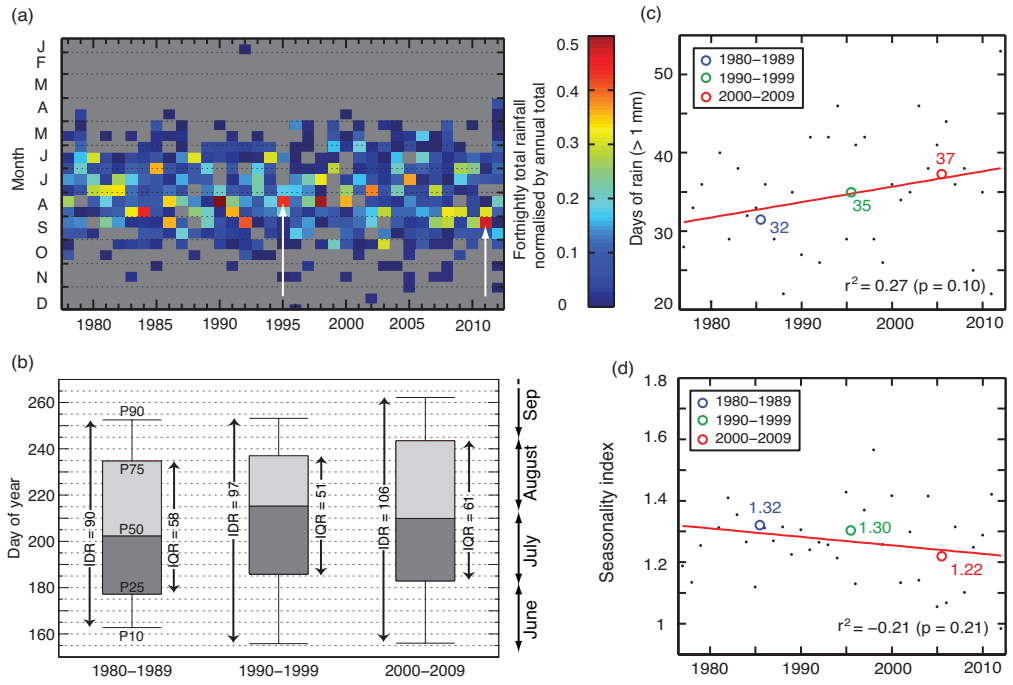

Figure 6.14: Trends in the seasonal distribution of rainfall in Kangerlussuaq (a) fortnightly total rainfall normalised by the annual mean. Heavy rainfall events, such as those in August 1995 and August-September 2011 that are indicated by white arrows, show up as orange-to-red blocks, (b) box and whisker plot showing the decadal mean day of year on which the percentiles in total annual rainfall were achieved. The interquartile (IQR) and interdecile (IDR) range with units of days are annotated, (c) the number of days with more than 1 mm of rain per year, and (d) the rainfall seasonality index, which varies from 0 if all the months have equal rainfall to 1.83 if all the rain falls in one month. On (c) and (d) coloured circles show the decadal means and the red line shows the linear trend.

The number of days of rain (> 1 mm) per year also shows an increasing trend ($r^2 = 0.27, p = 0.10$) of approximately 3 days per decade (Fig. 6.14c). The greatest number of

rain days occurred during the anomalously high melt year of 2012 (e.g. Nghiem and others, 2012) with 53 days of > 1 mm of rain, which is 2.4 standard deviations above the mean and 0.93 standard deviations above the next highest year. Examining the percentile day of year statistics (Fig. 6.14b) provides insight into the detail of the dispersion: rainfall has become earlier and later in the season between 1980 and 2012 with the IDR increasing by an average of 6.5 days per decade. The pace of the 10^{th} percentile day of year becoming earlier (3.4 days per decade) was surpassed by the rate of the 90^{th} percentile day of year becoming later (4.9 days per decade) and the dispersion is therefore asymmetric with rain falling disproportionally later in the season. This observation is consistent with results from a three-model ensemble that predicts the greatest increase in Greenland precipitation during the next century will occur in autumn (Schuenemann and Cassano, 2010).

The timing of heavy rainfall events was investigated by calculating the fortnightly totals of rainfall for the entire Kangerlussuaq precipitation record. To normalise the influence of exceptional events between years, the fortnightly precipitation sums were divided by their respective annual total (Fig. 6.14a). Heavy rainfall events, identified as orange-to-red blocks on Figure 6.14a, tend to occur more frequently in late summer and autumn, coinciding with the period of highest rainfall (Cappelen and others, 2001), peak longwave radiation, densest cloud cover (van den Broeke and others, 2008a) and peak cyclonic activity (Serreze and others, 1993) in this region.

Recent studies suggest that precipitation over Greenland will change in three ways: (1) changes in the frequency of synoptic patterns that bring precipitation, (2) changes in the precipitation that occurs when a certain synoptic pattern occurs, and (3) changes in the phase of precipitation i.e. the ratio of rainfall to snowfall. These are expanded below:

1. Schuenemann and Cassano (2010) found that 83% of the predicted increase in precipitation from 35.8 to 45.0 cm yr^{-1} over Greenland by the end of the twenty-first

century can be attributed to a rise in precipitable water in the atmosphere as a result of higher air and ocean temperatures and reduced sea ice cover. Climate warming is expected to enhance ocean evaporation and the moisture carrying capacity of the air, resulting in an increase in precipitable water and higher precipitation over the ice sheet (e.g. Fettweis and others, 2011).

2. Schuenemann and Cassano (2010) also predict that the frequency of Baffin Bay cyclones over Greenland will increase from 3% of days in 1961-99 to 4% of days in 2081-2100. The frequency of other cyclonic weather systems that bring precipitation to Greenland is also expected to increase with a northward shift in North Atlantic storm tracks.

3. The rainfall fraction is expected to increase under a warmer climate as warmer air temperatures cause more precipitation to fall as rain (e.g. Ettema and others, 2009; Box and others, 2012; Franco and others, 2013).

Climate model projections provide further evidence for a future increase in rainfall in Greenland. Results from 50 years of RACMO-GR modelling indicate that the contribution of rainfall to the surface mass balance of the Greenland Ice Sheet increased by $\sim 200\,\mathrm{Gt}$ between 2000 and 2009 (see Fig. 3c of van den Broeke and others, 2009). Furthermore, a recent modelling study suggests the rainfall fraction will continue to increase over the next century (see Fig. S2d of Franco and others, 2013). According to Ettema and others (2009), the rain fraction over the entire Greenland Ice Sheet increased from 6.2% between 1990 and 2008 to 8.5% during the anomalously warm year of 2007. These assertions are supported by further modelling results, which indicate that the ratio of rain to snow increased between 2000 and 2011 (Box and others, 2012).

The changes in precipitation are not homogenous. Annual snowfall is expected to increase

in the interior of the ice sheet, while a substantial proportion of snowfall in south Greenland is expected to turn to heavy rainfall (see Fig. S6b of Franco and others, 2013). This supports the assertion of Schuenemann and Cassano (2010) that the greatest changes in precipitation are expected in southwest Greenland.

6.6 Conclusions

This chapter has analysed records of ice motion, meteorology and hydrology during a transient acceleration event driven by high melt and rainfall in late August 2011 to gain insights into basal hydrological forcing on Greenland ice sheet motion. Simultaneous borehole water pressure and high-frequency ice motion data confirm that the rapid transition to an inefficient winter-type drainage mode, under ice that is several hundreds of metres thick, acts to re-prime the ice sheet for a high-magnitude velocity response to subsequent water inputs.

The acceleration was widespread — extending to at least 88 km in to the ice sheet's interior — and sustained — persisting through the day and night for six days. The analysis conducted during this investigation reveals that a previous acceleration event detected by Palmer and others (2011) in August 1995 was caused by similar meteorological conditions. Using the August 2011 event as a natural experiment this chapter has revealed that the ice sheet is sensitive to atypical meteorological conditions associated with cyclonic weather systems.

The advection of warm, moist air masses and rainfall over Greenland is predicted to increase in frequency and magnitude during the next century, in response to a warmer and cloudier regional climate and a northward shift in North Atlantic storm tracks (Schuenemann and Cassano, 2010; Fettweis and others, 2011; Franco and others, 2013). Hence,

such melt, rainfall and acceleration events are anticipated to become more common in the future.

Consequently, models that neglect the influence of cyclonic weather conditions will underestimate melt and ice velocities as the predicted increase in cyclonic activity over Greenland (Schuenemann and Cassano, 2010) may result in widespread off-season melt, rainfall and flow acceleration across the ice sheet. Such events may play an increasingly important — and hitherto undocumented — role in the future of the Greenland Ice Sheet and its contribution to sea level rise under a changing climate.

Acknowledgements

The Greenland Analogue Project (GAP), SKB/Posiva and The Netherlands Organisation for Scientific Research (NOW/PPP) funded this project, the latter of which generously supported the K-transect measurements. TanDEM-X data were provided by the German Aerospace center (DLR) within the framework of the XTI_GLAC0433 project. UNAVCO, the Danish Meteorological Institute, MIT, TEQC software (Estey and Meertens, 1999), Bent Hasholt, John Cappelen, Rickard Pettersen, Katrin Lindback, and Andrew Fitzpatrick are thanked for help with data collection and processing. Thanks are extended to Matthew Westoby for comments on a draft. Ice thickness data from the NASA IceBridge project and MODIS data from the Land Processes Distributed Active Archive Center (LP DAAC) located at the USGS EROS Center (`http://lpdaac.usgs.gov`) were used.

Chapter 7

Results IV: Persistent flow acceleration within the interior of the Greenland Ice Sheet

Author contributions

Several authors contributed to the research presented in this chapter which was published in Geophysical Research Letters as Doyle and others (2014) and is included in Appendix A. Andrew Fitzpatrick provided the supraglacial lake dataset, which is adapted and extended from Fitzpatrick (2013) and Fitzpatrick and others (2014). Dirk van As collected the meteorological datasets, Andreas Mikkelsen provided the proglacial discharge record, and Rickard Pettersson made the radio-echo sounding measurements. Sam Doyle processed the GPS record and wrote the text. In addition to those already mentioned, Alun and Bryn Hubbard provided advice and comments on the manuscript. Comments from Peter

Jansson and an anonymous reviewer led to several improvements.

7.1 Summary

This chapter presents surface velocity measurements from a high-elevation site (S10) located 140 km from the western margin of the Greenland Ice Sheet, and $\sim$ 50 km into its accumulation area. Annual velocity increased each year from $51.78 \pm 0.01\,\mathrm{m\,yr^{-1}}$ in 2009 to $52.92 \pm 0.01\,\mathrm{m\,yr^{-1}}$ in 2012 — a net increase of 2.2 %. These data also reveal a strong seasonal velocity cycle of up to 8.1 % above the winter mean, driven by seasonal melt and supraglacial lake drainage. Sole and others (2013) recently argued that ice motion in the ablation area is mediated by reduced winter flow following the development of efficient subglacial drainage during warmer, faster, summers. The velocity data from S10 presented in this chapter extend this analysis and reveal a year-on-year increase in annual velocity above the ELA, where despite surface melt increasing, it is still sufficiently low to hinder the development of efficient drainage under thick ice.

7.2 Introduction

Our knowledge of the dynamics of the Greenland Ice Sheet (GrIS) has improved markedly over the last decade. The recent observation that reduced winter velocities offset faster summer velocities in warmer years (Sole and others, 2013), consolidated the seemingly contradictory findings that the magnitude of the summer acceleration correlates with surface melt intensity (Zwally and others, 2002), yet the long-term trend is of a slight decline in annually-averaged flow despite an increasingly negative surface mass-balance (van de Wal and others, 2008). Sole and others (2013) argued that this regulating reduction in winter

motion is caused by the evolution of a larger, more extensive subglacial drainage system in warmer summers, which drains regions of high basal water pressure and increases subsequent ice-bed coupling and traction. Although this process may hold for marginal areas of the ice sheet that experience intense summer surface melt and extensive delivery of meltwater to the basal interface (where the data supporting the hypothesis of Sole and others were collected), it may be less effective at higher elevations, where melt rates are lower and ice thicknesses greater. Hence, it is hypothesised that there exists an inland zone, most likely within and around the wet-snow zone, that is characterised by enough surface melt to induce a seasonal acceleration but which is insufficient to develop the effective subglacial drainage required to regulate this acceleration through subsequent reduced winter flow. Although it has been speculated that the inland expansion of melt and supraglacial lakes (SGLs) will influence ice motion in this difficult to access zone (e.g. Liang and others, 2012; Howat and others, 2013), to date, velocity data have not been available to test this hypothesis. This chapter tests this hypothesis and by doing so specifically addresses concerns raised in the fourth assessment report of the IPCC:

> 'Much uncertainty remains, especially related to ... whether access of melt water to the bed through more than 1 km of cold ice would migrate inland if warming caused surface melting to migrate inland (Alley and others, 2005b). This could thaw ice that is frozen to the bed, allowing faster flow through enhanced basal sliding or sub-glacial sediment deformation. Data are not available to assess whether effects of increased surface melting in Greenland have been transmitted to the bed and contributed to ice flow acceleration.' (Lemke and others, 2007, p. 368)

Field-based Global Positioning System (GPS) measurements are currently the only method capable of determining long-term changes in flow within the ice sheet's interior; remote-

sensing techniques fail due to a lack of coherence for interior, snow-covered regions of the ice sheet (e.g. Joughin and others, 2010).

Figure 7.1: Photo of the GPS installation at S10. In the background is the KAN_U weather station (left) and stake assembly (right). 4 May 2012.

This chapter presents a five-year (September 2008 – September 2013) time-series of ice surface velocity measurements recorded by a dual-frequency GPS receiver located within the accumulation area. The aims of this analysis are (i) to report and evaluate the nature of the site's velocity record, particularly in relation to seasonality and inter-annual change, and (ii) to evaluate the transferability of the self-regulation model of Sole and others (2013) to higher elevations within the ice sheet's interior.

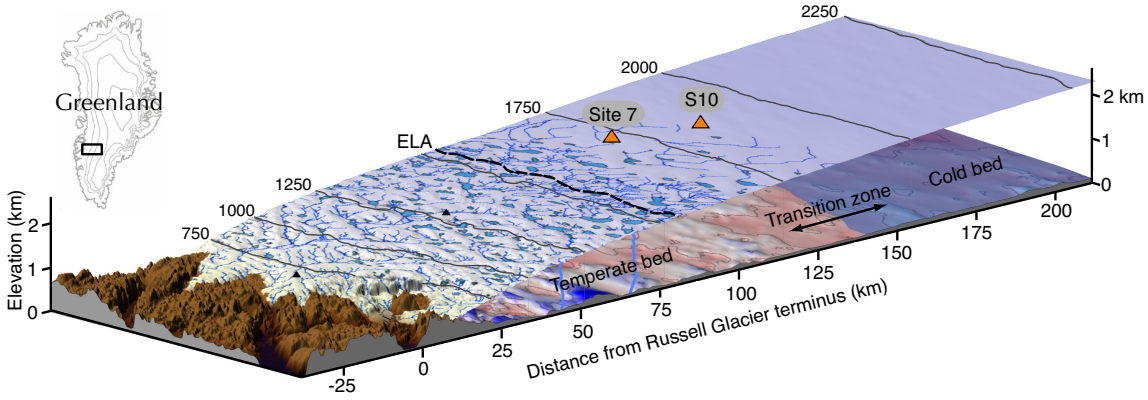

Figure 7.2: Cross-section of Russell Glacier catchment showing the locations of the GPS sites, including S10 of this study and Site 7 of Sole and others (2013). The surface elevation is from Howat and others (2014), the bed topography is from Bamber and others (2013), and the basal thermal regime is conceptual. The maximum SGL and stream extent between 2002 and 2012, adapted from Fitzpatrick and others (2014), and the mean 1990 to 2011 ELA of 1553 m a.s.l. as estimated by van de Wal and others (2012) are also shown. The black box on the inset map shows the location of the study area in Greenland.

7.3 Data and methods

Rigorous processing was applied to dual-frequency GPS data sampled at a 10 second interval from September 2008 onwards by a receiver deployed at the highest site (S10) on the land-terminating K-transect in West Greenland (Figs. 7.1 and 7.2). S10 (N67.00°, W47.02°) is co-located with an automated weather station (AWS) at 1840 m a.s.l., 140 km from the ice margin and more than 50 km inland from the 21-year-mean mass-balance equilibrium line altitude (ELA) of 1553 m a.s.l., as estimated by van de Wal and others (2012). A Trimble Zephyr Geodetic antenna was installed on a 4.5-m-long, 48-mm-diameter steel pipe, consisting of three 1.5-m-long sections drilled 3.5 m into the ice surface. The pole subsequently froze in and due to the slightly positive surface mass balance (SMB) at this site in the accumulation area (mean SMB between 1994 and 2010 of + 0.27 m w.e., van de

Wal and others, 2012), it has not been necessary to relocate the antenna horizontally since it was installed. In 2010, the antenna was raised to keep it above the snow surface by replacing the upper 1.5-m-long pole with a 2-m-long pole. A dual-frequency Trimble R7 GPS receiver logged data continuously at a 10-second-interval whenever sufficient power was available. Power was provided by a 100 Ah battery bank, charged by a 48 W solar panel and a Forgen wind generator. Despite this, periods of power outage reduced the continuity of the GPS measurements especially prior to April 2011 when the GPS installation was serviced. Although these outages do not degrade the long-term velocity records (Fig. 7.4) they restrict analysis of transient velocity variations to the period May 2011 to September 2013 (Fig. 7.3a).

7.3.1 Calculation of velocity

Mean ice flow at S10 is $\sim$ 52 m yr^{-1} (equivalent to 14 cm day^{-1}) and previous studies (Bartholomew and others, 2011a; Sole and others, 2013) suggest a small, if not undetectable, seasonal velocity variation should exist at this site. An L1 GPS receiver deployed at S10 in 1996 shows no significant variation in velocity (van de Wal and others, 2008), although a small seasonal variation may be undetectable given the estimated uncertainty of this positioning technique of $\pm$1.6 m (Den Ouden and others, 2010). Approximately 50 km down-glacier of S10, Sole and others (2013) report a 0.2 % (2009) to 7.2 % (2010) increase above the mean winter velocity from a dual-frequency GPS receiver located at their Site 7 (1715 m a.s.l.), which moved at $\sim$ 63 m yr^{-1} between 2009 and 2011. The lowest recorded seasonal increase in velocity at Site 7 of 0.2 % in 2009 is equivalent to an increase in annual displacement of just 0.13 m, which is less than the sites average daily displacement of 0.17 m. Further up-glacier, the seasonal velocity variation is expected to be lower.

In response, a rigorous processing strategy was applied to the dataset and the uncertainties

were carefully examined. Dual-frequency GPS data were processed at a 30 second interval kinematically (King, 2004) relative to bedrock-mounted reference stations using the differential carrier-phase positioning software, Track v. 1.27 (Chen and others, 1997; Herring and others, 2010), and precise ephemeris from the International GNSS Service (Dow and others, 2011). Reference stations were located on bedrock, 1 km from the terminus of Russell Glacier (BASE) and at Kellyville (KELY), giving baseline lengths of 141 and 171 km respectively. Wherever possible, the baseline length was minimised by using data from the BASE receiver. Problems inherent to relative GPS processing over long baselines include differential ionospheric-delay of the GPS signal received at each site and the problem that receivers separated by long distances may not co-observe the same satellites, which reduces the number of double differences that can be calculated (King, 2004; Leick, 2004). To address these issues daily maps of the ionosphere were input into Track software, using the IONEX format (Schaer and others, 1998), and applied strict quality control to the output position time series. Solutions were discarded unless carrier-phase ambiguities were fixed to the correct integer and unless a sufficient number (> 4) of double-difference calculations were made.

To detect small variations in velocity at this relatively-slowly moving site it was necessary to calculate the average velocity over longer time intervals than the daily or sub-daily intervals typically used in studies of faster, lower-elevation ice (e.g. Shepherd and others, 2009; Bartholomew and others, 2010). Assuming the velocity (v) was linear between two epochs (t_1 and t_2) the magnitude of velocity was calculated as the Euclidian displacement normalised for time (Eq. 7.1).

$$v = \frac{\sqrt{(X_2 - X_1)^2 + (Y_2 - Y_1)^2}}{t_2 - t_1} \tag{7.1}$$

A conservative estimate of the uncertainty in the positions estimated by Track software of ±1 cm was assumed and this uncertainty is propagated through the velocity calculation (see Subsection 3.2.3). This positioning uncertainty can be conservative as the standard deviation in the horizontal positioning of the static Kellyville reference station, using 4 months of 30-second interval data and the same kinematic processing technique, was 5 mm in the northing and 6 mm in the easting (see Fig. 3.6). Furthermore, rather than differencing single epoch positions to obtain velocity, which could adversely incorporate any remaining anomalies, the position was averaged over a 6-hour period before differencing.

Long-term trends in velocity are reported using summer (1 May to 10 September), winter (10 September to 1 May) and annual (1 May to 1 May) periods (see Table 7.1). The 10 September was selected as representative of the end of summer on the basis that all melt at the mid-elevation (1280 m a.s.l.) KAN_M automated weather station (AWS) (see Fig. 3.1, van As and others, 2012) had ceased by this date, and S10 GPS data were available on this day in all years. Similarly, the 1 May was selected as melt onset at KAN_M commenced after this date in all years. As data were not available on exactly 1 May in all years it was necessary to use the next closest days in 2010 (27 April) and 2011 (6 May). By experimenting with other available data in 2009 and 2012 (i.e. from neighbouring days) it was found that the mean velocity calculations were relatively insensitive to small changes (4 to 5 days) in the interval, suggesting that the lack of a precisely consistent interval is unlikely to have significantly affected the results. The uncertainty in velocity reduces for longer time intervals and for annual, winter and summer velocities the uncertainty is estimated at 0.01, 0.02 and 0.04 m yr^{-1} respectively; these uncertainties are inline with previous studies (e.g. Bartholomew and others, 2011a; Sole and others, 2013).

The uncertainty of daily averaged velocities is typically ±5 m yr^{-1} (Shepherd and others, 2009; Sole and others, 2013) and it was found that this was too large to detect the seasonal

velocity variation at S10. A 15-day interval was selected following experimentation with intervals ranging from 1 to 30 days as it proved optimal with regard to both the temporal resolution and the estimated uncertainty. The 15-day interval was applied wherever the dataset allowed but longer gaps were necessary to complete the time series, especially during winter when the receiver powered down. These longer intervals are shown on Figure 7.3 as dashed lines. Over a 15-day interval the receiver is expected to move by 2.1 m on average and it was found that the seasonal velocity signal was significantly above the uncertainty of ± 0.3 m yr^{-1} (Fig. 7.3).

7.3.2 Supporting datasets

These data, from five contrasting melt seasons (2009 to 2013), and encompassing high seasonal and inter-annual variability in melt conditions, are compared to a range of contemporaneous datasets from Russell Glacier catchment. Supraglacial lake statistics, including the elevation of the highest lake, and the areal extent of lakes above 1400 m a.s.l., were calculated following Fitzpatrick and others (2014). Annual total proglacial discharge was gauged following the method of Hasholt and others (2013) at Watson Bridge near Kangerlussuaq. Positive degree days (PDDs; e.g. Braithwaite, 1993; Hock, 2003) were calculated from hourly temperature data from the KAN_U AWS, which is co-located with the S10 GPS receiver at 1840 m a.s.l. (Fig. 7.1, van As and others, 2012).

7.4 Results

The mean rate of ice motion at S10 between September 2008 and September 2013 was 52.26 ± 0.01 m yr^{-1} to the west (274.5°). Over this period, ice flow was consistently faster during the summer than the winter, and the timing and amplitude of the seasonal velocity

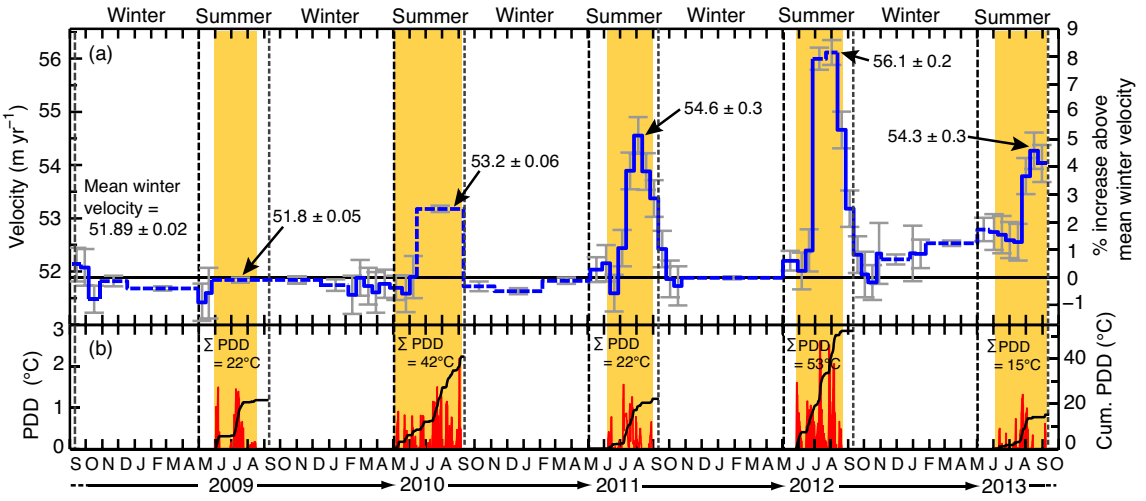

Figure 7.3: (a) Velocity at S10 between September 2008 and October 2013. Dashed lines indicate averaging periods longer than 15 days, which may reduce the apparent amplitude of velocity variations, particularly during summer 2009 and summer 2010. The horizontal grey line represents the mean winter velocity, averaged over all five winters, of 51.89 m yr^{-1}, (b) positive degree-days (PDD) at S10 in red, with the cumulative PDD in black. The orange shading highlights the melt seasons at S10. The vertical dashed black lines and arrows delineate the summer (1 May to 10 September), winter (10 September to 1 May) and annual (1 May to 1 May) averaging periods used in this study.

cycle correlates with the duration and intensity of the melt season (Fig 7.3). In 2011 and 2012, an initial acceleration in May of ∼1 % above the mean winter velocity (51.89 m yr^{-1}), was followed by larger (5.2 % in 2011 and 8.1 % in 2012), and longer, mid-summer velocity increases between June and September (Fig. 7.3a). In the cooler 2013 summer, this seasonal pattern was still apparent but was retarded with an initial small acceleration of 1.3 to 1.7 % above the winter mean persisting for longer into July before flow increased to 4.6 % above winter values in early August (Fig. 7.3a). Maximum velocity occurred in early August and in years with available data velocities returned to mean winter values, or below, by the end of September (Fig. 7.3a). These patterns are consistent with previous observations from Greenland (Zwally and others, 2002; Joughin and others, 2008, 2010;

Fitzpatrick and others, 2013), which reveal that ice flow gradually increases over winter from an all year minimum in autumn. Within error, no short-term variation in surface elevation was detected, which lowered commensurate with down-slope ice motion at a mean rate of $1.08 \pm 0.06\,\mathrm{m\,yr^{-1}}$ (Fig. 7.6).

The velocity record from S10 (Figs. 7.3a and 7.4a) supports observations of faster summer flow during warmer years (e.g. Zwally and others, 2002; Sole and others, 2013). Mean summer velocity increased during successively warmer years, from $51.82 \pm 0.04\,\mathrm{m\,yr^{-1}}$ in 2009 to $52.65 \pm 0.04\,\mathrm{m\,yr^{-1}}$ in 2010 and $52.94 \pm 0.04\,\mathrm{m\,yr^{-1}}$ in 2011, and was notably higher ($53.96 \pm 0.04\,\mathrm{m\,yr^{-1}}$) during the record melt year of 2012 (Fig. 7.4a). In contrast to previous studies (e.g. van de Wal and others, 2008), there is also evidence for a long-term increase in ice velocity at S10. Summer of 2013 was still the second fastest ($53.18 \pm 0.04\,\mathrm{m\,yr^{-1}}$) on record despite cool conditions, and the previous winter velocity of $52.33 \pm 0.02\,\mathrm{m\,yr^{-1}}$ was substantially above average even exceeding the 2009 mean summer velocity by $0.5\,\mathrm{m\,yr^{-1}}$. Excluding winter 2010/11, year-on-year winter flow accelerated by $\sim 0.05 \pm 0.03\,\mathrm{m\,yr^{-2}}$ between 2009 and 2012 (Fig. 7.4a; Table 7.1). These cumulative trends in summer and winter flow yield a long-term increase in mean annual surface velocity at S10 (Fig. 7.4a; Table 7.1).

7.5 Discussion

Drawing on existing glacio-hydrological theory Sole and others (2013) posited that enhanced ice motion across the ablation area during warmer summers is offset by reduced winter velocities caused by the drainage of areas of high basal water pressure by larger and more extensive subglacial channels. Our observations at S10 of higher winter velocities following warmer, faster summers and the ensuing year-on-year increase in net flow

Table 7.1: Mean winter, annual and summer velocities at S10

Year	t_1	t_2	Velocity ($m\,yr^{-1}$)
Winter velocities:			
2009	7 Sep 2008	1 May 2009	51.73 ± 0.02
2010	10 Sep 2009	27 Apr 2010	51.78 ± 0.02
2011	10 Sep 2010	6 May 2011	51.72 ± 0.02
2012	10 Sep 2011	1 May 2012	51.90 ± 0.02
2013	10 Sep 2012	1 May 2013	52.33 ± 0.02
Annual velocities from spring to spring:			
2009	1 May 2009	27 Apr 2010	51.78 ± 0.01
2010	27 Apr 2010	6 May 2011	52.07 ± 0.01
2011	6 May 2011	1 May 2012	52.27 ± 0.01
2012	1 May 2012	1 May 2013	52.92 ± 0.01
Summer velocities:			
2009	1 May 2009	10 Sep 2009	51.82 ± 0.04
2010	27 Apr 2010	10 Sep 2010	52.66 ± 0.04
2011	6 May 2011	10 Sep 2011	52.94 ± 0.04
2012	1 May 2012	10 Sep 2012	53.96 ± 0.04
2013	1 May 2013	10 Sep 2013	53.18 ± 0.04
Annual velocities from autumn to autumn:			
2009	7 Sep 2008	10 Sep 2009	51.77 ± 0.01
2010	10 Sep 2009	10 Sep 2010	52.11 ± 0.01
2011	10 Sep 2010	10 Sep 2011	52.15 ± 0.01
2012	10 Sep 2011	10 Sep 2012	52.65 ± 0.01
2013	10 Sep 2012	10 Sep 2013	52.64 ± 0.01

(Fig. 7.4), contrasts with these findings of Sole and others (2013), which are based on the analysis of GPS data from sites within the ablation area . The year-on-year annual flow increase measured at S10 (1840 m a.sl.) is, however, consistent with their uppermost GPS site (Site 7; 1715 m a.s.l.), which is also located above the ELA (Fig. 7.5). Between 2009 and 2012, the mean annual (May to May) increase in velocity at S10 of 0.7 % per year is directly comparable to the 0.9 % increase per year between 2009 and 2011 at Site 7 of Sole and others (2013). The seasonal variations in velocity — the percentage summer increase above the subsequent winter mean — are also similar, with the 0.1 % (2009), 1.8 % (2010),

2.0 % (2011) and 3.0 % (2012) measured at S10 comparable to, though expectedly lower, than the 0.2 % (2009), 7.2 % (2010) and 6.9 % (2011) seasonal accelerations measured at Site 7.

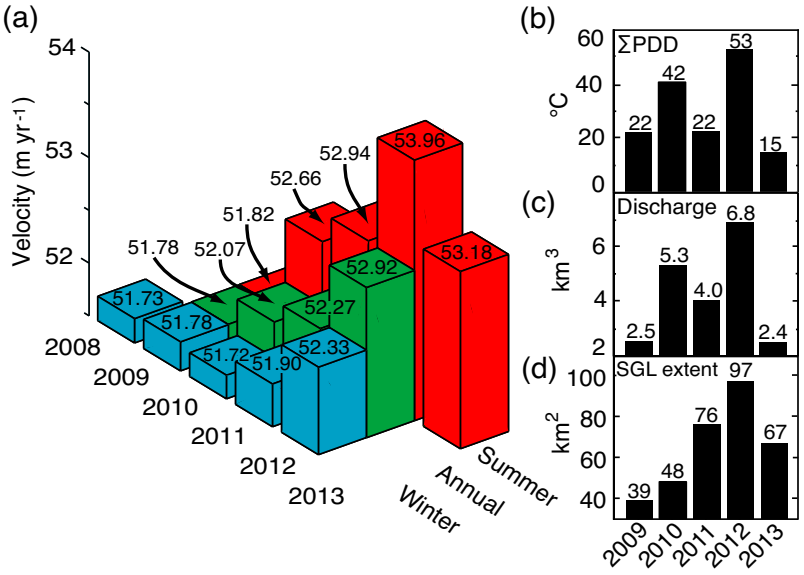

Figure 7.4: (a) Mean winter, annual and summer velocities at S10 between 2009 and 2013, (b) the PDD sum at S10, (c) the total annual proglacial discharge at Watson River Bridge, and (d) the areal extent of high-elevation SGLs (those above 1400 m a.s.l.) in our study area. The data contributing to subplot (a) are listed in Table 7.1. Correlation coefficients between these variables are listed in Table 7.2.

It is hypothesied that although the observations of net flow acceleration at S10 and Site 7 conflict with the main conclusions of Sole and others (2013), they remain compatible with generalised glacio-hydrological theory (e.g. Röthlisberger and Lang, 1987; Hubbard and Nienow, 1997; Iken and Truffer, 1997; Fountain and Walder, 1998; Schoof, 2010) by considering the reduced likelihood of developing an effective subglacial drainage system in the ice sheet's interior. Such development will be hindered by at least two factors. First, lower rates of surface meltwater production and runoff over a shorter melt season at higher elevations results in substantially lower volumes of melt being delivered to the ice sheet's

basal drainage system (van As and others, 2012), thereby reducing the capacity of that system to develop an efficient network (Pimental and Flowers, 2010; Schoof, 2010). Second, across and above the ELA, and away from the relatively thin ablation area, ice thickness exceeds 1200 m (Fig. 7.2; Bamber and others, 2013; Lindback and others, 2014). At S10, radio echo sounding indicates an ice thickness of 1590 ± 17 m. Under these conditions high overburden pressures at the bed would theoretically force rapid ($\sim$1 hour at S10) creep closure of any subglacial channel or cavity not completely pressurised to overburden (e.g. Nye, 1953; Hooke and others, 1990; Chandler and others, 2013). This compares with several days for creep-closure of ice of a few hundred meters thickness at the margin (Nye, 1953; Chandler and others, 2013). Both of these inferences are supported by recent observations. Repeat tracing experiments suggest that (i) an efficient, channelised subglacial drainage system does develop during the melt season up to at least 41 km from the ice margin, (ii) that this system is pressurised more than 7 km from the margin, and (iii) that an inefficient, distributed drainage system is likely to dominate further inland (Chandler and others, 2013). Furthermore, at two sites, 17 and 34 km from the ice margin, Meierbachtol and others (2013) observed continuously high borehole water-pressures, which, although spatially limited, are inconsistent with drainage through an extensive network of low-pressure channels. Given these theoretical inferences and limited observations from up to 50 km from the ice margin it is plausible that the mechanism of self-regulation invoked by Sole and others (2013) across the ablation area may not be prevalent at higher elevations within the ice sheet's interior.

The five contrasting melt seasons analysed in this study provide an opportunity to examine the dynamic response of the GrIS's interior to variations in atmospherically-forced melt, which is characterised using positive degree-days (PDDs) and proglacial discharge (Fig. 7.4). For the five melt seasons (2009 to 2013) the respective total PDDs at S10 were 21.7,

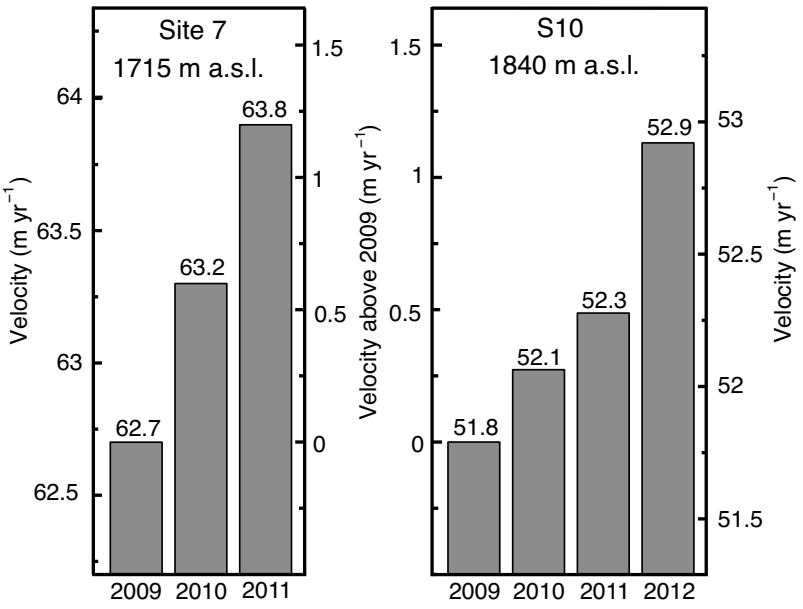

Figure 7.5: Annual velocity at Site 7 of Sole and others (2013) and S10. The centre axes show the speed above the respective 2009 velocity. To keep consistency with Sole and others velocities were calculated from May in the labeled year to May in the following year.

42.0, 21.9, 53.1 and 15.1° C (Fig. 7.4b). The corresponding totals in proglacial discharge of 2.5, 5.3, 4.0, 6.8 and 2.4 km^3 show a similar inter-annual variation as the PDD sum ($r^2 = 0.96, p = 0.01$), with the exception of 2011 when discharge was disproportionately large (Fig. 7.4c; Table 7.2). The fastest annual and summer flow at S10 occurred in 2012: a record melt season (Nghiem and others, 2012) distinguished by unprecedented proglacial discharge and the highest PDD sum at S10 (Fig. 7.4). In contrast, the year with the lowest annual and summer velocity, 2009, had the second lowest PDD sum (21.9°C) and proglacial discharge (Fig. 7.4). Comparing the S10 velocities during the two coldest years (2009 and 2013) reveals that the PDD sum cannot, however, fully explain the inter-annual variations in velocity at S10. During 2009 (second coldest) velocities were low and the seasonal variation was minimal (0.1 %). In contrast, the coldest summer of 2013 was the

second fastest with a distinct, albeit lagged, seasonal acceleration (Figs. 7.3 and 7.4).

Table 7.2: Correlation coefficients (r) between selected measurements. The probability (p), given in brackets, is the likelihood that the correlation coefficient can be explained by random variation. Text in bold indicates that the correlation coefficient is significant at the $p < 0.1$ level. The sample size is $n = 5$ years except where an asterisk (*) indicates $n = 4$ years.

	Σ PDD	Discharge	High-elevation SGL extent
Σ PDD	N/A	**0.96 (0.01)**	0.43 (0.47)
Discharge	**0.96 (0.01)**	N/A	**0.96 (0.01)**
High-elevation SGL extent	0.43 (0.47)	0.60 (0.29)	N/A
Mean summer velocity	0.52 (0.37)	0.66 (0.23)	**0.93 (0.02)**
Preceding winter mean velocity	-0.30 (0.62)	-0.30 (0.62)	0.24 (0.70)
Subsequent winter mean velocity	0.64 (0.36)*	0.71 (0.29)*	**0.92 (0.08)***
Annual (May to May)	0.74 (0.25)*	0.87 (0.13)*	**0.96 (0.04)***
Annual (Sep to Sep)	0.27 (0.66)	0.37 (0.55)	0.79 (0.11)

A lack of observable crevasses, moulins and seasonal surface uplift (Fig. 7.6) infers that water is not necessarily accessing the bed directly beneath S10. Nevertheless, strain perturbations can be transmitted on the order of tens of kilometres by longitudinal (along-flow) stress-gradient coupling (Kamb and Echelmeyer, 1986; Hindmarsh, 2006; Price and others, 2008). Hence, the flow perturbations at S10 could have their origin down-glacier where the presence of crevasses, rapidly-draining SGLs and moulins indicate that surface meltwater is directly accessing the bed. Although melt is inherently diffuse, the delivery of surface water to the bed is focused — in both space and time — by SGL drainage. Indeed, it is widely recognised that SGLs, which have formed at successively higher elevations during warmer summers over the last three decades (Fig. 7.7 Liang and others, 2012; Howat and others, 2013; Fitzpatrick and others, 2014), play an important role in establishing the hydraulic pathways that enable surface water to directly access the ice-bed interface through kilometre-thick ice (Das and others, 2008; Doyle and others, 2013; Tedesco and others, 2013, Chapter 5).

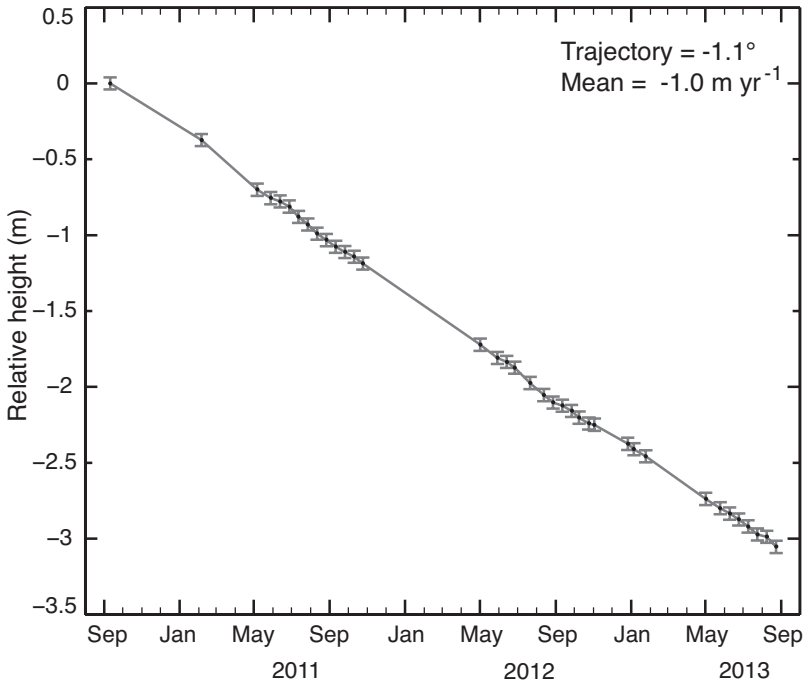

Figure 7.6: The relative height of the S10 GPS antenna between September 2010 and September 2013 with error bars indicating the uncertainty in the height measurements of ±0.04 m. The mean rate of height change and the trajectory are given.

In West Greenland, the elevation of the highest SGL increased from 1670 m a.s.l. in the mid-1980s to above 1800 m a.s.l. in 2011 — representing an inland expansion of SGLs of 30 km that closely tracked the rising ELA (Howat and others, 2013). The elevation of the highest SGL in our study area increased from 1689 m a.s.l. in 2009 to 1790 m a.s.l. in 2010 and 1827 m a.s.l. in 2011, where it reformed in 2012 and 2013 (Fig. 7.7). That no higher SGLs formed during the record melt year of 2012 compared to 2011 suggests a limit or pause in the inland expansion of SGLs. Although it has been suggested that the paucity of surface depressions in the interior may hinder the formation of SGLs (Howat and others, 2013), it is also possible that the storage capacity of the firn has not yet been attained at these higher elevations (Harper and others, 2012). That the same high-elevation SGLs

formed again in the relatively cold year of 2013 does, however, suggest that SGLs are self-sustaining — possibly through deepening of the lake bed by increased radiation absorption, and through the establishment of a surface drainage network which feeds them and persists from year to year. Hence, once established SGLs appear to reform readily in the same, high-elevation surface depressions in subsequent summers even if significantly cooler.

In our study area, the spatial extent of SGLs above 1400 m a.s.l. (hereafter termed the high-elevation SGL extent), which increased each year from 2009 to 2012, appears to scale with ice motion at S10 (Fig. 7.4). The high-elevation lake extent shows significant positive correlation ($r^2 > 0.9; p < 0.1$) with mean summer, winter and annual velocities at S10 (Table 7.2). The rate of inland SGL expansion even surpassed increases in atmospheric forcing. For example, despite a lower PDD sum in 2011, high-elevation SGLs were still more extensive than they were in 2010 (Fig. 7.4). Annual total proglacial discharge was also disproportionately large in 2011 relative to the PDD sum (Fig. 7.4). This disparity can be explained by abnormally low snowfall during the previous winter (Box and others, 2011) and the progressive inter-annual decline in surface albedo (Box and others, 2012), which increased melt generation and runoff disproportionately at high elevations during 2011 (Box and others, 2011; van de Wal and others, 2012). Furthermore, the areal extent and upper limit of high-elevation SGLs was abnormally large during the relatively cold 2013 melt season (Figs. 7.4c and 7.7). Hence, together with an inland migration of the ELA (van de Wal and others, 2012) and the associated decrease in storage and refreeze potential of the firn, it can be suggested that low snowfall and surface albedo were responsible for the disproportionate increase in melt and SGL formation at high elevations between 2009 and 2013.

As SGLs expand inland, surface water may reach new areas of the bed, increasing the energy flux to this potentially frozen zone. The release of latent and sensible heat by surface

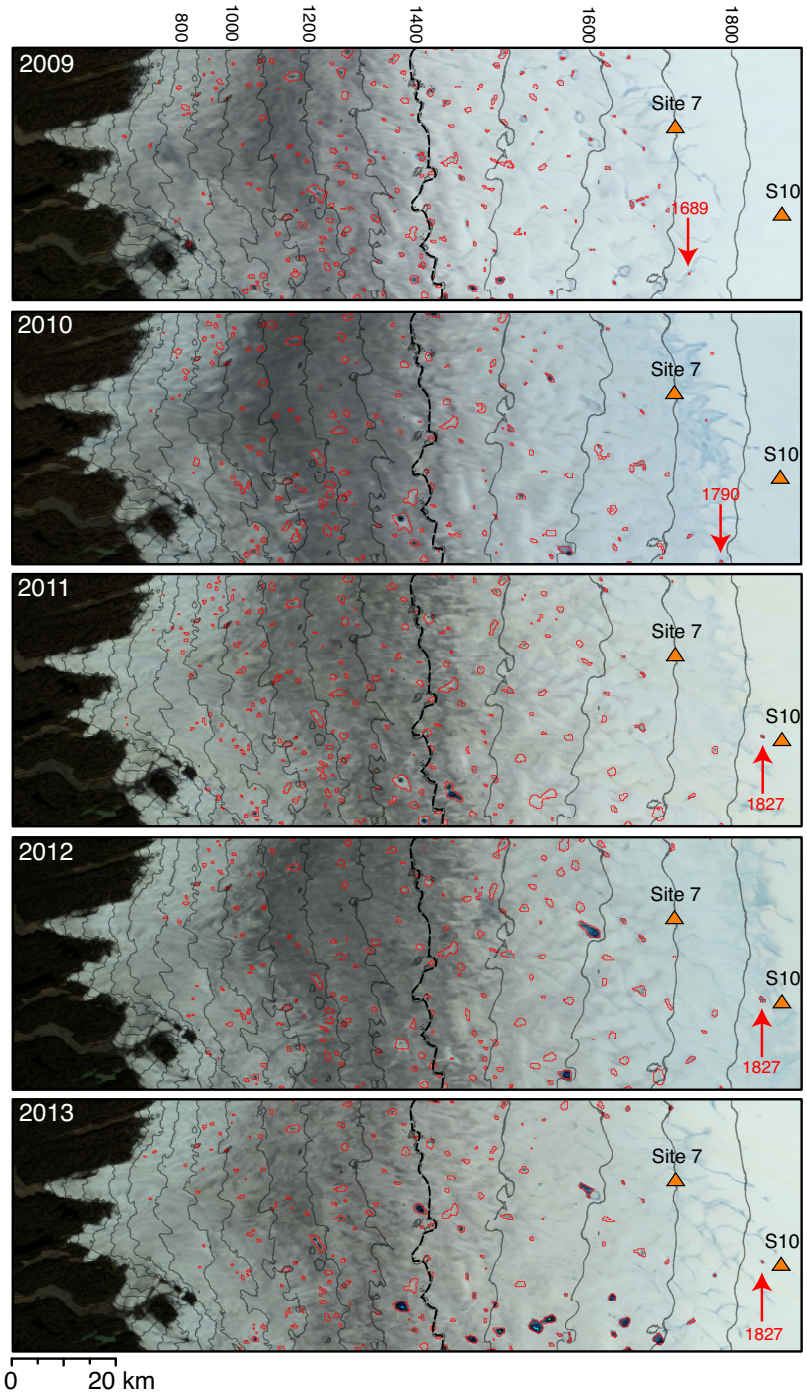

Figure 7.7: The maximum extent of supraglacial lakes (outlined in red) between 2009 and 2013. The red arrow indicates the highest lake. The background MODIS images were selected to portray the highest elevation lake in each year and were acquired on 8 August 2009, 20 August 2010, 17 August 2011, 21 July 2012 and 11 August 2013 respectively.

water refreezing has recently been hypothesised to warm the ice, reducing its viscosity and enhancing internal deformation (Phillips and others, 2010). The increase in mean winter velocity at S10 following the exceptional 2012 melt season (Fig. 7.4) — which cannot be directly attributed to surface melt water accessing the bed during winter — could reflect such changes in rheology or basal conditions (Phillips and others, 2010). That annual ice velocity was faster at S10 during the record melt year of 2012 compared to the relatively cold year of 2009 is at odds with the observations of Tedstone and others (2013) from the ablation area, which extend the time series of Sole and others (2013) into 2012. Furthermore, the subsequent winter (2012/13) at S10 was substantially faster ($52.33 \pm 0.02\,\mathrm{m\,yr^{-1}}$) than all previous winters (mean = $51.75 \pm 0.02\,\mathrm{m\,yr^{-1}}$) and even exceeded the 2009 summer mean. These results suggest that the exceptional runoff during the 2012 melt season caused a fundamental change in basal conditions and ice dynamics in the vicinity of S10. Possible explanations include increased water storage at the bed following the 2012 melt season resulting in sustained higher subglacial water pressures and reduced basal traction, or increased energy flux into this potentially frozen zone, warming the ice, enhancing internal deformation and/or decoupling frozen sticky-spots. Thus, although summer flow acceleration at S10 reveals a direct response to surface meltwater production, the important observation that winter flow is also increasing suggests a longer-term structural change in the subglacial hydro-thermal regime, possibly associated with an increased flux of meltwater and energy to the ice-bed interface. Further and more direct observations (e.g. borehole instrumentation and repeat geophysical surveys to determine changes in the material and thermal properties of the bed) would be required to explain definitively why the velocity at S10 increased between 2009 and 2012, especially with regard to the increase in mean winter velocity following the exceptional melt in summer 2012.

Although the 2.2 % net velocity increase at S10 between 2009 and 2012 is modest, it should

be noted that it is has been previously assumed (e.g. Colgan and others, 2009; Colgan and others, 2012; Phillips and others, 2013) that the ice sheet's interior does not experience any variation in flow. The implicit assumption in these studies is that ice motion can be attributed to internal deformation alone, which would not be expected to vary on short, seasonal timescales. Furthermore, from mass continuity considerations, as the ice thickness at S10 (1590 m) greatly exceeds that closer to the margin, the impact of any given net change in ice flow on mass flux here will be substantially greater compared to downstream zones, nearer the ice margin. Finally, although these observations of a year-on-year increase in annual velocity are limited to just two locations above the ELA, it can be speculated that such behaviour could be pervasive over a broader lateral swath of the ice sheet's wet snow zone, since flow in this interior region may be less constrained by basal topography, which channels flow into distinct outlet units within the ablation zone (Joughin and others, 2008, 2010; Palmer and others, 2011; Fitzpatrick and others, 2013).

7.6 Conclusions

A five-year time-series of surface velocity measurements from a GPS receiver located 140 km from the ice margin reveals that seasonal variations in ice motion, of up to 8 % above the winter mean, occur at least 50 km inland from the long-term mean ELA. Summer velocities at this site reflect variations in surface melt modulated by SGL drainage. The year-on-year increase in annual velocities at S10 between 2009 and 2012 suggests that an increased penetration of water to the ice-bed interface at increasingly large distances from the ice margin is driving faster ice motion at high elevations on the GrIS.

Two distinct patterns of ice dynamic response to atmospheric forcing have now been observed. In the ablation area, Sole and others (2013) argued that channelised subglacial

hydrology regulates ice flow through reduced winter velocities following warmer, faster summers. Above the ELA, winter, summer and annual velocities all followed an increasing trend between 2009 and 2013. Finally, in accordance with Truffer and others (2005), the results presented in this chapter caution against extending observations from Alaskan glaciers (Burgess and others, 2013) as well as from the ablation zone (Sole and others, 2013; Tedstone and others, 2013) into interior regions of the Greenland Ice Sheet, where greater ice thicknesses and lower melt hinders the development of efficient subglacial drainage systems and its regulating influence on ice flow.

Acknowledgements

This research was funded by SKB-Posiva through the Greenland Analogue Project (Subproject A) and UK Natural Environmental Research Council grant NE/G005796. UNAVCO, MIT, Matt King, Katrin Lindback, and Heidi Sevestre are thanked for help with data collection and processing.

Chapter 8

Synthesis and discussion

This thesis has, in the preceding three chapters, focussed on particular sites and events that provide insight into basal hydrological controls on Greenland Ice Sheet motion. The following chapter draws upon the results of recent publications to place the three experiments presented in Chapters 5, 6, and 7 into a broader context. Finally, it identifies the limitations of our current techniques and knowledge before suggesting directions for future research.

8.1 The state of knowledge prior to 2010

At the turn of the millennium the Greenland Ice Sheet was thought to be relatively stable on millennial time scales and hydrological coupling — the subject of this thesis and many other studies over the last decade — was thought impossible for the contemporary ice sheets (e.g. Clarke and others, 1999). In 2002, the correlation between summer velocity and surface melt intensity at a site near the ELA led to the concept of a positive feedback

mechanism between atmospheric warming and basal sliding that could accelerate the ice sheet's dynamic contribution to sea level rise under a warmer climate by transporting more ice to lower, and therefore warmer, elevations (Zwally and others, 2002; Parizek and Alley, 2004). This led to widespread reporting in the media with headlines of 'Ice sheet slip-sliding away' and 'Greenland's warming ice flowing faster' (Kirby, 2002; Hotz, 2006). Such media attention put glaciology in the spotlight and encouraged the plethora of recent investigations of Greenland Ice Sheet dynamics. In 2008, Das and others captured the hydrofracture mechanism capable of establishing the surface-to-bed connection draining a large supraglacial lake in hours. Although the hydraulically driven propagation of fractures to the bed of ice masses had been considered theoretically (e.g. Weertman, 1971a,b, 1973), and had been observed on an arctic glacier (Boon and Sharp, 2003), it was not known to occur in Greenland. The observations by Das and others (2008) of the dramatic effect of rapid in situ supraglacial lake drainage events on ice sheet motion, and by Shepherd and others (2009) of the close coupling between melt and ice sheet motion, further contributed towards speculation that the ice sheet's response to climate warming would be faster than previously expected.

8.2 Progress between 2010 and 2014

Since these initial observations, our knowledge of the dynamics of land-terminating regions of the Greenland Ice Sheet has developed considerably. The following sections discuss recent developments within the main research themes relevant to this thesis. It discusses how the research aims, which are listed in Section 1.5, have been met by the work presented in this thesis within the framework of contemporaneous studies.

8.2.1 Variations in ice motion

Surface velocities recorded by the GPS receivers installed across Russell Glacier catchment (Fig. 3.1) are consistent with the characteristic seasonal cycle identified by previous studies: an initial maximum at melt onset is typically followed by gradual deceleration into mid-summer and an all year low in autumn when declining melt inputs are easily accommodated by the drainage system developed over the course of the summer (e.g. Fig. 4.2, Bartholomew and others, 2010, 2011a; Hoffman and others, 2011; Colgan and others, 2011; Bartholomew and others, 2012; Colgan and others, 2012). Following the cessation of melt, velocities then increase steadily over the course of winter, presumably as the remaining basal water pressurises as conduits close (e.g. Fig. 4.13, Joughin and others, 2010; Fitzpatrick and others, 2013).

Transient acceleration events occur throughout the melt season whenever the drainage system is challenged by increasing water inputs (e.g. Fig. 4.6, Bartholomew and others, 2012). Such acceleration events occur due to high melt rates, rainfall events (e.g. Fig. 6.4), initiation of drainage into moulins (e.g. Fig. 4.2) and rapid supraglacial lake drainage (Fig. 4.3; Chapter 5). Once established shortly after the melt onset peak, diurnal velocity variations prevail throughout the melt season, albeit generally declining in amplitude as the melt season progresses (e.g. Fig. 4.6). Diurnal velocity variations are closely coupled to surface melt (e.g. Fig. 4.6, Shepherd and others, 2009) and the analysis presented in Chapter 4 demonstrates that the lag time between melt and velocity declines by ~ 3 hours over the course of the melt season as the ice sheet's supra-, en- and sub-glacial hydrological systems evolve to greater efficiency (e.g. Fig. 4.7). The results presented in Chapter 4 and 5 also confirm that peak velocity typically coincides with peak rates of surface uplift, not maximum vertical displacement (Fig. 4.10), which was interpreted by Iken (1981) as indicative of cavity opening at the bed. Throughout the melt season, short periods of low

melt result in low daily-averaged velocities and reset the subglacial drainage system: when high melt rates return a 'mini spring event' commonly occurs with velocities temporarily higher than during the preceding period of high melt rates. All these observations are consistent with the theoretical findings of Schoof (2010) who concluded from modelling that:

> 'Drainage channelization under glaciers and ice sheets suppresses the ability of steady surface water supply to cause further ice acceleration, but faster ice flow can be caused instead by water input variations.' (Schoof, 2010, p. 805).

Consistent with previous studies (e.g. Engelhardt, 1978; Gordon and others, 1998; Harper and others, 2002, 2005, 2007) the relationships between borehole water pressure, regional subglacial water pressure and horizontal surface velocity are less easy to discern. The relationship appears to be time variant with localised borehole water level sometimes, but not always, reflecting regional water pressure which in turn either leads or lags peak horizontal surface velocity by varying degrees at different stages in the melt season. As explained previously (e.g. Harper and others, 2007) the often disparate relationship between borehole water level and velocity can also be explained by the different spatial scales over which their governing processes operate. Ice velocity is theorised to be driven by variations in regional basal traction whereas borehole water pressure represents a discrete, localised measurement of a property which is likely to have great spatial variability. During high-magnitude events, like the late August event in 2011, localised borehole water pressure appears to be in unison with regional basal water pressures and widespread acceleration ensues (e.g. Fig. 6.8, Gordon and others, 1998; Harper and others, 2007).

8.2.2 Ice sheet acceleration driven by supraglacial lake drainage

This thesis has extended our knowledge of rapid in situ supraglacial lake drainage events, providing the most in depth geophysical experiment of this phenomenon to date that will provide modelling studies (e.g. Bougamont and others, 2012; Dow and others, 2012) with essential parameters.

The detailed GPS measurements presented in Chapter 5 reveal that the rapid acceleration during lake drainage was predominantly caused by fracture motion, which reversed and is therefore not indicative of a long-lasting displacement of ice towards the margin (Fig. 5.10). Such reversal in ice motion is evident in all the existing studies of lake drainage (Das and others, 2008; Bartholomew and others, 2012; Tedesco and others, 2013) yet had remained unexplained until the detailed observations from four GPS receivers presented in Chapter 5. This finding is important as it reveals that a substantial component of measured ice motion during lake drainage events is not attributable to basal sliding. The long-term impact of such events on the annual ice flux has yet to be ascertained. This question was partially addressed by Tedesco and others (2013) who asserted that the more rapid and higher volume lake drainage events had a more rapid and higher magnitude dynamic impact. Unfortunately, however, the comparisons made by Tedesco and others (2013) of the dynamic impact of rapid in situ lake drainage events with overland drainage into a moulin still do not reveal the long term impact of lake drainage events on net ice sheet motion.

Hoffman and others (2011) argued that 83% of 62 lake drainage events identified from satellite imagery were not detectable in the velocity records from a nearby GPS transect, suggesting that the dynamic impact of lake drainage events must be spatially and temporally limited. The vast majority of these lakes were, however, small and the rapid

drainage of larger lakes (> 1 km in diameter) in their study, of which there were three, were all associated with high magnitude acceleration events that represented peak annual velocities. Notwithstanding this observation, Hoffman and others (2011, p. 9) argued that despite 'such dramatic transient effects, these presumed lake drainage events accounted for at most 5% of the total summer motion at any station.' Assessing the importance of lake drainage events on ice flow by quantifying the transient effects is not, however, assessing the full picture. The full impact of lake drainage events includes the long-lasting effects of the moulins and subglacial hydraulic pathways created by lake drainage events that remain open for the remainder of the melt season (e.g. Das and others, 2008; Doyle and others, 2013, Chapter 5). To date no study has specifically addressed this question.

Nevertheless, as the lake drainage event reported in Chapter 5 falls within the time period of the study of Sole and others (2013) we may assert that within the ablation zone lake drainage events did not lead to a discernible acceleration in annually-averaged flow between 2009 and 2011. It could also be argued that lake drainage events, and the continued drainage into the moulins they create, have established efficient subglacial drainage — which itself remains a contentious issue especially under kilometre-thick ice — causing an extra slow-down during winter, and a subsequent reduction in annual velocities. At higher elevations, however, the measurements presented in Chapter 7 demonstrate that ice velocities at two GPS sites above the ELA accelerated over the same time-period. Annually-averaged flow at the highest site increased by 2.2% between 2009 and 2012. This acceleration in the accumulation area shows strong positive correlation with the expansion of supraglacial lakes to higher elevations, which even outpaced the increase in regional melt (Fig. 7.4 and Table 7.2). These observations support the hypothesis that the observed expansion of supraglacial lakes to higher elevations in warmer years (Sundal and others, 2009; Liang and others, 2012; Howat and others, 2013; Fitzpatrick and others, 2014) would

lead to an inland migration of velocity variations.

The southwestern sector of the Greenland Ice Sheet accounts for 60% of all the 'fast' (< 1 day) supraglacial lake drainage events in Greenland (Selmes and others, 2011). Hence, observations of supraglacial lake dynamics and resulting ice motion from the southwestern sector may not be applicable to the rest of the ice sheet margin, especially the south-east where steep surface slopes and heavy crevassing limits the abundance of surface lakes.

8.2.3 Melt-induced acceleration

In 2007 the IPCC stated:

> "Data are not available to assess whether effects of increased surface melting in Greenland have been transmitted to the bed and contributed to ice flow acceleration." (Lemke and others, 2007, p. 368)

These data are now available, and the short answer to this question is yes. Increased surface melt has accelerated ice flow, albeit only at higher elevations. The evidence for this acceleration is, however, still limited to just two GPS sites in the accumulation area (see Chapter 7). Sites below the equilibrium line show no long-term acceleration, and Sole and others argue that increased melt may even drive deceleration as the subglacial hydrological system becomes more efficient.

The concern that increased melt would accelerate ice flow — a positive feedback mechanism hypothesised to enhance Greenland's contribution to global sea level rise (Zwally and others, 2002; Bartholomew and others, 2010) — has since been questioned by several studies that have argued the ice sheet's subglacial hydrological system will adapt to increased melt inputs (Sole and others, 2013; Tedstone and others, 2013). These observations support previous hypotheses (e.g. Shepherd and others, 2009; Schoof, 2010; Sundal and others, 2011)

that predicted that subglacial hydrology would regulate annual ice velocities in Greenland in a similar manner as that which occurs on smaller valley glaciers (e.g. Anderson and others, 2004; Truffer and others, 2005). In the ablation zone, and on Alaskan glaciers, it is argued (Burgess and others, 2013; Sole and others, 2013; Tedstone and others, 2013) that the observed positive correlation between summer velocity and melt intensity (Zwally and others, 2002) is offset (and sometimes more than offset) by an ensuing reduction in winter velocities.

Sole and others posited that faster, warmer summers are followed by slower winters due to the development and persistence of a larger and more extensive channelised subglacial drainage system, which persists into winter and efficiently drains areas of high basal water pressure — increasing subsequent ice bed coupling and traction. Although never mentioned in Zwally and others (2002), the mediation of annual velocities by reduced winter velocities following faster, warmer summers is evident in the dataset they presented (Fig. 8.1). The cumulative additional displacement above the winter mean of 1.6 m was greater during the relatively cool year of 1997 compared to the warm years of 1998 (1.1 m) and 1999 ($\sim$0.7 m). (Note that the 1999 record is incomplete and a conclusive comparison cannot be made for this year.) This regulation of annual velocities by efficient subglacial drainage is hypothesised to mediate the response of the ice sheet to the predicted increase in surface meltwater delivery to the bed (Sole and others, 2013). Although Sole and others (2013) and Burgess and others (2013) invoke the alpine analogue to explain their results from the ablation zone and arctic valley glaciers, several arguments have been proposed to suggest that it may not hold under thicker ice with shallower surface slopes.

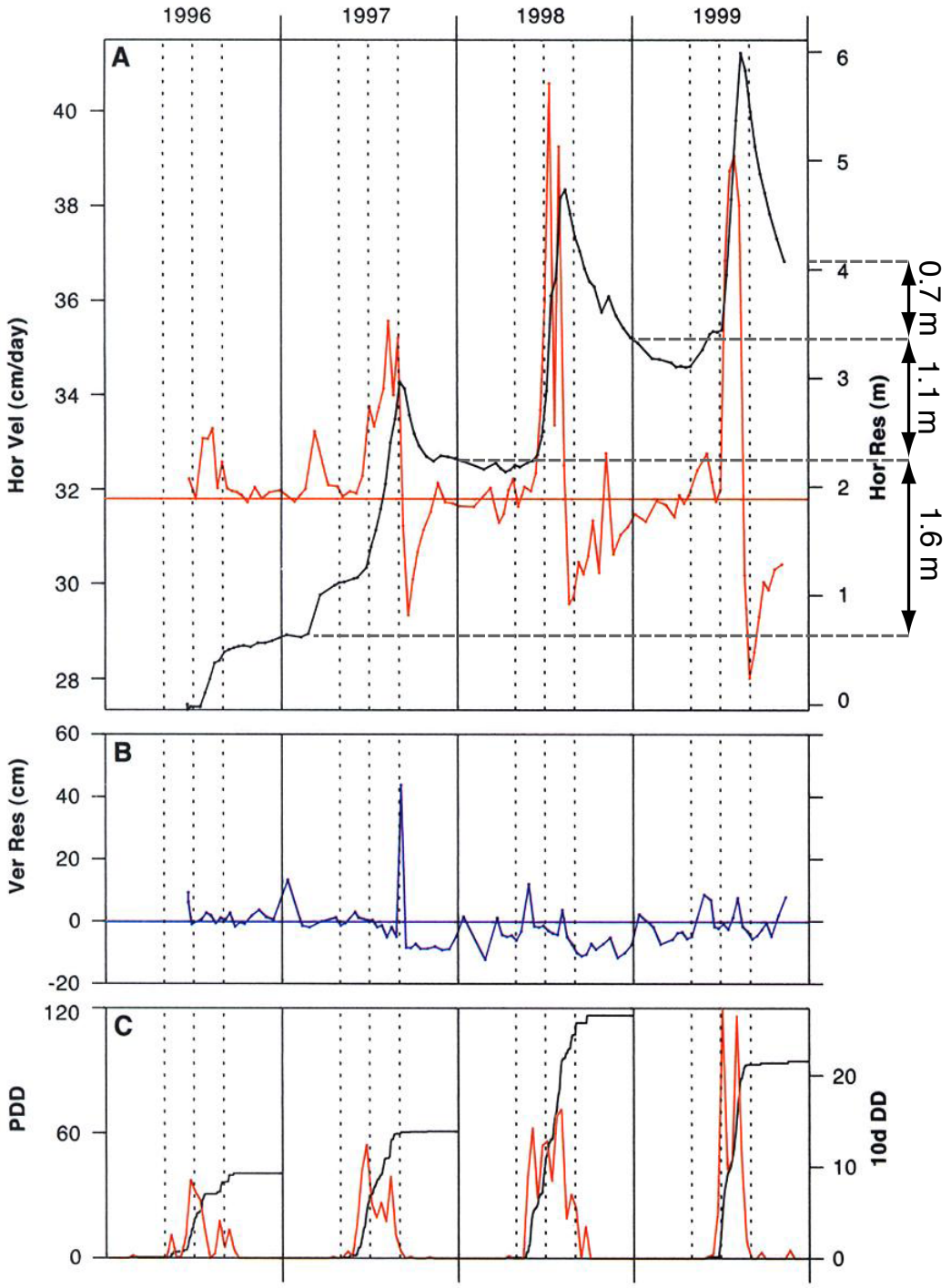

Figure 8.1: Annual displacement above the winter mean at Swiss Camp, located 35 km from the margin, annotated on Figure 1.3. The subplots compare (a) horizontal ice velocity with (b) relative vertical ice motion and (c) PDDs and cumulative PDD. Adapted from Zwally and others (2002).

8.2.4 How applicable is the alpine analogue?

Several previous studies have argued that the ablation area and land-terminating outlet glaciers of the Greenland Ice Sheet respond to melt inputs in a manner analogous to alpine glaciers, with a late-summer slowdown caused by the development of efficient subglacial drainage, leading to lower basal water pressures and increased basal traction (Colgan and others, 2009; Bartholomew and others, 2010, 2011a; Sole and others, 2013). Although the alpine analogue appears to hold for the outlet glaciers and ablation area (e.g. Sole and others, 2013), there are significant geometrical differences between the Greenland Ice Sheet and smaller alpine and arctic valley glaciers that should be considered before the model is applied to the whole ice sheet. First, ice thicknesses on the Greenland Ice Sheet far exceed those of smaller valley glaciers (Bamber and others, 2013; Lindback and others, 2014). As a result the basal thermal regime is likely to be significantly different and creep closure rates are expected to be much faster (Bartholomaus and others, 2008; Chandler and others, 2013). Second, the melt season is substantially shorter and less intense on the Greenland Ice Sheet, especially at higher elevations and latitudes, compared to typical alpine and arctic valley glaciers. Lower rates of water input would theoretically hinder the development of efficient channelised drainage systems (e.g. Schoof, 2010). Furthermore, surface and bed slopes are typically much lower for the ice sheet compared to valley glaciers, and this would hinder the development of efficient subglacial drainage by limiting conduit expansion caused by frictional heating (e.g. Meierbachtol and others, 2013). These inferences caution against extending patterns observed in the ablation area of the Greenland Ice Sheet (Sole and others, 2013; Tedstone and others, 2013) and on Alaskan glaciers (Truffer and others, 2005; Burgess and others, 2013) to higher elevations on the Greenland Ice Sheet, where greater ice thicknesses, lower melt rates and shallower surface slopes theoretically hinder the development of efficient subglacial drainage systems, and their preservation beyond

the melt season. Until further data are collected these inferences will, however, remain speculative.

The observation of acceleration at S10 and Site 7 of Sole and others (2013) presented in Chapter 7 demonstrate that the alpine analogue is, at the least, not universally applicable. The results presented by Sole and others (2013) and in Chapter 7 from a single transect over four years (2009 to 2012) are, however, spatially and temporally limited. The observed correlation between ice velocities and the expansion of high-elevation supraglacial lakes is limited to two sites: S10 and Site 7 of Sole and others (2013). Further observations from different glacier catchments must be undertaken to check these results are not just specific to Russell Glacier catchment. They are also based solely on surface GPS observations and inferring basal changes is wholly speculative. It should also be noted that as the ablation area expands under a warmer climate, the zone experiencing late-summer or winter slow-down could also expand. This hypothesis could be tested by using the same methodology as this thesis.

8.2.5 The contribution of remote sensing measurements

A comprehensive study of changes in surface ice velocity across Greenland's outlet glaciers revealed that the majority of land-terminating regions decelerated between 2005 and 2010:

> 'Most (70%) of the land-terminating glaciers [in Greenland] with a notable trend slowed during 2005 to 2010 — a continuing trend for half of them. The scale of these changes, however, is close to the measurement error and seasonal variability (Joughin and others, 2008), and orders of magnitude smaller than changes seen on many fast-flowing glaciers.' (Moon and others, 2012, p. 576).

These results support the arguments made by Sole and others (2013) that the basal drainage system of Greenland's outlet glaciers adapts to an increased surface water flux resulting in a net slowdown. Currently-available remote sensing observations, however, are not well-suited to detecting small changes in ice velocity on the Greenland Ice Sheet, especially at higher elevations. Satellite imagery is typically only available at long (e.g. 11 day) sampling intervals with only the poor resolution imagery — that is unsuitable for deriving velocity maps (e.g. MODIS) — available daily (Fitzpatrick, 2013). Furthermore, velocity maps are usually impossible to derive for the accumulation area due to a lack of features to track or a lack of coherence in InSAR measurements (Joughin and others, 2010). Accordingly, many remote sensing studies are restricted to close to the ice margin (e.g. up to 40 km inland for Sundal and others, 2011), with very few remote sensing studies extending further up-glacier during the melt season (InSAR methods are able to extend further up-glacier during winter when there is no melt, e.g. Joughin and others, 2010). The spatial and temporal variations in velocity across Russell Glacier catchment revealed by Palmer and others (2011) are, however, a unique exception. Palmer and others exploited a unique overlap of the ERS satellites to map velocities over an unprecedented, and to date unrepeated, spatial scale and detail (see Fig. 1.9). Subsequent radar measurements of ice thickness and bed elevation by Lindback and others (2014) demonstrate that the discrete fast-flow units identified by Palmer and others correspond to the locations of subglacial valleys.

Remote sensing measurements are also limited by their accuracy, which is typically ± 5 m yr^{-1} (Fitzpatrick and others, 2013). Hence, it is unsurprising that the acceleration at S10 described in Chapter 7 was not detected using satellite-derived velocity maps. Dual-frequency GPS measurements remain the only method for determining such small changes in ice velocity in the ice sheet's interior. More GPS-based investigations akin to the methodology presented in Chapter 7 are required to examine zonal variations in ice velocity. Investiga-

tions should, for example, be undertaken to determine if acceleration is also occurring in the interior of other glacier catchments in Greenland: it is likely that such measurements are already being pursued.

Given that GPS measurements of ice motion (e.g. Hoffman and others, 2011; Bartholomew and others, 2012, Chapters 4 and 5) reveal that ice velocities vary over short timescales it is difficult to accurately attribute velocity variations averaged over long time periods (e.g. 11 days) to specific processes or events. Dual-frequency GPS measurements of ice motion are therefore also necessary to investigate variations in ice motion over the time scale on which the driving mechanisms operate.

8.3 Ice sheet response to a warmer, wetter climate

Several changes have taken place across Russell Glacier catchment over the last 20–30 years. Surface mass balance shows a significant decrease between 1990 and 2011 at least within 10 km of the margin (van de Wal and others, 2012). Meanwhile, supraglacial lakes expanded to higher elevations (Sundal and others, 2009; Liang and others, 2012; Howat and others, 2013; Fitzpatrick and others, 2014) and albedo persistently declined between 2000 and 2011 (Box and others, 2012). These changes are consistent with warming temperatures over Greenland (Box, 2002; van As and others, 2012) and are coincident with a slight increase in ice flow above the equilibrium line (Chapter 7) and little change below it (van de Wal and others, 2008; Sole and others, 2013).

The high frequency of extreme melt years between 2000 and 2012 (e.g. 2003, 2007, 2010 and 2012), the increasing trend in annual total melt, and the decrease in albedo between 2000 and 2012 are attributed to a persistently negative North Atlantic Oscillation (NAO) anomaly, which favoured the occurrence of anti-cyclonic conditions over Greenland causing

increased short-wave radiation absorption and lower rates of snowfall (Tedesco and others, 2011, 2012; van As and others, 2012; Box and others, 2012; Hanna and others, 2014). The observations presented in Chapter 6 demonstrate that cyclonic weather conditions can also drive high-magnitude melt and acceleration events. Many studies (e.g. van den Broeke and others, 2009; Schuenemann and Cassano, 2010) predict that Greenland's climate will become wetter and cloudier in the future, yet few studies have considered how this change will influence melt and ice dynamics.

Given the effect of rainfall events on alpine glaciers (e.g. Barrett and Collins, 1997; Collins, 1998; Gordon and others, 1998; Gudmundsson and others, 2000) it is surprising that so few studies to date have considered the implications of a warmer, wetter and cloudier climate over Greenland. Precipitation over Greenland is predicted to increase by 26% by the end of the twenty-first century as precipitable water in the atmosphere increases in response to higher air and ocean temperatures and reduced sea ice cover (Schuenemann and Cassano, 2010; Fettweis and others, 2011). North Atlantic storm tracks are also expected to shift north, increasing the frequency of cyclonic weather systems that track over the ice sheet. Baffin Bay cyclones similar to the weather pattern behind the late August 2011 event described in Chapter 6, are, for example, predicted to increase from 3% of days in 1961-99 to 4% of days in 2081-2100 (Schuenemann and Cassano, 2010). Other cyclonic weather patterns are expected to increase by similar amounts. Warmer air temperatures would ensure that a larger fraction of this increasing precipitation will fall as rain in the future (Ettema and others, 2009; Box and others, 2012; Franco and others, 2013; van den Broeke and others, 2009). Across Russell Glacier catchment, net longwave radiation receipt peaks in August due to increased cloudiness, which absorbs and re-radiates incoming longwave radiation back to the surface, and a melting ice surface, which negates the emission of longwave radiation from the surface (van den Broeke and others, 2008a). In the future,

this aspect of Greenland's surface energy balance may become more important as cyclonic activity increases along with a rise in precipitable water in the atmosphere and warmer air temperatures.

Schoof (2010) hypothesised that the expected increase in rain events over Greenland would lead to ice sheet acceleration and also speculated that a shift to a wetter climate may have played a role in the rapid demise of the Laurentide Ice Sheet. Chapter 6 demonstrated that rainfall events driven by cyclonic weather systems produce large quantities of surface melt (up to 15% of the annual total) and rainfall, which can overwhelm the glacier's hydrological system, driving enhanced basal motion. During the late August 2011 event melt was widespread (extending at least 140 km inland) and atypically sustained through the day and night, resulting in acceleration that exceeded the magnitude and spatial scale of other perturbations to the basal system (e.g. during the spring event or rapid supraglacial lake drainage).

8.4 Directions for future research

The attention that land-terminating ice sheet dynamics has received from the public and scientific community may abate in the coming decade in response to the wealth of publications that have furthered our understanding, and have overall downplayed the significance of the dynamic contribution of land-terminating regions of the ice sheet to sea level rise. Nevertheless, important concerns remain, in particular the dynamic response of the interior ice sheet to climate warming. Chapter 7 addressed this issue but observations from two sites can only be considered as a beginning: more observations are required.

Future studies should be directed at furthering our understanding of basal processes and conditions in Greenland, especially under thick ice. Continuous or repeat radar experi-

ments, seismic surveys and borehole instrumentation would all help reduce the number of assumptions in ice sheet models.

In accordance with Lüthi (2013), gaining new insights into the relationship between subglacial water pressure and ice motion will require sustained and coordinated efforts. Studies involving single boreholes and a limited number of GPS receivers are unlikely to reveal new knowledge of how these systems work. Measurements of water level in single boreholes (e.g. Lüthi and others, 2002; Smeets and others, 2012; Meierbachtol and others, 2013) provide a limited picture of the regional basal water pressure and multiple boreholes (e.g. Hubbard and others, 1995; Harper and others, 2007) are desirable if we are to determine the physical relationship between surface water inputs, subglacial water pressure and the resulting uplift and acceleration. Instrumentation of multiple boreholes as previously undertaken on Alpine and Arctic glaciers (e.g. Hubbard and Nienow, 1997; Gordon and others, 1998; Harper and others, 2007) should therefore be repeated in Greenland; this requires substantial logistical effort.

Critical to the response of ice flow to surface water inputs is whether the ice sheet is underlain by hard bedrock or soft sediment. The presence of deforming sediment at the ice-bed interface can have a strong influence on basal motion by reducing basal roughness and facilitating flow by sediment deformation (Alley and others, 1986; Boulton and Hindmarsh, 1987; Smith and others, 2013). Previous studies (e.g. Bartholomew and others, 2010; Schoof, 2010; Hewitt, 2013; Shannon and others, 2013) assumed that the Greenland Ice Sheet rests on a hard-bed, yet all published observations indicate the presence of mechanically-weak sediment (Clarke and Echelmeyer, 1996; Booth and others, 2012; Wittlinger and Farra, 2012; Dow and others, 2013; Christianson and others, 2014; Walter and others, 2014). Proglacial discharge that is characterised by a high sediment load (Bartholomew and others, 2011b; Cowton and others, 2012, 2013; Hasholt and others,

2013) further suggests the presence of sediments under the Greenland Ice Sheet. The role of sediment deformation in Greenland Ice Sheet motion requires further investigation, and fieldwork should be undertaken to characterise the material properties of the bed.

The basal thermal regime has received even less attention than the geological controls on ice sheet flow. Whether the ice sheet is frozen to its bed remains an important unanswered question that will determine how the Greenland Ice Sheet will respond to the observed, and expected, expansion of surface melt to higher elevations. If the inland expansion of melt and supraglacial lakes thaws frozen sticky spots then the ice sheet will respond much faster than if the bed is already at the pressure melting point. Furthermore, borehole instrumentation should be undertaken to test whether the hypothesised warming of the ice sheet en- and sub-glacially by the sensible and latent heat released by surface water freezing, is enhancing rates of internal deformation in Greenland (Phillips and others, 2010, 2013).

Further research is also required into the role of moulins in delivering surface water to the ice bed interface, including the mechanisms involved in their formation and reactivation. Previous studies (Chapter 5, Das and others, 2008; Hoffman and others, 2011) focussed on the more dramatic rapid in situ drainage of lakes, neglecting the fact that the majority of lakes drain overland into moulins. It remains unknown at what pressure moulins on the Greenland Ice Sheet operate, or the extent to which they close during the winter. Such information is important to understanding ice sheet hydrology and may provide insight into the nature of subglacial conduits.

More studies should be undertaken that combine GPS- and remote-sensing-based measurements of ice motion: these complementary techniques should be used side-by-side more frequently. High-precision, fast-repeat (e.g. daily) acquisition of satellite imagery suitable for determining glacier velocities may become available in the future. The TanDEM-X

satellite, which follows the TerraSAR-X satellite in a tandem orbit (Krieger and others, 2007) is already allowing more detailed insight into spatial and temporal changes in velocity (e.g. Fig. 6.1). Developments of other techniques for determining ice velocity that bridge between the poor temporal sampling of satellite imagery and the poor spatial sampling of GPS surveying also offer great potential. Such techniques include time-lapse (e.g. Ahn and Box, 2010) and UAV-based (Whitehead and others, 2013; Ryan and others, 2014) photogrammetry.

Much of the previous work on Greenland Ice Sheet dynamics (e.g. Shepherd and others, 2009; Bartholomew and others, 2010, 2011b,a) has reiterated studies undertaken on Alpine glaciers (e.g. Iken and others, 1983; Hubbard and Nienow, 1997; Nienow and others, 2005). This should continue but the full array of glaciological techniques should be realised (e.g. the instrumentation of multiple boreholes) and the geometric and thermal differences between Alpine glaciers and the Greenland Ice Sheet should be carefully considered.

Chapter 9

Conclusions

An efficient and robust technique for acquiring, processing and interpreting dual-frequency GPS measurements of surface ice motion was developed to determine variations in ice surface velocities on relatively slow ($\sim$ 100 m yr^{-1}) moving ice. The resulting datasets were used to investigate horizontal and vertical variations in ice motion over inter-annual to sub-hourly time-scales at a number of sites across land-terminating Russell Glacier catchment in West Greenland. Records of ice motion were compared to contemporaneous meteorological, hydrological and remote sensing datasets using specific events and sites as standalone experiments to gain insight into basal hydrological forcing.

The characteristic seasonal velocity cycle recorded by the GPS network is consistent with previous studies: an initial maximum occurs at melt onset, followed by gradual deceleration into mid-summer, and an all-year low immediately following the cessation of melt. Transient accelerations occur throughout the melt season and are caused by enhanced melt, rainfall and supraglacial lake drainage events. The fastest-moving site on the K-transect, site SHR, was used as a case study for studying variations in ice motion driven by the

diurnal melt cycle. Detailed analysis confirmed that horizontal velocity is closely coupled to surface melt with the lag between melt and velocity decreasing as the melt season progresses. Consistent with the theory of cavity opening, peak horizontal velocity coincided with peak vertical velocity not maximum vertical displacement. Ice velocity quickly responded to short periods of low melt, which presumably reset the subglacial drainage system as when high melt returned 'mini spring events' occurred, with notably higher velocities than during the preceding period.

The investigation of a combined rainfall and melt event in August 2011 provided detailed insight into basal hydrological forcing. A Baffin Bay cyclone advected warm, moist air across the southern half of the Greenland Ice Sheet driving widespread, high magnitude rainfall and melt after the end of the main melt season. The future climate over Greenland is expected to be warmer, wetter and cloudier due to an increase in precipitable water in the atmosphere and a northwards shift in North Atlantic storm tracks. Rainfall in Kangerlussuaq shows an increasing trend since 1973 and has become more temporally dispersed, occurring later in the year that it previously did. Combined, these observations and predictions portend a future where Greenlandic outlet glaciers experience rainfall/melt events evolving towards those which are currently characteristic of Alaskan glaciers.

The detection of a rapid lake drainage event in the 2009 SKB3 GPS record directed a comprehensive targeting of the same lake in 2010. This experiment involved an array of GPS receivers, water level loggers and seismometers and represents the most detailed measurement of this phenomenon to date. The datasets produced will help constrain future modelling studies of rapid in situ lake drainage events. Importantly, this study reveals that the rapid acceleration during lake drainage was largely caused by fracture motion, which reversed, and is therefore not indicative of an immediate and persistent displacement of ice towards the ice margin. The long term influence of lake drainage events on the dynamics

of the Greenland Ice Sheet may instead be the effect of continued drainage of surface water into the moulins created during rapid drainage. The establishment of moulins through kilometre-thick ice during lake drainage events may be most important at higher elevations, where surface water is able to access new, potentially frozen, areas of the bed.

Concomitant to the observed expansion of supraglacial lakes to higher elevations annually-averaged ice flow above the ELA accelerated year-on-year between 2009 and 2012. At a high-elevation interior site located 140 km from the ice margin ice flow was consistently faster during the summer than during winter, and annually-averaged velocity increased from 51.78 ± 0.01 m yr^{-1} in 2009 to 52.92 ± 0.01 m yr^{-1} in 2012 - a net increase of 2.2%.

Two distinct patterns of ice flow response to surface water inputs have now been observed. In the ablation area faster summer flow during warmer years has been argued to be mediated by reduced velocities through the following winter. At higher elevations, ice flow accelerated year-on-year between 2009 and 2012 coincident with an expansion of supraglacial lakes into this zone. Further observations are required to confirm whether these patterns hold for other areas of the ice sheet and to see whether they continue into the future. While the main objectives of this investigation have been met there remain many questions to answer about basal controls on the motion of the Greenland Ice Sheet.

References

Agassiz, L., 1847. Système glaciaire ou recherches sur les glaciers, leur mécanisme, leur ancienne extension et le rôle qu'ils ont joué dans l'histoire de la terre: Nouvelles études et expériences sur les glaciers actuels, leur structure, leur progression et leur action physique sur le sol, Victor Masson.

Ahn, Y. and J. Box, 2010. Glacier velocities from time-lapse photos: technique development and first results from the Extreme Ice Survey (EIS) in Greenland, *Journal of Glaciology*, **56**(198), 723–733.

Alexandersson, H, 2003. Korrektion av nederbörd enligt enkel klimatologisk metodik. SMHI, Meteorologi, Nr 111.

Alley, R.B., D.D. Blankenship, C.R. Bentley, and S. Rooney, 1986. Deformation of till beneath ice stream B, West Antarctica, *Nature*, **322**, 57–59.

Alley, R.B., P.U. Clark, P. Huybrechts and I. Joughin, 2005a. Ice-sheet and sea-level changes, *Science*, **310**(5747), 456–460.

Alley, R.B., T.K. Dupont, B.R. Parizek and S. Anandakrishnan, 2005b. Access of surface meltwater to beds of sub-freezing glaciers: preliminary insights, *Annals of Glaciology*, **40**, 8–13.

Alt, B. T., 1978. Synoptic climate controls of mass-balance variations on Devon Island Ice Cap, *Arctic and Alpine Research*, **10**(1), pp. 61–80.

Ambach, W., 1974. The influence of cloudiness on the net radiation balance of a snow surface with high albedo, *Journal of Glaciology*, **13**(67), 73–84.

Anderson, R.S., S.P. Anderson, K.R. MacGregor, E. D. Waddington, S. O'Neel, C.A. Riihimaki and M.G. Loso, 2004. Strong feedbacks between hydrology and sliding of a small alpine glacier, *Journal of Geophysical Research*, **109**, F03005.

van As, D., 2011. Warming, glacier melt and surface energy budget from weather station observations in the Melville Bay region of northwest Greenland, *Journal of Glaciology*, **57**(202), 208–220.

van As, D., A.L. Hubbard, B. Hasholt, A.B. Mikkelsen, M.R. van den Broeke and R.S. Fausto, 2012. Large surface meltwater discharge from the Kangerlussuaq sector of the Greenland ice sheet during the record-warm year 2010 explained by detailed energy balance observations, *The Cryosphere*, **6**, 199–209.

Bamber, J.L., R. Alley and I. Joughin, 2007. Rapid response of modern day ice sheets to external forcing, *Earth and Planetary Science Letters*, **27**, 1–13.

Bamber, J.L., R.L. Layberry and S.P. Gogineni, 2001. A new ice thickness and bed data set for the Greenland Ice Sheet 1. Measurment, data reduction and errors, *Journal of Geophysical Research Atmospheres*, **106**, 3377380.

Bamber, J. L., J. A. Griggs, R. T. W. L. Hurkmans, J. A. Dowdeswell, S. P. Gogineni, I. Howat, J. Mouginot, J. Paden, S. Palmer, E. Rignot and D. Steinhage, 2013. A new bed elevation dataset for Greenland, *The Cryosphere*, **7**(2), 499–510.

Bar-Sever, Y., P. Kroger and J. Borjesson, 1998. Estimating horizontal gradients of tropospheric path delay with a single GPS receiver, *Jounal of Geophysical Research*, **103**, 5019–5035.

Barrett, A.P. and D.N. Collins, 1997. Interaction between water pressure in the basal drainage system and discharge from an Alpine glacier before and during a rainfall-induced subglacial hydrological event, *Journal of Glaciology*, **24**, 288–292.

Bartholomaus, T.C., R.S. Anderson and S.P. Anderson, 2008. Response of glacier motion to transient water storage, *Nature Geoscience*, **1**, 33–37.

Bartholomew, I., P. Nienow, D. Mair, A. Hubbard, M.A. King and A. Sole, 2010. Seasonal

evolution of subglacial drainage and acceleration in a Greenland outlet glacier, *Nature Geoscience*, **3**, 408–411.

Bartholomew, I., P. Nienow, A. Sole, D. Mair, T. Cowton and M.A. King, 2012. Short-term variability in Greenland Ice Sheet motion forced by time-varying meltwater drainage: Implications for the relationship between subglacial drainage system behavior and ice velocity, *Journal of Geophysical Research*, **117**, F03002.

Bartholomew, I., P. Nienow, A. Sole, D. Mair, T. Cowton, M.A. King and S. Palmer, 2011a. Seasonal variations in Greenland Ice Sheet motion: Inland extent and behaviour at higher elevations, *Earth and Planetary Science Letters*, **307**, 271–278.

Bartholomew, I., P. Nienow, A. Sole, D. Mair, T. Cowton, S. Palmer and J.S. Wadham, 2011b. Supraglacial forcing of subglacial drainage in the ablation zone of the Greenland ice sheet, *Geophysical Research Letters*, **38**, L08502.

Bennartz, R., M.D. Shupe, D.D. Turner, V.P. Walden, K. Steffen, C.J. Cox, M.S. Kulie, N.B. Miller and C. Pettersen, 2013. July 2012 Greenland melt extent enhanced by low-level liquid clouds, *Nature*, **496**, 83–86.

Berthier, E., H. Vadon, D. Baratoux, Y. Arnaud, C. Vincent, K.L. Feigl, C. Ramy and B. Legrasy, 2005. Surface motion of mountain glaciers derived from satellite optical imagery, *Remote Sensing of Environment*, **95**(1), 14–28.

Blake, E.W., U.H. Fischer and G.K.C. Clarke, 1994. Direct measurement of sliding at the glacier bed, *Journal of Glaciology*, **40**, 595–599.

Boon, S. and M. Sharp, 2003. The role of hydrologically-driven ice fracture in drainage system evolution on an Arctic glacier, *Geophysical Research Letters*, **30**(18), 1916.

Booth, A.D., R.A. Clark, B. Kulessa, T. Murray, J. Carter, S. Doyle and A. Hubbard, 2012. Thin-layer effects in glaciological seismic amplitude-versus-angle (AVA) analysis:

implications for characterising a subglacial till unit, Russell Glacier, West Greenland, *The Cryosphere*, **6**(4), 909–922.

Bosmans, J.H.C., 2009. The effect of surface meltwater induced basal lubrication on the evolution of the greenland ice sheet., (PhD thesis), Master's Thesis, University of Utrecht.

Bosson, E., T. Lindborg, S. Berglund, L.-G. Gustagsson, J.-O. Selroos, H. Laudon, L. Claesson-Liljedahl and G Destouni, 2013. Water balance and its intra-annual variability in a permafrost catchment: hydrological interactions between catchment, lake and talik, *Hydrology and Earth System Sciences Discussions*, **10**, 9271–9308.

Bougamont, M.H., P. Christoffersen, A. Hubbard, A. Fitzpatrick, S.H. Doyle, S.P. Carter, H.A. Fricker and R. Pettersson, 2012. Connecting hydrology and evolving properties of subglacial sediment beneath Russell Glacier, Greenland, *AGU Fall Meeting Abstract 0595*, **1**.

Boulton, G.S. and R.C.A. Hindmarsh, 1987. Sediment deformation beneath glaciers: rheology and geological consequences, *Journal of Geophysical Research*, **92**(B9), 9059–9082.

Box, J.E., 2002. Survey of Greenland instrumental temperature records: 1873- 2001, *International Journal of Climatology*, **22**, 1829–1847.

Box, J.E., R.J. Benson, D Decker and D.H. Bromwich, 2009. Greenland ice sheet snow line variations 2000-2008, Association of American Geographers Annual Meeting, Las Vegas, NV, 22-27 March 2009.

Box, J.E. and C. Chen, 2012. Greenland Ice Sheet snowline datasets, `http://bprc.osu.edu/wiki/Greenland_Ice_Sheet_Snowline`.

Box, J.E. and K. Ski, 2007. Remote sounding of Greenland supraglacial melt lakes: implications for subglacial hydraulics, *Journal of Glaciology*, **53**(181), 257–265.

Box, J. E., J. Cappelen, C. Chen, X. Fettweis D. Decker and, D. Hall, E. Hanna, B. V. Jrgensen, N. T. Knudsen, W. H. Lipscomb, S. H. Mernild, T. Mote, N. Steiner, M. Tedesco,

R. S. W. van de Wal and J. Wahr, 2011. Arctic Report Card 2011, NOAA, chap. Greenland Ice Sheet, 117–138.

Box, J. E., X. Fettweis, J. C. Stroeve, M. Tedesco, D. K. Hall and K. Steffen, 2012. Greenland ice sheet albedo feedback: thermodynamics and atmospheric drivers, *The Cryosphere*, **6**(4), 821–839.

Braithwaite, R.J., 1993. Positive degree day factors for ablation on the Greenland ice sheet studied by energy-balance modelling, *Journal of Glaciology*, **41**, 153–173.

Brecher, H.H., 1986. Surface velocity determination on large polar glaciers by aerial photogrammetry, *Annals of Glaciology*, **8**, 22–26.

van den Broeke, M., J. Bamber, J. Ettema, E. Rignot, E. Schrama, W.J. van de Berg, E. van Meijgaard, I. Velicogna and B. Wouters, 2009. Partitioning Recent Greenland Mass Loss, *Science*, **326**(5955), 984–986.

van den Broeke, M.R., C.J.J.P. Smeets and R.S.W. van de Wal, 2011. The seasonal cycle and interannual variability of surface energy balance and melt in the ablation zone of the west Greenland ice sheet, *The Cryosphere*, **5**, 377–390.

van den Broeke, M., P. Smeets, J. Ettema and P.K. Munneke, 2008a. Surface radiation balance in the ablation zone of the west Greenland ice sheet, *Journal of Geophysical Research*, **113**(D13), D13105.

van den Broeke, M., P. Smeets, J. Ettema, C. van der Veen, R. van der Wal and J. Oerlemans, 2008b. Partitioning of melt energy and meltwater fluxes in the ablation zone of the west Greenland ice sheet, *The Cryosphere*, **2**, 179–189.

Burgess, E.W., C.F. Larsen and R.R. Forster, 2013. Summer melt regulates winter glacier flow speeds throughout Alaska, *Geophysical Research Letters*, **40**(23), 6160–6164.

Cappelen, E., J. (ed.) Laursen, C. Kern-Hansen, L. Boas, P. Wang, B. Jørgensen and L.S.

Carstensen, 2012. Weather and Climate Data from Greenland 1958-2011, *Tech. Rep. 12–15*, Danish Meterological Institute.

Cappelen, E.V., J. (ed.) Laursen, C. Kern-Hansen, L. Boas, P. Wang, B. Jørgensen and L.S. Carstensen, 2013. Weather observations from Grenland 1958-2012, *Tech. Rep. 13–11*, Danish Meterological Institute.

Cappelen, J., B.V. Jørgensen, E.V. Laursen, L.S. Stannius and R.S. Thomsen, 2001. The observed climate of Greenland, 1958-99 - with climatological standard normals, 1961-90., *Tech. Rep. 00-18*, Danish Meteorlogical Institute.

Cappelen, J. (ed), E.V. Laursen, P.V. Jørgensen and C.v Kern-Hansen, 2011. DMI Monthly Climate Data Collection 1768-2010, Denmark, The Faroe Islands and Greenland, *Tech. Rep. 11-05*, Danish Meteorlogical Institute.

Chandler, D.M., J.L. Wadham, G.P. Lis, T. Cowton, A. Sole, I. Bartholomew, J. Telling, P. Nienow, E.B. Bagshaw, D. Mair, S. Vinen and A. Hubbard, 2013. Evolution of the subglacial drainage system beneath the Greenland Ice Sheet revealed by tracers, *Nature Geoscience*, **6**(3), 195–198.

Chen, G., 1998. GPS kinematic positioning for the airborne laser altimetry at Long Valley, California, (PhD thesis), Mass. Inst. of Technol., Cambridge.

Chen, Q., D.H. Bromwich and L. Bai, 1997. Precipitation over Greenland Retrieved by a Dynamic Method and Its Relation to Cyclonic Activity, *Journal of Climate*, **10**(5), 839–870.

Christianson, K., L.E. Peters, R.B. Alley, S. Anandakrishnan, R.W. Jacobel, K.L. Riverman, A. Muto and B.A. Keisling, 2014. Dilatant till facilitates ice-stream flow in northeast Greenland, *Earth and Planetary Science Letters*, **401**(0), 57–69.

Church, J.A., J.M. Gregory, P. Huybrechts, M. Kuhn, K. Lambeck, M.T. Nhuan, Q. Qin and P.L. Woodworth, 2001. Changes in sea levels, Houghton, J.T., Y. Ding, D.J. Griggs,

M. Noguer, P.J. van der Linden, X. Dai, K. Maskell and C.A. Johnson, eds., Climate Change 2001: The Scientific Basis. Contribution of Working Group I to the Third Assessment Report of the International Panel on Climate Change., Cambridge University Press, Cambridge, United Kingdom and New York, NY, USA,, 641–684.

Clarke, G.K.C., S.J. Marshall, C. Hillaire-Marcel, G. Bilodeau and C. Veiga-Pires, 1999. A Glaciological Perspective on Heinrich Events, American Geophysical Union.

Clarke, T.S. and K. Echelmeyer, 1996. Seismic-reflection evidence for a deep subglacial trough beneath Jakobshavns Isbræ, West Greenland, *Journal of Glaciology*, **43**, 219–232.

Clason, C., D.W.F. Mair, D.O. Burgess and P.W. Nienow, 2012. Modelling the delivery of supraglacial meltwater to the ice/bed interface: application to southwest Devon Ice Cap, Nunavut, Canada, *Journal of Glaciology*, **58**(208), 361–374.

Cloos, E., 1955. Experimental analysis of fracture patterns, *Bulletin of the Geological Society of America*, **66**(3), 241–256.

Colgan, W., H. Rajaram, R. Anderson, K. Steffen, T. Phillips, I. Joughin, J. Zwally and W. Abdalati, 2011. The annual glaciohydrology cycle in the ablation zone of the Greenland ice sheet: Part 1. Hydrology model, *Journal of Glaciology*, **57**(204), 697–709.

Colgan, W., H. Rajaram, R.S. Anderson, K. Steffen, J.H. Zwally, T. Phillips and W. Abdalati, 2012. The annual glaciohydrology cycle in the ablation zone of the Greenland Ice Sheet: Part 2. Observed and Modeled Ice Flow, *Journal of Glaciology*, **58**(207), 51–64.

Colgan, W. T., T. P. Phillips, R. S. Anderson, H. J. Zwally, W. Abdalati, H. Rajaram and K. Steffen, 2009. Similarities in basal sliding between Greenland and Alpine Glaciers, *AGU Fall Meeting Abstracts*, B499.

Collins, D.N., 1998. Rainfall-induced high-magnitude runoff events in highly-glacierized

Alpine basins, Kovar, K., U. Tappeiner, N.E. Peters and R.G. Craig, eds., Hydrology, Water Resources and Ecology in Headwaters, vol. IAHS Publication no. 248, 69–78.

Copland, L., J. Harbor, M. Minner and M. Sharp, 1996. The use of borehole inclinometry in determining basal sliding and internal deformation at Haut Glacier d'Arolla, Switzerland, *Annals of Glaciology*, **24**, 331–337.

Copland, L., M.J. Sharp and P.W. Nienow, 2003. Links between short-term velocity variations and the subglacial hydrology of a predominantly cold polythermal glacier, *Journal of Glaciology*, **49**(166), 337–348.

Cowton, T, P Nienow, I Bartholomew, A Sole and D Mair, 2012. Rapid erosion beneath the Greenland ice sheet, *Geology*, **40**(4), 343–346.

Cowton, T., P. Nienow, A. Sole, J. Wadham, G. Lis, I. Bartholomew, D. Mair and D. Chandler, 2013. Evolution of drainage system morphology at a land-terminating Greenlandic outlet glaciers, *Journal of Geophysical Research: Earth Surface*, **118**.

Cuffey, K.M and W.S.B. Peterson, 2010. The Physics of Glaciers, Elsevier, fourth ed.

Das, S.B., I. Joughin, M.D. Behn, I.M. Howat, M.A. King, D. Lizarralde and M.P. Bhatia, 2008. Fracture propagation to the base of the Greenland Ice Sheet during supraglacial lake drainage, *Science*, **320**, 778–781.

Den Ouden, M.A.G., C.H. Reijmer, L. Pohjola, R.S.W. van de Wal, J. Oerlemans and W. Boot, 2010. Stand-alone single-frequency GPS ice velocity observations on Nordenskiöldbreen, Svalbard, *The Cryosphere*, **4**(4), 593–604.

Dow, C.F., A. Hubbard, A.B. Booth, S.H. Doyle, A. Gusmeroli and B. Kulessa, 2013. Seismic evidence of mechanically-weak sediments underlying Russell Glacier, West Greenland, *Annals of Glaciology*, **54**(64), 135–141.

Dow, C.F., J.L. Kavanaugh, J.W. Sanders, K.M. Cuffey and K.R. MacGregor, 2011. Sub-

surface hydrology of an overdeepened cirque glacier, *Journal of Glaciology*, **57**(206), 1067–1078.

Dow, C.F., B. Kulessa, S. Pimental, V.C. Tsai, S.H. Doyle, I.C. Rutt, G.A. Jones, A.D. Booth and A. Hubbard, 2012. Modelling of subglacial hydrological development during a rapid lake drainage event, West Greenland, *AGU Fall Meeting Abstract 0598*, **1**.

Dow, J.M., R. E. Neilan and C. Rizos, 2009. The International GNSS Service in a changing landscape of Global Navigation Satellite Systems, *Journal of Geodesy*, **83**, 191–198.

Doyle, S.H., A.L. Hubbard, C.F. Dow, G.A. Jones, A. Fitzpatrick, A. Gusmeroli, B. Kulessa, K. Lindback, R. Pettersson and J.E. Box, 2013. Ice tectonic deformation during the rapid in situ drainage of a supraglacial lake on the Greenland Ice Sheet, *The Cryosphere*, **7**(1), 129–140.

Doyle, S.H., A. Hubbard, A.A.W. Fitzpatrick, D. van As, A. B. Mikkelsen, R. Pettersson and B. Hubbard, 2014. Persistent flow acceleration within the interior of the Greenland ice sheet, *Geophysical Research Letters*, **41**, 899–905.

Dunse, T., T.V. Schuler, J.O. Hagen and C.H. Reijmer, 2012. Seasonal speed-up of two outlet glaciers of Austfonna, Svalbard, inferred from continuous GPS measurements, *The Cryosphere*, **6**(2), 453–466.

Echelmeyer, K., T.S. Clarke and W.D. Harrison, 1991. Surficial glaciology of Jakobshavn Isbrae, West Greenland: Part I. Surface morphology, *Journal of Glaciology*, **37**(127), 368–382.

Eiken, T., J.O. Hagen and K. Melvold, 1996. Kinematic GPS survey of geometry changes on Svalbard glaciers, *Annals of Glaciology*, **24**, 157–163.

Engelhardt, H.F., 1978. Water in glaciers: observations and theory of the behaviour of water levels in boreholes., *Z. Gletscher. Glazialgeol.*, **14**, 35–60.

Erten, E., A. Reigber, O. Hellwich and P. Prats, 2009. Glacier velocity monitoring by

maximum likelihood texture tracking, *IEEE Transactions on Geoscience and Remote Sensing*, **47**(2), 394 405.

Estey, L.H. and C.M. Meertens, 1999. TEQC: The multi-purpose toolkit for GPS/GLONASS data, *GPS Solutions*, **3**(1), 42–29.

Ettema, J., M.R. van den Broeke, E. van Meijgaard, W.J. van de Berg, J.L. Bamber, J.E. Box and R.C. Bales, 2009. Higher surface mass balance of the Greenland ice sheet revealed by high-resolution climate modeling, *Geophysical Research Letters*, **36**(L12501).

Fahnestock, M., M. Truffer, M. Lüthi, R. Motyka, J. Amundson and J. Brown, 2007. GPS and conventional surveying measurement of glacier and iceberg motion in the Jakobshavns Isbrae system, *AGU Fall Meeting Abstracts*, C3.

Fettweis, X., A. Belleflamme, M. Erpicum, B. Franco and S. Nicolay, 2011. Estimation of the sea level rise by 2100 resulting from changes in the surface mass balance of the Greenland ice sheet, Blanco, J. and H. Kheradmand, eds., Climate Change Geophysical Foundations and Ecological Effects, 503–520.

Fitzpatrick, A.A.W, 2013. The dynamic response of the Greenland Ice Sheet to climatic change, (PhD thesis), Aberystwyth University.

Fitzpatrick, A.A.W., A.L. Hubbard, J.E. Box, D.J. Quincey, D. van As, A.P.B. Mikkelsen, S.H. Doyle, C.F. Dow, B. Hasholt and G.A. Jones, 2014. A decade (2002 - 2012) of supraglacial lake volume estimates across Russell Glacier, West Greenland, *The Cryosphere*, **8**(1), 107–121.

Fitzpatrick, A.A.W., A.L. Hubbard, I. Joughin, D.J. Quincey, D. van As, A.P.B. Mikkelsen, S.H. Doyle, B. Hasholt and G.A. Jones, 2013. Ice flow dynamics and surface meltwater flux at a land-terminating sector of the Greenland Ice Sheet, *Journal of Glaciology*, **59**(216), 687–696.

Fountain, A.G., 1994. Borehole water-level variations and implications for the subglacial

hydraulics of South Cascade Glacier, Washington State, VSA, *Journal of Glaciology*, **40**(135), 293–304.

Fountain, A.G. and J.S. Walder, 1998. Water flow through temperate glaciers, *Journal of Glaciology*, **36**(3), 299–328.

Franco, B., X. Fettweis and M. Erpicum, 2013. Future projections of the Greenland ice sheet energy balance driving the surface melt, *The Cryosphere*, **7**(1), 1–18.

Fudge, T.J., J.T. Harper, N.F. Humphrey and W.T. Pfeffer, 2009. Rapid glacier sliding, reverse ice motion and subglacial water pressure during an autumn rainstorm, *Journal of Glaciology*, **50**(52), 101–107.

Gao, J. and Y. Liu, 2001. Applications of remote sensing, GIS and GPS in glaciology: a review, *Progress in Physical Geography*, **24**(4), 520–540.

Gascon, G., M. Sharp and A. Bush, 2013. Changes in melt season characteristics on Devon Ice Cap, Canada, and their association with the Arctic atmospheric circulation, *Annals of Glaciology*, **54**(63), 101–110.

Georgiou, S., A Shepherd, M. McMillan and P. Nienow, 2009. Seasonal evolution of supraglacial lake volume from ASTER imagery, *Annals of Glaciology*, **50**(52), 95–100.

Gordon, S., M. Sharp, B. Hubbard, C. Smart, B. Ketterling and I. Willis, 1998. Seasonal reorganization of subglacial drainage system of Haut Glacier dArolla, Valais, Switzerland, inferred from measurements in boreholes, *Hydrological Processes*, **12**, 105–133.

Greve, R. and S. Sugiyama, 2009. Decay of the Greenland Ice Sheet due to surface-meltwater induced acceleration of basal sliding, Published online: `http://arxiv.org/abs/0905.2027v1`.

Gudmundsson, G.H., A. Bassi, M. Vonmoos, A. Bauder, U.H. Fischer and M. Funk, 2000. High-resolution measurements of spatial and temporal variations in surface velocities of Unteraargletscher, Bernese Alps, Switzerland, *Annals of Glaciology*, **31**(1), 63–68.

Gudmundsson, H., 2006. Fortnightly variations in the flow velocity of Rutford Ice Stream, West Antarctica, *Nature*, **444**, 1063–1064.

Gudmundsson, H., 2007. Tides and the flow of Rutford Ice Stream, *Journal of Geophysical Research*, **112**, 1–8.

Hagen, J. O., T. Eiken, J. Kohler and K. Melvold, 2005. Geometry changes on Svalbard glaciers: mass-balance or dynamic response?, *Annals of Glaciology*, **42**(1), 255–261.

Hanna, E., X. Fettweis, S.H. Mernild, J. Cappelen, M.H. Ribergaard, C.A. Shuman, K. Steffen, L. Wood and T.L. Mote, 2014. Atmospheric and oceanic climate forcing of the exceptional Greenland ice sheet surface melt in summer 2012, *International Journal of Climatology*, **34**(4), 1022–1037.

Harper, J.T., N.F. Humphrey and M.C. Greenwood, 2002. Basal conditions and glacier motion during the winter/spring transition, Worthington Glacier, Alaska, U.S.A., *Journal of Glaciology*, **48**(160), 42–50.

Harper, J.T., N.F. Humphrey and W.. Pfeffer, 1998. Three-Dimensional Deformation Measured in an Alaskan Glacier, *Science*, **281**(5381), 1340–1342.

Harper, J., N. Humphrey, W.T. Pfeffer, J. Brown and X. Fettweis, 2012. Greenland ice-sheet contribution to sea-level rise buffered by meltwater storage in firn, *Nature*, **491**, 240–243.

Harper, J.T., N.F. Humphrey, W. Pfeffer, T. Fudge and S. O'Neel, 2005. Evolution of subglacial water pressure along a glacier's length, *Annals of Glaciology*, **40**(1), 31–36.

Harper, J.T., N.F. Humphrey, W.T. Pfeffer and B. Lazar, 2007. Two modes of accelerated glacier sliding related to water, *Geophysical Research Letters*, **34**, L12503.

Hasholt, B., A.B. Mikkelsen, M.H. Nielsen and M.A.D Larsen, 2013. Observations of runoff and sediment and dissolved loads from the Greenland ice sheet at Kangerlussuaq, West Greenland, 2007 to 2010., *Zeitschrift für Geomorphologie*, **57**(Suppl. 2), 3–27.

Herring, T.A., R.W. King and S.C. McClusky, 2010. GAMIT Reference Manual, Release 10.4, Cambridge: Massachusetts Institute of Technology.

Hewitt, I.J., 2013. Seasonal changes in ice sheet motion due to melt water lubrication, *Earth and Planetary Science Letters*, **371-372**(0), 16–25.

Hindmarsh, R.C.A., 2006. The role of membrane-like stresses in determining the stability and sensitivity of the Antarctic ice sheets: back pressure and grounding line motion, *Philosophical Transactions of the Royal Society a-Mathematical Physical and Engineering Sciences*, **364**(1884), 1733–1767.

Hinze, H. and G. Seeber, 1988. Ice-motion determination by means of satellite positioning systems, *Ann. Glaciol*, **11**, 36–41.

Hock, R., 2003. Temperature index melt modelling in mountain areas, *Journal of Hydrology*, **282**, 104–115.

Hock, R., 2005. Glacier melt: a review of processes and their modelling, *Progress in Physical Geography*, **29**(3), 362–391.

Hoffman, M.J., G.A. Catania, T.A. Neumann, L.C. Andrews and J.A. Rumrill, 2011. Links between acceleration, melting, and supraglacial lake drainage of the western Greenland Ice Sheet, *Journal of Geophysical Research*, **116**, F04035.

Hooke, R.LeB., 1989. Englacial and Subglacial Hydrology: A Qualitative Review, *Arctic and Alpine Research*, **21**(3), pp. 221–233.

Hooke, R.L., T. Laumann and J. Kohler, 1990. Subglacial water pressures and the shape of subglacial conduits, *Journal of Glaciology*, **36**(122), 67–71.

Hotz, R.L., 2006. Greenland's ice sheet is slip-sliding away, *Los Angeles Times, 25 June*.

Howat, I.M., I. Joughin and T.A. Scambos, 2007. Rapid changes in ice discharge from Greenland outlet glaciers, *Science*, **315**(5818), 1559–1561.

Howat, I. M., A. Negrete and B. E. Smith, 2014. The Greenland Ice Mapping Project

(GIMP) land classification and surface elevation datasets, *The Cryosphere Discussions*, **8**(1), 453–478.

Howat, I. M., S. de la Peña, J. H. van Angelen, J. T. M. Lenaerts and M. R. van den Broeke, 2013. Brief Communication"Expansion of meltwater lakes on the Greenland ice sheet", *The Cryosphere*, **7**, 201–204.

Howat, I. M., S. Tulaczyk, E. Waddington and H. Björnsson, 2008. Dynamic controls on glacier basal motion inferred from surface ice motions, *Jounal of Geophysical Research*, **113**, F03015.

Hubbard, B., 2002. Direct measurement of basal motion at a hard-bedded, temperate glacier: Glacier de Tsanfleuron, Switzerland, *Journal of Glaciology*, **48**(160), 1–8.

Hubbard, B. and P. Nienow, 1997. Alpine Subglacial Hydrology, *Qauternary Science Reviews*, **16**, 939–955.

Hubbard, B.P., M.J. Sharp, I.C. Willis, M.K. Nielsen and C.C. Smart, 1995. Borehole water-level variations and the structure of the subglacial hydrological system of Haut Glacier d'Arolla, Valais, Switzerland, *Journal of Glaciology*, **41**(139), 572–583.

Huggell, C., A. Kääb, W. Haeberli, P. Teysseire and F. Paul, 2002. Remote sensing based assessment of hazards from glacier lake outbursts: a case study in the Swiss Alps, *Canadian Geotechnical Journal*, **39**, 316–330.

Huybrechts, P. and J. de Wolde, 1999. The dynamic response of the Greenland and Antarctic ice sheets to multiple-century warming, *Journal of Climate*, **21**, 21692188.

Iken, A., 1981. The effect of the subglacial water pressure on the sliding velocity of a glacier in an idealized numerical model, *Journal of Glaciology*, **27**(97), 407–421.

Iken, A., H. Rothlisberger, A. Flotron and W. Haeberli, 1983. The uplift of Unteraargletscher at the beginning of the melt season - a consequence of water storage at the bed, *Journal of Glaciology*, **29**(101), 28–47.

Iken, A. and M. Truffer, 1997. The relationship between subglacial water pressure and velocity of Findelgletscher, Switzerland, during its advance and retreat, *Journal of Glaciology*, **43**(144), 328–338.

Johannessen, O.M, K. Khvorostovsky, M.W. Miles and L.P. Bobylev, 2005. Recent ice-sheet growth in the interior of Greenland, *Science*, **310**(5750), 1013–1016.

Johansson, A.M., 2012. Remote sounding of supra-glacial lakes on the west Greenland Ice Sheet, (PhD thesis), Stockholm University.

Johansson, P., A.M.and Jansson and I.A. Brown, 2012. Spatial and temporal variations in lakes on the Greenland Ice Sheet, *Journal of Hydrology*.

Jones, G. A., B. Kulessa, S.H. Doyle, C. F. Dow and A. Hubbard, 2013. An automated approach to the location of icequakes using seismic waveform amplitudes, *Annals of Glaciology*, **54**(64), 1–9.

Joughin, I., 2002. Ice-sheet velocity mapping: a combined interferometric and speckle-tracking approach, *Annals of Glaciology*, **34**, 195–201.

Joughin, I., W. Abdalati and M. Fahnestock, 2004. Large fluctuations in speed on Greenland's Jakobshavn Isbrae Glacier, *Nature*, **432**, 608–610.

Joughin, I., S.B. Das, G.E. Flowers, M.D. Behn, R.B. Alley, M.A. King, B.E. Smith, J. Bamber, M.R. van den Broeke and J.H. van Angelen, 2013. Influence of ice-sheet geometry and supraglacial lakes on seasonal ice-flow variability, *The Cryosphere*, **7**, 1185–1192.

Joughin, I., S.B. Das, M.A. King, B.E. Smith, I.M. Howat and T. Moon, 2008. Seasonal speedup along the western flank of the Greenland Ice Sheet, *Science*, **320**, 781–783.

Joughin, I., B.E. Smith, I. Howat, T. Scambos and T. Moon, 2010. Greenland flow variability from ice-sheet-wide velocity mapping, *Journal of Glaciology*, **56**(16), 415–430.

Joughin, I., S. Tulaczyk, M. Fahnestock and R. Kwok, 1996. A mini-surge on the Ryder

Glacier, Greenland, observed by satellite radar interferometry, *Science*, **274**(5285), 228–230.

Kalnay, E., M. Kanamitsu, R. Kistler, W. Collins, D. Deaven, L. Gandin, M. Iredell, S. Saha, G. White, J. Woollen and others, 1996. The NCEP/NCAR 40-year reanalysis project, *Bulletin of the American meteorological Society*, **77**(3), 437–471.

Kamb, B., 1987. Glacier surge mechanism based on linked-cavity configuration of the basal water conduit system, *Journal of Geophysical Research*, **92**(B9), 9083–9100.

Kamb, B. and K.A. Echelmeyer, 1986. Stress-gradient coupling in glacier flow: I. Longitudinal averaging of the influence of ice thickness and surface slope, *Journal of Glaciology*, **32**(111), 267–298.

Kamb, B., C.F. Raymond, W.D. Harrison, H. Engelhardt, K.A. Echelmeyer, N. Humphrey, M.M. Brugman and T. Pfeffer, 1985. Glacier surge mechanism: 1982-1983 surge of Variegated Glacier, Alaska, *Science*, **227**(4686), 469–479.

Kaplan, D.E., ed., 1996. Understanding GPS Principles and Applications, Artech House Publications.

King, M., 2004. Rigorous GPS data-processing strategies for glaciological applications, *Journal of Glaciology*, **50**(171), 601–607.

King, M., S. Edwards and P.J. Clarke, 2002. Precise point positioning: breaking the monopoly of relative GPS processing, *Engineering Surveying Showcase*, 40–41.

Kirby, A., 2002. Greenland's warming ice flows faster, *BBC News World Edition, 7 June*.

Klobuchar, J.A., 1991. Ionospheric effects on GPS, *GPS World*, 1–4.

Krabill, W., W. Adbalati, E. Frederick, S. Manizade, C. Martin, J. Sonntag, R. Swift, R. Thomas, W. Wright and J. Yungel, 2000. Greenland Ice Sheet: high-elevation balance and peripheral thinning, *Science*, **289**, 428–430.

Krabill, W., E. Frederick, S. Manizade, C. Martin, J. Sonntag, R. Swift, R. Thomas,

W. Wright and J. Yungel, 1999. Rapid thinning of parts of the southern Greenland Ice Sheet, *Science*, **283**(5407), pp. 1522–1524.

Krawczynski, M.J., M.D. Behn, S.B Das and I. Joughin, 2009. Constraints on the lake volume required for hydro-fracture through ice sheets, *Geophysical Research Letters*, **36**(L10501), 1–5.

Krieger, G., A. Moreira, H. Fiedler, I. Hajnsek, M. Werner, M. Younis and M. Zink, 2007. TanDEM-X: A satellite formation for high-resolution SAR interferometry, *Geoscience and Remote Sensing, IEEE Transactions on*, **45**(11), 3317–3341.

Kulessa, B., A.D. Booth, A.L. Hubbard, H. Doyle, S, R.A. Clark, A. Gusmeroli, C.F. Dow, G.A. Jones and T. Murray, 2012. Seismic detection and characterisation of unlithified subglacial sediments beneath the West Greenland Ice Sheet, Boise Cryospheric Geophysics Conference.

Lampkin, D.J., 2011. Supraglacial lake spatial structure in western Greenland during the 2007 ablation season, *Journal of Geophysical Research*, **116**(F4), F04001.

Lampkin, D.J. and J. VanderBerg, 2011. A preliminary investigation of the influence of basal and surface topography on supraglacial lake distribution near Jakobshavn Isbrae, western Greenland, *Hydrological Processes*, **25**(21), 3347–3355.

Larson, K.M., J. Plumb, J. Zwally and W. Abdalati, 2002. Analysis of GPS data collected on the Greenland ice sheet, *Polar Geography*, **25**(1), 22–40.

Leeson, A.A., A. Shepherd, S. Palmer, A. Sundal and X. Fettweis, 2012. Simulating the growth of supraglacial lakes at the western margin of the Greenland ice sheet, *The Cryosphere*, **6**, 1077–1086.

Leick, A., 2004. GPS Satellite Surveying, John & Wiley Sons, Inc., third edition ed.

Lemke, P., J. Ren, R.B. Alley, I. Allison, J. Carrasco, G. Flato, Y. Fujii, G. Kaser, P. Mote, R.H. Thomas and T. Zhang, 2007. Observations: Changes in Snow, Ice and Frozen

Ground., Solomon, S., D. Qin, M. Manning, Z. Chen, M. Marquis, K.B. Averyt, M. Tignor and H.L. Miller, eds., Climate Change 2007: The Physical Science Basis. Contribution of Working Group I to the Fourth Assessment Report of the Intergovernmental Panel on Climate Change, Cambridge University Press, Cambridge, United Kingdom and New York, NY, USA., 339–378.

Lettang, F.J., R.I. Crocker, W.J. Emery and J.A. Maslanik, 2013. Estimating the extent of drained supraglacial lakes on the Greenland Ice Sheet, *International Journal of Remote Sensing*, **34**(13), 4754–4768.

Liang, Y-L., W. Colgan, Q. Lv, K. Steffen, W. Abdalati, J. Stroeve, D. Gallaher and N. Bayou, 2012. A decadal investigation of supraglacial lakes in West Greenland using a fully automatic detection and tracking algorithm, *Remote Sensing of Environment*, **123**, 127–138.

Liestol, O., K. Repp and B. Wold, 1980. Supra-glacial lakes in Spitsbergen, *Norsk Geografisk Tidsskrift*, **34**, 89–92.

Lindback, K., R. Pettersson, S.H. Doyle, A. Hubbard, C. Helanow, P. Jansson, E. Lintz Christensen, S. Savstrup Kristensen, L. Stenseng and R. Forsberg, 2014. High-resolution ice thickness and bed topography of a land-terminating section of the Greenland Ice Sheet, *Earth Science Systems Data Discussions*, **7**, 129–148.

Luckman, A., T. Murray, R. de Lange and E. Hanna, 2006. Rapid and synchronous ice-dynamic changes in East Greenland, *Geophysical Research Letters*, **33**, L03503.

Lüthi, M., 2013. Gauging Greenland's Subglacial Water, *Science*, **341**(6147), 721–722.

Lüthi, M., M. Funk, A. Iken, S. Gogineni and M. Truffer, 2002. Mechanisms of fast flow in Jakobshavn Isbrae, West Greenland: Part III. Measurements of ice deformation, temperature and cross-borehole conductivity in boreholes to the bedrock, *Journal of Glaciology*, **48**(162), 369–385.

Lüthje, M., L.T. Pedersen, N. Reeh and W. Gruell, 2006. Modelling the evolution of supraglacial lakes on the West Greenland ice-sheet margin, *Journal of Glaciology*, **52**(179), 608–618.

MacGregor, K. R., C. A. Riihimaki and R.S. Anderson, 2005. Spatial and temporal evolution of rapid basal sliding on Bench Glacier, Alaska, USA, *Journal of Glaciology*, **51**(15), 49–63.

Mair, D.W.F., M.J. Sharp and I.C. Willis, 2002. Evidence for basal cavity opening from analysis of surface uplift during a high-velocity event: Haut Glacier d'Arolla, Switzerland, *Jounal of Glaciology*, **48**(161), 208–216.

Mair, D., I. Willis, U.H. Fischer, B. Hubbard, P. Nienow and A. Hubbard, 2003. Hydrological controls on patterns of surface, internal and basal motion during three "spring events": Haut Glacier dArolla, Switzerland, *Journal of Glaciology*, **49**(167), 555–567.

McGrath, D., W. Colgan, K. Steffen, P. Lauffenburger and J. Balog, 2011. Assessing the summer water budget of a moulin basin in the Sermeq Avannarleq ablation region, Greenland ice sheet, *Journal of Glaciology*, **57**(205), 954–963.

McMillan, M., P. Nienow, A. Shepherd, T. Benham and A. Sole, 2007. Seasonal evolution of supra-glacial lakes on the Greenland Ice Sheet, *Earth and Planetary Science Letters*, **262**, 484–492.

Meierbachtol, T., J. Harper and N. Humphrey, 2013. Basal drainage system response to increasing surface melt on the Greenland Ice Sheets, *Science*, **341**(6147), 777–779.

Moon, T, I Joughin, B Smith and I Howat, 2012. 21st-century evolution of Greenland outlet glacier velocities, *Science*, **336**(6081), 576–578.

Morriss, B. F., R. L. Hawley, J. W. Chipman, L. C. Andrews, G. A. Catania, M. J. Hoffman, M. P. Lüthi and T. A. Neumann, 2013. A ten-year record of supraglacial lake evolution

and rapid drainage in West Greenland using an automated processing algorithm for multispectral imagery, *The Cryosphere*, **7**(6), 1869–1877.

Neave, K.G. and J.C. Savage, 1970. Icequakes on the Athabasca Glacier, *Journal of Geophysical Research*, **75**(8), 1361–1362.

Nghiem, S.V., D.K. Hall, T.L. Mote, M. Tedesco, M.R. Albert, K. Keegan, C.A. Shuman, N.E. DiGirolamo and G. Neumann, 2012. The extreme melt across the Greenland ice sheet in 2012, *Geophysical Research Letters*, **39**(20), L20502.

Nienow, P.W., A.L. Hubbard, B.P. Hubbard, D.M. Chandler, D.W.F. Mair, M. Sharp and I.C. Willis, 2005. Hydrological controls on diurnal ice flow variability in valley glaciers, *Jounal of Geophysical Research*, **110**(F04002).

Nye, J.F., 1953. The flow law of ice from measurements in glacier tunnels, laboratory experiments and the Jungfraufirn borehole experiment, *Proceedings of the Royal Society of London. Series A. Mathematical and Physical Sciences*, **219**(1139), 477–489.

Oerlemans, J., 1991. The mass balance of the Greenland ice sheet: sensitivity to climate change as revealed by energy balance modelling, *Holocene*, **1**, 40–49.

O'Neel, S., K.A. Echelmeyer and R.J. Motyka, 2001. Short-term flow dynamics of a retreating tidewater glacier: LeConte Glacier, Alaska, U.S.A., *Journal of Glaciology*, **47**(159), 567–578.

Palmer, S., A. Shepherd, P. Nienow and I. Joughin, 2011. Seasonal speedup of the Greenland Ice Sheet linked to routing of surface water, *Earth and Planetary Science Letters*, **302**(3-4), 423–428.

Parizek, B.R. and R.B. Alley, 2004. Implications of increased Greenland surface melt under global warming scenarios: ice-sheet simulations, *Quaternary Science Reviews*, **23**, 1013–1027.

Pettersson, R., P. Christoffersen, J.A. Dowdeswell, V.A. Pohjola, A.L. Hubbard and

T. Strozzi, 2011. Ice thickness and basal conditions of Vestfonna Ice Cap, Eastern Svalbard, *Geografiska Annaler: Series A, Physical Geography*, **93**, 311–322.

Phillips, T., H. Rajaram, W. Colgan, K. Steffen and W. Abdalati, 2013. Evaluation of cryo-hydrologic warming as an explanation for increased ice velocities in the wet snow zone, Sermeq Avannarleq, West Greenland, *Journal of Geophysical Research*, **118**, 1–16.

Phillips, T., H. Rajaram and K. Steffen, 2010. Cryo-hydrologic warming: A potential mechanism for rapid thermal response of ice sheets, *Geophysical Research Letters*, **37**, L20503.

Pimental, S. and G. Flowers, 2010. A numerical study of hydrologically driven glacier dynamics and subglacial flooding, *Proceedings of the Royal Society*, **467**, 537–558.

Price, N.J. and J.W. Cosgrove, 1994. Analysis of geological structures, University Press, Cambridge.

Price, S.F., A.J. Payne, G.A. Catania and T.A. Neumann, 2008. Seasonal acceleration of inland ice via longitudinal coupling to marginal ice, *Journal of Glaciology*, **54**(185), 213–218.

Pritchard, H., R.J. Arthern, D.G. Vaughan and L.A. Edwards, 2009. Extensive dynamic thinning on the margins of the Greenland and Antarctic ice sheets, *Nature*, **461**, 971–975.

Pryor, S.C. and J.T Schoof, 2008. Changes in the seasonality of precipitation over the contiguous USA, *Journal of Geophysical Research*, **113**(D21).

Quincey, D.J. and A. Luckman, 2009. Progress in satellite remote sensing of ice sheets, *Progress in Physical Geography*, **33**(4), 547–567.

Rignot, E. and P. Kanagaratnam, 2006. Changes in the velocity structure of the Greenland Ice Sheet, *Science*, **311**, 986–990.

Roberts, M.J., A.J. Russell, F.S. Tweed and Ó. Knudsen, 2000. Ice fracturing during

jökulhlaups: implications for englacial floodwater routing and outlet development, *Earth Surface Processes and Landforms*, **25**(13), 1429–1446.

Röthlisberger, H., 1972. Water pressure in intra- and subglacial channels, *Journal of Glaciology*, **11**(62), 177–203.

Röthlisberger, H. and A. Iken, 1981. Plucking as an fffect of water-pressure variations at the Glacier Beds, *Annals of Glaciology*, **2**(1), 57–62.

Röthlisberger, H and H Lang, 1987. Glacial hydrology, *Glacio-Fluvial Sediment Transfer: An Alpine Perspective.*, 207–284.

Roux, P.-F., F. Walter, P. Riesen, S. Sugiyama and M. Funk, 2010. Observation of surface seismic activity changes of an Alpine glacier during a glacier-dammed lake outburst, *Journal of Geophysical Research*, **115**, F03014.

Russell, A.J., 1993. Correspondence. Supraglacial lake drainage near Sondre Stromfjord, Greenland, *Journal of Glaciology*, **39**(132), 431–433.

Ryan, J. C., A. L. Hubbard, J. Todd, J. R. Carr, J. E. Box, P. Christoffersen, T. O. Holt and N. Snooke, 2014. Repeat UAV photogrammetry to assess calving front dynamics at a large outlet glacier draining the Greenland Ice Sheet, *The Cryosphere Discussions*, **8**(2), 2243–2275.

Schaer, S., W. Gurtner and J. Feltens, 1998. IONEX: The IONOosphere Map Exchange Format Version 1, Proceedings of the IGS AC Workshop, Darmstadt, Germany, February 9-11.

Schoof, C., 2010. Ice-sheet acceleration driven by melt water supply variability, *Nature*, **468**, 803–806.

Schuenemann, K.C. and J.J. Cassano, 2009. Changes in synoptic weather patterns and Greenland precipitation in the 20th and 21st centuries: 1. Evaluation of late 20th century

simulations from IPCC models, *Journal of Geophysical Research: Atmospheres*, **114**, D20113.

Schuenemann, K. C. and J. J. Cassano, 2010. Changes in synoptic weather patterns and Greenland precipitation in the 20th and 21st centuries: 2. Analysis of 21st century atmospheric changes using self-organizing maps, *Journal of Geophysical Research*, **115**, D05108.

Selmes, N., T. Murray and T.D. James, 2011. Fast draining lakes on the Greenland Ice Sheet, *Geophysical Research Letters*, **38**, L15501.

Serreze, M.C., J.E. Box, R.G. Barry and J.E. Walsh, 1993. Characteristics of Arctic synoptic activity, 1952–1989, *Meteorology and Atmospheric Physics*, **51**, 146–164.

Shannon, S.R., A.J. Payne, I.D. Bartholomew, M.R. van den Broeke, T.L. Edwards, X. Fettweis, O. Gagliardini, F. Gillet-Chaulet, H. Goelzer, M.J. Hoffman, P. Huybrechts, D.F. Mair, P.W. Nienow, M. Perego, S.F. Price, P. Smeets, A.J. Sole, R.S.W. van de Wal and T. Zwinger, 2013. Enhanced basal lubrication and the contribution of the Greenland ice sheet to future sea-level rise, *Proceedings of the National Academy of Sciences*, **110**(35), 14156–14161.

Shepherd, A., A. Hubbard, P. Nienow, M. King, M. McMillan and I. Joughin, 2009. Greenland ice sheet motion coupled with daily melting in late summer, *Geophysical Research Letters*, **36**, 1–4.

Shepherd, A., E.R. Ivins, A Geruo, V.R. Barletta, M.J. Bentley, S. Bettadpur, K.H. Briggs, D.H. Bromwich, R. Forsberg, N. Galin and others, 2012. A reconciled estimate of ice-sheet mass balance, *Science*, **338**(6111), 1183–1189.

Shi, L., C.T. Allen, J.R. Ledford, F. Rodriguez-Morales, W.A. Blake, B.G. Panzer, S.C. Prokopiack, C.J. Leuschen and S. Gogineni, 2010. Multichannel Coherent Radar Depth

Sounder for NASA Operation Ice Bridge, Geoscience and Remote Sensing Symposium (IGARSS), 2010 IEEE International, 1729–1732.

Shreve, R.L., 1972. Movement of water in glaciers, *Journal of Glaciology*, **11**(62), 205–214.

Smeets, C.J.P.P., W. Boot, A. Hubbard, R. Pettersson, F. Wilhelms, M.R. Van Den Broeke and R.S.W. Van De Wal, 2012. Instruments and Methods - A wireless subglacial probe for deep ice applications, *Journal of Glaciology*, **58**(211), 841–848.

Smith, A.M., T.A. Jordan, F. Ferraccioli and R.G. Bingham, 2013. Influence of subglacial conditions on ice stream dynamics: Seismic and potential field data from Pine Island Glacier, West Antarctica, *Journal of Geophysical Research*, **118**, 1471–1482.

Sneed, W.A. and G.S. Hamilton, 2007. Evolution of melt pond volume on the surface of the Greenland Ice Sheet, *Geophysical Research Letters*, **34**, L03501.

Sneed, W.A. and G.S. Hamilton, 2011. Validation of a method for determining the depth of glacial melt ponds using satellite imagery, *Annals of Glaciology*, **52**(59), 15–22.

Sole, A., P. Nienow, I. Bartholomew, D. Mair, T. Cowton, A. Tedstone and M. King, 2013. Winter motion mediates dynamic response of the Greenland Ice Sheet to warmer summers, *Geophysical Research Letters*, **40**, 3940–3944.

Sole, A., T. Payne, J. Bamber, P. Nienow and W. Krabill, 2008. Testing hypotheses of the cause of peripheral thinning of the Greenland Ice Sheet: is land-terminating ice thinning at anomalously high rates?, *The Cryosphere*, **2**, 215–218.

Stenborg, T., 1968. Glacier drainage connected with ice structures, *Geografiska Annaler*, **50A**(1), 25–53.

Strozzi, T., A. Luckman, T. Murray, U. Wegmuller and C.L. Werner, 2002. Glacier motion estimation using SAR offset-tracking procedures, *Geoscience and Remote Sensing, IEEE Transactions on*, **40**(11), 2384–2391.

Sugiyama, S., A.. Bauder, M. Huss, P. Riesen and M. Funk, 2008. Triggering and drainage

mechanisms of the 2004 glacier-dammed lake outburst in Gornergletscher, Switzerland, *Journal of Geophysical Research*, **113**, F04019.

Sugiyama, S. and G.H. Gudmundsson, 2004. Short-term variations in glacier flow controlled by subglacial water pressure at Lauteraargletscher, Bernese Alps, Switzerland, *Journal of Glaciology*, **50**(170), 353–362.

Sundal, A.V., A. Shepherd, P. Nienow, E. Hanna, S. Palmer and P. Huybrechts, 2009. Evolution of supra-glacial lakes across the Greenland Ice Sheet, *Remote Sensing of Environment*, **113**, 2164–2171.

Sundal, A.V., A. Shepherd, P. Nienow, E. Hanna, S. Palmer and P. Huybrechts, 2011. Melt-induced speed-up of Greenland ice sheet offset by efficient subglacial drainage, *Nature*, **469**, 521–524.

Sunil, P.S., C.D. Reddy, M. Ponraj, A. Dhar and D. Jayapaul, 2007. GPS determination of the velocity and strain-rate fields on Schirmacher Glacier, central Dronning Maud Land, Antarctica, *Journal of Glaciology*, **53**(183), 558–564.

Tedesco, M., X. Fettweis, M.R. van den Broeke, R.S.W. van de Wal, C.J.P.P. Smeets, W.J. van de Berg, M.C. Serreze and J.E. Box, 2011. The role of albedo and accumulation in the 2010 melting record in Greenland, *Environmental Research Letters*, **6**, 1–6.

Tedesco, M., X. Fettweis, T. Mote, J. Wahr, P. Alexander, J. E. Box and B. Wouters, 2013. Evidence and analysis of 2012 Greenland records from spaceborne observations, a regional climate model and reanalysis data, *The Cryosphere*, **7**(2), 615–630.

Tedesco, M., M. Lthje, K. Steffen, N. Steiner, X. Fettweis, I. Willis, N. Bayou and A. Banwell, 2012. Measurement and modeling of ablation of the bottom of supraglacial lakes in western Greenland, *Geophysical Research Letters*, **39**, L02502.

Tedstone, A.J., P.W. Nienow, A.J. Sole, D.W.F. Mair, T.R. Cowton, I.D. Bartholomew

and M.A. King, 2013. Greenland ice sheet motion insensitive to exceptional meltwater forcing, *Proceedings of the National Academy of Sciences*, **110**(49), 19719–19724.

Truffer, M., W.D. Harrison and R.S. March, 2005. Record negative glacier balances and low velocities during the 2004 heatwave in Alaska, USA: implications for the interpretation of observations by Zwally and others in Greenland, *Journal of Glaciology*, **51**(175), 663–664.

Vavrus, S.J., 2013. Extreme Arctic cyclones in CMIP5 historical simulations, *Geophysical Research Letters*, **40**(23), 6208–6212.

van der Veen, C.J., 1998. Fracture mechanics approach to penetration of surface crevasses on glaciers, *Cold Regions Science & Technology*, **27**, 31–47.

van der Veen, C.J., 2007. Fracture propagation as means of rapidly transferring meltwater to the base of glaciers, *Geophysical Research Letters*, **34**, L01501.

van de Wal, R.S.W., W. Boot, M.R. van den Broeke, C.J.P.P. Smeets, C.H. Reijmer, J.J.A. Donker and J. Oerlemans, 2008. Large and rapid melt-induced velocity changes in the ablation zone of the Greenland Ice Sheet, *Science*, **321**, 111–113.

van de Wal, R.S.W., W. Greurell, M.R. van den Broeke, C.H. Reijmer and J. Oerlemans, 2005. Surface mass-balance observations and automatic weather station data along a transect near Kangerlussuaq, West Greenland, *Annals of Glaciology*, **42**, 311–316.

van de Wal, R.S.W. and J.s Oerlemans, 1997. Modelling the short-term response of the Greenland ice-sheet to global warming, *Climate Dynamics*, **13**(10), 733–744.

van de Wal, R.S.W. and A. J. Russell, 1994. A comparison of energy balance calculations, measured ablation and meltwater runoff near Sndre Strmfjord, West Greenland., *Global and Planetary Change*, **9**(1-2), 29–38.

van de Wal, R S.W., W. Boot, C.J.P.P. Smeets, H. Snellen, M.R. van den Broeke and J.s

Oerlemans, 2012. Twenty-one years of mass balance observations along the K-transect, West Greenland, *Earth System Science Data*, **4**(1), 31–35.

Walder, J.S., 1982. Stability of sheet flow of water beneath temperate glaciers and implications for glacier surging, *Journal of Glaciology*, **28**(99), 273–293.

Walder, J.S., D.C. Trabant, M. Cunico, S.P. Anderson, R.S. Anderson and A.G. Fountain, 2005. Fault-dominated deformation in an ice dam during annual filling and drainage of a marginal lake., *Annals of Glaciology*, **40**, 174178.

Walsh, R.P.D. and D.M. Lawler, 1981. Rainfall seasonality: description, spatial patterns and change through time, *Weather*, **36**(7), 201–208.

Walter, F., J. Chaput and M.P. Luthi, 2014. Thick sediments beneath Greenland's ablation zone and their potential role in future ice sheet dynamics, *Geology*, **42**(6), 487–490.

Walter, F., N. Deichmann and M. Funk, 2008. Basal icequakes during changing subglacial water pressures beneath Gornergletscher, Switzerland, *Journal of Glaciology*, **54**(186), 511–521.

Wang, G.-Q., D.M. Boore, G. Tang and X. Zhou, 2007. Comparisons of ground motions from colocated and closely spaced one-sample-per-second Global Positioning System and accelerograph recordings of the 2003 M 6.5 San Simeon, California, earthquake in the Parkfield region, *Bulletin of the Seismological Society of America*, **97**(1B), 76–90.

Weertman, J., 1971a. Theory of water-filled crevasses in glaciers applied to vertical magma transport beneath oceanic ridges, *Journal of Geophysical Research*, **76**, 1171–1183.

Weertman, J., 1971b. Velocity at which liquid-filled cracks move in the earths crust or in glaciers, *Journal of Geophysical Research*, **76**, 8544–8553.

Weertman, J., 1973. Can a water filled crevasse reach the bottom surface of a glacier?, *IAHS Publications*, **95**, 139–45.

Whitehead, K., B.J. Moorman and C.H. Hugenholtz, 2013. Low-cost, on-demand aerial

photogrammetry for glaciological measurement, *The Cryosphere Discussions*, **7**(3), 3043–3057.

Willis, I., D. Mair, B. Hubbard, P. Nienow, U.H. Fischer and A. Hubbard, 2003. Seasonal variations in ice deformation and basal motion across the tongue of Haut Glacier dArolla, Switzerland, *Annals of Glaciology*, **36**, 157–167.

Wittlinger, G. and V. Farra, 2012. Observation of low shear wave velocity at the base of the polar ice sheets: Evidence for enhanced anisotropy:, *Geophysical Journal International*, **190**, 391–405.

Zwally, J.H., W. Abdalati, T. Herring, K. Larson, J. Saba and K. Steffen, 2002. Surface melt-induced acceleration of Greenland Ice-Sheet Flow, *Science*, **297**, 218–222.

Appendices

Appendix A

Publications

The following articles were published during the course of this study. They are based on Chapters 5 and 7 respectively and they are included in order below.

Doyle, S.H., Hubbard, A.L., Dow, C.F., Jones, G.A., Fitzpatrick, A., Gusmeroli, A., Kulessa, B., Lindback, K. Pettersson, R. & Box, J.E. 2012. Ice tectonic deformation during the rapid in situ drainage of a supraglacial lake on the Greenland Ice Sheet, *The Cryosphere*, **7**, 129-140. doi:10.5194/tc-7-129-2013.

Doyle, S.H., Hubbard, A., Fitzpatrick, A.A.W., van As, .D., Mikkelsen, A.B., Pettersson, R. & Hubbard, B. 2014. Persistent flow acceleration within the interior of the Greenland ice sheet, *Geophysical Research Letters*, **41**, doi:10.1002/ 2013GL058933.

The Cryosphere, 7, 129–140, 2013
www.the-cryosphere.net/7/129/2013/
doi:10.5194/tc-7-129-2013

The Cryosphere

Ice tectonic deformation during the rapid in situ drainage of a supraglacial lake on the Greenland Ice Sheet

S. H. Doyle[1], A. L. Hubbard[1], C. F. Dow[2], G. A. Jones[1,2], A. Fitzpatrick[1], A. Gusmeroli[2,*], B. Kulessa[2], K. Lindback[3], R. Pettersson[3], and J. E. Box[4]

[1]Centre for Glaciology, Institute of Geography and Earth Sciences, Aberystwyth University, Aberystwyth, SY23 3DB, UK
[2]Glaciology Group, College of Science, Swansea University, Swansea, SA2 8PP, UK
[3]Earth Sciences, Uppsala University, Villavägen 16, 752 36 Uppsala, Sweden
[4]Department of Geography, The Ohio State University, 1036 Derby Hall, 154 North Oval Mall, Columbus, Ohio 43210–1361, USA
[*]now at: International Arctic Research Center, University of Alaska Fairbanks, Fairbanks, Alaska, USA

Correspondence to: S. H. Doyle (sdd08@aber.ac.uk)

Received: 31 July 2012 – Published in The Cryosphere Discuss.: 18 September 2012
Revised: 19 December 2012 – Accepted: 3 January 2013 – Published: 28 January 2013

Abstract. We present detailed records of lake discharge, ice motion and passive seismicity capturing the behaviour and processes preceding, during and following the rapid drainage of a $\sim 4\,km^2$ supraglacial lake through 1.1-km-thick ice on the western margin of the Greenland Ice Sheet. Peak discharge of $3300\,m^3\,s^{-1}$ coincident with maximal rates of vertical uplift indicates that surface water accessed the ice–bed interface causing widespread hydraulic separation and enhanced basal motion. The differential motion of four global positioning system (GPS) receivers located around the lake record the opening and closure of the fractures through which the lake drained. We hypothesise that the majority of discharge occurred through a ~ 3-km-long fracture with a peak width averaged across its wetted length of $\sim 0.4\,m$. We argue that the fracture's kilometre-scale length allowed rapid discharge to be achieved by combining reasonable water velocities with sub-metre fracture widths. These observations add to the currently limited knowledge of in situ supraglacial lake drainage events, which rapidly deliver large volumes of water to the ice–bed interface.

1 Introduction

Variations in the delivery of surface water to the base of the Greenland Ice Sheet induce fluctuations in ice sheet velocity on inter-annual, seasonal, diurnal and sub-diurnal time scales (Zwally et al., 2002; van de Wal et al., 2008; Bartholomew et al., 2010, 2011; Shepherd et al., 2009; Das et al., 2008; Hoffman et al., 2011). For water to access the bed of the Greenland Ice Sheet, a hydraulic pathway must first be established through often kilometre-thick ice. Given sufficient water supply, a water-filled fracture will propagate to the base of an ice mass when the overburden stress at the fracture tip is offset by the density contrast between ice and water (Weertman, 1973; Alley et al., 2005; van der Veen, 2007).

Krawczynski et al. (2009) calculated that supraglacial lakes 250 to 800 m across and 2 to 5 m deep contain sufficient water to drive a fracture to the base of kilometre-thick ice. Many lakes on the Greenland Ice Sheet attain this size or larger (Box and Ski, 2007; Echelmeyer et al., 1991; Georgiou et al., 2009), of which a small proportion (13 % between 2005–2009) drain in less than 2 days (Selmes et al., 2011). Surface lakes can drain rapidly into moulins via supraglacial rivers; however, many drain by the in situ propagation of hydraulically driven fractures (e.g. Das et al., 2008), a process hereafter termed lake tapping.

Lake tapping events provide water fluxes that exceed the capacity of the subglacial drainage system, leading to transient high subglacial water pressures, hydraulic jacking and ice sheet acceleration (Bartholomaus et al., 2008; Das et al., 2008; Pimental and Flowers, 2010). The integrated effect of multiple lake tapping events, and continued water flow into the hydraulic pathways they create, has the capacity to

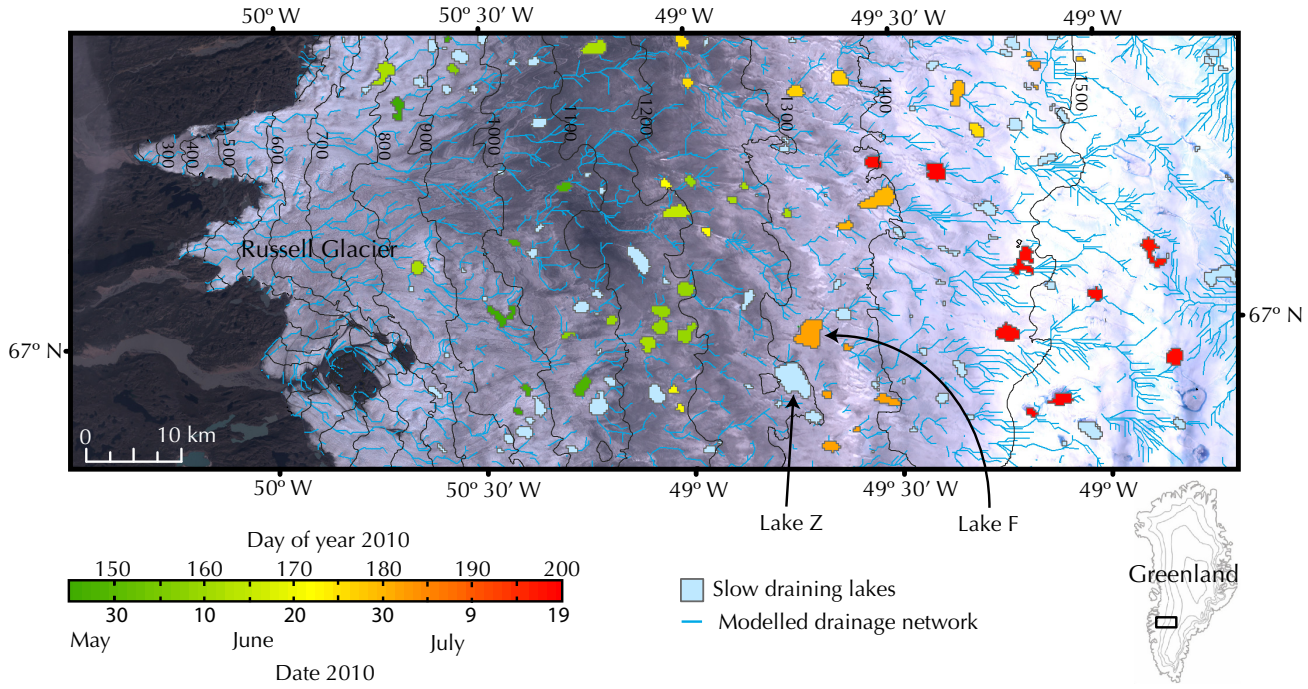

Fig. 1. The maximum extent of supraglacial lakes within the Russell Glacier catchment during the 2010 melt season and the location of the Field Site, Lake F. The green-red colour scheme indicates the timing of rapidly draining (< 4 days) lakes, with slow-draining (> 4 days) lakes in blue. The modelled supraglacial drainage network is shown. The background is a 30 m resolution Landsat image acquired on 18 August 2010.

impact the annual ice flux in future years, especially as, in a warming climate, lakes are expected to form and drain earlier in the season (Liang et al., 2012) and at higher elevations (Howat et al., 2012). It is, however, uncertain whether this increase in water delivery will enhance the annual ice flux through a net increase in basal lubrication (e.g. Zwally et al., 2002), or reduce it due to an earlier seasonal transition to an efficient subglacial drainage system (e.g. Sundal et al., 2011).

Whilst supraglacial lake-tapping events represent major perturbations of the subglacial hydrological system and provide natural experiments for process-based investigations of glacier hydromechanics, few studies have succeeded in capturing them. Boon and Sharp (2003) measured premonitory drainage events preceding the complete and rapid (< 1 h) drainage of a 6.9 m deep supraglacial pond through a 150 m thick Arctic glacier on Ellesmere Island. Das et al. (2008) observed horizontal and vertical ice motion and seismicity during the rapid (∼ 1.4 h) tapping of a large supraglacial lake through 980 m of ice to the bed of the Greenland Ice Sheet. Our study presents detailed measurements of ice motion, lake volume change and seismicity capturing the rapid tapping of a large supraglacial lake through 1.1-km-thick ice on the western margin of the Greenland Ice Sheet.

2 Field site and methods

The field site, Lake F (67.01° N, 48.74° W), is located 70 km from the terminus of Russell Glacier, West Greenland (Fig. 1). Russell Glacier catchment represents a typical land-terminating sector of the Greenland Ice Sheet which, during the melt season, accumulates supraglacial lakes (McMillan et al., 2007) and shows diurnal (e.g. Shepherd et al., 2009) and seasonal (e.g. Bartholomew et al., 2010) covariations in ice velocity and surface uplift.

Remote sensing observations indicate annually repeating growth and rapid drainage of Lake F in the same location, with a mean date of drainage between 2002 and 2009 of 14 July. During the abnormally warm melt seasons of 2003, 2007 and 2010 (see Cappelen et al., 2001; Cappelen, 2011) Lake F tapped 3 to 4 weeks earlier compared to other years in the 2002 to 2010 period.

On 26 June 2010, Lake F was instrumented with four global positioning system (GPS) receivers, six seismometers and two water-level sensors. Five days later at 01:40 on the 30 June, the lake drained completely in ∼ 2 h. Following drainage, the bathymetry of the lake bed and the locations of fractures and moulins were surveyed. Lake volume (V) and discharge (Q) are estimated by combining water-level measurements with the lake bathymetry. All times are expressed in Coordinated Universal Time (UTC), which is three hours ahead of West Greenland Time.

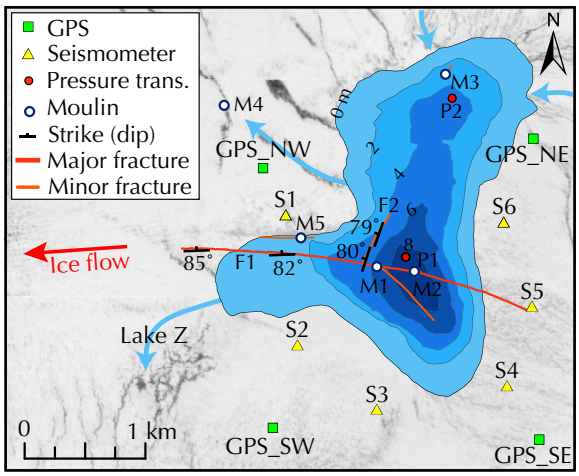

Fig. 2. Map of Lake F showing the instrument array, the fractures and moulins surveyed post-drainage, and the lake perimeter and depth immediately before rapid tapping. The direction of mean ice flow is indicated by the red arrow. The background image is a 5 m resolution SPOT image acquired 7 July 2008. The main supraglacial rivers entering and leaving Lake F are shown by blue arrows.

2.1 Measurements of ice motion

Four dual-frequency GPS receivers (Trimble R7 and Leica SR520) were installed surrounding Lake F (Fig. 2). GPS antennae were installed on 6 m poles drilled 5 m into the ice, which subsequently froze in and thereafter provided a record of 3-D ice surface motion. Data, sampled continuously at a 10 s interval, were processed against a bedrock-mounted reference station using the differential phase kinematic positioning software, Track v. 1.24 (Chen, 1998; Herring et al., 2010), and final precise ephemeris from the International GNSS Service (Dow et al., 2009). The reference station was located 1 km from the terminus of Russell Glacier giving baseline lengths ≤ 70 km. To improve solutions at the day boundary, 36-h files were processed and the first and last six hours of the output position time series were discarded. Assuming steady ice motion, uncertainties in the positions were estimated at < 0.02 m in the horizontal and < 0.05 m in the vertical by examining the detrended position time series for GPS_NW over a 2-day period in May 2011. The output position data are characterised by high-frequency noise caused by receiver and data processing errors. To suppress this high-frequency noise without causing a shift in phase, positions were filtered with a 1-h centred moving average. To quantify differential motion between GPS receivers, relative inter-GPS separation and the rate of separation were calculated from the filtered positions at a 10-min interval.

2.2 Measuring seismic activity

The passive seismic array consisted of six GS-11-D geophones with a natural frequency of 4.5 Hz and a bandwidth of 5 to 1000 Hz, continuously recording micro-seismic velocity at a 1 kHz sampling rate on to a RefTek-130 digitiser. To improve coupling with the ice, the geophones were mounted on 15 kg concrete slabs (dimensions $= 0.5 \times 0.25 \times 0.05$ m), buried to a depth of ~ 0.5 m and routinely reset every 3 to 5 days before they melted out.

The limited number of seismic stations together with the large array aperture (1 to 2 km) and the high rate of seismicity make it difficult to correlate particular onset times with individual events. The inability to identify individual events prevents the location of seismicity using standard methods (e.g. Walter et al., 2008; Roux et al., 2010). Whilst Jones et al. (2013) demonstrate that a technique based on amplitudes may be used to locate such seismicity, the application of this method is beyond the scope of this study.

In this study, the normalised root mean square (RMS) amplitude was calculated for each seismometer using an envelope function with 1-min time windows after applying a 2-pass, 4-pole Butterworth filter. The 5 to 50 Hz passband of the Butterworth filter was selected to reduce both high-frequency noise (> 50 Hz) associated with surface crevassing (e.g. Neave and Savage, 1970) and any low frequencies (< 5 Hz) associated with the instrument response. To identify step changes in seismicity, we calculated the normalised cumulative (seismic) energy from the RMS amplitudes.

2.3 Measurements of lake dynamics

Two pressure transducers (P1 and P2, Solinst M15 Levelogger) were installed in Lake F, logging pressure in metres of water head at two minute intervals with a specified accuracy of ± 1 cm (Fig. 2). The records of P1 and P2 were compensated for changes in atmospheric pressure using a third Solinst Levelogger located at GPS_NW.

Post-tapping, six transects were surveyed across the lake bed with a Leica SR520 GPS receiver recording at 1 Hz. The transects were differentially corrected and interpolated to form a digital elevation model (DEM) of the lake bathymetry with a grid spacing of 10 m. Time series of lake volume (V) and discharge (Q) were calculated by combining the DEM with the water-level data. We estimate the uncertainty in the lake volume and discharge at $\pm 8400\,\mathrm{m}^3$ and $\pm 130\,\mathrm{m}^3\,\mathrm{s}^{-1}$, respectively.

To extend the lake volume record, a time series of Lake F volume was estimated from daily-acquired atmospherically-corrected Moderate-resolution Imaging Spectroradiometer (MODIS) images by applying the method of Box and Ski (2007). Uncertainty in this method was estimated at ± 15 % by comparing MODIS-derived lake volumes with an independently collected lake bathymetry dataset.

To investigate the extent and timing of rapid-draining lakes within the Russell Glacier catchment, an automatic lake classification was applied to daily-acquired, cloud-free MODIS images. Lakes were classified using the Normalised Difference Water Index (NDWI) following the method described

in Huggel et al. (2002). An empirically determined NDWI threshold was used to distinguish between water and other objects with a low NDWI (e.g. ice with a low albedo). The lake classification was trained using lake perimeter measurements derived from Landsat 7 images and differential GPS surveys. In combination with the NDWI threshold, thresholds for both the red and blue bands were used to further reduce misclassification of pixels with a similar spectral signal to water. Images with partial cloud cover were manually inspected. We define rapid draining as lakes that disappear within a 4-day interval, and the date of drainage as the midpoint between the date it was last seen and the date it disappeared. Typically, slow-draining lakes took much longer to drain than the 4-day threshold, and there is a clear distinction between lakes that drain rapidly and those that drain slowly. Figure 1 shows the date of drainage of rapidly draining lakes and the maximum extent of all lakes across the Russell Glacier catchment in 2010. The drainage network shown in Fig. 1 was created using hydrological modelling software (ArcGIS hydrological toolkit) from a 30 m resolution DEM derived from Système Pour l'Observation de la Terre (SPOT) data acquired on 2 July 2008.

2.4 Mapping hydraulic potential gradients

Basal and surface elevation DEMs collected by skidoo-based radio echo sounding following the method of Pettersson et al. (2011) were used to calculate the gradients of hydraulic potential, assuming basal water pressures were everywhere equal to the ice overburden pressure (Shreve, 1972). The resulting hydraulic potential gradients (Fig. 11) can only be used to approximate the direction of subglacial water flow due to the variability in subglacial water pressure and basal hydraulic conductivity.

3 Results

3.1 Regional scale lake dynamics

Within Russell Glacier catchment in 2010, 45 % of the lakes were classified as rapid (< 4 days) draining. The earliest rapid drainage occurred in late May and the latest in mid-July and in general lower-elevation lakes drained earlier than those located at higher elevations. Rapid lake drainage events occur in clusters; multiple lakes within the same elevation band drain simultaneously (Fig. 1). The rapid tapping of Lake F coincided with the rapid drainage of several adjacent lakes and an isolated peak (30 June to 2 July) in the discharge of catchment-wide proglacial Watson River (see Fig. 8 of van As et al., 2012).

3.2 Formation and drainage of Lake F

In 2010 Lake F began to form on 5 June, attaining its maximum extent on 24 June with an area of 4.5 km^2 and a volume of 1.8×10^7 m^3 (Fig. 3). Following the installation of the pressure transducers on 26 June the lake volume steadily decreased at a mean rate of 13.8 m^3 s^{-1} from 1.1×10^7 m^3 to 7.4×10^6 m^3 immediately prior to rapid tapping. This period of low discharge amounts to a volume of 3.6×10^6 m^3 and could be entirely accounted for by supraglacial discharge into Lake Z and moulin M4 (see Figs. 1 and 2). On 28 June 2010, water from Lake F travelled through a slow-flowing series of elongate ponds before a < 1 m wide supraglacial stream fed the water into moulin M4. During the slow period of drainage, the majority of water left Lake F via a 5-m-wide supraglacial river feeding into Lake Z.

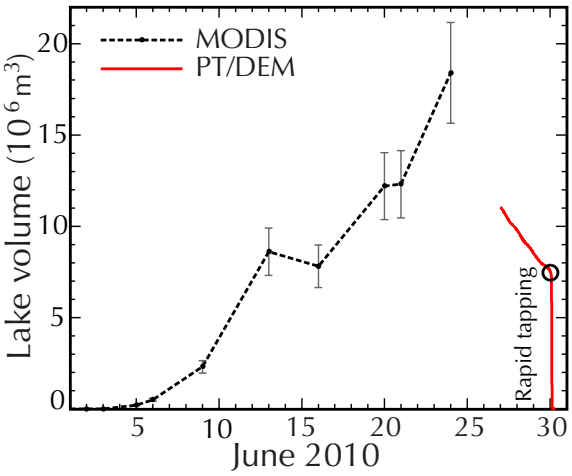

Fig. 3. Time series of Lake F volume in 2010 estimated from MODIS using the method of Box and Ski (2007) and the pressure transducer (PT)/digital elevation model (DEM) calculations. The transition from slow drainage to rapid tapping is indicated by the black circle. Error bars indicate the ± 15 % uncertainty in the lake volumes calculated from MODIS.

Rapid discharge (here defined as $Q > 50$ m^3 s^{-1}), associated with the tapping of the lake via in situ fracture propagation, occurred between 01:40 and 03:15 on the 30 June 2010 with the discharge peaking at $Q_{max} = 3300$ m^3 s^{-1} at 02:47. Lake F had completely drained by 03:50. Immediately prior to rapid tapping, Lake F had a maximum depth of 9.9 m, an area of 3.8 km^2 and a volume of 7.4×10^6 m^3.

3.3 Observations

On 29 June 2010, a healed crevasse, similar to Fig. S5 of Krawczynski et al. (2009), was observed from the western margin of the lake running through the lake in a W–E direction. Closed moulins were observed in the approximate positions of M1 and M5. It is likely that these relic features were formed by lake tapping events in previous years.

At 04:50 on 30 June 2010, less than 2 h after the end of rapid discharge, ∼ 0.3 m deep standing water was observed in the centre of the lake, overflowing across the clean-cut

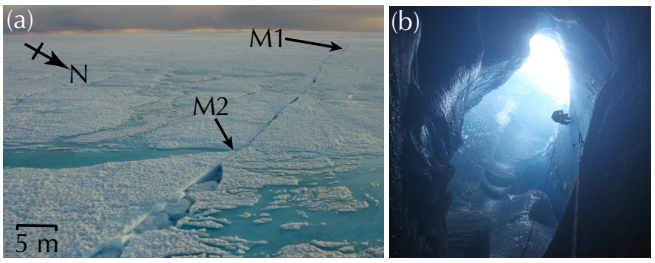

Fig. 4. Photos of Lake F post-drainage: **(a)** the main fracture 8 days after lake tapping, showing the location of moulins M1 and M2 with the deepest region of the lake located 10 m east of M2; and **(b)** the largest moulin M1, ∼ 10 m in diameter. Fallen ice blocks blocked the moulin at 45 m below the surface.

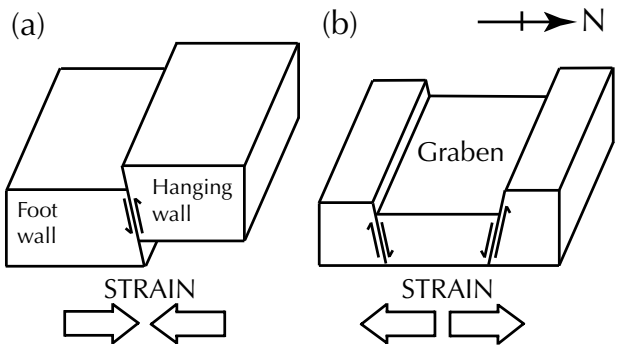

Fig. 5. Supraglacial fracture structures observed along F1: **(a)** a reverse dip-slip fault, dipping 82 to 85° to the north, with the northern hanging wall vertically displaced above the southern foot wall, is evidence for a compressional strain regime; and **(b)**, a high-angle normal fault with a dropped graben, is evidence for extension across F1. Note the greater vertical offset of the northern wall compared to the southern. The diagrams are based on field measurements interpreted with the aid of Price and Cosgrove (1994).

edge of the main fracture F1. Fracture F2 was clean cut and open by ∼ 0.2 m.

On 1 July the location, dip and strike of fractures were surveyed. The main fracture, F1, was mapped for 3 km but extended beyond this as a thin (< 1 cm wide) crack. F1 and F2 were sub-vertical, dipping towards the north and west, respectively (Fig. 2). Differential vertical displacement was observed along F1 with the northern hanging wall displaced typically 0.1 to 0.3 m (but up to 1 m near the centre of the lake) above the southern foot wall. This structure can be interpreted as a reverse dip-slip fault and evidence for transverse (cross-flow) compression (Fig 5a). The largest vertical displacement was measured in the deepest region of the lake, ∼10 m east of M2.

Along F1 a number of ice blocks, detached from the ice surface, had subsided into the fracture or been uplifted by floatation (see Fig. 4a). The structure of the subsided blocks is that of a high-angle normal fault with a dropped 2 to 5 m wide graben (Fig. 5b). Normal faults are evidence for transverse (cross-flow) extension across F1 (Cloos, 1955; Price and Cosgrove, 1994). Similar supraglacial fracture structures associated with hydraulic fracturing were observed following the Skeiðárjökull and Sólheimajökull jökulhaups in 1996 and 1999, respectively (see Fig. 12 of Roberts et al., 2000).

Five moulins (M1 to 5) were also mapped on 1 July (Fig. 2). The largest moulin (M1), ∼ 10 m in diameter, was explored to a depth of 45 m below the surface (Fig. 4b). At 45 m depth M1 continued vertically downwards, but access was restricted by fallen blocks of ice. Water entering M2 could be heard to flow englacially along F1 at a shallow depth before descending vertically down M1.

The main ∼ 5-m-wide supraglacial river flowing into Lake F from the north was intercepted by a fracture, forming three moulins collectively named M3 (Fig. 2). The evolution of the M3 moulins was observed over a number of days and is consistent with Stenborg (1968). Initially, water flowed into the clean-cut fracture at three discrete points and began to cut channels due to the frictional heat of melting. Over time the channels became wider and deeper. The channel of the largest moulin incised the fastest and ultimately captured all the flow. A similar evolution was observed for M2, which also continued to receive water throughout the melt season. Moulins M1 and M5 were not connected to supraglacial streams after rapid tapping.

3.4 Ice displacement

The horizontal and vertical ice motion recorded by the GPS receivers preceding, during and following the lake tapping event are depicted on Fig. 6. The first abnormal GPS motion occurred on 29 June when GPS_SE accelerated to the west, concomitant with ∼ 0.2 m of uplift. GPS_NE and GPS_SW also accelerate, albeit with a lower magnitude. The northern two GPS receivers (GPS_NW and GPS_NE) show anomalous motion in the north–south plane, including transient reverse ice flow at GPS_NW. The mean daily vector for 29 June is of a lower magnitude for the western GPS stations compared to the eastern GPS stations, implying a compressive strain regime that is also evident in the decreasing separations between GPS NW–SE, NW–NE and SW–SE (Fig. 7a, b and f).

A detailed time series of discharge (Q), rate of discharge ($\mathrm{d}Q/\mathrm{d}t$), uplift (Z) and rate of uplift ($\mathrm{d}Z/\mathrm{d}t$) is presented in Fig. 8. At 01:15 on 30 June 2010 the uplift rate at GPS_SW suddenly increases, leading to a maximum 0.34 m of uplift at 02:09. In this period, GPS_NW and GPS_NE are uplifted by 0.07 m and 0.1 m, respectively, and there is no discernible uplift at GPS_SE. Coincident with the start of rapid discharge at 01:40, the uplift rate at GPS_NW increases. In the interval 01:40–02:00, the lake volume decreases by $1.75 \times 10^5\,\mathrm{m}^3$ (2.4 % of the lakes pre-tapping volume) and GPS_NW and GPS_SW move north-west (Fig. 6a and b) with slight compression (Fig. 7c). At 02:00, GPS_NW continues to move in the north–west direction, accelerating and

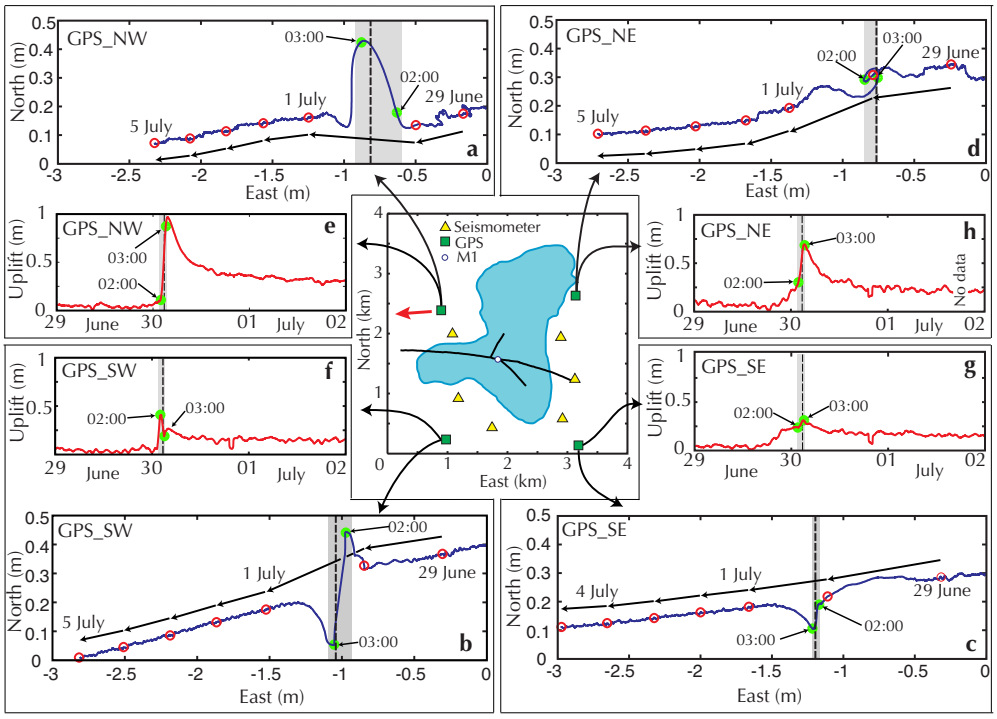

Fig. 6. Horizontal and vertical ice motion recorded by the four GPS receivers. Plots **(a–d)** are plan views of the horizontal motion and **(e–h)** are time series of vertical uplift. To emphasise the transverse (cross-flow) motion the y-axes of **(a–d)** are exaggerated by a factor of 2. The red arrow on the map shows the direction of mean ice flow. On **(a–d)** hollow red circles indicate day boundaries and arrows represent daily vectors. On **(a–h)** solid green circles indicate the times of 02:00 and 03:00; the grey shade indicates the period of rapid ($Q > 50\,\mathrm{m^3\,s^{-1}}$) discharge; and the vertical dashed line indicates the time of maximum discharge $Q_{\max}$.

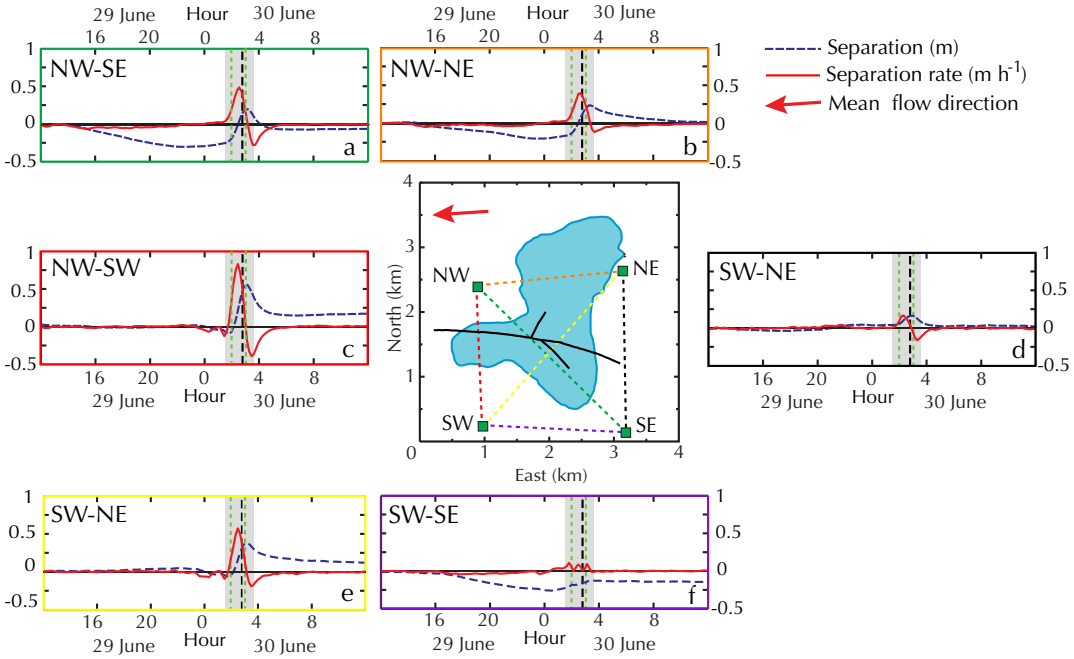

Fig. 7. Inter-GPS separation (blue dashed line) and rate of separation (solid red line). The colour of the axes correspond to the dashed lines on the central map. The red arrow shows the direction of mean ice flow. The grey shade indicates the time of rapid ($Q > 50\,\mathrm{m^3\,s^{-1}}$) discharge, the black dashed line indicates the time of peak discharge $Q_{\max}$ and the green dashed lines indicate the times of 02:00 and 03:00.

reaching a maximum displacement to the north of 0.3 m. At the same time (02:00), GPS_SW reverses in direction, moving to the south–west (Fig. 6b) coincident with a step increase in the discharge (Fig. 8a and b), seismicity (Fig. 9), uplift rate at GPS_NW (Fig. 8c), and separation rate between all the GPS receivers with the exception of GPS SW–SE (Fig. 7). Rapid separation continues until 03:00 when GPS_SW reverses to the north (Fig. 6b) and GPS_NW reverses to the south (Fig. 6a), causing the separation rates to become negative (Fig. 7). The maximum discharge $Q_{\max}$ of $3300\,m^3\,s^{-1}$ occurs at 02:47 simultaneous with the peak uplift rate at GPS_NW of $0.8\,m\,h^{-1}$ (Fig. 8). The maximum relative separation between GPS NW–SW, NW–SE, NW–NE and SW–NE is attained at 03:00 (Fig. 7), simultaneous with a lull in seismicity across all six seismometers (Fig. 9) and a transient $1\,m^3\,s^{-2}$ increase in the discharge rate (dQ/dt) which remains negative (Fig. 8b). At 03:00 there is a short-lived (15-min) period of uplift at GPS_SW. Post 03:00 inter-GPS separations decrease as the discharge reduces. Rapid discharge ends at 03:15 with $V = 4.8 \times 10^4\,m^3$ (0.65 % remaining). Peak uplift at GPS_NW of 0.9 m is not reached until 03:40. Following peak uplift, GPS_NW subsides at a gradually reducing rate (mean uplift rate of $-0.07\,m\,h^{-1}$) remaining 0.3 m above its pre-tapping elevation by the end of 30 June 2010. Accordingly, GPS_SW, GPS_SE and GPS_NE remain uplifted by 0.1, 0.18 and 0.24 m, respectively.

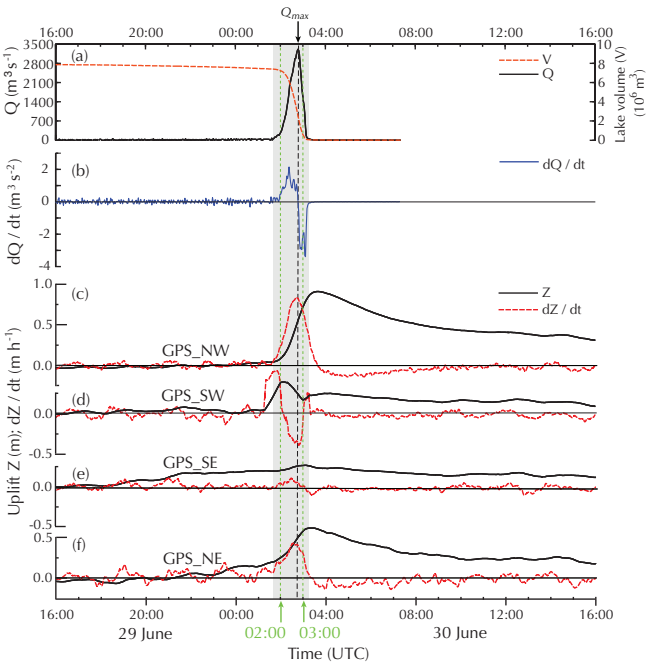

Fig. 8. Time series of **(a)** volume V and discharge Q, **(b)** rate of discharge dQ/dt, and **(c–f)** uplift Z and the rate of uplift dZ/dt for each GPS receiver. The grey shade indicates the time of rapid ($Q > 50\,m^3\,s^{-1}$) discharge. The black dashed line indicates the time of peak discharge $Q_{\max}$ and the green dashed lines indicate the times of 02:00 and 03:00.

4 Interpretation and discussion

On the basis of the observations described above, the rapid in situ tapping of Lake F on the 30 June 2010 can be decomposed into three episodes: (1) initial drainage (01:40–02:00); (2) fracture opening (02:00–03:00); and (3) fracture closure (03:00–03:15). The horizontal and vertical ice surface velocities during each episode are illustrated on Fig. 10. These episodes are bounded by the duration of rapid discharge and it should be noted that closure of fractures extended beyond 03:15 (see Fig. 7). The timings of each episode, together with the time of $Q_{\max}$, are indicated on Figs. 6, 7 and 8.

Episode 1 begins at the onset of rapid discharge and ends when GPS_SW changes direction to the south, causing north–south extension across the lake (Fig. 10a). In episode 1, a small ($1.7 \times 10^5\,m^3$, 2.4 % of the lakes pre-tapping volume) amount of water drains coincident with uplift concentrated at GPS_SW and an increase in seismicity for the western half of the seismic array (S1–3, Fig. 9). Little or no increase in seismicity is recorded by the eastern seismometers (S4–6, Fig. 9).

As the fractures open in episode 2, Q rapidly increases peaking at 02:47 ($Q_{\max} = 3300\,m^3\,s^{-1}$) simultaneous to the maximum rate of uplift at GPS_NW ($dZ/dt = 0.8\,m\,h^{-1}$), indicating that water rapidly attained the ice–bed interface causing hydraulic ice–bed separation. The divergence of GPS NW–SE, NW–SW, SE–NE and SW–NE (Fig. 7a, c, d and e) are interpreted as the opening of the main fracture F1 (Fig. 10b). Likewise, short-term longitudinal (with-flow) extension between GPS_NW and GPS_NE of ~ 0.2 m (Fig. 7b), involving the reverse motion of GPS_NE commencing at 02:00 (see Fig. 6d), is interpreted as the opening of subsidiary fracture F2. The opening of F2 involves the displacement of GPS_NE to the east up the bed slope (Fig. 11). As soon as discharge begins to decrease after 02:47 the force holding F2 open reduces and, aided by the bed slope, GPS_NE reverses in direction to the west (Fig. 6d), closing F2. The circular path of GPS_NE during lake tapping (Fig. 6d) can be interpreted as the combined effect of fractures F1 and F2 opening and closing. In episode 2, 90 % ($6.7 \times 10^6\,m^3$) of the lakes pre-tapping volume drained compared to just 6.8 % ($5.1 \times 10^5\,m^3$) in episode 3.

At 03:00, the boundary between episodes 2 and 3, the fractures attain their maximum width, and the short respite in fracturing is coincident with a lull in seismicity evident in the records for all six seismometers (Fig. 9). This quiescence suggests that seismicity is predominantly generated by the opening and closure of fractures and not by water flow which was continuing at a high rate ($Q = 1450\,m^3\,s^{-1}$).

Immediately after 03:00, there was a step increase in seismicity particularly evident at seismometer S4 (Fig. 9j), as the inter-GPS separation rates between GPS 1–3, 1–4, 1–2, 3–4 and 2–4 became negative (Fig. 7) as the fractures

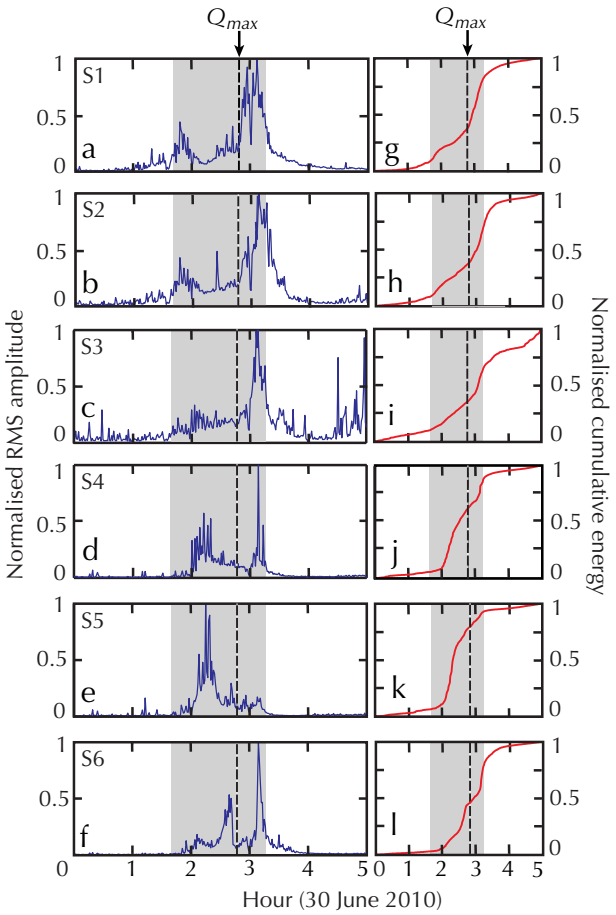

Fig. 9. Normalised seismic RMS amplitude (**a–f**) and normalised seismic cumulative energy (**g–l**) for the passive seismic array ordered anticlockwise from west (S1) to east (S6). The time of rapid ($Q > 50\,m^3\,s^{-1}$) discharge (grey shade) and the time of maximum discharge (dashed vertical line) are indicated.

closed (Fig. 10c). Episode 3 is characterised by decreasing discharge and uplift (Fig. 8). Following the end of rapid discharge, the rate of closure reduces, but it takes several hours before the inter-GPS separation rates stabilise (Fig. 7). We attribute the elevated seismicity post-03:15 (Fig. 9) to continuing fracture closure (Fig. 10c) and the subsidence of GPS_NW and GPS_NE (Fig. 8c and f).

Following lake tapping, the inter-GPS separations show a stable increase in length between GPS NW–SW/blackbox[CE]For the consistency of all pages, please change the hyphens to endashes in the directions within Fig. 7 graphs and GPS SW–NE and a stable shortening between GPS SW–SE and NW–SE (Fig. 7). This supports the observation of juxtaposed extensional and compressional supraglacial fracture structures (Fig. 5). The separation between GPS NW–NE and GPS SE–NE reduces to ~ 0 m by 12:00 on 30 June, suggesting the total closure of F2 and the most eastern section of F1, respectively. This observation is consistent with the small (cm-scale) fracture width measured in the field.

The characteristics of the rapid tapping of Lake F are consistent with Das et al. (2008), who observed the rapid (1.4 h) drainage of a 4.4×10^7 m^3 supraglacial lake through 980 m-thick ice on the western margin of the Greenland Ice Sheet at 68.7° N. The reverse and circular motion of the singular GPS station of Das et al. are comparable to those of GPS_NE which was similarly located on westerly flowing ice, north of a longitudinal (with-flow) fracture and west of a transverse (cross-flow) fracture. The step increases in seismicity observed during the tapping of Lake F (Fig. 9) are also comparable (see Fig. S3 of Das et al., 2008).

Prior to lake tapping, a healed crevasse consistent with Fig. S5 of Krawczynski et al. (2009), was observed running from the western margin of the lake easterly towards its centre. Closed moulins were observed in the approximate positions of M1 and M5. It is likely that the healed crevasse and the closed moulins are relic features formed during tapping events in previous years. It is possible that the rapid tapping in 2010 was the re-opening of fractures and moulins formed in previous years; however, our observations do not reveal whether tapping involved the formation of a new fracture or the re-activation of a healed crevasse.

4.1 Initiation mechanism

Drainage of water into moulin M4, located to the west of Lake F, during the slow-discharge period prior to rapid tapping could theoretically cause localised uplift and acceleration leading to longitudinal (with-flow) extension. Alley et al. (2005) assert that the tensile stress caused by the acceleration of downstream ice may be important for initiating hydrofractures. However, discharge into 1-m-wide M4 was relatively low and prior to the tapping of Lake F there is no evidence for longitudinal (with-flow) extension (Fig. 7). On the contrary, the two western GPS receivers (GPS_NW and GPS_SW) were uplifted and accelerated several hours later than the two eastern GPS receivers (GPS_SE and GPS_NE), causing longitudinal (with-flow) compression across the lake in the hours preceding lake tapping (Fig. 7b and f).

The observation of a compressive strain regime prior to lake tapping is in agreement with Krawczynski et al. (2009), who found that water-filled crevasses can propagate without longitudinal (with-flow) tension and that a given volume of water has the propensity to propagate a water-filled crack further in regions with less tension (or even slight compression), as thinner cracks require less water to remain water filled.

Although it is possible that small drainage events were masked by variations in supraglacial discharge, the lack of notable changes in the lake volume prior to 01:40 on 30 June 2010 (Fig. 8a) suggests that premonitory drainage events as observed by Boon and Sharp (2003) did not occur.

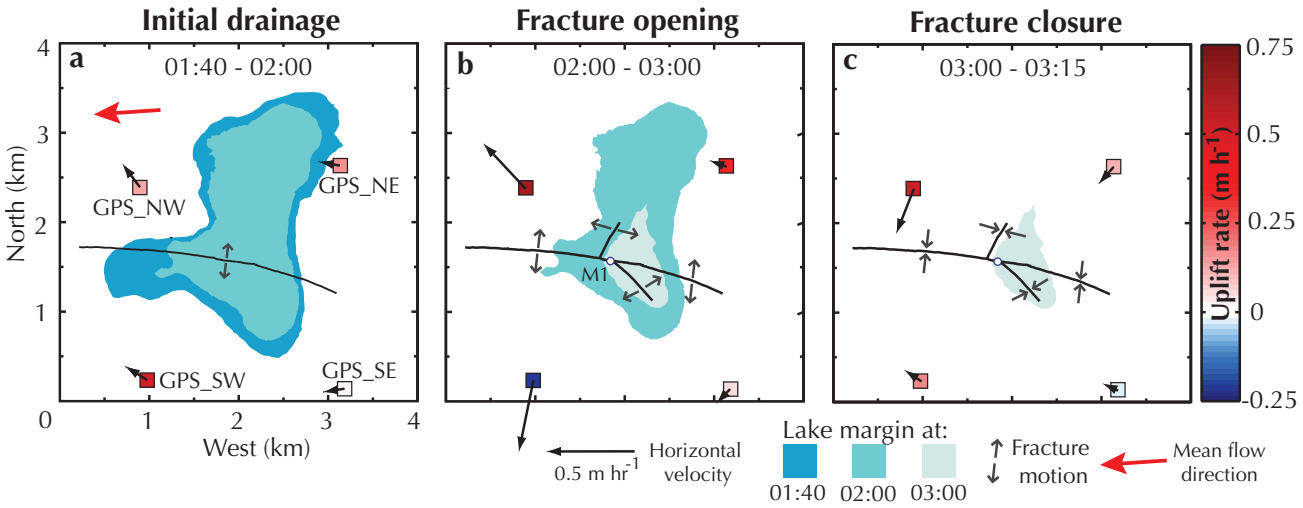

Fig. 10. Horizontal and vertical velocities during the three episodes of Lake F's rapid drainage: **(a)** initial drainage; **(b)** fracture opening; and **(c)** fracture closure. Black arrows represent horizontal velocity vectors. The red arrow represents the mean ice flow direction and is not scaled by magnitude. The colour of each GPS symbol represents the mean uplift rate. The lake margin at each time step is shown.

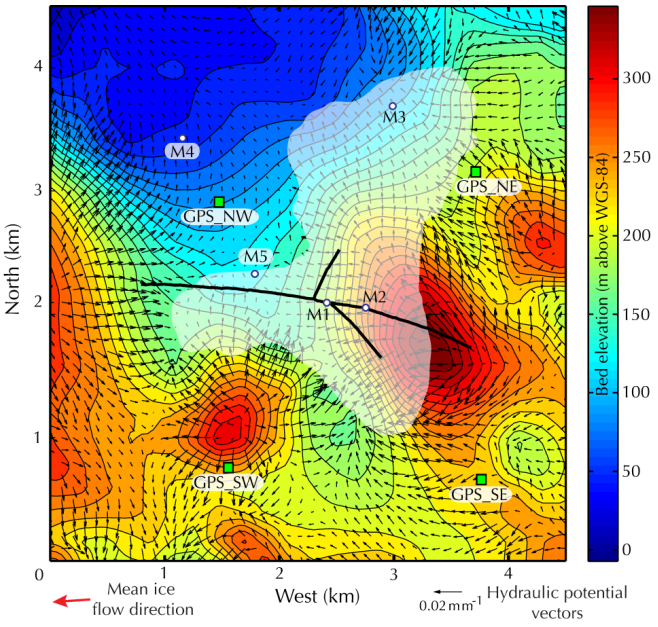

Fig. 11. Map of the hydraulic potential gradients and subglacial topography for Lake F. The black arrows are vectors of hydraulic potential gradient scaled by the metres of hydraulic potential change per metre. The gradients of hydraulic potential were calculated assuming basal water pressures were everywhere equal to the ice overburden pressure. The lake margin immediately prior to lake tapping is shown together with the locations of moulins, fractures and GPS receivers. The contour interval for the basal topography is 10 m.

4.2 Hydraulic pathways

We assert that during lake tapping, discharge occurred along most of the fractures' lengths. Assuming first that the inter-GPS separation is entirely a result of fracturing, and second following Krawczynski et al. (2009) that the fractures are parallel-sided with constant width, the fractures' cross-sectional area at the time of peak separation (03:00) can be estimated. Interpolating the maximum separation between GPS NW–SW, NW–SE, SW–NE and SE–NE gives a peak fracture width averaged over F1's 2.6 km-wetted-length of 0.4 m and an estimated maximum cross-sectional area of 842 m^2. This fracture width agrees well with the modelling results of Krawczynski et al. (2009) that suggest an idealised conical lake of a similar size to Lake F (diameter = 2.2 km, area = 3.8 km^2) would drain via a 0.4-m-wide fracture across the width of the lake in ∼ 2 h. The maximum cross-sectional area of F2 is estimated at 140 m^2. Combined, F1 and F2 have a total cross-sectional area at 03:00 of 982 m^2. Dividing the discharge at 03:00 ($Q = 1450\,m^3\,s^{-1}$) by the combined cross-sectional area gives a mean flow velocity of 1.5 $m\,s^{-1}$. Hence, due to the length of the fractures, rapid discharge can be achieved by combining reasonable water velocities with sub-metre fracture widths. Assuming an ice thickness of 1100 m, the total volume of the fractures at 03:00 is 1.1×10^6 m^3, or 15 % of the lake volume prior to tapping. The actual volume of water that drained between 01:40 and 03:00 was much larger at 6.8×10^6 m^3.

During rapid discharge the frictional heat of turbulent flow would preferentially melt the sections of the fracture transporting the greatest flux, leading to the concentration of flow (Walder, 1982) and the development of moulins. There is a clear distinction between moulins that formed during rapid discharge and moulins that formed afterwards. Immediately, post-tapping moulins M1 and M5 were fully formed but dry whilst moulins M2 and M3 were clean-cut fractures accepting water. We assert that discharge was initially concentrated

down the largest (∼10 m diameter) moulin M1 (Fig. 4b). When the water level fell below the elevation of M1 surface water flow would have been concentrated through F1 in the deepest region of the lake, ∼10 m east of M2 (Fig. 2).

At 04:50 on 30 June 2010, < 2 h after rapid tapping, there were no supraglacial channels in the lake bed. A shallow (∼ 0.3 m deep) pond of water in the deepest region of the lake was overflowing the clean cut edge of F1. Over a number of days, channels formed by the frictional heat of preferential water flow, concentrating water flow into discrete moulins. Continued water flow into moulins would work to keep moulins open for the remainder of the melt season. On 1 July, sections of the fracture were water filled and water draining into moulin M2 could be heard to flow laterally along F1 at a shallow depth before draining into moulin M1, suggesting that post-tapping large sections of the fracture were closed.

4.3 Vertical ice surface motion

Ice surface uplift is typically attributed to bed-parallel motion, vertical strain and ice–bed separation due to high subglacial water pressures (Hooke et al., 1989). Fault displacement (Fig. 5) may also cause vertical ice motion (e.g. Walder et al., 2005). All four factors must be considered when interpreting the vertical motion of a GPS receiver installed on the ice surface.

The bed slope within the study area is highly variable (Fig. 11) and may be responsible for some of the differential ice motion (Fig. 6). In contrast to the smooth vertical motion of GPS_NW, GPS_SE and GPS_NE the vertical motion of GPS_SW is characterised by sudden steps coincident with the start and end of the fracture opening episode. GPS_SW is located on the strongest subglacial gradient of all the GPS receivers, south of a conical subglacial peak (see Fig. 11). Horizontal motion along the inclined bed slope can satisfactorily explain the vertical motion of GPS_SW. At 00:00 on 30 June 2010 the trajectory of GPS_SW was perturbed to the north-west, coincident with ∼5 cm of uplift. This vertical motion can be explained by north-westerly motion up the bed slope (Fig. 11). The subsequent southerly-motion of GPS_SW down the bed slope between 02:00 and 03:00 is coincident with subsidence. This lowering is simultaneous with uplift at GPS_NW, GPS_SE and GPS_NE, suggesting that the water delivered to the bed during rapid discharge did not access the bed beneath GPS_SW. Finally, at 03:00 when GPS_SW moves north up the bed slope there is a second low magnitude (10 cm) period of uplift exclusive to GPS_SW.

Sugiyama et al. (2008) observed the greatest uplift near to the drainage centre during the subglacial drainage of ice-marginal lake Gornersee in Switzerland and we therefore assert, like Das et al. (2008), that surface uplift was likely greater near the centre of the lake. The highest-magnitude uplift observed in this study of 0.9 m by GPS_NW is the most consistent with the 1.2 m of uplift measured by Das et al.. The bed slope underneath GPS_NW slopes down towards the north-west (Fig. 11) so north-west acceleration during the fracture opening episode is not responsible for the observed uplift at GPS_NW. Vertical strain cannot account for the uplift as extension (which would cause thinning and lowering) was observed for all the inter-GPS separations involving GPS_NW during this episode (Fig. 7a, b, c). Fault displacement in the form of vertical offset of the fracture walls in a reverse dip-slip fault is attributed to compressional strain (Fig. 5b) which is unlikely to have occurred during the fracture opening episode when all inter-GPS separations were extensional (Fig. 7). As neither motion along an inclined bed slope, vertical strain or fault displacement can explain the observed vertical motion of GPS_NW during the fracture opening episode, the uplift at GPS_NW can be attributed to ice–bed separation resulting from high subglacial water pressures caused by the delivery of a large quantity (6.7×10^6 m^3 or 90 % of the lakes pre-tapping volume) of water to the ice–bed interface.

4.4 Subglacial water routing

We argue subglacial water delivered to the ice–bed interface along F1 would be preferentially routed through a subglacial valley to the north-west (Fig. 11) . Field measurements of the fracture structure and the differential motion of the GPS receivers support this assertion. Based on the locations of F1 and F2, we can conceptualise the ice mass structurally into three semi–independent blocks: the southern, north-eastern and north-western. The direction of dip of sub-vertical fractures F1 and F2, to the north and west respectively (see Figs. 2 and 5), together with the permanent offset of the northern hanging wall above the southern foot wall of F1, suggest that during the fracture opening episode, the north-western block was preferentially uplifted and ejected to the north-west. This is consistent with the observation of the greatest horizontal and vertical motion of the north-western block on which GPS_NW was located (Fig. 6a and e) and the highest rate of seismicity recorded by the most western seismometers (S1–3, Fig. 9). In contrast to the slow subsidence of GPS_NW, GPS_SE and GPS_NE following the end of rapid discharge, the vertical motion of GPS_SW rapidly returned to a steady height (Fig. 8), suggesting that water was not routed or stored at the bed in this area.

5 Conclusions

Detailed measurements of ice surface motion, discharge and seismicity during the rapid in situ drainage of a large annually-tapping supraglacial lake through kilometre-thick ice on the western margin of the Greenland Ice Sheet contribute to the currently limited knowledge of rapid supraglacial lake tapping events.

Horizontal ice motion during lake tapping is dominated by ice tectonic deformation involving the transient opening and closure of multiple fractures. We assert that during rapid discharge, water flowed down most of the fractures' lengths. By reconstructing the peak cross-sectional area of the fractures from the inter-GPS separations, we find that the fractures' kilometre-scale lengths allow rapid discharge to be achieved by combining reasonable water velocities with submetre fracture widths.

The maximum uplift rate of $0.8\,\mathrm{m\,h^{-1}}$ occurred simultaneously with the maximum discharge of $3300\,\mathrm{m^3\,s^{-1}}$ providing evidence that water rapidly attained the ice–bed interface, raising subglacial water pressures above overburden over a large area of the bed. Basal topography and the gradient of hydraulic potential exerted control on water routing, horizontal ice motion and uplift. The greatest horizontal displacement and vertical uplift was observed above the preferential subglacial drainage route. Lake tapping events rapidly deliver large pulses of surface water to the bed of the Greenland Ice Sheet, causing transient ice–bed separation and acceleration; however, it remains unclear what impact this water delivery will have on the annual ice flux.

Acknowledgements. This research was funded by the Greenland Analogue Project, Sub-Project A and by UK Natural Environment Research Council (NERC) grants NE/G007195/1 and NE/G005796/1. The seismic instruments were provided by Seis-UK at the University of Leicester. S. H. D. is supported by an Aberystwyth University doctoral scholarship. C. F. D. and A. F. are supported by NERC doctoral scholarships and G. A. J. is supported by NERC research grant NE/G007195/1. Ian Bartholomew and Matt King are thanked for advice on GPS processing. Christian Helanow, Adam Booth and Henry Patton are thanked for assistance in the field. Nolwenn Chauché is thanked for helpful discussion. Shin Sugiyama, Mauri Pelto and an anonymous reviewer are thanked for constructive comments. TEQC software was used to convert the raw GPS data to Receiver INdependent EXchange (RINEX) format (Estey and Meertens, 1999). MODIS data are distributed by the Land Processes Distributed Active Archive Center (LP DAAC), located at the USGS EROS Center (http://lpdaac.usgs.gov). Landsat data are distributed by the US Geological Survey (http://glovis.usgs.gov).

Edited by: G. H. Gudmundsson

References

Alley, R., Dupont, T., Parizek, B., and Anandakrishnan, S.: Access of surface meltwater to beds of sub-freezing glaciers: preliminary insights, Ann. Glaciol., 40, 8–13, doi:10.3189/172756405781813483, 2005.

Bartholomaus, T., Anderson, R., and Anderson, S.: Response of glacier motion to transient water storage, Nat. Geosci., 1, 33–37, doi:10.1038/ngeo.2007.52, 2008.

Bartholomew, I., Nienow, P., Mair, D. and Hubbard, A. and King, M.A. and Sole, A.: Seasonal evolution of subglacial drainage and acceleration in a Greenland outlet glacier, Nat. Geosci., 3, 408–411, doi:10.1038/ngeo863, 2010.

Bartholomew, I., Nienow, P., Sole, A., Mair, D., Cowton, T., King, M., and Palmer, S.: Seasonal variations in Greenland Ice Sheet motion: inland extent and behaviour at higher elevations, Earth Planet. Sc. Lett., 307, 271–278, doi:10.1016/j.epsl.2011.04.014, 2011.

Boon, S. and Sharp, M.: The role of hydrologically-driven ice fracture in drainage system evolution on an Arctic glacier, Geophys. Res. Lett., 30, 1–4, 1916, doi:10.1029/2003GL018034, 2003.

Box, J. and Ski, K.: Remote sounding of Greenland supraglacial melt lakes: implications for subglacial hydraulics, J. Glaciol., 53, 257–265, doi:10.3189/172756507782202883, 2007.

Cappelen, J.: DMI Monthly Climate Data Collection 1768–2010, Denmark, The Faroe Islands and Greenland, Danish Meteorlogical Institute, Tech. Rep., 11-05, pp. 54, 2011.

Cappelen, J., Jørgensen, B., Laursen, E., Stannius, L., and Thomsen, R.: The observed climate of Greenland, 1958–1999 – with climatological standard normals, 1961–1990, Danish Meteorlogical Institute, Tech. Rep., 0–18, 2001.

Chen, G.: GPS kinematic positioning for the airborne laser altimetry at Long Valley, California, Ph. D. thesis, Mass. Inst. of Technol., Cambridge, available at: http://dspace.mit.edu/bitstream/handle/1721.1/9680/42583460.pdf?sequence=1, 1998.

Cloos, E.: Experimental analysis of fracture patterns, Bulletin of the Geological Society of America, 66, 241–256, 1955.

Das, S., Joughin, I., Behn, M., Howat, I., King, M., Lizarralde, D., and Bhatia, M.: Fracture propagation to the base of the Greenland Ice Sheet during supraglacial lake drainage, Science, 320, 778–781, doi:10.1126/science.1153360, 2008.

Dow, J., Neilan, R. E., and Rizos, C.: The International GNSS Service in a changing landscape of Global Navigation Satellite Systems, J. Geo., 83, 191–198, doi:10.1007/s00190-008-0300-3, 2009.

Echelmeyer, K., Clarke, T., and Harrison, W.: Surficial glaciology of Jakobshavn Isbrae, West Greenland: Part I, Surface morphology, J. Glaciol., 37, 368–382, 1991.

Estey, L. and Meertens, C.: TEQC: The multi-purpose toolkit for GPS/ GLONASS data, GPS Solut., 3, 42–29, 1999.

Georgiou, S., Shepherd, A., McMillan, M., and Nienow, P.: Seasonal evolution of supraglacial lake volume from ASTER imagery, Ann. Glaciol., 50, 95–100, doi:10.3189/172756409789624328, 2009.

Herring, T., King, R., and McClusky, S.: GAMIT Reference Manual, Release 10.4, Massachusetts Institute of Technology, Cambridge, available at: http://www-gpsg.mit.edu/~simon/gtgk/GAMIT_Ref.pdf, 2010.

Hoffman, M., Catania, G., Neumann, T., Andrews, L., and Rumrill, J.: Links between acceleration, melting, and supraglacial lake drainage of the Western Greenland Ice Sheet, J. Geophys. Res., 116, F04035, doi:10.1029/2010JF001934, 2011.

Hooke, R.L., Calla, P., Holmlund, P., Nilsson, M., and Stroeven, A.: A 3 year record of seasonal variations in surface velocity, Storglaciaren, Sweden, J. Glaciol., 35, 235–247, 1989.

Howat, I. M., de la Peña, S. and van Angelen, J. H., Lenaerts, J. T. M., and van den Broeke, M. R.: Brief Communication "Expansion of meltwater lakes on the Greenland ice sheet, The Cryosphere Discussions, 6, 4447–4454, doi:10.5194/tcd-6-4447-2012, 2012.

Huggell, C., Kaab, A., Haeberli, W., Teysseire, P. Paul, F.: Remote sensing based assessment of hazards from glacier lake outbursts: a case study in the Swiss Alps, Canadian Geotechnical Journal, 39, 316–330, 2002.

Jones, G. A., Kulessa, B., Doyle, S. H., Dow, C. F., and Hubbard, A.: An automated approach to the location of icequakes using seismic waveform amplitudes, Ann. Glaciol., 54, 1–9, doi:10.3189/2013AoG64A074, 2013.

Krawczynski, M., Behn, M., Das, S., and Joughin, I.: Constraints on the lake volume required for hydro-fracture through ice sheets, Geophys. Res. Lett., 36, 1–5, doi:10.1029/2008GL036765, 2009.

Liang, Y-L., Colgan, W., Lv, Q., Steffen, K., Abdalati, W., Stroeve, J., Gallaher, D., and Bayou, N.: A decadal investigation of supraglacial lakes in West Greenland using a fully automatic detection and tracking algorithm, Remote Sens. Environ., 123, 127–138, doi:10.1016/j.rse.2012.03.020, 2012.

McMillan, M., Nienow, P., Shepherd, A., Benham, T., and Sole, A.: Seasonal evolution of supra-glacial lakes on the Greenland Ice Sheet, Earth Planet. Sc. Lett., 262, 484–492, doi:10.1016/j.epsl.2007.08.002, 2007.

Neave, K. G. and Savage, J. C.: Icequakes on the Athabasca Glacier, J. Geophys. Res., 75, 1361–1362, doi:10.1029/JB075i008p01351, 1970.

Palmer, S., Shepherd, A., Nienow, P., and Joughin, I.: Seasonal speedup of the Greenland Ice Sheet linked to routing of surface water, Earth Planet. Sc. Lett., 302, 423–428, doi:10.1016/j.epsl.2010.12.037, 2011.

Pettersson, R., Christoffersen, P., Dowdeswell, J. A., Pohjola, V. A., Hubbard, A. L., and Strozzi, T.: Ice thickness and basal conditions of Vestfonna Ice Cap, Eastern Svalbard, Geografiska Annaler: Series A, Phys. Geogr., 93, 311–322, doi:10.1111/j.1468-0459.2011.00438.x, 2011.

Pimental, S. and Flowers, G.: A numerical study of hydrologically driven glacier dynamics and subglacial flooding, P. Roy. Soc., 467, 537–558, doi:10.1098/rspa.2010.0211, 2010.

Price, N. J., and Cosgrove, J. W.: Analysis of geological structures, University Press, Cambridge, 1994.

Roberts, M. J., Russell, A. J., Tweed, F. S., and Knudsen, Ó.: Ice fracturing during jökulhlaups: implications for englacial floodwater routing and outlet development, Earth Surf. Processes, 25, 1429–1446, 2000.

Roux, P.-F., Walter, F., Riesen, P., Sugiyama, S., and Funk, M.: Observation of surface seismic activity changes of an Alpine glacier during a glacier-dammed lake outburst, J. Geophys. Res., 115, F03014, doi:10.1029/2009JF001535, 2010.

Selmes, N., Murray, T., and James, T.: Fast draining lakes on the Greenland Ice Sheet, Geophys. Res. Lett., 38, L15501, doi:10.1029/2011GL047872, 2011.

Shepherd, A., Hubbard, A., Nienow, P., King, M., McMillan, M., and Joughin, I.: Greenland ice sheet motion coupled with daily melting in late summer, Geophys. Res. Lett., 36, 1–4, doi:10.1029/2008GL035758, 2009.

Shreve, R.: Movement of water in glaciers, J. Glaciol., 11, 205–214, 1972.

Stenborg, T.: Glacier drainage connected with ice structures, Geogr. Ann., 50, 25–53, 1968.

Sugiyama, S., Bauder, A., Huss, M., Riesen, P., and Funk, M.: Triggering and drainage mechanisms of the 2004 glacier-dammed lake outburst in Gornergletscher, Switzerland, J. Geophys. Res., 113, F04019, doi:10.1029/2007JF000920, 2008.

Sundal, A.V., Shepherd, A., Nienow, P., Hanna, E., Palmer, S., and Huybrechts, P.: Melt-induced speed-up of Greenland ice sheet offset by efficient subglacial drainage, Nature, 469, 521–524, doi:10.1038/nature09740, 2011.

van As, D., Hubbard, A. L., Hasholt, B., Mikkelsen, A. B., van den Broeke, M. R., and Fausto, R. S.: Large surface meltwater discharge from the Kangerlussuaq sector of the Greenland ice sheet during the record-warm year 2010 explained by detailed energy balance observations, The Cryosphere, 6, 199–209, doi:10.5194/tc-6-199-2012, 2012.

van de Wal, R., Boot, W., van den Broeke, M., Smeets, C., Reijmer, C., Donker, J., and Oerlemans, J.: Large and rapid melt-induced velocity changes in the ablation zone of the Greenland Ice Sheet, Science, 321, 111–113, doi:10.1126/science.1158540, 2008.

van der Veen, C.: Fracture propagation as means of rapidly transferring meltwater to the base of glaciers, Geophys. Res. Lett., 34, L01501, doi:10.1029/2006GL028385, 2007.

Walder, J.S.: Stability of sheet flow of water beneath temperate glaciers and implications for glacier surging, J. Glaciol., 28, 273–293, 1982.

Walder, J. S., Trabant, D. C., Cunico, M., Anderson, S. P., Anderson, R. S., and Fountain, A. G., Fault-dominated deformation in an ice dam during annual filling and drainage of a marginal lake, Ann. Glaciol., 40, 174–178, doi:10.3189/172756405781813456, 2005.

Walter, F., Deichmann, N., and Funk, M.: Basal icequakes during changing subglacial water pressures beneath Gornergletscher, Switzerland, J. Glaciol., 54, 511–521, doi:10.3189/002214308785837110, 2008.

Weertman, J.: Can a water filled crevasse reach the bottom surface of a glacier?, Symposium on the Hydrology of Glaciers: Water within glaciers II, Int. Assoc. Sci. Hydrol., 95, 139–145, 1973.

Zwally, J., Abdalati, W., Herring, T., Larson, K., Saba, J., and Steffen, K.: Surface melt-induced acceleration of Greenland Ice-Sheet Flow, Science, 297, 218–222, doi:10.1126/science.1072708, 2002.

AGU PUBLICATIONS

Geophysical Research Letters

RESEARCH LETTER
10.1002/2013GL058933

Key Points:
- Ice flow in the accumulation area accelerated year-on-year between 2009 and 2012
- The acceleration correlates with the inland expansion of supraglacial lakes
- This dynamic response contrasts with observations from the ablation zone

Supporting Information:
- Readme
- Tables S1 to S5
- Figure S1
- Figure S2
- Data and methods

Correspondence to:
S. H. Doyle,
sdd08@aber.ac.uk

Citation:
Doyle, S. H., A. Hubbard, A. A. W. Fitzpatrick, D. van As, A. B. Mikkelsen, R. Pettersson, and B. Hubbard (2014), Persistent flow acceleration within the interior of the Greenland ice sheet, *Geophys. Res. Lett.*, *41*, doi:10.1002/2013GL058933.

Received 3 DEC 2013
Accepted 13 JAN 2014
Accepted article online 15 JAN 2014

Persistent flow acceleration within the interior of the Greenland ice sheet

Samuel H. Doyle[1], Alun Hubbard[1], Andrew A. W. Fitzpatrick[1], Dirk van As[2], Andreas B. Mikkelsen[3], Rickard Pettersson[4], and Bryn Hubbard[1]

[1]Department of Geography and Earth Sciences, Aberystwyth University, Aberystwyth, UK, [2]Geological Survey of Denmark and Greenland, Copenhagen, Denmark, [3]Department of Geosciences and Natural Resource Management, University of Copenhagen, Copenhagen, Denmark, [4]Earth Sciences, Uppsala University, Uppsala, Sweden

Abstract We present surface velocity measurements from a high-elevation site located 140 km from the western margin of the Greenland ice sheet, and ~ 50 km into its accumulation area. Annual velocity increased each year from 51.78 ± 0.01 m yr^{-1} in 2009 to 52.92 ± 0.01 m yr^{-1} in 2012—a net increase of 2.2%. These data also reveal a strong seasonal velocity cycle of up to 8.1% above the winter mean, driven by seasonal melt and supraglacial lake drainage. Sole et al. (2013) recently argued that ice motion in the ablation area is mediated by reduced winter flow following the development of efficient subglacial drainage during warmer, faster, summers. Our data extend this analysis and reveal a year-on-year increase in annual velocity above the equilibrium line altitude, where despite surface melt increasing, it is still sufficiently low to hinder the development of efficient drainage under thick ice.

1. Introduction

Our knowledge of the dynamics of the Greenland ice sheet (GrIS) has improved markedly over the last decade. The recent observation that reduced winter velocities offset faster summer velocities in warmer years [*Sole et al*., 2013], consolidated the seemingly contradictory findings that the magnitude of the summer acceleration correlates with surface melt intensity [*Zwally et al*., 2002], yet the long-term trend is of a slight decline in annually-averaged flow despite an increasingly negative surface mass balance [*van de Wal et al*., 2008]. *Sole et al*. [2013] argued that this regulating reduction in winter motion is caused by the evolution of a larger, more extensive subglacial drainage system in warmer summers, which drains regions of high basal water pressure and increases subsequent ice-bed coupling and traction. Although this process may hold for marginal areas of the ice sheet that experience intense summer surface melt and extensive delivery of meltwater to the basal interface (where the data supporting the hypothesis of *Sole et al*. [2013] were collected), it may be less effective at higher elevations, where melt rates are lower and ice thicknesses greater. Hence, we hypothesize that there exists an inland zone, most likely within and around the wet snow zone, that is characterized by enough surface melt to induce a seasonal acceleration but which is insufficient to develop the effective subglacial drainage required to regulate this acceleration through subsequent reduced winter flow. Although it has been speculated that the inland expansion of melt and supraglacial lakes (SGLs) will influence ice motion in this difficult to access zone [e.g., *Howat et al*., 2013; *Liang et al*., 2012], to date, velocity data have not been available to test this hypothesis. Field-based Global Positioning System (GPS) measurements are currently the only method capable of determining long-term changes in flow within the ice sheet's interior; remote-sensing techniques fail due to a lack of coherence [e.g., *Joughin et al*., 2010].

In this paper, we present a 5 year (September 2008–September 2013) time series of ice surface velocity measurements recorded by a dual-frequency GPS receiver located within the accumulation area. The aims of this analysis are (i) to report and evaluate the nature of the site's velocity record, particularly in relation to seasonality and interannual change and (ii) to evaluate the transferability of the self-regulation model of *Sole et al.* [2013] to higher elevations within the ice sheet's interior.

2. Data and Methods

We applied rigorous processing to dual-frequency GPS data sampled at a 10 s interval from September 2008 onward by a receiver deployed at the highest site (S10) on the land-terminating K-transect in West Greenland

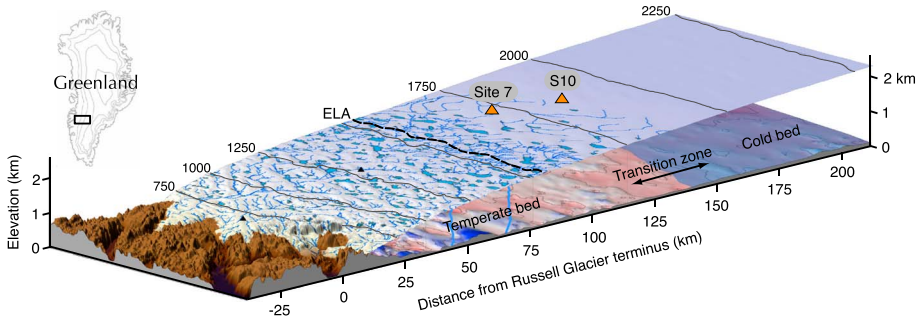

Figure 1. Cross section of Russell Glacier catchment showing the locations of the GPS sites, including S10 of this study and Site 7 of *Sole et al.* [2013]. The surface elevation is from *Howat et al.* [2014], the bed topography is from *Bamber et al.* [2013], and the basal thermal regime is conceptual. The maximum SGL and stream extent between 2002 and 2012, adapted from *Fitzpatrick et al.* [2014], and the mean 1990–2011 ELA of 1553 m asl [*van de Wal et al.*, 2012] are also shown. The black box on the inset map shows the location of the study area in Greenland.

(Figure 1). S10 (N67.00°, W47.02°) is colocated with an automated weather station at 1840 m above sea level (asl), 140 km from the ice margin and more than 50 km inland from the 21-year-mean mass balance equilibrium line altitude (ELA) of 1553 m asl, as estimated by *van de Wal et al.* [2012]. These data, from five contrasting melt seasons (2009 to 2013), encompass high seasonal and interannual variability in melt conditions. Periods of power outage reduced the continuity of GPS measurements prior to April 2011. Although these outages do not degrade the long-term velocity record, they prevent analysis of transient velocity variations during the summers of 2009 and 2010 (Figure 2a). Long-term trends in velocity are reported using summer (1 May to 10 September), winter (10 September to 1 May), and annual (1 May to 1 May) periods. These surface velocity data are compared with contemporaneous meteorological variables [*van As et al.*, 2012], proglacial discharge [*Hasholt et al.*, 2013], and SGL data [*Fitzpatrick et al.*, 2014]. Further details of the methods employed are given in the supporting information.

3. Results

The mean rate of ice motion at S10 between September 2008 and September 2013 was 52.26 ± 0.01 m yr^{-1} to the west (274.5°). Over this period, ice flow was consistently faster during the summer than the winter, and in the years with available data, the timing and amplitude of the seasonal velocity cycle correlates with the duration and intensity of the melt season (Figure 2). In 2011 and 2012, initial accelerations in May of ~1% above the mean winter velocity (51.89 m yr^{-1}), were followed by larger (5.2% in 2011 and 8.1% in 2012) and longer, midsummer velocity increases between June and September (Figure 2a). In the cooler 2013 summer, although still apparent, this seasonal pattern was retarded with a small initial acceleration of 1.3 to 1.7% above the winter mean persisting for longer into July before flow increased to 4.6% above winter values in early August (Figure 2a). Maximum velocity occurred in early August and in years with available data velocities returned to mean winter values, or below, by the end of September (Figure 2a). These patterns are consistent with previous observations from Greenland [*Fitzpatrick et al.*, 2013; *Joughin et al.*, 2010; *Joughin et al.*, 2008; *Zwally et al.*, 2002], which reveal that ice flow gradually increases over winter from an all year minimum in autumn. Within error, no short-term variation in surface elevation was detected, which lowered commensurate with downslope ice motion at a mean rate of 1.08 ± 0.06 m yr^{-1} (Figure S1).

Our velocity record from S10 (Figures 2a and 3a) supports observations of faster summer flow during warmer years [e.g., *Zwally et al.*, 2002; *Sole et al.*, 2013]. Mean summer velocity increased during successively warmer years, from 51.82 ± 0.04 m yr^{-1} in 2009 to 52.66 ± 0.04 m yr^{-1} in 2010 and 52.94 ± 0.04 m yr^{-1} in 2011, and was notably higher (53.96 ± 0.04 m yr^{-1}) during the record melt year of 2012 (Figure 3a). In contrast to previous studies [e.g., *van de Wal et al.*, 2008], we also find evidence for a long-term increase in ice velocity at S10. Summer of 2013 was still the second fastest (53.18 ± 0.04 m yr^{-1}) on record despite cool conditions, and the previous winter velocity of 52.33 ± 0.02 m yr^{-1} was substantially above average—even exceeding the 2009 mean summer velocity by 0.5 m yr^{-1}. Excluding winter 2010/2011, year-on-year winter flow accelerated by $\sim 0.05 \pm 0.03$ m yr^{-2} between 2009 and 2012 (Figure 3a; Table S1). These cumulative trends in summer and winter flow yield a long-term increase in mean annual surface velocity at S10 (Figure 3a; Table S2).

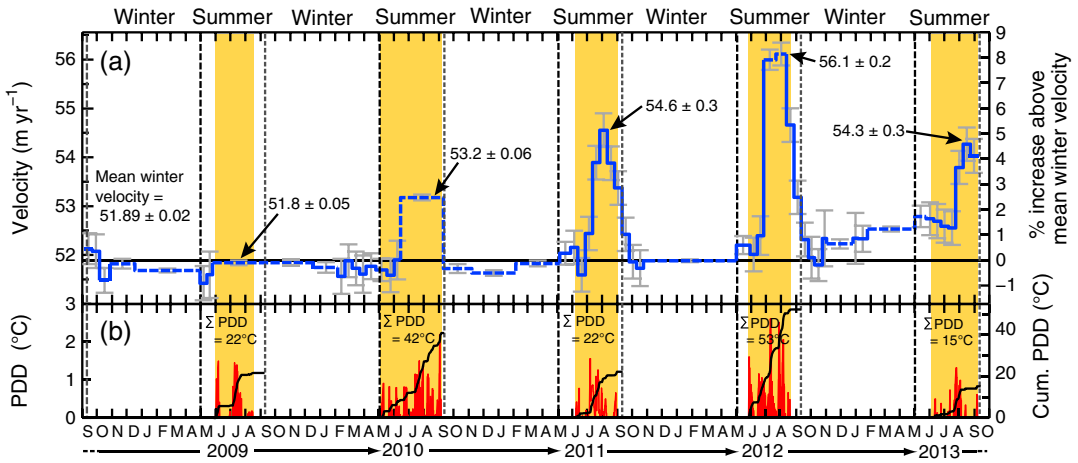

Figure 2. (a) Velocity at S10 between September 2008 and October 2013. Dashed lines indicate averaging periods longer than 15 days, which may reduce the apparent amplitude of velocity variations, particularly during summer 2009 and summer 2010. The horizontal grey line represents the mean winter velocity, averaged over all five winters, of 51.89 m yr^{-1}, (b) positive degree days (PDD) at S10 in red, with the cumulative PDD in black. The orange shading highlights the melt seasons at S10. The vertical dashed black lines and arrows delineate the summer (1 May to 10 September), winter (10 September to 1 May), and annual (1 May to 1 May) averaging periods used in this study.

4. Discussion

Drawing on existing glaciohydrological theory, *Sole et al.* [2013] posited that enhanced ice motion across the ablation area during warmer summers is offset by reduced winter velocities caused by the drainage of areas of high basal water pressure by larger and more extensive subglacial channels. Our observations at S10 of higher winter velocities following warmer, faster summers, and the ensuing year-on-year increase in net flow (Figure 3a), contrasts with these findings of *Sole et al.* [2013], which are based on the analysis of GPS data from sites within the ablation area. The year-on-year annual flow acceleration measured at S10 (1840 m asl) is, however, consistent with their uppermost GPS site (Site 7; 1715 m asl), which is also located above the ELA (Figure 4). Between 2009 and 2012, the mean annual (May to May) increase in velocity at S10 of 0.7% per year is directly comparable to the 0.9% increase per year between 2009 and 2011 at Site 7 of *Sole et al.* [2013]. The seasonal variations in velocity—the percentage summer increase above the subsequent winter mean—are also similar, with the 0.1% (2009), 1.8% (2010), 2.0% (2011), and 3.0% (2012) measured at S10 comparable to, though expectedly lower than the 0.2% (2009), 7.2% (2010) and 6.9% (2011) seasonal accelerations measured at Site 7.

We argue that although the observations of net flow acceleration at S10 and Site 7 conflict with the main conclusions of *Sole et al.* [2013], they remain compatible with generalized glaciohydrological theory [e.g., *Fountain and Walder*, 1998; *Hubbard and Nienow*, 1997; *Iken and Truffer*, 1997; *Rothlisberger and Lang*, 1987; *Schoof*, 2010] by considering the reduced likelihood of developing an effective subglacial drainage system in the ice sheet's interior. Such development will be hindered by at least two factors. First, lower rates of surface meltwater production and runoff over a shorter melt season at higher elevations result in substantially lower volumes of melt being delivered to the ice sheet's basal drainage system [*van As et al.*, 2012], thereby reducing the capacity of that system to develop an efficient network [*Pimental and Flowers*, 2010; *Schoof*, 2010]. Second, across and above the ELA, and away from the relatively thin ablation area, ice thickness exceeds 1200 m [*Bamber et al.*, 2013, Figure 1]. At S10, radio echo sounding indicates an ice thickness of 1590 ± 17 m. Under these conditions, high overburden pressures at the bed would theoretically force rapid (~ 1 h at S10) creep closure of any subglacial channel or cavity not completely pressurized to overburden [e.g., *Nye*, 1953; *Hooke et al.*, 1990; *Chandler et al.*, 2013]. This compares with several days for creep-closure of ice of a few hundred meters thickness at the margin [*Nye*, 1953; *Chandler et al.*, 2013]. Both of these inferences are supported by recent observations. Repeat tracing experiments suggest that (i) an efficient, channelized subglacial drainage system does develop during the melt season up to at least 41 km from the ice margin, (ii) that this system is pressurized more than 7 km from the margin, and (iii) that an inefficient, distributed drainage system is likely to dominate further inland [*Chandler et al.*, 2013]. Furthermore, at two sites, 17 and 34 km from the ice margin, *Meierbachtol et al.* [2013] observed continuously high borehole water pressures,

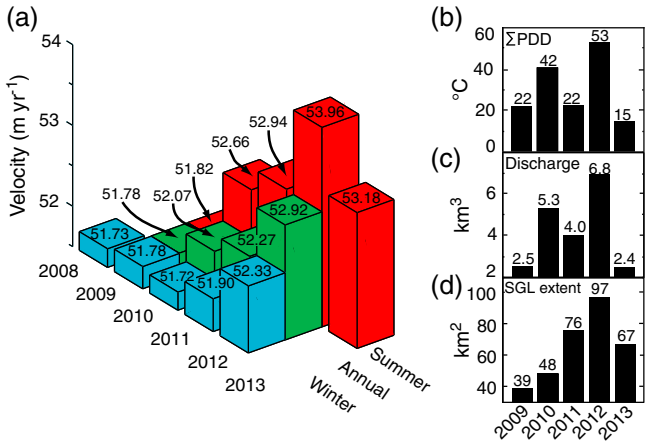

Figure 3. (a) Mean winter, annual, and summer velocities at S10 between 2009 and 2013, (b) the PDD sum at S10, (c) the total annual proglacial discharge at Watson River Bridge, and (d) the areal extent of high-elevation SGLs (those above 1400 m asl) in our study area. The data contributing to (a) are listed in Tables S1 to S3. Correlation coefficients between these variables are listed in Table S5.

which, although spatially limited, are inconsistent with drainage through an extensive network of low-pressure channels. Given these theoretical inferences and limited observations from up to 50 km from the ice margin, it is plausible that the mechanism of self-regulation invoked by *Sole et al.* [2013] across the ablation area is not prevalent at higher elevations within the ice sheet's interior.

The five contrasting melt seasons analyzed in this study provide an opportunity to examine the dynamic response of the GrIS's interior to variations in atmospherically forced melt, which we characterize using positive degree days (PDDs) and proglacial discharge (Figure 3). For the five melt seasons (2009 to 2013) the respective total PDDs at S10 were 21.7, 42.0, 21.9, 53.1, and 15.1°C (Figure 3b). The corresponding totals in proglacial discharge of 2.5, 5.3, 4.0, 6.8, and 2.4 km^3 show a similar interannual variation as the PDD sum ($r^2 = 0.96$, $p = 0.01$), with the exception of 2011 when discharge was disproportionately large (Figure 3c; Table S5). The fastest annual and summer flow at S10 occurred in 2012: a record melt season [*Nghiem et al.*, 2012] distinguished by unprecedented proglacial discharge and the highest PDD sum at S10 (Figure 3). In contrast, the year with the lowest annual and summer velocity, 2009, had the second lowest PDD sum (21.9°C) and proglacial discharge (Figure 3). Comparing the S10 velocities during the two coldest years (2009 and 2013) reveals that the PDD sum cannot, however, fully explain the interannual variations in velocity at S10. During 2009 (second coldest), velocities were low and the seasonal variation was minimal (0.1%). In contrast, the coldest summer of 2013 was the second fastest with a distinct, albeit lagged, seasonal acceleration (Figures 2a and 3).

A lack of observable crevasses, moulins, and seasonal surface uplift (Figure S1) indicates that surface water is unlikely to be accessing the bed directly beneath S10. Nevertheless, strain perturbations can be transmitted on the order of tens of kilometers by longitudinal (along-flow) stress-gradient coupling [*Hindmarsh*, 2006; *Kamb and Echelmeyer*, 1986; *Price et al.*, 2008]. Hence, the flow perturbations at S10 could have their origin down glacier where the presence of crevasses, rapidly draining SGLs, and moulins indicate that surface meltwater is directly accessing the bed. Although melt is inherently diffuse, the delivery of surface water to the bed is focused—in both space and time—by SGL drainage. Indeed, it is widely recognized that SGLs, which have formed at successively higher elevations during warmer summers over the last three decades [*Fitzpatrick et al.*, 2014; *Howat et al.*, 2013; *Liang et al.*, 2012, Figure S2], play an important role in establishing the hydraulic pathways that enable surface water to directly access the ice-bed interface through kilometer-thick ice [e.g., *Das et al.*, 2008; *Doyle et al.*, 2013].

In West Greenland, the elevation of the highest SGL increased from 1670 m asl in the mid-1980s to above 1800 m asl in 2011—representing an inland expansion of SGLs of 30 km that closely tracked the rising ELA [*Howat et al.*, 2013]. The elevation of the highest SGL in our study area increased from 1689 m asl in 2009 to 1790 m asl in 2010 and 1827 m asl in 2011, where it reformed in 2012 and 2013 (Figure S2). That no higher SGLs formed during the record melt year of 2012 compared to 2011 suggests a limit or pause in the inland expansion of SGLs. Although it has been suggested that the paucity of surface depressions in the interior may hinder the formation of SGLs [*Howat et al.*, 2013], it is also possible that the storage capacity of the firn has not

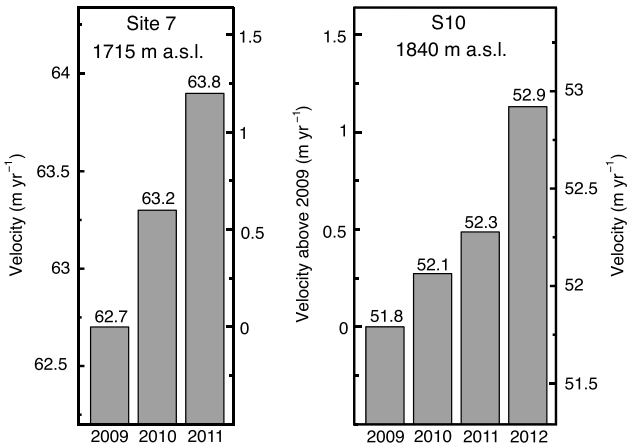

Figure 4. Annual velocity at Site 7 of *Sole et al.* [2013] and S10. The center axes show the speed above the respective 2009 velocity.

yet been attained at these higher elevations [*Harper et al.*, 2012]. That the same high-elevation SGLs formed again in the relatively cold year of 2013 does, however, suggest that SGLs are self-sustaining—possibly through deepening of the lake bed by increased radiation absorption, and through the establishment of a surface drainage network, which feeds them and persists from year to year. Hence, once established, SGLs appear to reform readily in the same, high-elevation surface depressions in subsequent summers even if significantly cooler.

In our study area, the spatial extent of SGLs above 1400 m asl (hereafter termed the high-elevation SGL extent), which increased each year from 2009 to 2012, appears to scale with ice motion at S10 (Figure 3). The high-elevation lake extent shows significant positive correlation ($r^2 > 0.9$; $p < 0.1$) with mean summer, winter, and annual velocities at S10 (Table S5). The rate of inland SGL expansion even surpassed increases in atmospheric forcing. For example, despite a lower PDD sum in 2011, high-elevation SGLs were still more extensive than they were in 2010 (Figure 3). Annual total proglacial discharge was also disproportionately large in 2011 relative to the PDD sum (Figure 3). This disparity can be explained by abnormally low snowfall during the previous winter [*Box et al.*, 2011] and the progressive interannual decline in surface albedo [*Box et al.*, 2012], which increased melt generation and runoff disproportionately at high elevations during 2011 [*Box et al.*, 2011; *van de Wal et al.*, 2012]. Furthermore, the areal extent and upper limit of high-elevation SGLs was abnormally large during the relatively cold 2013 melt season (Figures 3d and S2). Hence, together with an inland migration of the ELA [*van de Wal et al.*, 2012] and the associated decrease in storage and refreeze potential of the firn, we suggest that low snowfall and surface albedo were responsible for the disproportionate increase in melt and SGL formation at high elevations between 2009 and 2013.

As SGLs expand inland, surface water may reach new areas of the bed, increasing the energy flux to this potentially frozen basal zone. It has also been hypothesized that the latent and sensible heat released by refreezing will warm the ice sheet, reducing its viscosity and enhancing internal deformation [*Phillips et al.*, 2010]. The increase in mean winter velocity at S10 following the exceptional 2012 melt season (Figure 3a)—which cannot be directly attributed to surface melt water accessing the bed during winter—could reflect such changes in rheology or basal conditions [*Phillips et al.*, 2010]. That annual ice velocity was faster at S10 during the record melt year of 2012 compared to the relatively cold year of 2009 is at odds with the observations of *Tedstone et al.* [2013] from the ablation area, which extend the time series of *Sole et al.* [2013] into 2012. Furthermore, the subsequent winter (2012/2013) at S10 was substantially faster (52.33 ± 0.02 m yr^{-1}) than all previous winters (mean = 51.78 ± 0.02 m yr^{-1}) and even exceeded the 2009 summer mean. These results suggest that the exceptional runoff during the 2012 melt season caused a fundamental change in basal conditions and ice dynamics in the vicinity of S10. Possible explanations include increased water storage at the bed following the 2012 melt season resulting in sustained higher subglacial water pressures and reduced basal traction, or increased energy flux into this potentially frozen zone, warming the ice, enhancing internal deformation, and/or decoupling frozen sticky spots. Thus, although summer flow acceleration at S10 reveals a direct response to surface meltwater production, the important observation that winter flow is also increasing suggests a longer-term structural change in the subglacial hydrothermal regime, possibly associated with

an increased flux of meltwater and energy to the ice-bed interface. Further and more direct observations (e.g., borehole instrumentation and repeat geophysical surveys to determine changes in the material and thermal properties of the bed) would be required to explain definitively why the velocity at S10 increased between 2009 and 2012, especially with regard to the increase in mean winter velocity following the exceptional melt in summer 2012.

Although the 2.2 % net velocity increase at S10 between 2009 and 2012 is modest, it should be noted that it has been previously assumed [e.g., *Colgan et al*., 2009; 2012; *Phillips et al*., 2013] that the ice sheet's interior does not experience any variation in flow. The implicit assumption in these studies is that ice motion can be attributed to internal deformation alone, which would not be expected to vary on short, seasonal timescales. Furthermore, from mass continuity considerations, as the ice thickness at S10 (1590 m) greatly exceeds that closer to the margin, the impact of any given net change in ice flow on mass flux here will be substantially greater compared to downstream zones, nearer the ice margin. Finally, although these observations of a year-on-year increase in annual velocity are limited to just two locations above the ELA (and we are unaware of any other GPS observations from this interior zone of the ice sheet), we speculate that such behavior could be pervasive over a broader lateral swath of the ice sheet's wet snow zone, since flow in this interior region may be less constrained by basal topography, which channels flow into distinct outlet units within the ablation zone [*Palmer et al*., 2011; *Fitzpatrick et al*., 2013; *Joughin et al*., 2008; 2010].

5. Conclusions

A 5 year time series of surface velocity measurements from a GPS receiver located 140 km from the ice margin reveals that seasonal variations in ice motion, of up to 8% above the winter mean, occur at least 50 km upglacier of the long-term mean ELA. Summer velocities at this site reflect variations in surface melt modulated by SGL drainage. The year-on-year increase in annual velocities at S10 between 2009 and 2012 suggests that an increased penetration of water to the ice-bed interface at successively greater distances from the ice margin is driving faster ice motion at high elevations on the GrIS.

Two distinct patterns of ice dynamic response to atmospheric forcing have now been observed. In the ablation area, *Sole et al*. [2013] argued that channelized subglacial hydrology regulates ice flow through reduced winter velocities following warmer, faster summers. Above the ELA, we find that winter, summer, and annual velocities followed an increasing trend between 2009 and 2013. Finally, in accordance with *Truffer et al*. [2005], we caution against extending observations from Alaskan glaciers [*Burgess et al*.,2013], as well as from the ablation zone [*Sole et al*.,2013; *Tedstone et al*.,2013] to interior regions of the GrIS, where greater ice thickness and lower melt precludes the development of efficient subglacial drainage and its regulating influence on ice flow.

Acknowledgments

This research was funded by SKB-Posiva through the Greenland Analogue Project (Subproject A) and UK Natural Environmental Research Council grant NE/G005796. We thank UNAVCO, MIT, Matt King, Katrin Lindback, and Heidi Sevestre for help with data collection and processing. S.H.D. was supported by an Aberystwyth University doctoral scholarship.

The Editor thanks Peter Jansson and an anonymous reviewer for their assistance in evaluating this paper.

References

Bamber, J. L., et al. (2013), A new bed elevation dataset for Greenland, *Cryosphere*, *7*(2), 499–510, doi:10.5194/tc-7-499-2013.

Box, J. E., et al. (2011), Greenland ice sheet, in *Arctic Report Card 2011*, edited by J. Richter-Menge, M. O. Jeffries, and J. E. Overland, pp. 117–138. [Available at http://www.arctic.noaa.gov/report11/.]

Box, J. E., X. Fettweis, J. C. Stroeve, M. Tedesco, D. K. Hall, and K. Steffen (2012), Greenland ice sheet albedo feedback: Thermodynamics and atmospheric drivers, *Cryosphere*, *6*(4), 821–839, doi:10.5194/Tc-6-821-2012.

Burgess, E. W., C. F. Larsen, and R. R. Forster (2013), Summer melt regulates winter glacier flow speeds throughout Alaska, *Geophys. Res. Lett.*, *40*, 6160–6164, doi:10.1002/2013GL058228.

Chandler, D. M., et al. (2013), Evolution of the subglacial drainage system beneath the Greenland ice sheet revealed by tracers, *Nat. Geosci.*, *6*(3), 195–198, doi:10.1038/Ngeo1737.

Colgan, W., H. Rajaram, R. Anderson, K. Steffen, J. Zwally, T. Phillips, and W. Abdalati (2012), The annual glaciohydrology cycle in the ablation zone of the Greenland ice sheet: Part 2. Observed and modeled ice flow, *J. Glaciol.*, *58*, 51–64, doi:10.3189/2012JoG11J081.

Colgan, W. T., T. P. Phillips, R. S. Anderson, H. J. Zwally, W. Abdalati, H. Rajaram, and K. Steffen (2009), Similarities in basal sliding between Greenland and Alpine Glaciers, *Eos Trans. AGU, 90*(52), Fall Meet. Suppl., Abstract C23B-0499. [Available at http://adsabs.harvard.edu/abs/2009AGUFM.C23B0499C.]

Das, S. B., I. Joughin, M. D. Behn, I. M. Howat, M. A. King, D. Lizarralde, and M. P. Bhatia (2008), Fracture propagation to the base of the Greenland ice sheet during supraglacial lake drainage, *Science*, *320*(5877), 778–781, doi:10.1126/science.1153360.

Doyle, S. H., A. L. Hubbard, C. F. Dow, G. A. Jones, A. Fitzpatrick, A. Gusmeroli, B. Kulessa, K. Lindback, R. Pettersson, and J. E. Box (2013), Ice tectonic deformation during the rapid in situ drainage of a supraglacial lake on the Greenland ice sheet, *Cryosphere*, *7*(1), 129–140, doi:10.5194/Tc-7-129-2013.

Fitzpatrick, A., A. L. Hubbard, I. R. Joughin, D. J. Quincey, D. van As, A. P. B. Mikkelsen, S. H. Doyle, B. Hasholt, and A. G. Jones (2013), Ice flow dynamics and surface meltwater flux at a land-terminating sector of the Greenland ice sheet, *J. Glaciol.*, *59*(216), 687–696, doi:10.3189/2013JoG12J143.

Fitzpatrick, A. A. W., A. L. Hubbard, J. E. Box, D. J. Quincey, D. van As, A. P. B. Mikkelsen, S. H. Doyle, C. F. Dow, B. Hasholt, and G. A. Jones (2014), A decade (2002 – 2012) of supraglacial lake volume estimates across Russell Glacier, West Greenland, *Cryosphere*, *8*, 107–121, doi:10.5194/tc-8-107-2014.

Fountain, A. G., and J. S. Walder (1998), Water flow through temperate glaciers, *Rev. Geophys.*, *36*(3), 299–328, doi:10.1029/97rg03579.

Harper, J., N. Humphrey, W. T. Pfeffer, J. Brown, and X. Fettweis (2012), Greenland ice-sheet contribution to sea-level rise buffered by meltwater storage in firn, *Nature*, *491*(7423), 240–243, doi:10.1038/nature11566.

Hasholt, B., A. B. Mikkelsen, M. H. Nielsen, and M. A. D. Larsen (2013), Observations of runoff and sediment and dissolved loads from the Greenland ice sheet at Kangerlussuaq, West Greenland, 2007 to 2010, *Z. Geomorphol.*, *57*(Suppl. 2), 3–27, doi:10.1127/0372-8854/2012/S-00121.

Hindmarsh, R. C. A. (2006), The role of membrane-like stresses in determining the stability and sensitivity of the Antarctic ice sheets: Back pressure and grounding line motion, *Philos. Trans. R. Soc., A*, *364*(1844), 1733–1767, doi:10.1098/Rsta.2006.1797.

Hooke, R., T. Laumann, and J. Kohler (1990), Subglacial water pressures and the shape of subglacial conduits, *J. Glaciol.*, *36*(122), 67–71.

Howat, I. M., S. de la Peña, J. H. van Angelen, J. T. M. Lenaerts, and M. R. van den Broeke (2013), Brief communication: "Expansion of meltwater lakes on the Greenland ice sheet", *Cryosphere*, *7*, 201–204, doi:10.5194/tc-7-201-2013.

Howat, I. M., A. Negrete, and B. E. Smith (2014), The Greenland Ice Mapping Project (GIMP) land classification and surface elevation datasets, *Cryosphere Discuss.*, *8*, 453–478, doi:10.5194/tcd-8-453-2014.

Hubbard, B., and P. Nienow (1997), Alpine subglacial hydrology, *Quat. Sci. Rev.*, *16*(9), 939–955, doi:10.1016/S0277-3791(97)00031-0.

Iken, A., and M. Truffer (1997), The relationship between subglacial water pressure and velocity of Findelgletscher, Switzerland, during its advance and retreat, *J. Glaciol.*, *43*(144), 328–338.

Joughin, I., S. B. Das, M. A. King, B. E. Smith, I. M. Howat, and T. Moon (2008), Seasonal speedup along the western flank of the Greenland ice sheet, *Science*, *320*(5877), 781–783, doi:10.1126/science.1153288.

Joughin, I., B. E. Smith, I. M. Howat, T. Scambos, and T. Moon (2010), Greenland flow variability from ice-sheet-wide velocity mapping, *J. Glaciol.*, *56*(197), 415–430, doi:10.3189/002214310792447734.

Kamb, B., and K. A. Echelmeyer (1986), Stress-gradient coupling in glacier flow: I. Longitudinal averaging of the influence of ice thickness and surface slope, *J. Glaciol.*, *32*(111), 267–298.

Liang, Y. L., W. Colgan, Q. Lv, K. Steffen, W. Abdalati, J. Stroeve, D. Gallaher, and N. Bayou (2012), A decadal investigation of supraglacial lakes in West Greenland using a fully automatic detection and tracking algorithm, *Remote Sens. Environ.*, *123*, 127–138, doi:10.1016/J.Rse.2012.03.020.

Meierbachtol, T., J. Harper, and N. Humphrey (2013), Basal drainage system response to increasing surface melt on the Greenland ice sheet, *Science*, *341*(6147), 777–779, doi:10.1126/science.1235905.

Nghiem, S. V., D. K. Hall, T. L. Mote, M. Tedesco, M. R. Albert, K. Keegan, C. A. Shuman, N. E. DiGirolamo, and G. Neumann (2012), The extreme melt across the Greenland ice sheet in 2012, *Geophys. Res. Lett.*, *39*, L20502, doi:10.1029/2012gl053611.

Nye, J. F. (1953), The flow law of ice from measurements in glacier tunnels, laboratory experiments and the Jungfraufirn borehole experiment, *Proc. Roy. Soc. Lond. Math. Phys. Sci.*, *219*(1139), 477–489, doi:10.1098/Rspa.1953.0161.

Palmer, S., A. Shepherd, P. Nienow, and I. Joughin (2011), Seasonal speedup of the Greenland ice sheet linked to routing of surface water, *Earth Planet. Sci. Lett.*, *302*, 423–428, doi:10.1016/j.epsl.2010.12.037.

Phillips, T., H. Rajaram, and K. Steffen (2010), Cryo-hydrologic warming: A potential mechanism for rapid thermal response of ice sheets, *Geophys. Res. Lett.*, *37*, L20503, doi:10.1029/2010gl044397.

Phillips, T., H. Rajaram, W. Colgan, K. Steffen, and W. Abdalati (2013), Evaluation of cryo-hydrologic warming as an explanation for increased ice velocities in the wet snow zone, Sermeq Avannarleq, West Greenland, *J. Geophys. Res. Earth Surf.*, *118*, 1–16, doi:10.1002/jgrf.20079.

Pimental, S., and G. Flowers (2010), A numerical study of hydrologically driven glacier dynamics and subglacial flooding, *Proc. R. Soc.*, *467*, 537–558, doi:10.1098/rspa.2010.0211.

Price, S. F., A. J. Payne, G. A. Catania, and T. A. Neumann (2008), Seasonal acceleration of inland ice via longitudinal coupling to marginal ice, *J. Glaciol.*, *54*(185), 213–219, doi:10.3189/002214308784886117.

Rothlisberger, H., and H. Lang (1987), Glacial hydrology, in *Glacio-Fluvial Sediment Transfer: An Alpine Perspective*, edited by A. M. Gurnell and M. J. Clark, pp. 207–284, John Wiley, New York.

Schoof, C. (2010), Ice-sheet acceleration driven by melt water supply variability, *Nature*, *468*, 803–806, doi:10.1038/nature09618.

Sole, A., P. Nienow, I. Bartholomew, D. Mair, T. Cowton, A. Tedstone, and M. King (2013), Winter motion mediates dynamic response of the Greenland ice sheet to warmer summers, *Geophys. Res. Lett.*, *40*, 3940–3944, doi:10.1002/grl.507764.

Tedstone, A. J., P. W. Nienow, A. J. Sole, D. W. F. Mair, T. R. Cowton, I. D. Bartholomew, and M. A. King (2013), Greenland ice sheet motion insensitive to exceptional meltwater forcing, *Proc. Natl. Acad. Sci.*, doi:10.1073/pnas.1315843110.

Truffer, M., W. Harrison, and R. March (2005), Record negative glacier balances and low velocities during the 2004 heatwave in Alaska, USA: Implications for the interpretation of observations by Zwally and others in Greenland, *J. Glaciol.*, *51*, 663–664.

van As, D., A. L. Hubbard, B. Hasholt, A. B. Mikkelsen, M. R. van den Broeke, and R. S. Fausto (2012), Large surface meltwater discharge from the Kangerlussuaq sector of the Greenland ice sheet during the record-warm year 2010 explained by detailed energy balance observations, *Cryosphere*, *6*, 199–209, doi:10.5194/tc-6-199-2012.

van de Wal, R. S. W., W. Boot, M. R. van den Broeke, C. J. P. P. Smeets, C. H. Reijmer, J. J. A. Donker, and J. Oerlemans (2008), Large and rapid melt-induced velocity changes in the ablation zone of the Greenland ice sheet, *Science*, *321*(5885), 111–113, doi:10.1126/science.1158540.

van de Wal, R. S. W., W. Boot, C. J. P. P. Smeets, H. Snellen, M. R. van den Broeke, and J. Oerlemans (2012), Twenty-one years of mass balance observations along the K-transect, West Greenland, *Earth Syst. Sci. Data*, *4*(1), 31–35, doi:10.5194/essdd-5-351-2012.

Zwally, J. H., W. Abdalati, T. Herring, K. Larson, J. Saba, and K. Steffen (2002), Surface melt-induced acceleration of Greenland ice-sheet flow, *Science*, *297*(5579), 218–222, doi:10.1126/science.1072708.